Gran Sasso Science Institute

Scuola Internazionale Superiore di Studi Avanzati

Optimization of the CUORE detector during the commissioning phase

PhD thesis

submitted February 20, 2017

PhD Candidate

Stefano Dell'Oro

Advisors

Oliviero Cremonesi
INFN, Sezione di Milano-Bicocca

Paolo Gorla
INFN, Laboratori Nazionali del Gran Sasso

Tutor

Lucia Canonica
Massachusetts Institute of Technology

Gran Sasso Science Institute

Ciclo XXIX – A. A. 2013-2016

Optimization of the CUORE detector during the commissioning phase

S. Dell'Oro

Abstract

This thesis work is developed in the framework of the CUORE experiment. CUORE (Cryogenic Underground Observatory for Rare Events) is presently (January 2017) in the initial phase of the detector commissioning at the Laboratori Nazionali del Gran Sasso (Italy). CUORE will search for the neutrinoless double beta decay ($0\nu\beta\beta$) of ^{130}Te with an array of 988 bolometers.

The first part of the thesis introduces the Physics and the technology of interest for CUORE. In particular, the general overview of $0\nu\beta\beta$ is inserted within the frame of the current theoretical understanding, and the results of original works and analyses are reported. Concerning the introduction to bolometers, a wider and technical overview is followed by the more specific description of the use of TeO_2 crystals for the $0\nu\beta\beta$ search, briefly summarizing the long chain of experiments leading to CUORE and stressing the importance of the recent results coming from the CUORE-0 detector.

The core of the thesis focuses on the commissioning of the CUORE experimental apparatus. After a detailed description of the cryogenic system, the relevant steps of the commissioning phase are reviewed. In particular, the analyses of the cryogenic data are presented together with the developments that allowed the cryostat to reach its final configuration, and thus be ready to host the CUORE detector.

The final part is devoted to the description of the analysis and of the results obtained with the first prototype detector operated as a bolometer inside the CUORE cryostat. In fact, its study proved to be fundamental to understand how to optimize the system cryogenic performance in view of the forthcoming (much complex) CUORE detector.

The CUORE cryostat commissioning phase was long and complex, but indeed an indispensable prerequisite for a stable and long operation in extreme conditions of low temperature, noise and activity, opening the way to one of the most sensitive search for $0\nu\beta\beta$.

Contents

Introduction

The discovery of neutrino masses through the observation of oscillations has boosted the importance of neutrinoless double beta decay ($0\nu\beta\beta$). This rare process is a direct probe of Beyond the Standard Model Physics, since it violates the lepton number by two units. Furthermore, $0\nu\beta\beta$ allows us to investigate the Dirac/Majorana nature of the neutrino and to get information on the neutrino absolute mass scale and ordering.

This thesis work is developed in the framework of the CUORE experiment. CUORE (Cryogenic Underground Observatory for Rare Events) will search for the $0\nu\beta\beta$ of ^{130}Te with an array of 988 bolometers. The experiment is currently (January 2017) in the initial phase of the detector commissioning at the Laboratori Nazionali del Gran Sasso (Italy).

CUORE, with its total detector mass of over 740 kg of TeO_2, represents today the state of art of bolometric detectors. Bolometers satisfy the requirements of extremely low background and excellent energy resolution fundamental for the search for $0\nu\beta\beta$. They also offer the feasible prospect of experiments with large mass, thus promising to play a key role in the near future. Indeed, tonne-scale detectors will be needed to push the sensitivity down to the Inverted Hierarchy of the neutrino mass spectrum.

In the first part of the thesis, the Physics of interest for CUORE and the experimental aspects are introduced. A general overview of $0\nu\beta\beta$ is presented in Chapter 1. Starting from the concept of Majorana neutrinos, the $0\nu\beta\beta$ process is investigated within the particle physics scenario in which the Majorana mass of ordinary neutrinos dominate the decay rate. The phenomenological discussion briefly reviews the current knowledge on the neutrino masses, updating the predictions from oscillations and combining these with the data from the cosmological surveys. While considering the nuclear physics behind the $0\nu\beta\beta$, special attention is paid to the uncertainties, with the study on the impact of the quenching of the axial vector coupling constant in the nuclear medium. The experimental discussion pans over the challenges of the $0\nu\beta\beta$ search and presents the various techniques employed. By joining the information from the theoretical and the experimental sides, it was possible to assess the sensitivity of present and near future detectors and to analyze the prospects for a further future hunt for $0\nu\beta\beta$.

Concerning the thermal detectors, a wider overview is presented in Chapter 2. The fundamental elements of a bolometer are inserted in a simplified thermal model for the description of the signal generation. The bolometric technique performance and operating principle are illustrated in the case of interest for the CUORE (and similar) detectors. The last part of the chapter focuses on the cryogenic environment needed to run a thermal detector, introducing the experimental apparatus of the dilution refrigerator.

In Chapter 3, the role of TeO_2 crystals in the search for $0\nu\beta\beta$ is discussed. This material is particularly suitable for the use in cryogenic particle detectors, as the long and successful chain of TeO_2 bolometric experiments leading to CUORE proves. The recent results from CUORE-0, reported in the chapter, are an example of the excellent performance that can be achieved with the bolometric technique. An example is the energy resolution of 5 keV FWHM reached in the ^{130}Te $0\nu\beta\beta$ region of interest. At the same time, CUORE-0 set one of the current most stringent limits on the $0\nu\beta\beta$ half-life, $4.0 \cdot 10^{24}$ yr (@ 90% C. L.). The target of CUORE is even more ambitious, both in the cryogenic performance and in the Physics goal. In fact, its target sensitivity is $9.5 \cdot 10^{25}$ yr (@ 90% C. L.).

The core of the thesis focuses on the commissioning of the CUORE experimental apparatus. In Chapter 4, a general overview of the CUORE cryostat is presented, together with a detailed described of all its sub-systems. Special attention is paid to the solutions identified in order to satisfy the very stringent experimental requirements. In fact, the radio-purity and low-noise environment requests of a rare event physics experiment had to be each time added to the material, dimensioning and mechanical constraints imposed by cryogenics.

Chapter 5 reviews the relevant steps of the cryostat commissioning phase. For each test run, the progresses in the preparatory and cool down phases are described and, depending on the specific case and goals, different aspects and results are more deeply investigated.[1] The analysis of the cryogenic data was crucial to allow the series of developments that led cryostat to reach its final and complete configuration. The compliance with the designed specification and the check of the cryogenic performance, a stable base temperature of 6 mK and a cooling power of 3 μW at 10 mK, were the first fundamental requirements to satisfy before proceeding with the installation of the CUORE detector.

A peculiar aspect of the CUORE experiment is the use of Roman lead of archaeological origin for one of the detector shield. This lead has unique properties in terms of poor intrinsic radioactivity, being it completely depleted of the contaminant ^{210}Pb, which make it ideal for a $0\nu\beta\beta$ experiment. In Chapter 6, the preparation and casting operations of the Roman lead shield are carefully described. In fact, handling and manufacturing what are to all effects archaeological artifacts, i. e. the Roman ingots, required additional efforts during every activity and working phase of the shield production. Anyway, its successful integration in the cryostat will guarantee the protection from the γ radioactivity, crucial for the background abatement down to 0.01 counts keV^{-1} kg^{-1} yr^{-1}in the ^{130}Te $0\nu\beta\beta$ region of interest.

Finally, Chapter 7 illustrates the results obtained with the first prototype array op-

[1]The cryogenic studies are supported by Appendix A in the calculations and analysis tools.

erated as a bolometer inside the CUORE cryostat, the Mini-Tower detector. The study of the Mini-Tower allowed to understand how to reduce the system noise and to identify an optimal working configuration in view of the forthcoming (much complex) CUORE detector.

The main contribution of this work has been proving that the CUORE cryostat is a suitable environment for a large bolometric array searching for rare events. The long commissioning phase for a very complex cryogenic system was concluded delivering a reliable and stable base temperature. The analysis of the results from the Mini-Tower proved the capability of operating bolometric detectors inside the cryostat, despite the not yet complete optimization of the system. Moreover, the production and installation of the internal lead shields and the strict selection and handling procedures for every cryostat component will guarantee a relevant suppression of natural radioactive background.

As widely described, the comprehension and check of the cryostat and of its subsystems was indeed crucial to allow a complete understanding of the technical aspects, which are a crucial ingredient of the experimental sensitivity. The obtained success represented the start of a new era of tonne-scale bolometric detectors and opened the way to one of the most sensitive searches for $0\nu\beta\beta$.

Chapter 1

Neutrinoless double beta decay

In 1937, almost ten years after Dirac's description of the electron [1, 2], Majorana proposed a new way to represent fermions in a relativistic quantum field theory [3] and remarked that his formalism could be useful for neutral particles. A single Majorana quantum field characterizes the situation in which particles and antiparticles coincide, as it happens for the photon. Racah stressed that such a field could fully describe massive neutrinos, noting that the theory by Majorana leads to physical predictions essentially different from those coming from Dirac's theory [4]. Two years later, Furry studied a new process that could take place within this scenario [5]. This process was similar to the "double beta disintegration", introduced by Goeppert-Mayer in 1935 [6].[1] It was the double beta decay without neutrino emission, or *neutrinoless double beta decay* ($0\nu\beta\beta$).

The $0\nu\beta\beta$ transition assumes a simple form, namely

$$(A, Z) \rightarrow (A, Z+2) + 2\mathrm{e}^-. \tag{1.1}$$

The Feynman diagram of the $0\nu\beta\beta$ process, written in terms of the particles we know today and of massive Majorana neutrinos, is given Fig. 1.1.

The main feature of $0\nu\beta\beta$ is the explicit violation of the number of leptons and, more precisely, the creation of a pair of electrons. The discovery of $0\nu\beta\beta$ would therefore demonstrate that lepton number, L, is not a symmetry of nature. This, in turn, could support the exciting theoretical picture that leptons played a part in the creation of the matter-antimatter asymmetry in the universe (see e. g. Ref. [8]).

In the attempt to investigate the nature of the $0\nu\beta\beta$ process, various theoretical possibilities were considered. We find, for example, the postulation of new super-weak interactions [10, 11], models with right-handed currents [12], left-right symmetric models [13] and many other proposals. Anyway, the general interest has always remained focused on

[1] Two-neutrino double beta decay ($2\nu\beta\beta$) is a rare nuclear transition in which two neutrons inside a nucleus are simultaneously transformed into two protons accompanied by the emission of two electrons and two antineutrinos. $2\nu\beta\beta$ is a second-order process in the Standard Model of electroweak interactions and thus is strongly suppressed. Almost 80 years after its prediction, this has been observed in 12 nuclei with half-lives ranging from about 10^{19} yr to 10^{24} yr. See Ref. [7] for a review on $2\nu\beta\beta$.

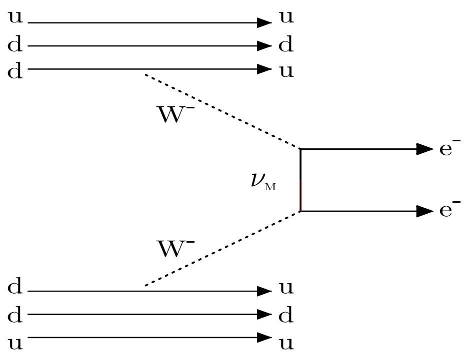

FIG. 1.1: Diagram of the $0\nu\beta\beta$ process due to the exchange of massive Majorana neutrinos, here denoted generically by ν_M. Figure from Ref. [9].

the neutrino mass mechanism. In fact, this scenario is supported by two important facts:

- *the Majorana neutrino mass operator is the least suppressed.* On the theoretical side, the triumph of the Standard Model (SM) of electroweak interactions in the 1970s [14–16] led to formulate the discussion of new physics signals using the language of effective operators. These are suppressed by powers of the new physics mass scale. Among the operators that violate the global symmetries of the SM and, more precisely, L, there is only one operator that is suppressed by one power of the new mass scale. This is the operator that gives rise to Majorana neutrino masses [17] (see also Refs. [18–21]). All the other operators that could contribute to the $0\nu\beta\beta$ are more strongly suppressed (this discussion will be recalled in Sec. 1.2);

- *neutrinos have non-zero mass.* On the experimental side, some anomalies in neutrino physics, which emerged in throughout 30 years, found their natural explanation in terms of oscillations of massive neutrinos [22]. This explanation was confirmed by several experiments (see e. g. Refs. [23, 24] for reviews). Thus, although oscillation phenomena are not sensitive to the Majorana nature of neutrinos [25], the concept of neutrino mass has changed its status from hypothesis to observed fact. This, of course, strengthened the case for light massive neutrinos to play a major role for the $0\nu\beta\beta$ transition.

These consideration enhance even more the importance of $0\nu\beta\beta$. Not only this process is a direct probe of physics beyond the SM. It is a also a key tool for studying neutrinos, probing whether their nature is the one of Majorana particles and providing us with precious information on the neutrino mass scale and ordering.

In this thesis, the $0\nu\beta\beta$ process will be discussed within the theoretical framework of ordinary neutrinos endowed Majorana masses as mediators of the transition.

1.1 Majorana neutrinos

The theory of massive and "real" fermions proposed by Majorana contains less states for the fields than the one used by Dirac for the description of the electron and, in this

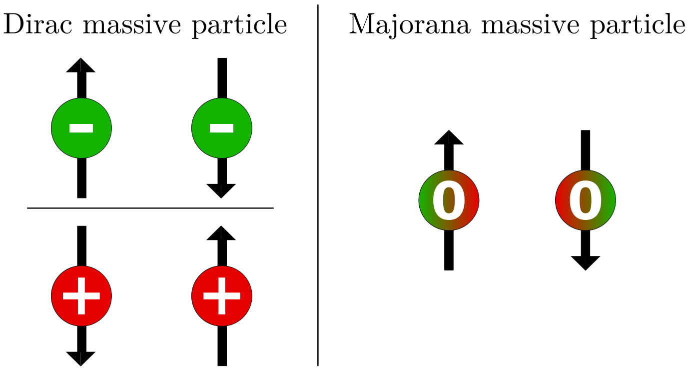

FIG. 1.2: Massive fields in their rest frames. The arrows show the possible directions of the spin. (Left) The 4 states of Dirac massive field. The signs indicate the charge that distinguishes particles and antiparticles, e. g. the electric charge of an electron. (Right) The 2 states of Majorana massive field. The symbol “zero” indicates the absence of any $U(1)$ charge: particles and antiparticles coincide. Figure from Ref. [9].

sense, it is simpler. By using the original formalism introduced by Fermi in 1933 for the description of the β decay [26], the condition of reality for a quantized fermionic field can be written as:

$$\chi = C\bar{\chi}^t \tag{1.2}$$

where C is the charge conjugation matrix, while $\bar{\chi} \equiv \chi^\dagger\gamma_0$ is the Dirac conjugate of the field. In particular, Majorana advocated a specific choice of the Dirac γ-matrices, such that $C\gamma_0^t = 1$, which simplifies various equations. The free particle Lagrangian density formally coincides with the usual one:

$$\mathcal{L}_{\text{Majorana}} = \frac{1}{2}\bar{\chi}(i\partial\!\!\!/ - m)\chi. \tag{1.3}$$

Following Majorana’s notation, the decomposition of the quantized fields into oscillators is:

$$\chi(x) = \sum_{\mathbf{p},\lambda} [a(\mathbf{p}\lambda)\ \psi(x;\mathbf{p}\lambda) + a^*(\mathbf{p}\lambda)\ \psi^*(x;\mathbf{p}\lambda)] \tag{1.4}$$

where $\lambda = \pm 1$ is the relative orientation between the spin and the momentum (helicity).[2] For any value of the momentum, there are 2 spin (or helicity) states:

$$a^*(\mathbf{p}+)|\text{vac.}\rangle = |\mathbf{p}\uparrow\rangle \quad \text{and} \quad a^*(\mathbf{p}-)|\text{vac.}\rangle = |\mathbf{p}\downarrow\rangle. \tag{1.5}$$

A Majorana neutrino is incompatible with any $U(1)$ transformation, such as L. More in general, L will be violated by the presence of Majorana mass. Fig. 1.2 illustrates the comparison between the particle content both of a Dirac and a Majorana field in the case $\mathbf{p} = 0$ (rest frame).

No elementary process where the number of leptons or the number of hadrons varies

[2]The normalizations for the wave functions: $\int d\mathbf{x}|\psi(t,\mathbf{x})|^2 = 1$, and for the oscillators: $a(\mathbf{p}\lambda)\, a^*(\mathbf{p}'\lambda') + a^*(\mathbf{p}'\lambda')\, a(\mathbf{p}\lambda) = \delta_{\mathbf{p}\mathbf{p}'}\delta_{\lambda\lambda'}$ are adopted.

has been observed yet. This suggests the hypothesis that L and B (baryon number) are subject to conservation laws. However, we do not have any deep justification for which these laws should be exact. In fact, it is possible to suspect that their validity is just approximate or circumstantial, since it is related to the range of energies that we can explore in laboratories.[3] In the minimal formulation of the SM, B and L are "accidental" global symmetries, due to the specific particle content of the model and to the hypothesis of renormalizability. However, this is sufficient to forbid the $0\nu\beta\beta$ transition completely in the SM. In other words, a hypothetical evidence for such a transition would directly point out to physics beyond the SM.

In the SM, the charged current (which contains the neutrino field) always includes the left chiral projector

$$P_L \equiv \frac{1-\gamma_5}{2}. \tag{1.6}$$

Therefore, the neutrino field only appears in the combination

$$\psi_L = P_L\ \psi. \tag{1.7}$$

It is then possible to implement the hypothesis of Majorana in the most direct way by defining the real field

$$\chi \equiv \psi_L + C\bar{\psi}_L^t \tag{1.8}$$

and, conversely, to obtain the SM field by a projection:

$$\psi_L \equiv P_L\chi. \tag{1.9}$$

Like in the SM, the equivalence between chirality and helicity holds for massless neutrinos. In fact, in this case the Dirac equation becomes equivalent to two Weyl independent equations [27] corresponding to the Hamiltonian functions

$$\mathcal{H}_{\nu/\bar{\nu}} = \mp c\mathbf{p}\,\sigma \tag{1.10}$$

where σ are the three Pauli matrices. The two signs apply to the neutral leptons that thanks to the interaction produce charged leptons of charge ∓ 1, respectively. In other words, we can define these states as neutrinos and antineutrinos, respectively. Moreover, by looking at Eq. (1.10), one can see that the energy eigenstates are also helicity eigenstates. In particular, the spin of the neutrino (antineutrino) is antiparallel (parallel) to its momentum. See Fig. 1.3 for illustration.

In the case of massive neutrinos, the previous argument can be applied only in the ultra-relativistic limit, when the mass is negligible. In this condition, the one-to-one connection between chirality and helicity still holds. Anyway, this is the case relevant for detectable neutrinos, since the weak interaction cross sections are bigger at larger energies.

[3] It has also to be noticed that the fact that neutral leptons (i. e. neutrinos or antineutrinos) are very difficult to detect further restricts the possibilities for an experimental investigation.

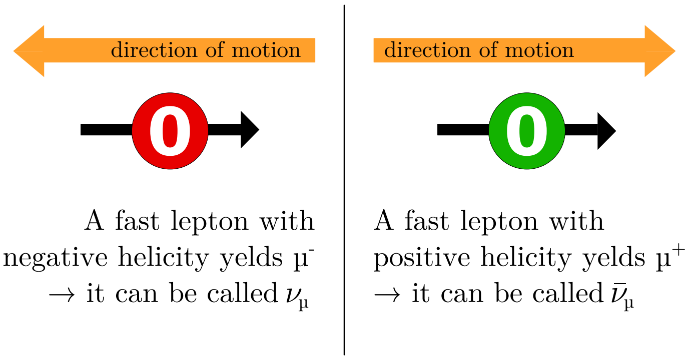

FIG. 1.3: The chiral nature of weak interactions allows us to define what is a neutrino and what it an antineutrino in the ultrarelativistic limit, when chirality coincides with helicity and the value of the mass plays only a minor role. Figure from Ref. [9].

A consequence of the chiral nature of weak interactions is that, if we assume that neutrinos have the type of mass introduced by Dirac, we have a couple of states that are sterile under weak interactions in the ultrarelativistic limit. Conversely, in the hypothesis of Majorana, the fact that the left chiral state exists does not require the introduction of the right chiral one, as instead required by the Dirac hypothesis. Most importantly, it has to be noticed that in the case of Majorana mass it is not possible to define the difference between a neutrino and an antineutrino in a Lorentz invariant way. In order to do this, we have to search for new processes and the most promising investigation is indeed $0\nu\beta\beta$.[4]

1.2 $0\nu\beta\beta$ via neutrino exchange mechanism

The exchange of Majorana neutrinos is the original mechanism considered in Furry's formulation of the $0\nu\beta\beta$ [5] and today it continues to draw the largest attention of the $0\nu\beta\beta$ community. As already mentioned, this scenario is supported both by theoretical and experimental considerations.

By using the language of the SM, it is possible to describe effective (non-renormalizable) operators that respect the gauge symmetry $\mathrm{SU}(3)_c \times \mathrm{SU}(2)_L \times \mathrm{U}(1)_Y$, but violate L and/or B [17, 29]. The new terms can then be added to the Lagrangian and Hamiltonian densities

$$\mathcal{H}_{\text{Weinberg}} = \frac{(l_L H)^2}{M} + \frac{l_L q_L q_L q_L}{M'^2} + \frac{(l_L q_L d_R^c)^2}{M''^5} \; (+\, \dots) \tag{1.11}$$

In general, l and q denote the matter fields, H is the Higgs field, while $M, M', \dots$ are the scales of the new physics.

The cases in Eq. (1.11) represent a small sub-group of all the possibilities (a more complete list can be found in Refs. [30, 31]) Anyway, the first term in this Hamiltonian

[4] In principle, very low energy neutrinos, like those composing the Cosmic Neutrino Background, could be used to determine if they are Majorana or Dirac particles. In fact, in the former case, the states with positive helicity (by definition, antineutrinos) will act just as neutrinos (since almost at rest) in a suitable interaction, such as an inverse β decay. Instead, in the latter case, they will remain antineutrinos and will not react, thus generating a factor 2 difference in the expected rate (see e. g. Ref. [28]).

density represents the only operator meeting the demands of respecting the SM symmetries and breaking L at the same time to be suppressed by one power of the new mass scale. All the other operators are more strongly suppressed. This (dimension-5) operator is the one that generates the Majorana neutrino masses.

Therefore, if we assume that the scales of the new physics are much higher than the electroweak scale, and thus the higher the exponential of M, the more suppressed the corresponding operator, it will reasonable to expect that the leading mechanism behind the $0\nu\beta\beta$ is indeed the exchange of neutrinos endowed with Majorana mass.

In order to describe the neutrino exchange mechanism, a key quantity needs to be introduced. It is the propagator of virtual Majorana neutrinos. Since these fields are real, Eq. (1.3) can lead to new types of propagators that do not exist within the Dirac theory. In fact, in this case we can use the antisymmetry of the charge conjugation matrix and get:

$$\langle 0|T[\chi(x)\chi(y)]|0\rangle = -\Delta(x-y)\,C \tag{1.12}$$

where Δ denotes the usual propagator

$$\Delta(x) \equiv \int \frac{d^4q}{(2\pi)^4}\frac{i(\hat{q}+m)}{q^2-m^2+i0}\mathrm{e}^{-iqx}. \tag{1.13}$$

In the low energy limit (relevant for β decay processes) the interaction of neutrinos are well described by the current-current 4-fermion interactions, corresponding to the Hamiltonian density

$$\mathcal{H}_{\mathrm{Fermi}} = \frac{G_F}{\sqrt{2}}\,J^{a\dagger}J_a \tag{1.14}$$

where G_F is the Fermi coupling, and we introduced the current $J^a = J^a_{\mathrm{lept}} + J^a_{\mathrm{hadr}}$ for $a = 0,1,2,3$, that decreases the charge of the system (its conjugate, $J^\dagger_a$, does the contrary). In particular, the leptonic current

$$J^a_{\mathrm{lept}} = \sum_{\ell=\mathrm{e},\mu,\tau} \bar{\psi}_\ell\,\gamma^a(1-\gamma_5)\,\psi_{\nu_\ell} \tag{1.15}$$

defines the ordinary neutrino with "flavor" ℓ. In order to implement the Majorana hypothesis, one can use Eq. (1.8) and introduce the field $\chi = \psi_L + C\bar{\psi}^t_L$.

Nothing changes in the interactions if one substitutes the field ψ_{ν_ℓ} with the corresponding field χ_{ν_ℓ}, since the chiral projector selects only the first piece, $\psi_{\nu_\ell\,L}$.

Let us assume that the field χ is a mass eigenstate. A contribution to the $0\nu\beta\beta$ transition arises at the second order of the Fermi interaction. By contracting the neutrino fields in the operator:

$$-\,G_F^2\int d^4x\,J^{a\dagger}_{\mathrm{hadr}}(x)\,\bar{\psi}_{\mathrm{e}}(x)\gamma_a P_L\chi_{\nu_{\mathrm{e}}}(x)\int d^4y\,J^{b\dagger}_{\mathrm{hadr}}(y)\,\bar{\psi}_{\mathrm{e}}(y)\gamma_b P_L\chi_{\nu_{\mathrm{e}}}(y). \tag{1.16}$$

the leptonic part becomes

$$\bar{\psi}_{\rm e}(x)\;\gamma^a\,P_L\,\Delta(x-y)P_L\,\gamma^b\,C\bar{\psi}^t_{\rm e}(y) \tag{1.17}$$

while the ordinary propagator, sandwiched between two chiral projectors, reduces to

$$P_L\,\Delta(x)P_L = P_L\int\frac{d^4q}{(2\pi)^4}\,\frac{i\,m}{q^2-m^2+i0}\mathrm{e}^{-iqx}. \tag{1.18}$$

The need to integrate over the neutrino 4-momentum represents the virtuality of this particle. In fact, q is free to vary and its value is connected to the momenta of the final state electrons and of the intermediate virtual nucleons. In particular, since these are confined in the nucleus, the typical 3-momentum is of the order of the inverse of the nucleonic size, namely

$$|\vec{q}| \sim \hbar c/\mathrm{fm} \sim \text{ a few } 100\,\mathrm{MeV}. \tag{1.19}$$

The last component of the 4-momentum, the energy q_0, is instead small, since it is limited by the Q-value of the transition, which is of the order of a few MeV.

It is worth to notice that, so far, no indication on the absolute value on the neutrino mass was provided. The previous discussion is valid both for ordinary and more “exotic” neutrinos (generically seen as neutral leptons endowed with a Majorana mass component). The comparison between the scale in Eq. (1.19) and the one of the neutrino mass identifies and separates “light” from “heavy” neutrinos for what concerns $0\nu\beta\beta$. Given the present mass limits (see Sec. 1.3.1), ordinary neutrinos definitely belong to the former group.[5]

1.3 Neutrino mass and $0\nu\beta\beta$

The three ordinary neutrinos are identified by their charged current interactions i. e. they have “flavor” $\ell = \mathrm{e}, \mu, \tau$. The Majorana mass terms in the Lagrangian density is thus described by a symmetric matrix:

$$\mathcal{L}_{\rm mass} = \frac{1}{2}\sum_{\ell,\,\ell'\,=\,\mathrm{e},\,\mu,\,\tau}\nu^t_\ell\,C^{-1}M_{\ell\ell'}\,\nu_{\ell'} + h.\,c.\,. \tag{1.20}$$

The only term that violates the electronic number by two units is $M_{\rm ee}$, and this simple consideration motivates the fact that the amplitude of the $0\nu\beta\beta$ has to be proportional to this parameter, while the width to its squared modulus. The neutrino mass matrix can be diagonalized by mean of a unitary matrix

$$M = U^t\,\mathrm{diag}(m_1, m_2, m_3)\,U^\dagger \tag{1.21}$$

[5] It is as well possible to build up models with heavy Majorana neutrinos as mediators of the $0\nu\beta\beta$ process (see e. g. Ref. [12] for a review).

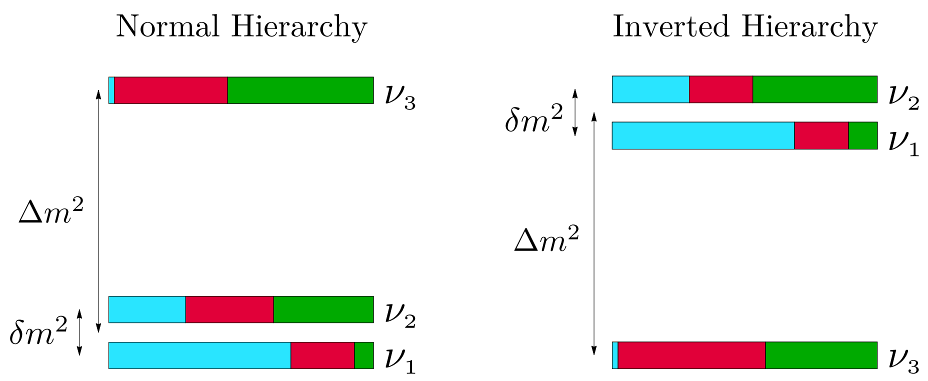

FIG. 1.4: Graphic view of the probability of finding one of the flavor eigenstates if the neutrino is in a certain mass eigenstate. The value $\phi = 0$ for the CP-violating phase is assumed.

where the neutrino masses m_i are real and non-negative. Thus, we can define:

$$m_{\beta\beta} \equiv \left| \sum_{i=1,2,3} U_{\mathrm{e}i}^2 \; m_i \right| \tag{1.22}$$

where the index i runs on the 3 light neutrinos with given mass. This parameter is often called *effective Majorana mass*. It can be thought as the "electron neutrino mass" that rules the $0\nu\beta\beta$ transition.

The previous intuitive argument in favor of this definition is corroborated by calculating the Feynman diagram of Fig. 1.1. Firstly, it has to be noted that the electronic neutrino ν_{e} is not a mass eigenstate in general. Then, substituting Eq. (1.21) into Eq. (1.20), we see that we go from the flavor basis to the mass basis by setting

$$\nu_\ell = \sum_{i=1,2,3} U_{\ell i} \; \nu_i . \tag{1.23}$$

Therefore, in the neutrino propagators of Fig. 1.1, we will refer to the masses m_i (that in our case are "light") while, in the two leptonic vertices, we will have $U_{\mathrm{e}i}$. Taking the product of these factors, we get the expression given in Eq. (1.22). Consistently with Eq. (1.23), the three massive states are given by

$$|\nu_i\rangle = \sum_{\ell=\mathrm{e},\mu,\tau} U_{\ell i} \, |\nu_\ell\rangle \, . \tag{1.24}$$

Thus, it is possible to estimate the probability of finding the component ν_ℓ of each mass eigenstate ν_i. This probability is just the squared module of the matrix element $U_{\ell i}$, since the matrix is unitary. The result is graphically shown in Fig. 1.4.

It should be noted that the leptonic mixing matrix U as introduced above differs from the $U|_{\mathrm{osc.}}$, the ordinary leptonic Pontecorvo-Maki-Nakagawa-Sakata (PMNS) mixing matrix used in neutrino oscillation analyses. Indeed, the latter is given after rotating away the phases of the neutrino fields and observing that oscillations depend only upon the combination $MM^\dagger/(2E)$. This matrix contains only one complex phase which plays a role in oscillations (the "CP-violating phase"). Instead, in the case of $0\nu\beta\beta$ the observable is different. It is just $|M_{\text{ee}}|$. Here, there are new phases that cannot be rotated away and that play a physical role: the "Majorana phases". Their contribution can be made explicit by rewriting Eq. (1.22) as follows:

$$m_{\beta\beta} = \left| \sum_{i=1,2,3} \mathrm{e}^{i\xi_i} \, |U_{\mathrm{e}i}^2| \, m_i \right| . \tag{1.25}$$

We can now identify $U_{\mathrm{e}i}$ of Eq. (1.25) with the mixing matrix used in neutrino oscillation analyses. In particular, it has to be noted that:

- it is possible to adopt a convention for the neutrino mixing matrix such that the 3 mixing elements $U_{\mathrm{e}i}$ are real and positive. However, in the most common convention $U_{\mathrm{e}3}$ is defined to be complex;

- only 2 Majorana phases play a physical role, the third one just being matter of convention;

- it is not possible even in principle to reconstruct the Majorana mass matrix simply on experimental bases, unless we find another observable which depends on the Majorana phases.

Although the absolute neutrino mass scale is still unknown, it has been possible to measure, through oscillation experiments, the squared mass splittings and the mixing angles between the three active neutrinos. In Table 1.5, these parameters are reported according to the global analysis results of Ref. [32]. In particular, the authors' notation is followed in the definition of the mass splitting parameters:

$$\delta m^2 \equiv m_2^2 - m_1^2 \quad \text{and} \quad \Delta m^2 \equiv m_3^2 - \frac{m_1^2 + m_2^2}{2}. \tag{1.26}$$

The former is measured through the observation of solar neutrino oscillations, while the latter comes from atmospheric neutrino data. Practically, δm^2 regards the splitting between ν_1 and ν_2, while Δm^2 refers to the distance between the ν_3 mass and the mid-point of ν_1 and ν_2 masses.

The sign of δm^2 could be determined by observing matter enhanced oscillations as explained within the MSW theory [33, 34] and it turned out to be positive [35]. Instead, the sign of Δm^2 is still unknown and it is not simple to measure it. This ambiguity is consistent with two possibilities for the neutrino mass spectrum: the so-called "Normal Hierarchy" (NH, $\Delta m^2 > 0$) and the "Inverted Hierarchy" (IH, $\Delta m^2 < 0$).

The oscillation data are analyzed by writing $U|_{\text{osc.}}$ in terms of the mixing angles θ_{12},

TABLE 1.5: Results of the global 3ν oscillation analysis, in terms of best-fit values and allowed 3σ range for the 3ν mass-mixing parameters as reported in Ref. [32]. The last column is our estimate of the σ while assuming symmetric uncertainties.*

Parameter	Best fit	3σ range	$\sigma_{\text{symmetric}}$
NH			
$\sin^2(\theta_{12})$	$2.97 \cdot 10^{-1}$	$(2.50 - 3.54) \cdot 10^{-1}$	$0.17 \cdot 10^{-1}$
$\sin^2(\theta_{13})$	$2.14 \cdot 10^{-2}$	$(1.85 - 2.46) \cdot 10^{-2}$	$0.11 \cdot 10^{-2}$
$\sin^2(\theta_{23})$	$4.37 \cdot 10^{-1}$	$(3.79 - 6.16) \cdot 10^{-1}$	-
δm^2 [eV^2]	$7.37 \cdot 10^{-5}$	$(6.93 - 7.97) \cdot 10^{-5}$	$0.17 \cdot 10^{-5}$
Δm^2 [eV^2]	$2.50 \cdot 10^{-3}$	$(2.37 - 2.63) \cdot 10^{-3}$	$0.04 \cdot 10^{-3}$
IH			
$\sin^2(\theta_{12})$	$2.97 \cdot 10^{-1}$	$(2.50 - 3.54) \cdot 10^{-1}$	$0.17 \cdot 10^{-1}$
$\sin^2(\theta_{13})$	$2.18 \cdot 10^{-2}$	$(1.86 - 2.48) \cdot 10^{-2}$	$0.12 \cdot 10^{-2}$
$\sin^2(\theta_{23})$	$5.69 \cdot 10^{-1}$	$(3.83 - 6.37) \cdot 10^{-1}$	-
δm^2 [eV^2]	$7.37 \cdot 10^{-5}$	$(6.93 - 7.97) \cdot 10^{-5}$	$0.17 \cdot 10^{-5}$
Δm^2 [eV^2]	$2.46 \cdot 10^{-3}$	$(2.33 - 2.60) \cdot 10^{-3}$	$0.05 \cdot 10^{-3}$

*Actually, the uncertainties from the reference are not completely symmetric around the best fit point, but the deviations are quite small.

θ_{13} and θ_{23} and of the CP-violating phase ϕ according to the (usual) representation

$$U|_{\text{osc.}} = \begin{pmatrix} c_{12}c_{13} & s_{12}c_{13} & s_{13}\mathrm{e}^{-i\phi} \\ -s_{12}c_{23} - c_{12}s_{13}s_{23}\mathrm{e}^{i\phi} & c_{12}c_{23} - s_{12}s_{13}s_{23}\mathrm{e}^{i\phi} & c_{13}s_{23} \\ s_{12}s_{23} - c_{12}s_{13}c_{23}\mathrm{e}^{i\phi} & -c_{12}s_{23} - s_{12}s_{13}c_{23}\mathrm{e}^{i\phi} & c_{13}c_{23} \end{pmatrix} \tag{1.27}$$

where $s_{ij}, c_{ij} \equiv \sin\theta_{ij}, \cos\theta_{ij}$.

With this convention, it is possible to obtain Eq. (1.25) by defining

$$U \equiv U|_{\text{osc.}} \cdot \operatorname{diag}\left(\mathrm{e}^{-i\xi_1/2}, \mathrm{e}^{-i\xi_2/2}, \mathrm{e}^{i\phi - i\xi_3/2}\right). \tag{1.28}$$

Thanks to the knowledge of the oscillation parameters, it is possible to put a first series of constraints on $m_{\beta\beta}$. However, as already recalled, since the complex phases of the mixing parameters in Eq. (1.25) cannot be probed by oscillations, the allowed regions for $m_{\beta\beta}$ are obtained letting them vary freely. The expressions for the resulting extremes (i. e. the $m_{\beta\beta}$ maximum and minimum values due to the phase variation) can be found in Ref. [9]. In Fig. 1.6, the graphical representation of $m_{\beta\beta}$ introduced in Ref. [36]: $m_{\beta\beta}$ in bi-logarithmic scale as a function of the mass of the lightest neutrino, m_{lightest}, for both the cases of NH and IH. It is important to notice that the two obtained regions depict two mutually exclusive scenarios.

Depending on the value of $m_{\beta\beta}$ that could be extracted from an hypothetical observation of $0\nu\beta\beta$ (see the discussion in Secs. 1.4 and 1.5 for the procedure), different

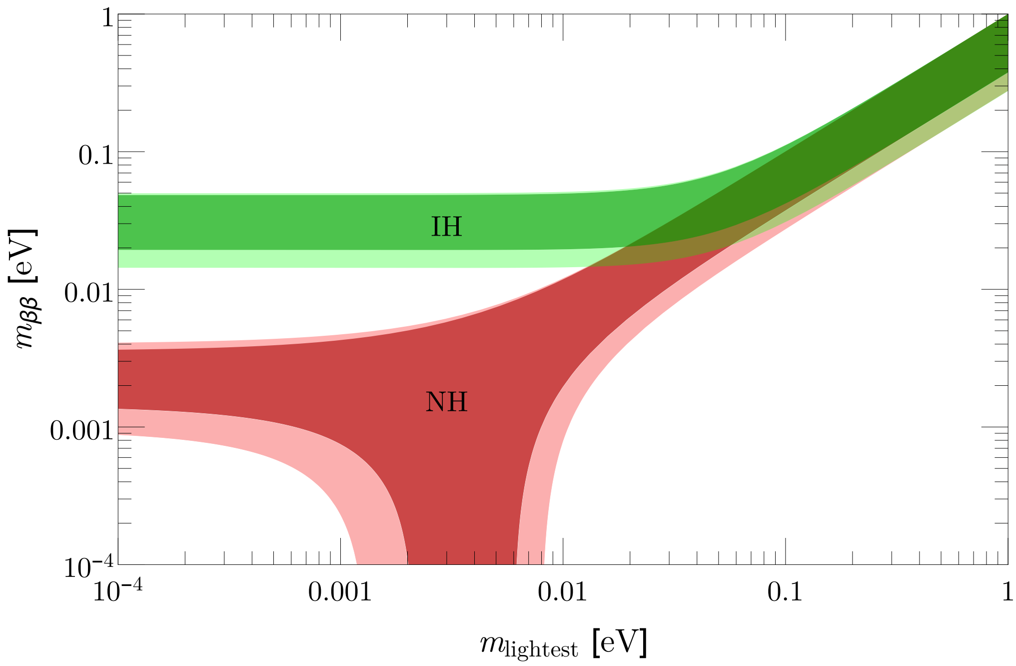

FIG. 1.6: Updated predictions on $m_{\beta\beta}$ from oscillations as a function of the lightest neutrino mass in the two cases of NH and IH. The shaded areas correspond to the 3σ regions due to error propagation of the uncertainties on the oscillation parameters.

considerations on m_{lightest} could me made.[6] A few representative cases are the following:

- if $m_{\beta\beta}$ turned out to be 200 meV, the bound $(0.2 \lesssim m_{\text{lightest}} \lesssim 0.7)$ eV could be set in both the NH and IH scenarios;
- if $m_{\beta\beta}$ turned out to be 20 meV, a bound $(0.02 \lesssim m_{\text{lightest}} \lesssim 0.08)$ eV could be set in case of NH, while an upper limit $m_{\text{lightest}} \lesssim 0.02$ eV could be placed in case of IH;
- if $m_{\beta\beta}$ turned out to be 2 meV, the IH scenario could be excluded and the limit $m_{\text{lightest}} \lesssim 0.012$ eV could be set;
- if $m_{\beta\beta}$ turned out to be 0.2 meV, the IH scenario could be excluded and the bound $(0.001 \lesssim m_{\text{lightest}} \lesssim 0.009)$ eV could be set.

As it will be shown later in the discussion, probing smaller values of $m_{\beta\beta}$ always requires greater efforts on the experimental side. Therefore, the previous examples illustrate situations not equally achievable.

1.3.1 Complementary information on the neutrino mass

$0\nu\beta\beta$ is not the only process that allows the investigation of the neutrino masses. In fact, other potential sources of information are:

[6] As it will be shown in Sec. 1.6, a bound on $m_{\beta\beta}$ is always associated with an important uncertainty. This will be neglected in the following examples.

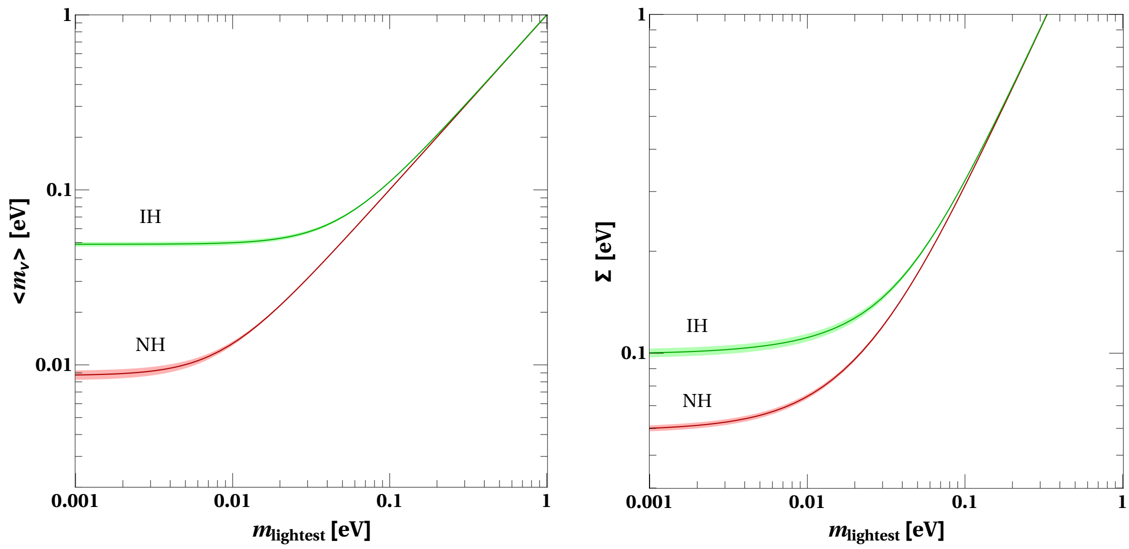

FIG. 1.7: Predictions on $\langle m_\nu \rangle$ (Left) and Σ (Right) from oscillations as a function of the lightest neutrino mass in the two cases of NH and IH. The shaded areas correspond to the 3σ regions due to error propagation of the uncertainties on the oscillation parameters.

- the investigation of the effect of the electron neutrino mass in β decay processes;
- the study of kinematic effects (in particular of supernova neutrinos);
- the cosmological observation of the total gravitational neutrino charge.

The combination of the analysis and the results from the different experiments and surveys can can provide us with stronger constraints on the single observables and improve our knowledge on the neutrino absolute mass scale and ordering.

Direct measurement of the electron neutrino mass

The direct measurement of the electron neutrino mass involves pure kinematics considerations and it is therefore the most sensitive model independent approach to assess the neutrino mass absolute value. Furthermore, this method has the big advantages of being obtained in controlled conditions, i. e. in the laboratory.

A non-zero neutrino mass distorts the electron spectrum in the β decay of a nucleus. Therefore, it is possible to kinematically constraint the neutrino mass by examining the "visible" energy released in a single decay. The obtained spectra are normally analyzed by studying the Kurie plot of the decay [37] in order to get a quantity generally linear with the kinetic energy of the emitted electron:

$$\langle m_\nu \rangle \equiv \sqrt{\sum_i \left| U_{ei}^2 \right| m_i^2}. \tag{1.29}$$

Similarly to the case of $m_{\beta\beta}$ for the $0\nu\beta\beta$, $\langle m_\nu \rangle$ can be thought as the effective electron neutrino mass that rules the β decay transition. However, in this case we have an incoherent sum and the expression in Eq. (1.29) is not sensitive to the Majorana phases. The knowledge of the oscillation parameters allows to put a first series on constraints on $\langle m_\nu \rangle$ depending on the value of the lightest neutrino mass. The result is shown in the left panel of Fig. 1.7.

The present limit is of about 2 eV [38, 39] and comes from the spectrometric searches of the ^{3}H β decay. This bound is not tight enough to have consequences for the $0\nu\beta\beta$ search. Anyway, the next generation of spectrometers is expected to lower this limit by a factor of $\sim$ 10 [40] and the use of new detection technologies in the future is also foreseen. These are based on ^{3}H sources (microwave antennas, [41]) and on the electron capture of ^{163}Ho (micro-calorimeters, [42–44]) and will have the potential to go far below the eV in sensitivity.

A joint analysis of the data from single β and $0\nu\beta\beta$ searches will soon provide complementary information on the neutrino mass. An example of this kind of studies can be found in Ref. [45].

Bounds on the neutrino mass from supernovae

This method consists in a time-of-flight measurement of the neutrino flux produced in a core-collapse supernova. The features of the collected data must be compared to the expectations from a specific theoretical model, anyway the effect of the neutrino mass results in a variation of the velocity. Applied to SN1987A, it produced a limit of about 6 eV on the electron antineutrino mass [46, 47]. The perspectives for the future are connected not only to new detectors, but also to favorable characteristics of the flux, such as the existence of antineutrino pulses in the first instants of a supernova emission. In favorable conditions, the ultimate sensitivity of this type of investigation in terms of neutrino mass could be pushed down to a fraction of eV [48].

The information coming from the detection of supernova neutrinos integrate those from the direct measurements of the neutrino mass.

Cosmology

Neutrinos are a key ingredient of the cosmological descriptions of the Universe. They affected its background evolution as well as the growth of cosmological perturbations. Therefore, within a specific theoretical framework, constraints on the neutrino masses can be obtained (see Ref. [49] for details) starting from cosmological observations at different scales, like the measurements of the temperature and polarization anisotropies of the Cosmic Microwave Background (CMB), or the distribution of large scale structures.

The physical quantity probed by the cosmological surveys is the sum of all the neutrino masses, Σ,[7] whose expression, within the three light neutrino scenario, is:

$$\Sigma \equiv m_1 + m_2 + m_3. \tag{1.30}$$

Depending on the mass hierarchy, Σ can be expressed as a function of the lightest neutrino mass m and of the oscillation mass splittings. In particular, in the case of NH:

$$m_1 = m, \qquad m_2 = \sqrt{m^2 + \delta m^2}, \qquad m_3 = \sqrt{m^2 + \Delta m^2 + \delta m^2/2} \tag{1.31}$$

while, in the case of IH:

$$m_1 = \sqrt{m^2 + \Delta m^2 - \delta m^2/2}, \qquad m_2 = \sqrt{m^2 + \Delta m^2 + \delta m^2/2}, \qquad m_3 = m. \tag{1.32}$$

The knowledge of the oscillation parameters thus allows to set a first series on Σ. The result is shown in the right panel of Fig. 1.7.

The constraints from cosmology are currently the ones providing the most stringent bounds on the neutrino masses. These are becoming so strict that they better agree with the NH spectrum, rather than with IH one [45, 50] (graphically, this means that the limits lie between the NH and the IH bands in the figure). Referring to the most recent years, the tightest experimental limits on Σ are obtained by combining data from different surveys, always including the recent CMB measurements performed by the Planck satellite [51]. The complementary information (both in scale and redshift) allows a more effective investigation of the neutrino induced suppression in terms of matter power spectrum. The results are of the order of $\Sigma \lesssim (120-180)\,\mathrm{meV}$ at 2σ C. L. [51–57]. More precise measurements from cosmological surveys are expected in the near future [58] and they will probably allow for even tighter limits on the neutrino masses.

The close connection between the neutrino mass measurements obtained in the laboratory and the cosmological observations was outlined long ago [59]. In order to discuss the implication for the $0\nu\beta\beta$ searches, it is useful to keep the representation of Fig. 1.6 ($m_{\beta\beta}$ *vs.* m). The cosmological constraints on Σ can be included at any desired confidence level n by considering the inequality

$$\frac{(y - m_{\beta\beta}(m))^2}{(n\,\sigma[m_{\beta\beta}(m)])^2} + \frac{m^2}{m(\Sigma_n)^2} < 1 \tag{1.33}$$

where $m_{\beta\beta}(m)$ is the effective Majorana mass expressed as a function of m, $\sigma[m_{\beta\beta}(m)]$ is the 1σ associated error (it depends on the uncertainties on the oscillation parameters) and $m(\Sigma_n)$ is the value of m calculated for an experimental limit on Σ at the C. L. n.[8]

An example is shown in Fig. 1.8, where the 2σ C. L. limit $\Sigma = 146\,\mathrm{meV}$ of Ref. [52] was

[7] The bounds on Σ are derived within specific models of global description of the Universe, where the contribution of the neutrino density to the Universe evolution is then estimated. For this reason, it is advisable to take these and similar results from cosmology with the due caution.

[8] Both Σ and $m_{\beta\beta}$ are a function of m. Therefore, one has to solve the (quartic) equation that gives m as a function of Σ and replace the solution in the expression for $m_{\beta\beta}$.

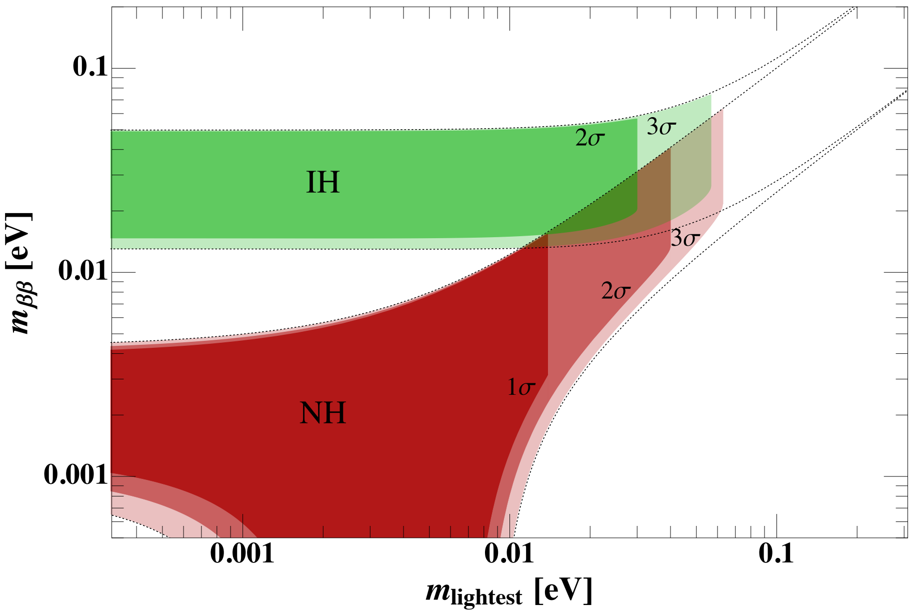

FIG. 1.8: Constraints from cosmological surveys are added to those from oscillations in the representation of $m_{\beta\beta}$ as a function of the lightest neutrino mass. The dotted contours represent the 3σ regions allowed considering oscillations only. The shaded areas show the effect of the inclusion of cosmological constraints at different C. L. . The absence of the 1σ region for the IH can be noticed. This case is in fact excluded at this C. L. . Figure from Ref. [50].

used (see Ref. [50] for details). The most evident feature of the figure is the clear difference in terms of expectations for both $m_{\beta\beta}$ and Σ in the two hierarchy cases. In particular, it is notable that the set of plausible values of $m_{\beta\beta}$ is highly restricted, being of less than 80 meV and 70 meV for the NH and IH cases, respectively, at 3σ. At 1σ, the IH is ruled out and the bound (in the lone NH case) is $m_{\beta\beta} < 20\,\text{meV}$. This has very important implications for the $0\nu\beta\beta$ search since the possibility of detecting a signal would be out of the reach of the next generation of experiments (see Sec. 1.6).

1.4 Experimental search for $0\nu\beta\beta$

The process described by Eq. (1.1) is actually just one of the forms that $0\nu\beta\beta$ can assume. Depending on the relative numbers of the nucleus protons and neutrons, four different mechanisms are possible:

$$(A, Z) \to (A, Z+2) + 2\mathrm{e}^- \qquad (\beta^-\beta^-) \tag{1.34a}$$

$$(A, Z) \to (A, Z+2) + 2\mathrm{e}^+ \qquad (\beta^+\beta^+) \tag{1.34b}$$

$$(A, Z) + 2\mathrm{e}^- \to (A, Z-2) \qquad (EC\,EC) \tag{1.34c}$$

$$(A, Z) + \mathrm{e}^- \to (A, Z-2) + \mathrm{e}^+ \qquad (EC\,\beta^+). \tag{1.34d}$$

Here, β^- (β^+) indicates the emission of an electron (positron) and EC stands for electron capture (usually a K-shell electron is captured).

The explicit violation of the number of leptons e, $\bar{\mathrm{e}}$, ν_e or $\bar{\nu}_{\mathrm{e}}$ is evident in all the processes described by Eq. (1.34). Therefore, these are equally important in pointing at new Physics beyond the SM and provide the same information on the neutrino mass.

However, the major effort in the experimental search for the $0\nu\beta\beta$ concentrates on the $\beta^-\beta^-$ transition. In fact, a sufficiently high $Q_{\beta\beta}$ is one of the requirements for the choice of a suitable isotope to look for the $0\nu\beta\beta$, since it directly influences the background level (see Sec. 1.4.1). In the cases of Eqs. (1.34b), (1.34c) and (1.34d), which actually describe 3 variants of the same $\beta^+\beta^+$ process, the Coulomb barrier reduces Q-value of the transition ($Q_{\beta\beta}$) of $4m_{\mathrm{e}}c^2$. Therefore, this is usually $\lesssim 2\,\mathrm{MeV}$.[9]

When referring to the $0\nu\beta\beta$ transition, the following discussion will focus on the process described by Eq. (1.34a).

1.4.1 Choice of the isotope

The identification of the best isotope to look for the decay is the first issue to deal with in order to set up a $0\nu\beta\beta$ experiment. A powerful search wants to maximize the sensitivity that can be achieved. As it will be shown in Sec. 1.4.3, this parameter directly depends on the background level and on the energy resolution. Therefore, it is fundamental to reduce the former as much as possible, while the latter needs to be optimized. The exposure, i. e. the product of the (isotope) mass times the live-time, is another key quantity and, since the live-time of the experiment cannot exceed some years, a large detector mass is thus required for an enhanced sensitivity. These considerations translate into a series of criteria to balance for the choice of this isotope:

- *high* $Q_{\beta\beta}$. This requirement is very important, since the value of $Q_{\beta\beta}$ directly influences the background. Two important markers are 2615 keV (^{208}Tl), which represents the end-point of the natural γ radioactivity, and 3270 keV (^{214}Bi), the highest energy β among the ^{222}Rn daughters (^{238}U chain). Furthermore, $Q_{\beta\beta}$ should never be positioned closed to a radioactivity peak (the maximum proximity being set by the detector resolution). The actual suitability of the $Q_{\beta\beta}$ value depends on the detector characteristics. For example, the $Q_{\beta\beta}$ of ^{130}Te is slightly lower than 2615 keV (Table 1.9), but this is not an issue for good energy resolution detectors like bolometers. The excellent γ rejection capability, instead, allows to study ^{76}Ge, whose $Q_{\beta\beta}$ is even lower;

- *high isotopic abundance*. This is a fundamental requirement to have experiments with sufficiently large number of candidate isotopes. With the only exception of the ^{130}Te, all the relevant isotopes have a natural isotopic abundance $< 10\%$. This practically means that the condition translates into *ease of enrichment* for the material, both from the economical and from the technological points of view. For example, this excludes the possibility of using ^{48}Ca, despite this isotope has the highest $Q_{\beta\beta}$ and

[9] Thanks to the different decay topology with respect to the $\beta^-\beta^-$, the $\beta^+\beta^+$ process could help in the identification of the underlying mechanism of the $0\nu\beta\beta$, in case this was finally observed.

TABLE 1.9: Isotopic abundance and Q-value for the most studied $2\nu\beta\beta$ emitters [7].

Isotope	i. a. (%)	$Q_{\beta\beta}$ [MeV]
^{48}Ca	0.187	4.263
^{76}Ge	7.8	2.039
^{82}Se	9.2	2.998
^{96}Zr	2.8	3.348
^{100}Mo	9.6	3.035
^{116}Cd	7.6	2.813
^{130}Te	34.1	2.527
^{136}Xe	8.9	2.459
^{150}Nd	5.6	3.371

it is by far the most abundant on the planet, unless the technical challenges related to the enrichment will be overcome;

- *availability of the isotope.* Despite appearing as obvious, this issue is becoming more and more relevant, since the next generations of $0\nu\beta\beta$ experiments will have a very large isotope mass, of the order of some tonnes. For example, the request of Xe for physics purposes (for both the next generation of $0\nu\beta\beta$ and Dark Matter searches), will represent non negligible fraction of the annual world production. In general, a very large cost (tens of M$) will have to be sustained for the material procurement, with the potential addition of the enrichment cost. Furthermore, the possibility of a relevant amount of time (years) for the same procurement operation should to be taken into account.

- *compatibility with a suitable detection technique.* It has to be possible to integrate the isotope of interest in a working detector. Furthermore, the detector has to be competitive in providing results and has to guarantee the potential for the mass scalability;

There is no single isotope clearly distinguishable because it fully satisfies all the mentioned requests. One has therefore to make a compromise and decide with aspect to privilege for a powerful search, anyway keeping in mind that the choice cannot be made looking at the isotope only, but at the "isotope + detector technique" combination. This results in a group of commonly studied isotopes among all the possible candidate $0\nu\beta\beta$ emitters. It includes: ^{48}Ca, ^{76}Ge, ^{82}Se, ^{96}Zr, ^{100}Mo, ^{116}Cd, ^{130}Te, ^{136}Xe and ^{150}Nd. The related $Q_{\beta\beta}$ and the isotopic abundance are reported in Table 1.9.

1.4.2 Detection techniques

The searches for a $0\nu\beta\beta$ signal rely on the detection of the two emitted electrons. In fact, being the energy of the recoiling nucleus negligible, the sum of kinetic energy of the

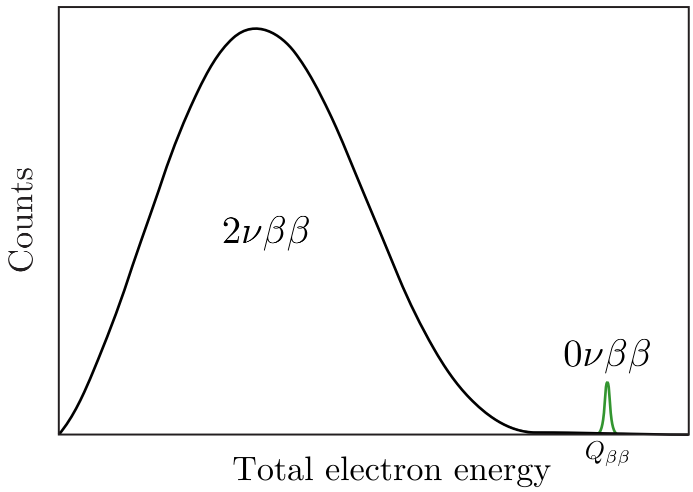

FIG. 1.10: Schematic view of the $2\nu\beta\beta$ and the $0\nu\beta\beta$ spectra.

two electrons is equal to $Q_{\beta\beta}$. Therefore, if we consider these as a single body, we expect to observe a monochromatic peak at $Q_{\beta\beta}$ (Fig. 1.10). Despite this very clear signature, due to the rarity of the process, the detection of the two electrons is complicated by the presence of background events in the same energy region (Region of Interest, ROI), which can mask the $0\nu\beta\beta$ signal.

The main contributions to the background come from the environmental radioactivity, the cosmic rays, and the $2\nu\beta\beta$ of the same isotope. In particular, the latter contribution has the problematic feature of being unavoidable in presence of finite energy resolution, since it is originated by the same isotope which is expected to undergo $0\nu\beta\beta$. In principle, any event producing an energy deposition similar to that of the $0\nu\beta\beta$ increases the background level, and hence spoils the experiment sensitivity. The capability of discriminate the background events is thus of great importance for this kind of search.

The desirable features for a suitable detector, able to observe the two emitted electrons and to collect their sum energy spectrum are thus [60]:

- *good energy resolution.* This is a fundamental requirement to identify the sharp $0\nu\beta\beta$ peak over an almost flat background, as shown in Fig. 1.11, and it is also the only protection against the intrinsic background induced by the tail of the $2\nu\beta\beta$ spectrum. Indeed, it can be shown that the ratio $R_{0\nu/2\nu}$ of counts due to $0\nu\beta\beta$ and those due to $2\nu\beta\beta$ in the peak region can be approximated by [61]:

$$R_{0\nu/2\nu} \propto \left(\frac{Q_{\beta\beta}}{\Delta}\right)^6 \frac{t^{2\nu}_{1/2}}{t^{0\nu}_{1/2}} \tag{1.35}$$

  Δ being, indeed, the energy resolution. This expression clearly indicates that a good energy resolution is critical. But it also shows that the minimum required value actually depends on the chosen isotope, considered a strong dependence of Eq. (1.35) upon the $2\nu\beta\beta$ and $0\nu\beta\beta$ half-lives $t^{2\nu}_{1/2}$ and $t^{0\nu}_{1/2}$;

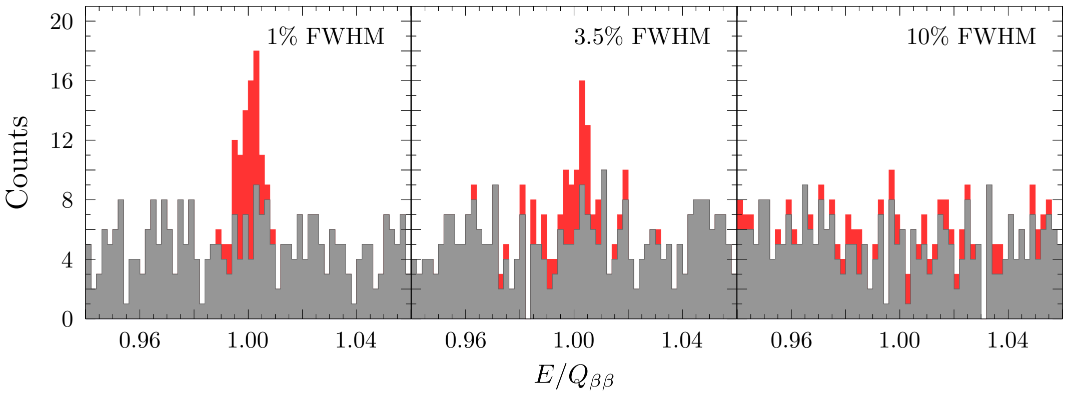

FIG. 1.11: Signal (red) and background (gray) in the ROI around $Q_{\beta\beta}$ for 3 Monte Carlo experiments with the same signal strength (50 counts) and background rate (1 count keV^{-1}), but different energy resolution: 1% FWHM (left), 3.5% FWHM (center), 10% FWHM (right). The signal is distributed normally around $Q_{\beta\beta}$, while the background is assumed flat. Figure from Ref. [62].

- *very low background*. Of course $0\nu\beta\beta$ experiments have to be located underground in order to be protected from cosmic rays. Moreover, radio-pure materials for the detector and the surrounding parts, as well as proper passive and/or active shielding are mandatory to protect against environmental radioactivity.[10] The specific target of the background rejection depend on the isotope and on the detector technique. For example, macro-bolometers are affected by alpha surface events, Ge diodes, due to the low $Q_{\beta\beta}$ of ^{76}Ge by gamma events;

- *large isotope mass*. Present experiments have masses of the order of some tens of kg up to a few hundreds kg. Tonnes will be required for experiments aiming to cover the IH region (see Sec. 1.6).

As for the choice of the isotope, it has to be noted that it is impossible to simultaneously optimize the listed features in a single detector. Therefore, it is again up to the experimentalists to choose which one to privilege in order to get the best sensitivity. Among the most successful examples, we find: solid state detectors and, in particular Ge-diodes for the study of ^{76}Ge, and macro-bolometers, which can be made of different compounds including $0\nu\beta\beta$ candidate emitters (e. g. ^{130}Te, ^{100}Mo, ^{82}Se, ...); liquid and gaseous Time Projection Chambers, especially filled with ^{136}Xe; liquid scintillators, that can be loaded with different $0\nu\beta\beta$ isotope (e. g. ^{136}Xe, ^{130}Te or ^{150}Nd); tracker + calorimeter, observing an external $0\nu\beta\beta$ source.

1.4.3 Sensitivity

The observable that is probed by the experiments searching for the $0\nu\beta\beta$ of a certain isotope is the half-life of the decay, $t^{0\nu}_{1/2}$. In the fortunate event of a $0\nu\beta\beta$ peak showing up in the energy spectrum, this parameter can be evaluated starting from the law of radioactive

[10] The longest living decays from natural radioactivity have half-lives of $(10^9 - 10^{10})$ yr *vs.* the $\gtrsim 10^{25}$ yr of $0\nu\beta\beta$.

decay:

$$t^{0\nu}_{1/2} = \ln 2 \cdot T \cdot \varepsilon \cdot \frac{N_{\beta\beta}}{N_{\text{peak}}} \tag{1.36}$$

where T is the measuring time, ε is the detection efficiency, $N_{\beta\beta}$ is the number of $\beta\beta$ decaying nuclei under observation, and N_{peak} is the number of observed decays in the peak. If we assume to know exactly the detector features (i. e. the number of decaying nuclei, the efficiency and the time of measurement), the uncertainty on $t^{0\nu}_{1/2}$ is only due to the statistical fluctuations of the counts:

$$\frac{\delta t^{0\nu}_{1/2}}{t^{0\nu}_{1/2}} = \frac{\delta N_{\text{peak}}}{N_{\text{peak}}}. \tag{1.37}$$

Since the expected number of events is "small", it seems reasonable to assume Poisson fluctuations on N_{peak}. However, the Poisson and Gaussian distributions give almost the same relative uncertainties (see Ref. [9] for a quantitative evaluation of the discrepancy between the two cases).

If no peak is detected, the sensitivity $S^{0\nu}$ of a given $0\nu\beta\beta$ experiment is usually defined as the process half-life corresponding to the maximum signal that could be hidden by the background fluctuations n_B (at a given statistical C. L.). To obtain an estimation for $S^{0\nu}$ as a function of the experiment parameters, it is sufficient to require that the $0\nu\beta\beta$ signal exceeds the standard deviation of the total detected counts in the interesting energy window. At the confidence level n_σ, this means that we can write:

$$n_{\beta\beta} \geq n_\sigma \sqrt{n_{\beta\beta} + n_B} \tag{1.38}$$

where $n_{\beta\beta}$ is the number of $0\nu\beta\beta$ events and Poisson statistics for counts is assumed. If one now states that the background counts scale linearly with the mass of the detector,[11] from Eq. (1.36) it is easy to find an expression for $S^{0\nu}$:

$$S^{0\nu} = \ln 2 \cdot T \cdot \varepsilon \cdot \frac{n_{\beta\beta}}{n_\sigma \cdot n_B} = \ln 2 \cdot \varepsilon \cdot \frac{1}{n_\sigma} \cdot \frac{x\,\eta\,N_A}{\mathscr{M}_A} \cdot \sqrt{\frac{M \cdot T}{B \cdot \Delta}} \tag{1.39}$$

where B is the background level per unit mass, energy, and time, M is the detector mass, Δ is the Full Width Half Maximum (FWHM) energy resolution, x is the stoichiometric multiplicity of the element containing the $\beta\beta$ candidate, η is the $\beta\beta$ candidate isotopic abundance, N_A is the Avogadro number and, finally, $\mathscr{M}_A$ is the compound molecular mass. Despite its simplicity, Eq. (1.39) has the advantage of emphasizing the role of the essential experimental parameters.

When the background level B is so low that the expected number of background events in the ROI along the experiment life is close to zero, the expression of Eq. (1.39) is no more valid. It is the so called "zero background" experimental condition. The transition between

[11] This is true if impurities are uniform inside the detector. However, this might not be always the case. For example, if the main component of the background is superficial, it is the surface over volume ratio that matters.

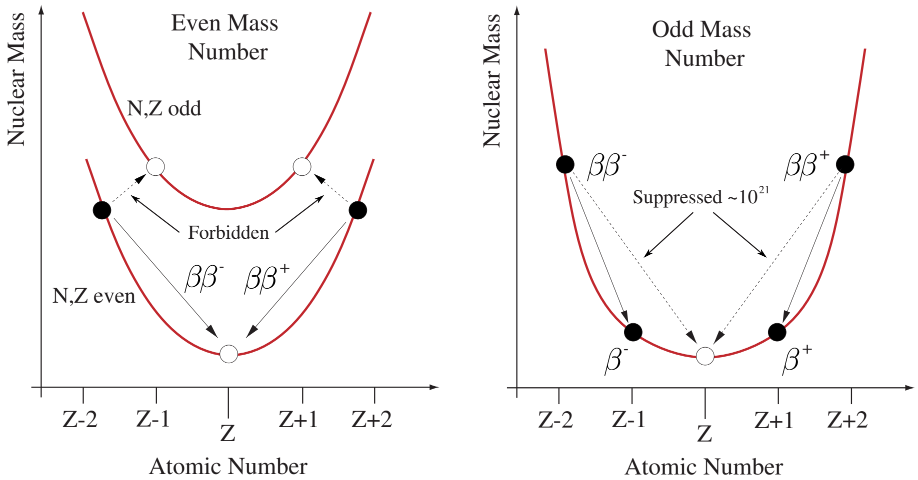

FIG. 1.12: Nuclear mass as a function of the atomic number Z in the case of an isobar candidate with A even (left) and A odd (right).

the two regimes can be identified with the intermediate situation in which the expected number of counts is of the order of unity:

$$M \cdot T \cdot B \cdot \Delta = \mathcal{O}(1). \tag{1.40}$$

In this case, n_B is a constant (the maximum number of counts compatible with no observed counts, at a given C. L.) and the expression for the sensitivity becomes:

$$S_{0B}^{0\nu} = \ln 2 \cdot T \cdot \varepsilon \cdot \frac{N_{\beta\beta}}{n_\sigma \cdot n_B} = \ln 2 \cdot \varepsilon \cdot \frac{x\,\eta\,N_A}{\mathscr{M}_A} \cdot \frac{M\,T}{N_{\mathrm{S}}}. \tag{1.41}$$

The constant N_{S} is now the number of observed events in the ROI.

Reaching the zero background condition is a goal of the experimental searches since, in this case, the sensitivity grows much more rapidly than in presence of background, as it can be seen by comparing Eqs. (1.39) and (1.41).

1.5 Role of nuclear physics

$0\nu\beta\beta$ is a nuclear process. Therefore, the transition has to be described taking into account the relevant aspects that concern nuclear structure and dynamics. More specifically, the $0\nu\beta\beta$ is a second order nuclear weak process that corresponds to the transition from a nucleus (A, Z) to its isobar $(A, Z + 2)$ with the emission of two electrons.

A nucleus (A, Z) can decay via double beta decay as long as the nucleus $(A, Z + 2)$ is lighter. Therefore, candidate isotopes for detecting the $0\nu\beta\beta$ are even-even nuclei that, due to the nuclear pairing force, are lighter than the odd-odd $(A, Z + 1)$ nucleus, making single β decay kinematically forbidden (Fig. 1.12). However, if the nucleus can also decay by single β decay, $(A, Z + 1)$, the branching ratio for the $0\nu\beta\beta$ will be too difficult to be observed due to the overwhelming background rate from the single β decay. It is worth noting that, since the $0\nu\beta\beta$ candidates are even-even nuclei, it follows immediately that their spin is always zero.

The theoretical expression of the half-life of the process can be factorized as:

$$\left[t_{1/2}^{0\nu}\right]^{-1} = G_{0\nu} \left|\mathcal{M}\right|^2 \left|f(m_i, U_{\mathrm{e}i})\right|^2 \tag{1.42}$$

where $G_{0\nu}$ is the phase space factor (PSF) of the transition (it represents the pure kinematic contribution to the $0\nu\beta\beta$), $\mathcal{M}$ is the nuclear matrix element (NME) (it takes into account the nuclear structure aspects) and $f(m_i, U_{\mathrm{e}i})$ is an adimensional function containing the particle physics beyond the SM that could explain the decay through the neutrino masses m_i and the mixing matrix elements $U_{\mathrm{e}i}$. In particular, in the case of ordinary neutrino exchange, the factor f is proportional to $m_{\beta\beta}$:

$$f(m_i, U_{\mathrm{e}i}) \equiv \frac{m_{\beta\beta}}{m_{\mathrm{e}}} = \frac{1}{m_{\mathrm{e}}} \left| \sum_{k=1,2,3} U_{\mathrm{e}k}^2 m_k \right|. \tag{1.43}$$

A mass in the definition of f is added for dimensional balancing. Conventionally, the electron mass m_{e} is used.

By inverting Eq. (1.42), an experimental (lower) limit on the $0\nu\beta\beta$ half-life can be translated into a corresponding limit on the effective Majorana mass:

$$m_{\beta\beta} \leq \frac{m_{\mathrm{e}}}{\mathcal{M}\,\sqrt{G_{0\nu}\, t_{1/2}^{0\nu}}}. \tag{1.44}$$

Therefore, one should try to maximize both the PSF and the NME in order to get more strict bounds on $m_{\beta\beta}$ with the same sensitivity in terms of $t_{1/2}^{0\nu}$. However, as recently discussed in Ref. [63], a uniform inverse correlation between the PSF and the square of the NME emerges in all nuclei (Fig. 1.13). This happens to be more a coincidence than something physically motivated but, as a consequence, no isotope is either clearly favored or disfavored for the search for the $0\nu\beta\beta$. It turns out that all isotopes have qualitatively the same decay rate per unit mass for any given value of $m_{\beta\beta}$.

1.5.1 Assessing the uncertainties

Referring to Eq. (1.44), one sees that, the estimation of the uncertainties both on $G_{0\nu}$ and $\mathcal{M}$ is crucial in order to constrain $m_{\beta\beta}$.

The theory behind the PSFs can be assumed to be well known, and the largest difficulties are related to computational issues. The present uncertainty on these parameters is around 7% [64]. Instead, the calculation of the NMEs for the $0\nu\beta\beta$ is a difficult task because the ground and many excited states of open-shell nuclei with complicated nuclear structure have to be considered. The most common methods are the "Interacting Shell Model" (ISM, [65, 66]), the "Quasiparticle Random Phase Approximation" (QRPA,

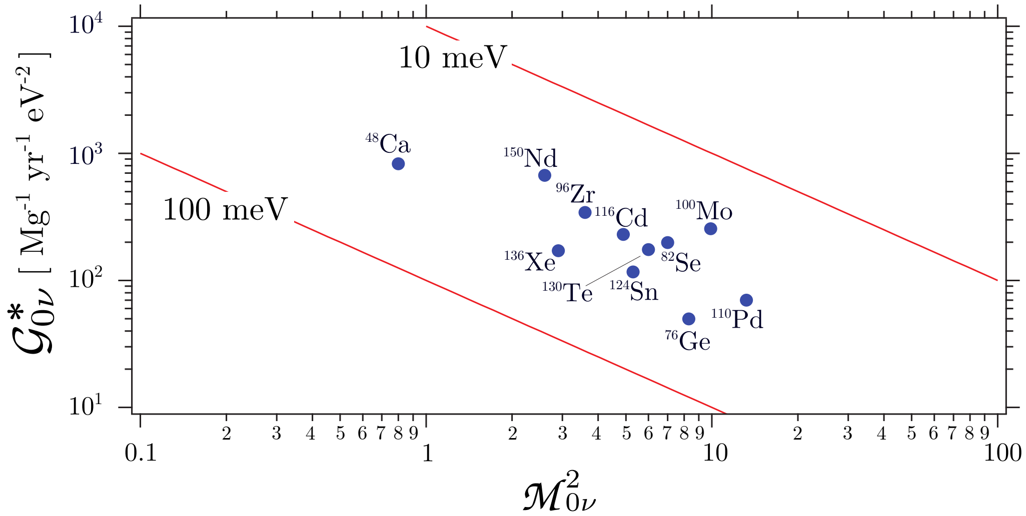

FIG. 1.13: Correlation between the PSFs ($G^*_{0\nu} \equiv \frac{\ln 2\, N_A}{A\, m_e^2} G_{0\nu}$, according to the author notation) and the square of the NMEs. The case $g_A = g_{\text{quark}}$ is assumed. Adapted from Ref. [63].

[67, 68]) and the "Interacting Boson Model" (IBM-2, [69]).[12] These are at present among the most accurate calculations. However, in order to judge their correctness, the comparison with an experimental result (i. e. with a positive $0\nu\beta\beta$ finding) remains unavoidable.

A convenient parametrization for the NMEs is the following [70]:

$$\mathcal{M} \equiv g_A^2\, \mathcal{M}_{0\nu} = g_A^2 \left(M_{GT}^{(0\nu)} - \left(\frac{g_V}{g_A}\right)^2 M_F^{(0\nu)} + M_T^{(0\nu)} \right) \tag{1.45}$$

where $M_{GT}^{(0\nu)}$ is the Gamow-Teller operator matrix element between initial and final states (spin-spin interaction), $M_F^{(0\nu)}$ is the Fermi contribution (spin independent interaction) and $M_T^{(0\nu)}$ is the tensor operator matrix element. g_V and g_A are the axial and vector coupling constants of the nucleon, respectively. The form of Eq. (1.45) emphasizes the role of the latter parameter. Indeed, $\mathcal{M}_{0\nu}$ mildly depends on g_A, if the same behavior (due to the nuclear environment) is assumed for both the vector and axial coupling constants [71].

The NMEs represent the main sources of uncertainties in the inference on $m_{\beta\beta}$. By considering an individual scheme of calculation, a relatively small error intrinsic of the model is usually estimated, being it $\lesssim 20\%$ [71–73]. However, the problem in assessing the uncertainties in the NMEs is far from being solved. In fact, each scheme of calculation can estimate its own uncertainty, but it is still hard to interpret the differences in the results among the models and thus give an overall error. Furthermore, it has been noted that when a process "similar" to the $0\nu\beta\beta$ is considered (single β decay, electron capture, $2\nu\beta\beta$) and the calculations are compared with the measured rates, the actual differences are much larger than 20% [71]. This suggests that it is not cautious to assume that the uncertainties on the $0\nu\beta\beta$ are instead subject to such a level of theoretical control.

[12] Other theoretical models are also present (see e. g. Ref. [9] for a more complete list).

The size of the axial coupling

Recently, there has been a lively interest in a specific and important issue, namely understanding the value of the axial coupling constant g_A, which could actually be (even much) lower than expected.

It is commonly expected that the free value $g_A \simeq 1.269$ measured in the weak interactions could be "renormalized" in the nuclear medium towards the value appropriate for quarks [72–74].

However, it was also argued that a further modification (reduction) is rather plausible [71, 75], thus hinting that the possibility of a "strong quenching" of g_A (i. e. $g_A < 1$) is actually favored. The same was also confirmed by recent study on single β decay and $2\nu\beta\beta$ [76]. Among the possible reasons for the quenching of g_A, it is possible to find causes both dependent and independent from the calculation model (see Ref. [77] for an updated discussion on the topic).

Therefore, the value of g_A in the nuclear medium cannot be regarded as a quantity that is reliably known. It is rather an important reason of uncertainty in the predictions and (at least) the cases

$$g_A \;=\; \begin{cases} g_{A,\,\text{nucleon}} & = 1.269 \\ g_{A,\,\text{quark}} & = 1 \end{cases} \tag{1.46}$$

should always be considered.

A conservative treatment should also include a quenched value for g_A. In Sec. 1.6, the following case will be considered:

$$g_A \;=\; g_{A,\,\text{phen.}} = g_{A,\,\text{nucleon}} \cdot A^{-0.18}. \tag{1.47}$$

The parametrization as a function of the atomic number A comes from the direct comparison between the theoretical half-life for the $2\nu\beta\beta$ process and its observation in different nuclei, as reported in Ref. [71]. From the matching between the theoretical half-life of the process and the experimental value it was possible to extract an effective value for g_A, thus determining its quenching. It is important to remark that the quenching could be or not the same in both the $0\nu\beta\beta$ and $2\nu\beta\beta$ transitions, depending on the causes of the same quenching [77].

The case of Eq. (1.47) is the one mostly affecting the experimental sensitivity in probing $m_{\beta\beta}$. In this sense, it is important to appreciate the relevance of the following argument. If the interpretation is correct and the value of the axial coupling in the nuclear medium is decreased by a factor δ, namely $g_A \;\to\; g_A \cdot (1 - \delta)$, the expected decay rate and therefore the number of signal events S will also decrease, approximatively as $S \cdot (1-\delta)^4$. This change can be compensated by increasing the time of data taking or the mass of the experiment. However, the figure of merit, namely $S/\sqrt{B}$, which quantifies the statistical significance of the measurement, changes only with the square root of the time or of the mass, in the typical case in which there are also background events B. For instance, if we have a

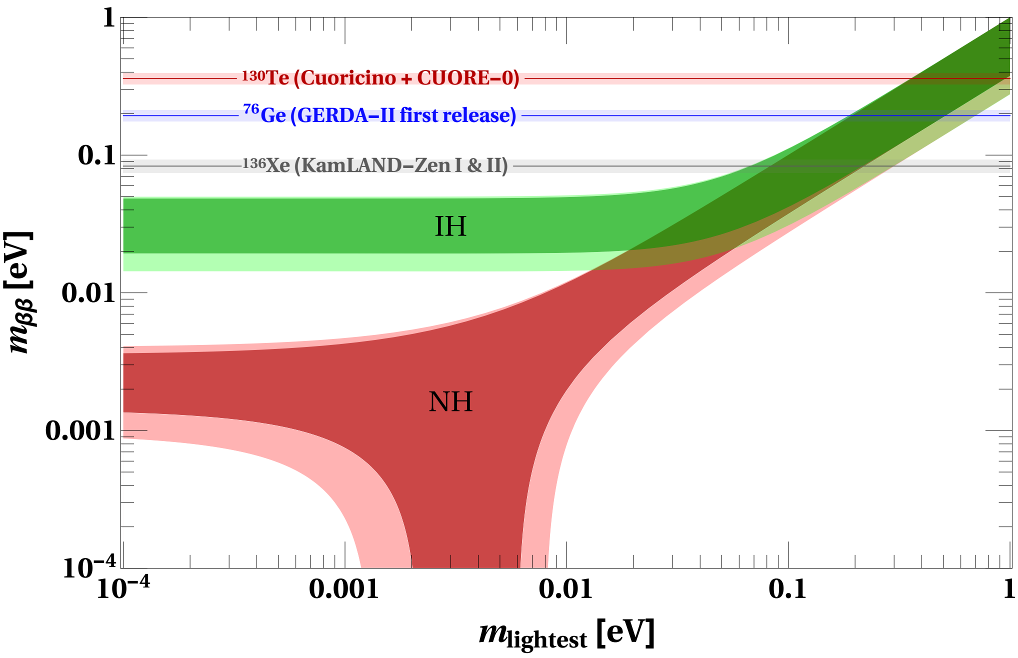

FIG. 1.14: Experimental limits on $m_{\beta\beta}$. The regions of $m_{\beta\beta}$ allowed by oscillations are shown with the relative the 3σ ranges (see also Fig. 1.6). The horizontal bands indicate the most stringent upper limits on $m_{\beta\beta}$ coming from the experimental searches of $0\nu\beta\beta$ of ^{130}Te [78], ^{76}Ge [79] and ^{136}Xe [80]. The NMEs and PSFs from Refs. [69] and [64], respectively, are used.

decrease by $\delta = 10\,(20)\%$ of the axial coupling, we will obtain the same measurement after a time that is larger by a factor of $1/(1-\delta)^8 = 2.3\,(6)$. In other words, an effect that could be naively considered small has instead a big impact for the experimental search for the $0\nu\beta\beta$.

The outcome of this discussion is that the question which is the "true value" of g_A is still open and introduces a considerable uncertainty in the inferences concerning the neutrino mass. From the point of view of the $0\nu\beta\beta$ search, this issue does not reduce the importance of this process as a probe of new physics. Rather, a reduced/quenched value of g_A affects competitiveness of the $0\nu\beta\beta$ in measuring the neutrino mass with respect to the other searches, with the possibility of conflicting with their results (see Sec. 1.3.1).

1.6 Constraints on $m_{\beta\beta}$

Once the experimental sensitivities are known in terms of $S^{0\nu}$, by using Eq. (1.44), it is possible to correspondingly find the upper bounds on $m_{\beta\beta}$. In Fig. 1.14, the most stringent limits up to date, coming from the $0\nu\beta\beta$ search of ^{76}Ge [79], ^{130}Te [78] and ^{136}Xe [80], are shown within the representation introduced in Sec. 1.3. These results have been obtained by using the PSFs from Ref. [64] and the NMEs from Ref. [69] (IBM-2 model). For the value of the axial coupling constant, the case $g_A = g_{A,\,\mathrm{nucleon}}$ has been assumed. The propagation of the uncertainties has thus been done starting from the (self) estimated intrinsic errors on both the PSFs and the NMEs (see Ref. [81] for the calculation). This

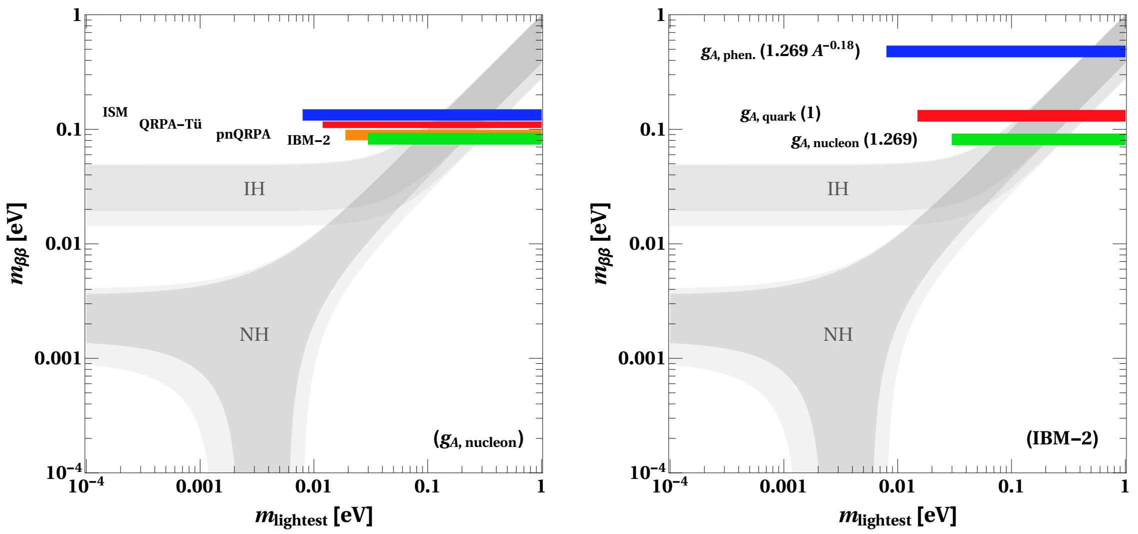

FIG. 1.15: Uncertainties on the currently most tight bound on $m_{\beta\beta}$ (coming from the search of the $0\nu\beta\beta$ of ^{136}Xe [80]). (Left) Dependence on the NME calculations [66–69]. (Right) Dependence on the value of the axial vector coupling constant, according to the cases in Eqs. (1.46) and (1.47).

choice for the quantities used in the derivation of the bounds is arbitrary, but it allows the comparison of the experimental sensitivities.

As discussed in Sec. 1.5.1, the uncertainties from the nuclear physics induce a shift in the bounds on $m_{\beta\beta}$. Graphically this translates into a broadening of the horizontal lines. The issue is indeed trying to quantify the width of the obtained bands. In order to have a conservative discussion, different calculations for the NMEs can be included. For historical reasons, this is usually the choice made when presenting new results from the experimental searches.

An alternative approach, perhaps even more conservative, could consist in fixing the NMEs but considering more values for g_A. The comparison between these two ways of proceeding is shown in Fig. 1.15, where present most stringent limit (that from the $0\nu\beta\beta$ search of ^{136}Xe of Fig. 1.14) analyzed. In particular, in the left panel, the NMEs from Refs. [66–69] have been used while, in the right panel, the cases in Eqs. (1.46) and (1.47) have been considered for g_A. It can be seen that the sensitivity for the same limit differs of a similar factor when considering more NMEs and the two cases $g_A = g_{A,\,\text{nucleon}}$ and $g_A = g_{A,\,\text{quark}}$. Instead, a $\gtrsim 5$ exists between the two cases of $g_{A,\,\text{nucleon}}$ and $g_{A,\,\text{phen.}}$. It is clear from the figure that this is the biggest uncertainty, with respect to all the other theoretical ones.

The latter approach for the discussion of the uncertainties has been used to evaluate the limits on $m_{\beta\beta}$ from the current (upper group) and future (lower group) $0\nu\beta\beta$ experiments (the formers are the same limits presented in Fig. 1.14). The results are reported in Table 1.16.

The current generation of experiments is probing the quasi degenerate part of the neutrino mass spectrum, with the limit from ^{136}Xe almost approaching the IH region. The forthcoming future experiments will start to probe the mass region below 100 meV (in case of unquenched value for g_A), covering (at least partially) the IH region. In case g_A is maximally quenched, instead, the situation is much worse.

Further future $0\nu\beta\beta$ searches

A fair way to conceive a future $0\nu\beta\beta$ experiment with enhanced sensitivity is to talk in terms of target exposure or of half-life time that can be probed. However, from the point of view of the neutrino physics, besides the hope of discovering the $0\nu\beta\beta$, the most exciting investigation that can be thought at present is the full exploration of the IH region of the neutrino mass spectrum. [13] Therefore, let us imagine a next-to-next generation experiment with zero background able to fully cover the IH region [81].

Referring to Eq. (1.41), by assuming $\varepsilon \simeq 1$ (detector efficiency of 100% and no fiducial volume cuts), $x \simeq \eta \simeq 1$ (all the mass is given by the candidate nuclei) and one observed event in the ROI ($N_\text{S} = 1$), we get the simplified expression

$$M \cdot T = \frac{\mathscr{M}_A \cdot S^{0\nu}_{0B}}{\ln 2 \cdot N_\text{A}}. \tag{1.48}$$

This is the equation we used to estimate the product $M \cdot T$ (exposure), and thus to assess the sensitivity of the hierarchy discrimination experiments.

The key input is the theoretical expression of $S^{0\nu}_{0B}$, which can be derived from Eq. (1.42), once all the input parameters have been fixed. As previously discussed, the PSFs are reliably known [64], while for the NMEs an arbitrary choice for a specific model can be made. In this case the NMEs from Ref. [69] have been used. We require a sensitivity $m_{\beta\beta} = 8\,\text{meV}$. This value allows us to exclude a possible overlap of the band for $m_{\beta\beta}$ with the IH region at more than 3σ, taking into account the residual uncertainties from the specific NME calculation and from the PSFs.

The calculated values of the exposures are shown in Table 1.17 for the nuclei ^{76}Ge, ^{130}Te and ^{136}Xe. The last column gives the maximum allowed value of the product $B \cdot \Delta$ that satisfies Eq. (1.40).

For the sake of the previous discussion, the three cases for the g_A values of Eqs. (1.46) and (1.47) are considered. It can be seen that, in first scenario, it is likely to expect that a tonne-scale experiment will be able to reach or, at least, get close to the target. However, it has to be noted that the constraints on the background are very tight. In the second scenario, instead, the situation is more critical and multi-tonne experiments will be required. Finally, in third scenario, which, represents the worst possible case, this target becomes extremely challenging for the present technological skills.

[13] This target will also allow to probe the sign of Δm^2 and to confirm/disprove the results from cosmology, whose bounds are starting to rule out the IH region (see Fig. 1.8).

TABLE 1.16: Upper bounds on $m_{\beta\beta}$ from the present (upper group) and future (lower group) $0\nu\beta\beta$ experiments. Refs. [64] and [69] were used for the PSFs and for the NME, respectively. The different results correspond to different values of g_A according to Eqs. (1.46) and (1.47).

Experiment	Isotope	$S^{0\nu}$ (90% C. L.) [yr]	Lower bound for $m_{\beta\beta}$ [eV]		
			$g_{A,\,\mathrm{nucleon}}$	$g_{A,\,\mathrm{quark}}$	$g_{A,\,\mathrm{phen.}}$
GERDA-II (first release), [79]	^{76}Ge	$5.3 \cdot 10^{25}$	0.19 ± 0.02	0.31 ± 0.03	0.91 ± 0.08
Cuoricino + CUORE-0, [78]	^{130}Te	$4.0 \cdot 10^{24}$	0.36 ± 0.03	0.58 ± 0.05	2.0 ± 1.0
KamLAND-ZEN I & II, [80]	^{136}Xe	$1.1 \cdot 10^{26}$	0.083 ± 0.009	0.13 ± 0.01	0.49 ± 05
GERDA-II, [82]	^{76}Ge	$1.5 \cdot 10^{26}$	0.11 ± 0.01	0.18 ± 0.02	0.54 ± 0.05
MAJORANA D., [83]	^{76}Ge	$3.0 \cdot 10^{25}$	0.25 ± 0.02	0.41 ± 0.04	1.2 ± 0.1
CUPID-0, [84]	^{82}Se	$1.8 \cdot 10^{25}$	0.20 ± 0.02	0.32 ± 0.03	0.97 ± 0.09
SuperNEMO, [85]	^{82}Se	$1.0 \cdot 10^{26}$	0.084 ± 0.008	0.14 ± 0.01	0.41 ± 0.04
AMoRE II, [86]	^{100}Mo	$1.1 \cdot 10^{27}$	0.018 ± 0.002	0.029 ± 0.003	0.094 ± 0.009
CUORE, [87]	^{130}Te	$9.5 \cdot 10^{25}$	0.074 ± 0.007	0.12 ± 0.01	0.43 ± 0.04
SNO+ Phase II, [88]	^{130}Te	$2.0 \cdot 10^{26}$	0.051 ± 0.005	0.083 ± 0.008	0.30 ± 0.03
EXO-200, [89]	^{136}Xe	$5.7 \cdot 10^{25}$	0.11 ± 0.01	0.18 ± 0.02	0.67 ± 0.07
KamLAND2-Zen , [90]	^{136}Xe	$1.0 \cdot 10^{27}$	0.027 ± 0.003	0.044 ± 0.005	0.16 ± 0.02
nEXO, [91]	^{136}Xe	$5.0 \cdot 10^{27}$	0.012 ± 0.001	0.019 ± 0.002	0.071 ± 0.008
NEXT-100, [92]	^{136}Xe	$6.0 \cdot 10^{25}$	0.11 ± 0.01	0.18 ± 0.02	0.65 ± 0.07
PandaX-III, [88]	^{136}Xe	$1.0 \cdot 10^{26}$	0.087 ± 0.010	0.14 ± 0.02	0.50 ± 0.06

TABLE 1.17: Sensitivity and exposure necessary to discriminate between NH and IH: the goal is $m_{\beta\beta} = 8\,\mathrm{meV}$. The 3 cases refer to the values of g_A listed in Eqs. (1.46) and (1.47). The calculations are performed assuming zero background experiments with 100% detection efficiency and no fiducial volume cuts. The last column shows the maximum value of the product $B \cdot \Delta$ in order to actually comply with the zero background condition.

Case	Isotope	$S^{0\nu}_{0B}$ [yr]	$M \cdot T$ [t yr]	$(B \cdot \Delta)_{0B}$ [kg^{-1} yr^{-1}]
$g_{A,\,\mathrm{nucleon}}$	^{76}Ge	$3.0 \cdot 10^{28}$	5.5	$1.8 \cdot 10^{-4}$
	^{130}Te	$8.1 \cdot 10^{27}$	2.5	$4.0 \cdot 10^{-4}$
	^{136}Xe	$1.2 \cdot 10^{28}$	3.8	$2.7 \cdot 10^{-4}$
$g_{A,\,\mathrm{quark}}$	^{76}Ge	$7.9 \cdot 10^{28}$	14	$7.0 \cdot 10^{-5}$
	^{130}Te	$2.1 \cdot 10^{28}$	6.5	$1.5 \cdot 10^{-4}$
	^{136}Xe	$3.0 \cdot 10^{28}$	9.8	$1.0 \cdot 10^{-4}$
$g_{A,\,\mathrm{phen.}}$	^{76}Ge	$6.9 \cdot 10^{29}$	125	$8.0 \cdot 10^{-6}$
	^{130}Te	$2.7 \cdot 10^{29}$	84	$1.2 \cdot 10^{-5}$
	^{136}Xe	$4.0 \cdot 10^{29}$	130	$7.7 \cdot 10^{-6}$

Chapter 2

Bolometric technique

Bolometers are calorimeters in which the energy released in an absorber by an interacting particle is converted into phonons and measured via temperature variation. These detectors can be operated only at cryogenic temperatures of about 10 or few tens of mK. In fact, the elementary excitation energy is of the order of 10 meV, with a typical corresponding temperature deviation of about a few tens-hundreds of μK per MeV.

Unlike most of the conventional spectroscopic techniques, which are based on the detection of the energy released in the form of ionization and/or excitation of the detector's molecules, the bolometric technique measures the phonon component. This is a great advantage since a considerable fraction, if not all, the released energy is indeed converted into phonon excitations inside the detector. The resulting excellent energy resolution makes these detectors very suitable for the use in rare event physics, such as the search for $0\nu\beta\beta$.

2.1 Simplified thermal model

A bolometer consists essentially of two elements: an energy absorber, in which the energy from the interacting particle is deposited, and a phonon sensor that converts this energy (i. e. the phonons) into a measurable signal.

In a very simplified model, a bolometer can be represented as a calorimeter with heat capacity C connected to a heat bath (with constant temperature T_0) through a thermal conductance G. If a certain energy is released in the absorber, this will produce a change in temperature ΔT equal to the ratio between E and C. Let $T(t)$ be the absorber temperature as a function of the time t and let us assume

$$\Delta T \equiv |T(t) - T_0| \ll T_0 \quad \forall t, \tag{2.1}$$

so that C and G can be considered as constant quantities. Then, the temperature variation can be described by the time evolution:

$$\Delta T(t) = \frac{E}{C}\, \mathrm{e}^{-t/\tau} \quad \text{with} \quad \tau \equiv \frac{C}{G}. \tag{2.2}$$

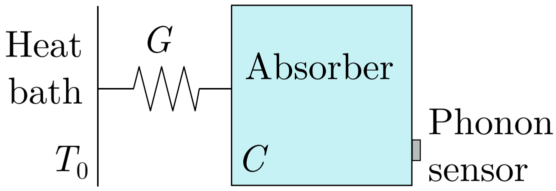

FIG. 2.1: Simplified bolometer thermal model. The detector is modeled as a single object with heat capacity C coupled to the heat bath (with constant temperature T_0) through the thermal conductance G. The phonon sensor plays no active role.

The characteristic time of the thermal pulse can be very long, from ms up to a few seconds, depending on the values of C and G.

From Eq. (2.2), the crucial importance of the heat capacity appears evident: to get a large signal amplitude, C has to be as small as possible. In order to minimize C, very low temperatures are needed and a suitable material for the absorber has to be chosen. In particular, dielectric and diamagnetic crystals or superconductors (below the transition phase) are preferred, so that the main contribution to C is the one from the crystal lattice. In this case, the Debye law for the specific heat at low temperatures can be applied:

$$C \propto \left(\frac{T}{\Theta_\mathrm{D}}\right)^3 \tag{2.3}$$

where the Θ_D is the Debye temperature and is a property of the material. Since this parameter depends on the mass number A and on the material density ρ as $\Theta_\mathrm{D} \propto A^{-1/3}\,\rho^{-1/6}$ [93], low atomic mass and low density should be preferred for their high Θ_D. At the same time, a high Z guarantees a larger detection efficiency for β radiation, while a high Z/A ratio a larger detection efficiency for for γs.

A real bolometer is much more complicated than the “monolithic” detector here represented. For example, the parameters C and G cannot be considered as global quantities, but rather as the sum of many contributions, each with different behaviour. Also the role of the phonon sensor is not negligible in the development of the signal (see e. g. Refs. [94, 95]). However, this simple description gives a qualitative idea of a bolometric detector.

2.2 Thermalization process

A more detailed description of the phonon propagation and thermalization phenomena can be found in Ref. [96].

After an interaction, the energy released into the absorber immediately downgrades. This process occurs through two main channels: nuclear and electronic [97]. In the former case, the energy is in part converted into vibrational excitations, i. e. phonons, and in part produces structural defects in the absorber lattice which, due to the low temperature, are stable and possibly constitute energy traps that worsen (of some eV) the energy resolution of the detector. In the latter case, the energy is spent to excite electron-hole (e-h) pairs all along the particle path (few μm in case of heavy particles or mm in case of electrons). These charge carriers interact in turn with each other and spread very quickly in the crystal. Once an equilibrium is reached, they undergo their final degradation interacting with the lattice. In this process a large fraction of the initial energy is thus transferred to the lattice as vibrational phonons. However, also "undesirable" processes can take place, in particular recombinations (with possible emission of photons) and trapping of electrons and holes in impurity sites or lattice defects.

In order to (qualitatively) understand the phonon thermalization process inside the crystal absorber, let us refer to the mono-dimensional representation of the phonon dispersion curves shown in Fig. 2.2. The e-h pair recombination across conduction and valence bands produces high energy-low momentum "athermal" phonons in the "optical" branch (out-of-phase movements of the atoms in the lattice). These primary phonons propagate from the particle interaction region and decay in a very short time, $(10 - 100)$ ps. Usually two phonons are created, each with half of the original energy. The decays, mainly in the "acoustic" branch (coherent movements of atoms of the lattice), result in a phonon cascade system. The average phonon energy is of the order of $E_{\mathrm{D}} = \hbar\omega_{\mathrm{D}}$, where ω_{D} is the Debye cut-off frequency of the crystal, the theoretical maximum frequency of vibration for the atoms of the crystal. This energy is much higher than the average energy of "thermal" phonons that, at the bolometer working temperature, is of some μeV.

At this point, phonon-phonon scattering, mass-defect impurity scattering and boundary scattering phenomena occur, leading to the final phonon energy degradation. In particular, the decay chain proceeds until the mean free path of the phonons becomes larger than crystal dimensions, i. e. there is a ballistic propagation of phonons until they reach the crystal surfaces. Here, a fraction of the phonons diffuses and is directly thermalized. Another fraction, instead, is reflected. These phonons can suffer other decay processes and, at the end, interact with the background thermal phonons with a final thermalization.

2.2.1 Energy resolution

The intrinsic energy resolution of a detector is primarily determined by the statistical fluctuation of the number of elementary events N contributing to the signal. In case of a sensor sensitive to thermal phonons (in thermal equilibrium), the fluctuation is caused by the continuous phonon exchange between the absorber and the heat sink. As an example, for a 750 g TeO_2 crystal at 10 mK (the heat capacity is known [98]), we have

$$N \simeq \frac{C(T)}{k_{\mathrm{B}}} \simeq 1.4 \cdot 10^{14} \tag{2.4}$$

k_{B} being the Boltzmann constant. It has to be noticed that N is much larger than the number of phonons produced in a typical energy depositions of a few MeV.

If we assume that the number of elementary events follows a Poisson distribution with $\Delta N = \sqrt{N}$, we thus have that the intrinsic energy resolution ΔE is proportional to the

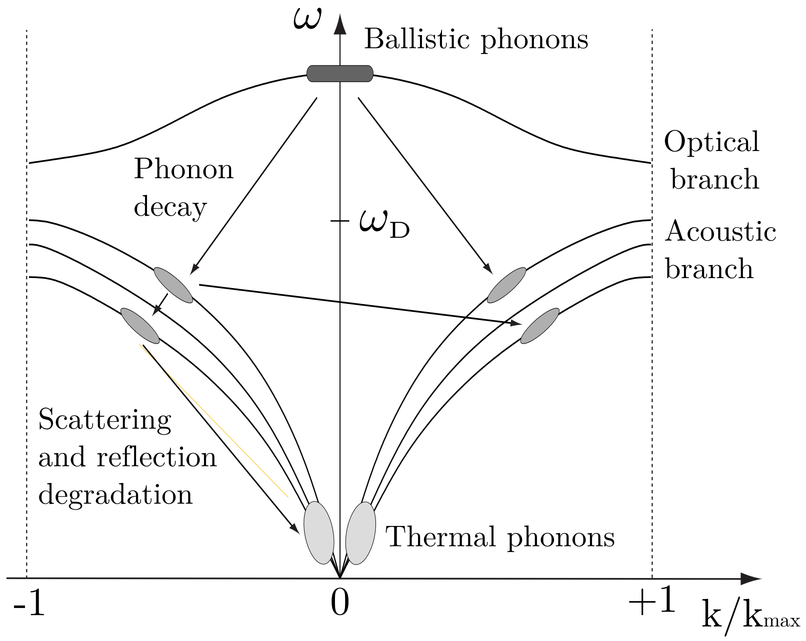

FIG. 2.2: Athermal model for the phonons thermalization. The abscissa k is the module of the crystal momentum.

mean energy required to produce an elementary excitation ($\varepsilon = k_B T$):

$$\Delta E = \varepsilon \, \Delta N = \xi \sqrt{k_B \, C(T) \, T^2}. \tag{2.5}$$

The factor ξ is a dimensionless factor that depends on the details of the real detector. It can be made of the order of unity with a proper optimization work. It is worth to notice that the expression obtained in Eq. (2.5) is independent of energy. To give an idea of the potentiality of these detectors, the intrinsic resolution for the considered 750 g TeO_2 crystal lays within the range $(20 - 100)$ eV.

The effective energy resolution is actually dominated by the "extrinsic" noise, i. e. the noise generated by all the sources which are dependent on the experimental setup. These include the noise due to the cryogenic system (thermal noise), the electronics read-out, the electromagnetic interferences and the mechanical microphonic noise. Eventually, this result in an energy resolution of the order of a few keV at 1 MeV, a value anyhow comparable with that of the best performing detectors.

2.3 Phonon sensor

The phonon sensor is a device that collects the phonons produced in the absorber and generates an electric signal. It is possible to identify many classes of phonon sensors, sensitive to phonons before or at the thermal equilibrium (see e. g. Ref. [99] for a review).

A simple version consists in the use of a thermistor whose resistance, as a function of temperature, has a steep slope. Thus, to a small variation of temperature, a measurable variation of resistance can correspond. In particular, since the series of experiments

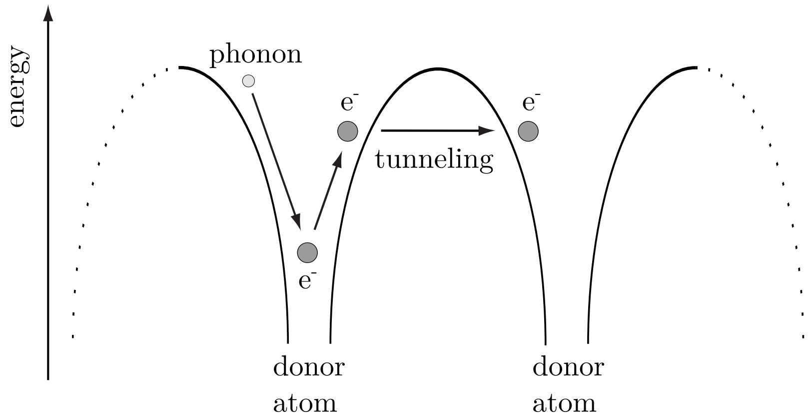

FIG. 2.3: Schematic representation of the hopping conduction mechanism.

considered in this work used, and currently use, semiconductor thermistors, we focus our attention only on this kind of sensors.

2.3.1 Semiconductor thermistors

Semiconductor thermistors are intrinsically slow devices and are mainly sensitive to thermal phonons. Therefore, they act as temperature sensors, giving information about the system in thermal equilibrium.

In general, a semiconductor thermistor consists of a small Ge (or Si) crystal with a doped region. A very uniform and large dopant distribution and a very accurate net dopant concentration are usually obtained through the Neutron Transmutation Doping (NTD) [100]. In this method, the semiconductor sample is bombarded with neutrons which induce nuclear reactions on the various target stable isotopes leading to the formation of n- and p-dopants.

For intrinsic semiconductors (i. e. without impurities) the conduction can happen only for thermal generation of electrons and holes across the band gap equal or larger than the energy gap, E_{gap}. Therefore, this mechanism is possible only at high T since $E_{\text{gap}} \sim 670\,\text{meV}$ for Ge while $k_B T \simeq 25\,\text{meV}$ at room temperature. Instead, if impurities are present in the semiconductor lattice, it is possible for the electronic conductance to take place also at lower T. The mechanisms of "banding" and "hopping" occur in semiconductors which are heavily doped and compensated (equal number of donors and acceptors), respectively. In these cases, the charge carriers move from one impurity to the next without reaching the band.

The former mechanism requires an impurity concentration high enough to lead to the substantial overlap between neighboring wave functions. The individual impurity states form an "impurity band" [101]. Depending on the number of doped atoms, therefore, the semiconductor can behave either as an insulator or as a metal, even at low T. In general, it exists a critical concentration N_c characterizing the (abrupt) transition between the two opposite situations, which is called the Metal-Insulator Transition (MIT) [102].

The latter mechanism, instead, occurs when compensating (or minority) impurities create a number of majority impurities which remain ionized down to $T = 0\,\mathrm{K}$. In this case, the charge carriers can "hop" from an occupied majority impurity site to an empty one via quantum mechanical tunneling through the potential barrier which separates the two dopant sites. The conduction is activated by phonon mediation, as schematically depicted in Fig. 2.3. The tunneling probability is exponentially dependent on the inter-impurity distance and this is why an extreme homogeneity of the dopant distribution is fundamental.

In particular, if the dopant concentration is slightly lower than N_c, then the resistivity is strongly dependent on the temperature. This is why it is usually chosen to operate semiconductor thermistors just below the MIT region. The conduction mechanism in these conditions takes the name of "variable range hopping", since the carriers can also migrate to far sites if their energy levels are localized around the Fermi energy. The resistivity as a function of the temperature is described by the following law:

$$\rho = \rho_* \exp\left(\frac{T_*}{T}\right)^{\gamma} \tag{2.6}$$

where ρ_* and T_* are parameters depending on the doping level and compensation. The exponential γ in the Mott model for a 3-dimensional crystal is equal to 1/4 for low compensation values [102]. It becomes 1/2 for large values of compensation, where the Coulomb repulsion among the electrons leads to the formation of a gap in the electron state density near the Fermi energy [103]. This is the value used for the NTDs considered in this work.

2.4 Detector operation

In order to obtain a voltage signal, a steady current $I_{\mathrm{bol}} = I_B$ (bias current) is sent through the thermistor by means of the bias circuit shown in the left panel of Fig. 2.4. The voltage generator is closed on a load resistor R_L in series with the thermistor R_{bol}, whose resistance is negligible in comparison to R_L ($R_L \gg R_{\mathrm{bol}}$ therefore I_{bol} is independent from R_{bol}).

Once a working point is set by forcing a bias current, a voltage drop $V_{\mathrm{bol}}(T) = I_B\, R_{\mathrm{bol}}(T)$ is established across the thermistor. The consequent power dissipation $P = I_B\, V_{\mathrm{bol}}$ produces a temperature raise and acts back on the resistance $R_{\mathrm{bol}}(T)$ until an equilibrium is reached:

$$T_{\mathrm{bol}} = T_0 + \frac{P}{G} \tag{2.7}$$

where G the thermal conductance between the detector and the heat sink (T_0).

This phenomenon makes the V-I relation deviate from linearity and leads to a non-ohmic behavior. It is often referred to as "electrothermal feedback". For a given I_B, the "static" resistance is simply the ratio $V_{\mathrm{bol}}/I_{\mathrm{bol}}$ while the "dynamic" resistance is the inverse of the tangent to the V-I curve. By further increasing I_B, the dynamic resistance crosses the so called "inversion point" (where it vanishes) and becomes negative. The intersection of the V-I curve, usually called *load curve*, with the load line imposed by the biasing system

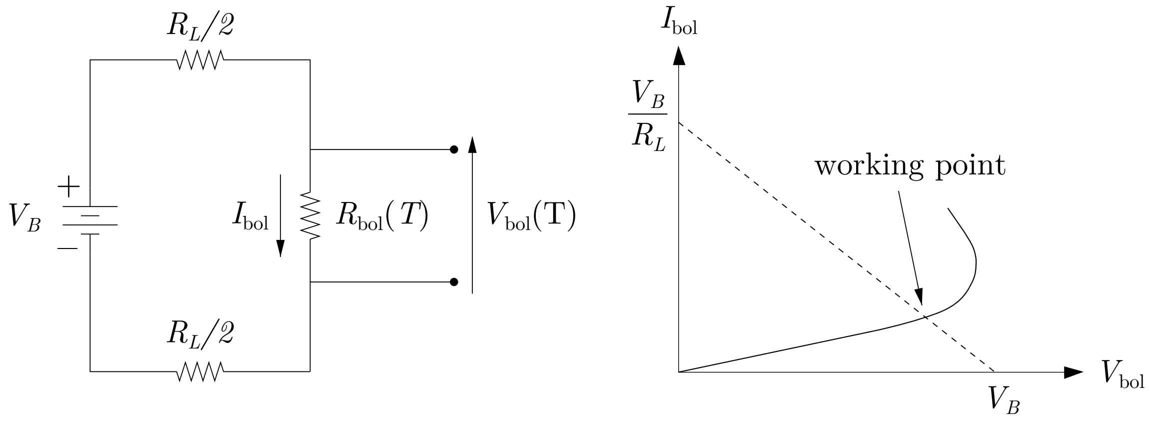

FIG. 2.4: (Left) Electric scheme of the biasing system used for the NTD read-out. (Right) typical load curve of a semiconductor thermistor. The working point is set as the intersection between the V-I characteristic curve and the load line $V_{\rm bol} = V_B - I_{\rm bol}\, R_L$.

determines the working point of the sensor (right panel of Fig. 2.4). This is typically chosen before the inversion point in order to maximize the signal amplitude and the signal-to-noise ratio. By a combined fit of load curves measured at different base temperatures, it is possible to evaluate the thermistor intrinsic parameters ρ_*, T_* and γ.

In first approximation, the thermal pulse produced by an energy release in the absorber is characterized by a very fast rise time (instantaneous if we assume the model described in Sec. 2.1 and a negligible thermalization time). The fall time, instead, follows an exponential decay whose time constant depends on the physical characteristic of the detector (recall Eq. (2.2)). The relationship between the electrical pulse height $\Delta V_{\rm bol}$ and the energy deposition E can be obtained by resolving the circuit of Fig. 2.4:

$$\Delta V_{\rm bol} = {\rm const} \cdot \gamma \left(\frac{T_*}{T_{\rm bol}}\right)^{\gamma} \cdot \frac{E}{C \cdot T_{\rm bol}} \cdot \sqrt{P \cdot R_{\rm bol}} \tag{2.8}$$

where P is the power dissipated in the thermistor $R_{\rm bol}$ by Joule effect. In particular, this expression vanishes in the limits $P \to \infty$ and $C \to \infty$.

To make an example, an energy deposition of 1 MeV in a 750 g TeO_2 absorber (see Sec. 3.3.1) typically produces a temperature increase of the $\Delta T \sim 75\,\mu$K, with a related voltage drop $\Delta V_{\rm bol} \sim 100\,\mu$V.

2.5 Response stabilization

A critical issue when operating bolometric detectors over long periods of time, for months or even for years, consists in maintaining a stable response (within a $\sim 0.1\%$ level), despite the unavoidable temperature fluctuations due to the cryogenic set-up.

An effective approach to this issue can be found in the use of a pulser able to periodically deliver a fixed (and extremely precise and stable) amount of energy to the detector and to generate a pulse as similar as possible to the signal corresponding to a real event [104]. In this way, the study of the variation of the detector response to the same energy deposition can be used to correct (off-line) the effects of the cryogenic instabilities.

Even if a particle-based stabilization could appear as a first possible way to realize an energy pulser, with the advantage of getting an identical detector response to the pulser and to the events of interest, this method presents some important drawbacks. A series of undesired cascade peaks would be generated by the same source and the Poisson time distribution of the events would limit the calibration rate. Furthermore, the calibration pulses could not be "flagged" and their off-line identification would be based only on their amplitude.

A resistive element thermally coupled to the crystal, instead, can be used to inject calibrated amounts of energy via Joule heating. This solution offers the advantage of a complete control of the calibration mechanism: the pulses can be equally spaced in time and their rate and amplitudes can be easily tuned to the necessity of the experiment. However, it must be noted that such a heating element needs to satisfy some (non-obvious) requirements. In particular, its resistance must be reasonably independent of the temperature and of the applied voltage, while its heat capacity must be negligible with respect to the detector's one. In order to provide an almost instantaneous energy release, the relaxation time to the crystal of the developed heat must be much shorter than all the typical thermal time constants. Finally, the mechanism of signal formation for particle interactions and for Joule heating must be similar enough to assure that the pulse amplitude dependence on time, baseline level and other operation conditions are the same for the two processes.

Steady resistances useful for this purpose can be realized through a heavily doped semiconductor, well above the MIT region, so that a low-mobility metallic behaviour is exhibited [105]. A detailed discussion on the use of heaters for the stabilization of the detector response for the considered bolometric experiments can be found in Ref. [104].

2.6 Cryogenic apparatus

In order to operate a bolometric detector, a system able to reach and maintain a stable working temperature of $\sim 10\,\mathrm{mK}$ for long periods is needed. The (only possible) solution is found in the use of a dilution refrigerator (DR).

A DR is a cryogenic device whose working principle relies on the ^{3}He/^{4}He mixture properties. The original idea was suggested by London in 1951 [106] and, about ten years later, the same London, Clarke and Mendoza published a proposal for realizing such a cooling system [107]. The first functioning DR was built in 1965 [108] and steady improvements followed since then, leading to a lowest (stable) temperature of $2\,\mathrm{mK}$ in 1978 [109] and of $1.75\,\mathrm{mK}$ in 1998 [110].

Since the late 1960s, it has also become possible to buy commercial DRs. This is the case for the ones used for the measurements described in this work. Today, "plug and play" DRs are on the market, thus avoiding the need of a deep knowledge of cryogenics to use of these very delicate devices.

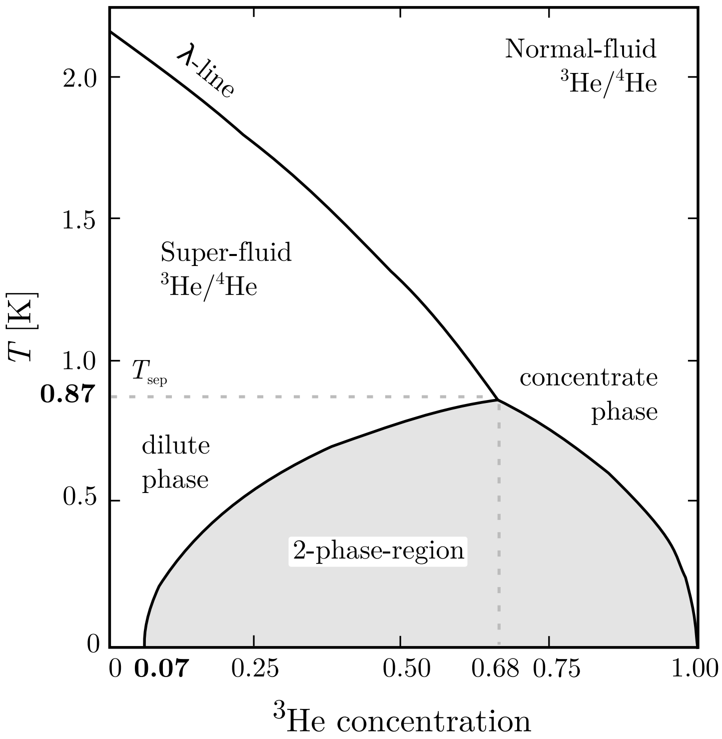

FIG. 2.5: Phase diagram of liquid ^{3}He/^{4}He mixture at saturated vapor pressure. The λ-line for the super-fluid transition of ^{4}He separates into two for $T = T_{\text{sep}}$ and sufficiently high concentration of ^{3}He. Below this temperature the two isotopes separate into a ^{4}He and a ^{3}He rich phase). Adapted from Ref. [111].

2.6.1 DR working principle

Let us consider the properties of the ^{3}He/^{4}He mixture by referring to Fig. 2.5. The picture shows the 'concentration *vs*. temperature' diagram for the liquid ^{3}He/^{4}He mixture at saturated vapor pressure.

Liquid ^{4}He becomes super-fluid at $T = 2.177\,\text{K}$, while ^{3}He does not show any phase transition down to some mK. However, the temperature of the super-fluid phase transition of the (Bose) liquid ^{4}He decreases if this is diluted into the (Fermi) liquid ^{3}He. Eventually, the ^{4}He super-fluidity ceases to exist for ^{3}He concentrations grater than 67.5% [111]. At this concentration and at $T = T_{\text{sep}} \equiv 0.867\,\text{K}$, the transition line between the ^{4}He normal-fluid and super-fluid phases, the so called λ-line, separates into two. Below this temperature, the two isotopes are only miscible for fixed concentrations, depending on the temperature. This means that the shaded region in the figure is not physically accessible.

Therefore, if we cool a ^{3}He/^{4}He mixture to temperatures below T_{sep}, the liquid will separate into two phases, one rich in ^{3}He and the other rich in ^{4}He (diluted in ^{3}He). In particular, due to its lower density, the ^{3}He-rich liquid will float over the ^{4}He-rich liquid. At a few mK, the former is almost pure ^{3}He. Instead, the ^{3}He concentration in the latter never drops to zero, but it reaches a constant concentration of $\sim$ 6.6% and this finite solubility is at the base DR technology.

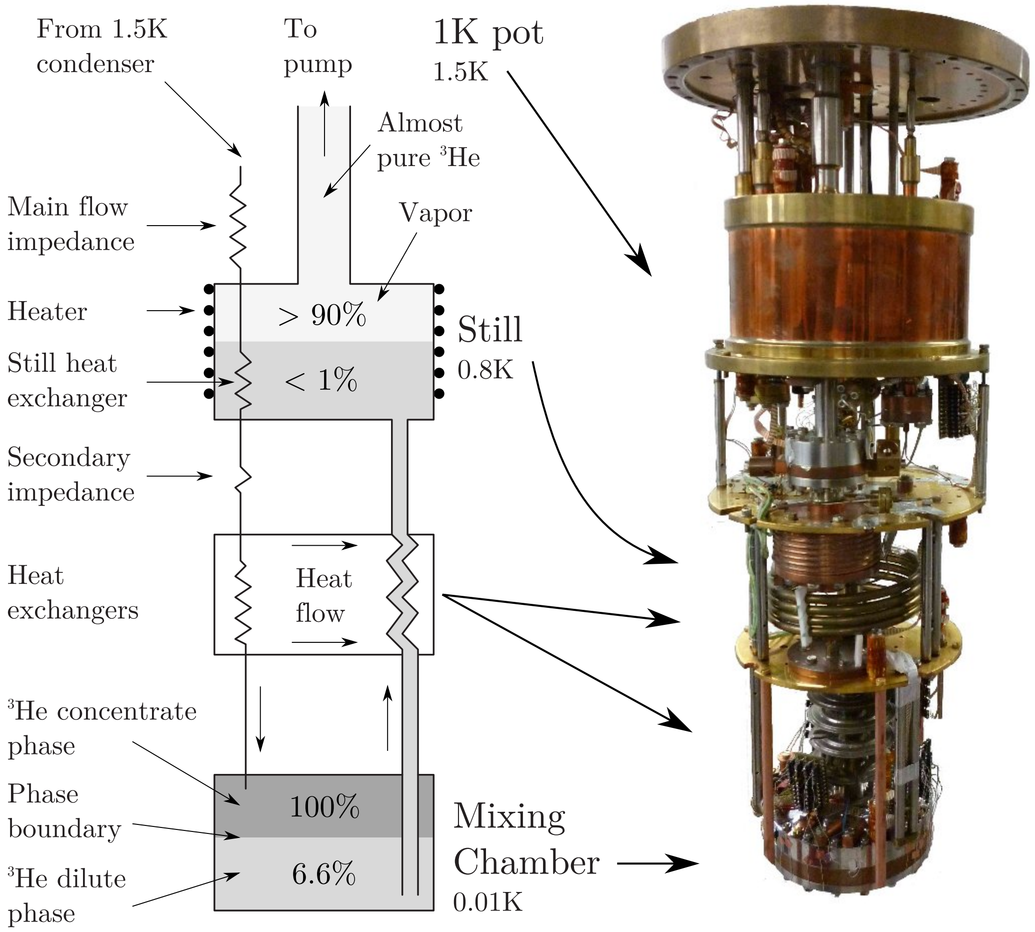

FIG. 2.6: (Left) Schematic of the inner circuit of a DR. Adapted from Ref. [93]. (Right) Picture of a DR similar to the one installed in Hall A at LNGS (see Sec. 3.2) [112].

Since the ^{3}He vapor pressure is much higher than the ^{4}He one, by pumping on the ^{4}He-rich phase it is possible to extract almost only ^{3}He, thus destroying the equilibrium in the concentration ratio. To restore the equilibrium, the ^{3}He from the concentrated phase has to cross the phase boundary to the diluted phase. However, since the enthalpy of ^{3}He in the dilute phase (H_d) is larger than the enthalpy of ^{3}He in the concentrated one (H_c), we have a cooling power occurring at the phase separation line when $\dot{n}_3$ moles of ^{3}He per unit time are transferred from the concentrated to the dilute phase:

$$\dot{Q} = \dot{n}_3 \, [H_\mathrm{d}(T) - H_\mathrm{c}(T)] \simeq 84 \, \dot{n}_3 \, T^2. \tag{2.9}$$

Typical values for $\dot{Q}$ for DR working at $\sim 10\,\mathrm{mK}$ are of the order of few µW.

A detailed (and quantitative) description of the operation of a DR can be found in Refs. [93, 111].

2.6.2 Schematic representation of a DR

To exploit the cooling properties of the ^{3}He/^{4}He mixture, a preliminary cooling is needed in order to reach $T = T_{\text{sep}}$, where the phase separation takes place.

A first step consists in cooling down the DR to about 4 K. With the older devices, this is usually done by "dipping" the DR itself into a liquid ^{4}He-bath ($T = 4.22$ K). More recent DR use cryo-coolers and, in particular Pulse Tube refrigerators (PTs, [113]), to reach approximately the same temperature. PTs avoid the need of a ^{4}He-bath cryostat with its infrastructure, guarantee a high reliability and, due to the absence of cryogens to refill, increase the total duty cycle of the experiment, thus allowing a longer live-time.

The cool down of the incoming mixture to approximately $(1-1.5)$ K in cryogen-based DR is realized by an evaporation refrigerator usually called 1 K pot. This is filled through a capillary by the same LHe from the ^{4}He-bath. By pumping the vapor above the liquid inside the 1 K pot, the temperature decreases. In cryogen-free DR, instead, the incoming mixture is cooled down to < 1 K thanks to the Joule-Thomson effect [114]. In both cases, this cooling phase is fundamental to condense the mixture.

The core of a DR essentially consists of three elements: the Mixing Chamber (MC), the Still and the Heat EXchangers (HEXs). This part of the apparatus is located in an inner vacuum chamber (also containing the 1 K pot or the Joule-Thomson impedance). A schematic representation and an example of real version are shown in Fig. 2.6. The relatively complex ^{3}He/^{4}He circuit is necessary to guarantee a sufficiently high circulation of ^{3}He, while maintaining a low heat load on the MC. The circulation of the mixture is driven by pumping the Still, which is heated to about 0.7 K to increase the pumping efficiency. Due to the higher vapor pressure, ^{3}He is predominantly evaporated from the liquid, although its concentration in the liquid in the Still is only $\sim 1\%$. Once it has been pumped, the ^{3}He is returned to the cryostat (after being cleaned in a LN_2 trap). After the 1 K pot (or the Joule-Thomson impedance), where a first condensing of the gas takes place thanks to a flow impedance, the ^{3}He is led into a series of counterflow HEXs. After passing through the HEXs, it enters the MC. The return line to the Still starts in the MC below the phase boundary (in the ^{4}He-rich phase). On the way back to the Still, the cold mixture again flows through the HEXs and in this way pre-cools the incoming ^{3}He. By pumping the Still, a concentration gradient of ^{3}He is created and this leads to an osmotic pressure that causes ^{3}He to flow from the MC to the Still. The cross of the phase boundary by the ^{3}He atoms in the MC cools down the system.

Chapter 3

The search for $0\nu\beta\beta$ of ^{130}Te with thermal detectors

The concept of calorimetric detection of energetic particles is very old, since it appears as a pure application of the first law of thermodynamics. In fact, the first example of thermal detection of radiation performed by Langley dates back to the end of the XIX century[1] [115] and the observation by Curie and Laborde of radioactive particles via their heat production is only a few years younger [116].

With the birth and evolution of Particle Physics, this idea was also applied to the detection of individual particles. In the late 1940s Andrews and collaborators were able to identify α single particles thanks to a superconducting calorimeter [117]. In fact, it had been earlier suggested by Simon that operating these detectors at cryogenic temperatures could significantly improve the sensitivity [118].

However, it was only in the 1980s that new generations of low temperature detectors could be proposed as competitors in several important applications in neutrino physics, nuclear physics and astrophysics [119–121]. Among these, the study of $0\nu\beta\beta$.[2]

In particular, the group of Fiorini and collaborators began to develop bolometers made of materials containing $\beta\beta$-emitters, focusing on the search for the $0\nu\beta\beta$ of ^{130}Te using TeO_2 crystals. The series of measurements performed by this group covers almost thirty years, proving TeO_2 bolometers to be competitive players in the search for $0\nu\beta\beta$. Starting with detectors of few grams and constantly increasing the mass and improving the performance, today the challenge is to run a tonne-scale detector, thus showing that these devices will continue to maintain their importance even in the next generations of experiments.

[1] Langley calls his new instrument *bolometer* (from the greek $\beta o\lambda\acute{\eta}$ + $\mu\acute{\epsilon}\tau\rho o\nu$ = ray + meter).

[2] Actually, one should distinguish between radiation and single particle detectors. The word bolometer refers to the former family of devices, the latter being indicated as macro/micro-calorimeters. This separation is especially remarked within the astrophysicist community. However, within the $0\nu\beta\beta$ community, only macro-calorimeter are considered, and these thermal detectors are simply called bolometers. Since this is the standard in the field of $0\nu\beta\beta$ search, the same choice is also adopted for this work.

3.1 Te-based bolometers

Although metallic Te is not suitable to be used as bolometer due to its intrinsic brittleness at low temperature [122], Tellurium dioxide (TeO_2) was found to be particular convenient for the use in cryogenic particle detectors. TeO_2 is the most stable oxide of Te [123] and presents favorable thermodynamic characteristics. TeO_2 crystals are both dielectric and diamagnetic with a relatively high value of the Debye temperature ($\Theta_D = (232 \pm 7)\,\mathrm{K}$ [98]). The very low heat capacity at cryogenic temperatures leads in turn to large temperature variations from tiny energy releases, which is at the base for a high energy resolution bolometer. Moreover, the fact that the thermal expansion of TeO_2 crystals is very close to that of copper [124, 125], allows the use of this metal for the detector mechanical support structure without placing too much strain on the crystals during the system cool down.

TeO_2 is present in nature in two mineral forms: orthorhombic tellurite (β-TeO_2) and paratellurite (α-TeO_2). In particular, the latter is a colorless tetragonal form of TeO_2. Due to its useful acoustic and optical properties, the potential usefulness of this compound in ultrasonic light deflectors and in laser light modulators was suggested long ago and today paratellurite is commercially produced at industrial scale [126]. The crystals have mechanical characteristics fully compliant with the requirements for the application in the $0\nu\beta\beta$ search. Numerous improvements in preparing the TeO_2 powder and in growing the crystals have allowed the production of almost perfect crystals (bubble-free, crack-free and twin-free [3]) with masses of the order of $\sim 750\,\mathrm{g}$ [127, 128] and more [129, 130].

Regarding radiopurity, the very stringent constraints for the application of TeO_2 in a $0\nu\beta\beta$ experiment set an upper limit for the level of impurities at $\lesssim 10^{-13}\,\mathrm{g/g}$ for both ^{232}Th and ^{238}U to allow an acceptable background rate in a tonne-scale detector [131]. Dedicated production lines for the raw material synthesis, the crystal growth and the surface processing have made TeO_2 crystals compliant with these requirements. Crystals with bulk contaminations of the order of $10^{-14}\,\mathrm{g/g}$ for both ^{238}U and ^{232}Th are available (e. g. crystals grown at the Shanghai Institute of Ceramics [128]). Furthermore, the surface treatments made in a clean room environment by using selected reagents for chemical etching and selected consumables for the final polishing resulted in crystal surface contamination of $\lesssim 10^{-8}\,\mathrm{Bq\,cm^{-2}}$ for both ^{238}U and ^{232}Th.

These technological achievements guarantee the "potential" scalability of this technique up to the tonne-scale.

3.2 A long chain of experiments

An Oxford Instruments DR was installed in the Hall A of the Laboratori Nazionali del Gran Sasso (LNGS, Assergi (AQ), Italy) of the Istituto Nazionale di Fisica Nucleare (INFN) in 1989 (Fig. 3.1, [132]). An underground environment is in fact a fundamental requirement

[3] Crystal twinning occurs when two separate crystals symmetrically share some of the same crystal lattice points, resulting in an inter-growth of two separate crystals in many possible configurations.

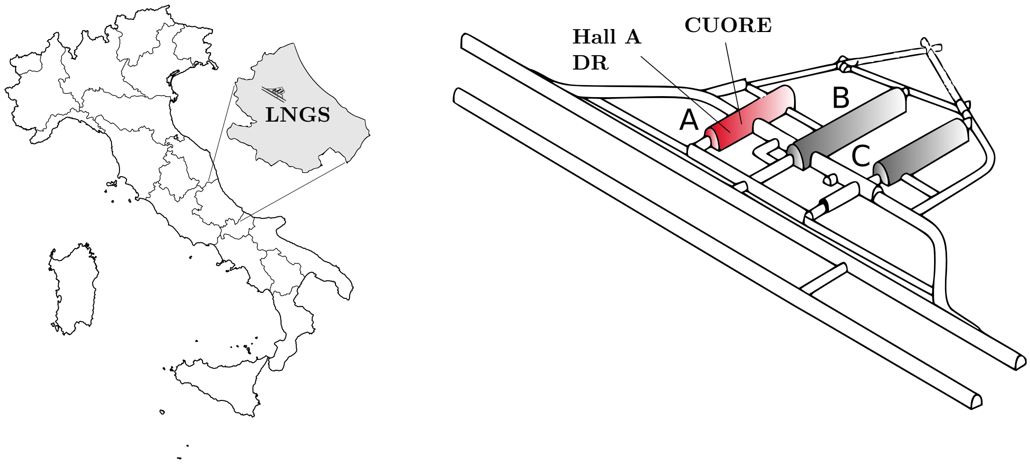

FIG. 3.1: (Left) Map of Italy with the location of LNGS in the Abruzzo region. (Right) Map of the underground experimental facilities. The DR and the CUORE hut position in the Hall A are indicated.

for experiments of rare event physics, such as the search for $0\nu\beta\beta$ (see Sec. 1.4.2). With its average coverage of about 3600 m. w. e. and its mostly calcareous rock composition [133], LNGS guarantee the very low muon and neutron fluxes of about $3 \cdot 10^{-8}\,\mathrm{cm^{-2}\,s^{-1}}$ and $4 \cdot 10^{-6}\,\mathrm{cm^{-2}\,s^{-1}}$, respectively [134, 135].

In particular, this DR was constructed with specially chosen low radioactivity components, with vessels and plates almost completely made of Oxygen-Free High thermal Conductivity (OFHC) copper. Samples of the refrigerator materials were previously tested for radioactivity with a germanium spectrometer. The DR is shielded against external radioactivity by two 10 cm lead layer placed immediately outside the cryostat, the inner one with reduced radioactivity (Fig. 3.2).

In addition, an internal shield made of ultra-low activity archaeological lead of Roman origin (see Sec. 6.2) was installed some years after the cryostat assembly. This directly surrounds the OFHC copper frame containing the detector.[4] The Rn contamination is reduced by fluxing nitrogen gas from a LN_2 evaporator in a Plexiglass box surrounding the cryostat. Finally, a 10 cm thick layer of borated polyethylene was used as neutron shielding. The DR itself and the read-out electronics are contained inside a Faraday cage to minimize electromagnetic interferences. The walls of the cage were then covered with sound and vibration absorbing material to reduce microphonic noise.

3.2.1 Measurements with single crystals

The first measurements of γ-ray spectroscopy with TeO_2 bolometers were carried out with a 5.7 g and a 20.9 g crystals in 1991 [137].[5] They allowed to set already competitive limits on the ^{130}Te $0\nu\beta\beta$ half-life, after being operated for about $(150-250)$ h. These were

[4] The shape and thickness of this shield will actually depend on the specific detector operated inside the DR. In fact, its design is every time optimized in order to match with the detector dimensioning.

[5] An earlier approach consisted in the use of a pure Te crystal of 2.1 g, but this was found to be too brittle at low temperatures [122].

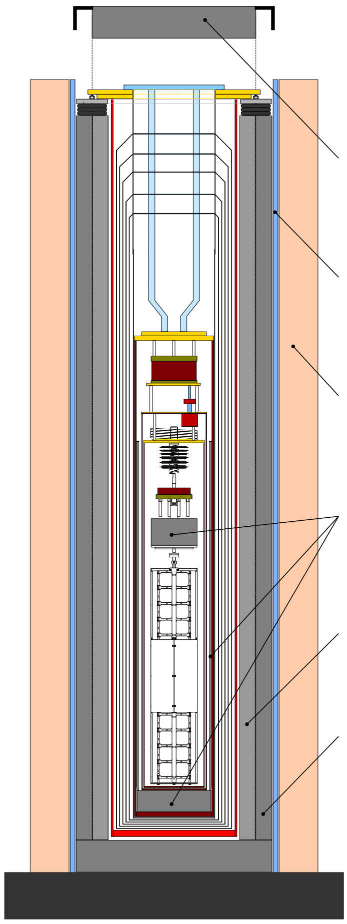

FIG. 3.2: Schematic of the Hall A DR cryostat and shielding at LNGS with the installed CUORE-0 detector. Adapted from Ref. [136].

the first physics results ever obtained with the bolometric technique (Table 3.4).

The subsequent measurements were performed with a 33.6 g [138] and a 73.1 g [139] crystals. The larger mass and live-time allowed to obtain an improved exposure and at the same time the energy resolution and the background were noticeably improved as well. The final energy resolution was almost comparable with that of a Ge diode, while an important factor for the background reduction was represented by the installation of the inner ultra-low activity lead shield surrounding the detector.

The successive measurement represented an important breakthrough for the bolometric technique. The new detector, a $30 \times 30 \times 60\,\mathrm{mm}^3$ crystal of 334 g [140], was indeed the largest thermal detector operated so far and more than 10500 h of effective running time [141] were collected in about 18 months. This translated into a factor 20 of increase in terms of exposure.

3.2.2 Detector arrays

During the period of the 334 g crystal run (around 1994), the growth technique for TeO_2 did not allow to produce specimens with mass larger than ~ 0.5 kg without risks of defects and fragility. Therefore, new improvements (in terms of mass and exposure) for the detectors had to come from the assembly of arrays of bolometers.

The first array of TeO_2 bolometers was constituted by 4 crystals equals (or, at least, very similar) both in mass and in dimensions to the last operated one [142]. This was the first bolometric system with over 1 kg of mass. The final exposure was thus very close to the one obtained with the 334 g crystal alone. However, this measurement proved that the same good conditions of background rate and resolution were achievable even with a complex system of bolometers. The 4 crystal array served thus as a prototype for more complex detectors.

In late summer of 1997, a tower made of 20 bolometers (5 floors of 4 crystal each) was assembled in the cryostat [143]. This experiment was later named MiDBD (Milan Double Beta Decay). The single module absorber consisted of a "standard" $30 \times 30 \times 60\,\mathrm{mm}^3$ crystal, corresponding to a total active mass of about 6.8 kg. MiDBD was the new largest operating cryogenic mass. The tower frame was made of OFHC copper and the crystals were fastened to this structure by means of PTFE supports.[6] The tower was in turn connected via an OFHC copper cold finger to the MC. To shield the detector from the intrinsic radioactive contamination of the dilution unit materials (e. g. from silver and stainless steel), a new framed 10 cm Roman lead shield was placed inside the cryostat itself, all around the tower. The major improvement with respect to the previous measurement consisted in the drastic (almost a factor 10) reduction of the background rate. Still, a further reduction was needed to get a better experimental sensitivity on the $0\nu\beta\beta$. Therefore, after a first phase of data taking, the MiDBD detector was completely dismounted and remounted in a new configuration at the beginning of 2001 (MiDBD-II, Fig. 3.3). In particular, both the crystals and the copper were cleaned in order to reduce their own radioactive contamination and that coming from the production process. A more compact assembling of the crystals was also adopted. Now each plane of the tower could be considered an independent module. This allowed to reinforce the internal shielding (an additional 2 cm Roman lead shield was introduced and the thickness of the shield between the MC and the detector was increased by 5 cm) and to perform a better anti-coincidence analysis (rejection of events on multiple crystals).

Already during the early preparation phase of the MiDBD experiment (summer 1997), a very ambitious project was proposed by Fiorini: to build "an array of 1000 cryogenic detectors of a mass between 0.5 and 1 kg each" [144]. The main goal remained the search for $0\nu\beta\beta$, but this experiment would have allowed also studies on interaction of WIMPS and of solar axions and on rare decays. The chosen name was CUORE, *Cryogenic Underground Observatory for Rare Events*. The realization of such a complex cryogenic setup will require the support of a numerous (international) collaboration and many years of preparation. As a first step towards CUORE, a simpler (and much less expensive) experiment was also

[6] PolyTetraFluoroEthene is a synthetic polymer. The best known brand name of PTFE-based formulas is Teflon. PTFE has an extremely high thermal expansion coefficient ($\sim 10^{-4}\,\mathrm{mm\,K^{-1}}$), that makes it suitable to firmly hold the crystals, also thanks to its low radioactivity content.

proposed. The original idea foresaw an array made of 100 $50 \times 50 \times 50\,\mathrm{mm}^3$ crystals for a total mass of about 75 kg, hence the name Cuoricino (italian for "small CUORE"). Cuoricino had not to be considered as a test, but rather as an experiment itself. In fact, apart from the fact that it would have become by far the new largest cryogenic detector, Cuoricino would have contained about 20 kg of ^{130}Te, a mass larger than the whole MiDBD and, more in general, larger than the $\beta\beta$-isotope mass of any other $0\nu\beta\beta$ experiment running at the time.

Cuoricino took the place of MiDBD in the Hall A cryostat. The cool down occurred at the beginning of 2003 and the start of the data taking shortly after (Run I). In its final configuration, the detector consisted of 44 $50 \times 50 \times 50\,\mathrm{mm}^3$ cubic crystals and 18 $30 \times 30 \times 60\,\mathrm{mm}^3$ crystals coming from MiDBD. These were disposed in 13 floors, 11 4-crystal modules and 2 9-crystal housing the small crystals (Fig. 3.3). The total mass of TeO_2 was 40.7 kg. Cuoricino was resized with respect to the proposed one due to very practical reasons, i. e. the experimental volume was extended as much possible without the risk of spoiling the DR performance and introducing additional background due to a too thin lead shield. Still, the mass was large enough to make it a competitive experiment for the $0\nu\beta\beta$ search and the new largest bolometric array.

At the end of 2003 the tower was warmed up to perform maintenance operations and to recover some lost connections. The data taking restarted the following year with all the channels operational. The total collected exposure was 19.75 kg yr of ^{130}Te. Cuoricino demonstrated the feasibility of running a very massive and complex bolometric detector array for almost five years with the best results obtained so far. The best performance, both in terms of background counts and resolution, were reached with the 5 cm-side bolometers. However, although very good, the same resolution and, especially, background rate were not yet compliant with the tight limits set for the future CUORE detector.

Table 3.4 summarizes the main features of the chain of bolometric experiments presented above, also including the CUORE-0 and CUORE experiments, that will be widely described in the following part of this work. It has to be noted that, to allow the direct comparison of the different parameters, some slight imprecision on the orginal values could have been introduced. This holds in particular for the older experiments. The huge improvements in a history of almost thirty years appear here evident. The detector mass has increased of more than 4 orders of magnitude and the exposure of almost a factor 10 millions.[7] At the same time the background rate has been reduced of almost 5 orders of magnitude and the resolution has significantly improved.

3.2.3 Towards the tonne-scale

In parallel with the Cuoricino data taking, many investigations were performed in view of the forthcoming CUORE. A big effort was paid to the study of the background sources.

[7] The table reports the total exposure of TeO_2. However, with the exceptions of MiDBD and Cuoricino that contained also enriched crystals, it is sufficient to multiply the value by ~ 0.278 to get the corresponding exposure of ^{130}Te.

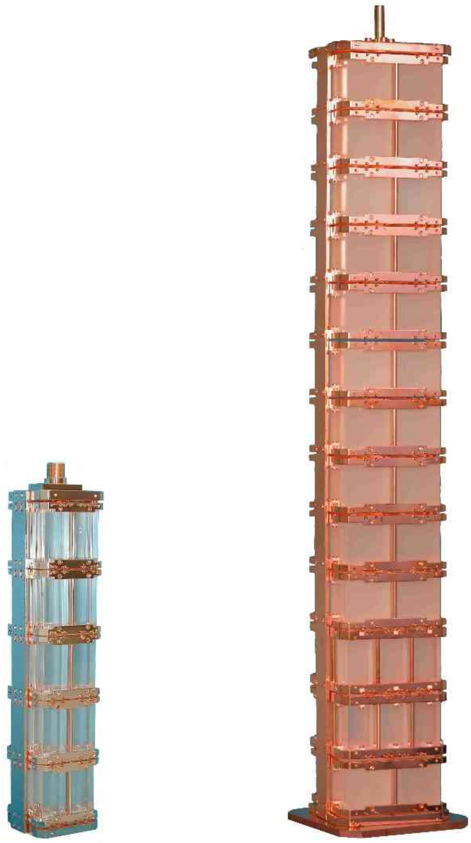

FIG. 3.3: From left to right: the MiDBD-II, Cuoricino and CUORE-0 towers in relative scale.

In particular, it was known that the main contribution was due to degraded αs from either the crystal surfaces or the support structure parts (copper and PTFE) [149]. Therefore, a new design for the detector structure was proposed, which reduced the amount of copper and the copper surfaces facing the TeO_2 crystals by a factor ~ 2. The bulk and surface contaminations were also checked, in order to validate a new production and treatment protocol for CUORE [128]. Indeed, up to Cuoricino, all the crystal surface treatments were performed in the clean room at LNGS. The idea was instead to completely process the crystals directly in the Shanghai Institute of Ceramics in China, the same place where they were grown. The conclusion on the crystal bulk contamination was that the new limits were comparable with the Cuoricino ones, already good enough for CUORE. Regarding the surface contamination, the measured level was lower than the Cuoricino one.[8]

However, to compare the achievements obtained with different surface treatments of the copper frames, a higher statistics measurement was needed. Therefore, at the end of Cuoricino, the Hall A DR hosted the Three Tower Test detector [151]. This consisted of 3 12-crystal arrays that underwent different procedures for the surface cleaning of the copper parts. Two "home made" polishing were performed at LNGS and one "industrialized" cleaning procedure was instead performed at the Laboratori Nazionali di Legnaro (see

[8]See e. g. Ref. [150] for a detailed description of the above mentioned tests.

TABLE 3.4: List of the TeO_2 bolometric experiments searching for the $0\nu\beta\beta$ of ^{130}Te performed at LNGS. The main characteristics are reported. The sensitivity in terms of $0\nu\beta\beta$ half-life is the combined value with the previous experiments.

Experiment	Running period	Crystals	Mass [kg]	Exposure [kg yr]	Bkg in the ROI [counts keV^{-1} kg^{-1} yr^{-1}]	FWHM @ $Q_{\beta\beta}$ [keV]	$S^{1/2}_{0\nu}$ (90% C. L.) [yr]
6 g crystal, [145]	Jan 1991 - Apr 1991	1	0.006	0.0002	123	50	$4.0 \cdot 10^{19}$
21 g crystal, [137]	May 1991 - Jun 1991	1	0.021	0.0004	88	20	$5.3 \cdot 10^{19}$
34 g crystal, [138]	Jul 1991 - Oct 1991	1	0.034	0.0041	79	30	$4.4 \cdot 10^{20}$
73 g crystal, [139]	Nov 1991 - Aug 1992	1	0.073	0.020	35 (Run I) / 17 (Run II)	7	$2.7 \cdot 10^{21}$
334 g crystal, [140, 141]	Jan 1993 - Aug 1994	1	0.334	0.40	3.4	15	$2.1 \cdot 10^{22}$
4 crystal array, [142]	Oct 1994 - Oct 1995	4	1.32	0.73*	4	$\lesssim 12$	$3.3 \cdot 10^{22}$
MiDBD, [143]	Apr 1998 - Dec 2001	20	6.8	4.25	0.6 (Run I) / 0.3 (Run II)	$5 - 15$	$2.1 \cdot 10^{23}$
Cuoricino, [146, 147]	Mar 2003 - Jun 2008	62	40.7	71.4	0.20 (Run I) / 0.15 (Run II)	5.8 ± 2.1	$2.8 \cdot 10^{24}$
CUORE-0, [78, 147]	Mar 2013 - Mar 2015	52	39.0	35.2	0.058 ± 0.004	4.9 ± 2.9	$4.0 \cdot 10^{24}$
CUORE (expected), [148]	2017 - 2023	988	742	3705	0.01	5	$9.5 \cdot 10^{25}$

*combined with 334 g crystal.

Ref. [151] for details). All the new copper cleaning techniques led to a reduction of a factor ~ 2 of the background in the $(3-4)$ MeV region, the one dominated by surface contaminations, with compatible values. Looking for the best compromise between cost, reproducibility and background control, the Legnaro protocol was validated for CUORE. The copper cleaning procedure consisted of 4 steps: tumbling, electro-polishing, chemical etching and magnetron plasma cleaning.

In Cuoricino, all the operations related to the detector assembly, e. g. the crystal surface treatments, the gluing and the bonding of sensors and heaters were still made "manually". The same held for the tower wiring. This was reflected in a quite broad range for the individual performance of the crystals. A standardization and automation of all the construction phases was needed for the handling of a detector almost 20 times bigger and much more complex as CUORE. At the same time, the high radiopurity levels of the components had to be conserved during (but also after) the various operations.

Therefore, completely new procedures were designed for the detector assembly and for the sensor gluing and bonding. The CUORE Tower Assembly Line (CTAL) [152] allowed to transform the over 10,000 ultra-clean pieces into 19 ultra-clean towers. To avoid recontamination of all the parts due to direct contact with less radiopure materials and exposure to solid (any powder) or gaseous (Rn) contaminants in the atmosphere, the whole CTAL process was confined into hermetic volumes constantly flushed with N_2, accessible only through sealed glove ports (Fig. 3.5). During the transportations, the crystals were always vacuum sealed into plastic bags in turn contained in a vacuum sealed box. The same principle also applied to the sensor gluing, which was performed by a robotic arm in a N_2 flushed glove box. Thermistors and heaters were thus pre-glued on the crystals. These then underwent the various operations: the mechanical assembly of the tower, the cabling, the bonding, the covering of the wire trays and the storage. Thanks to the new procedures, the CUORE crystals were never exposed to air from the moment of the polishing to the installation of the detector.

To validate the ultraclean assembly techniques and to test the radiopurity of materials for the upcoming CUORE, it was decided to run the first tower produced with the CTAL, called CUORE-0, in the Hall A DR.

3.3 The CUORE-0 detector

CUORE-0 [136] is a tower made of 52 $50 \times 50 \times 50\,\mathrm{mm}^3$ cubic crystals bolometers disposed on 13 4-crystal floors, for a total mass of 39 kg of TeO_2 (Figs. 3.3 and 3.6).[9] The crystals are housed in a copper structure and kept in position by PTFE holders. The holders are the only components directly touching the crystals (except for the glue used to couple the NTDs and the heaters to the crystals). Their supports are designed in a way

[9] Actually, the number of active bolometers is 51 since a NTD could not be bonded. The same happened for a heater and the electrical connection to another heater was lost during the initial cool down. Anyway, a new thermal gain stabilization technique [147], allowed to include the last two bolometers in the global $0\nu\beta\beta$ analysis.

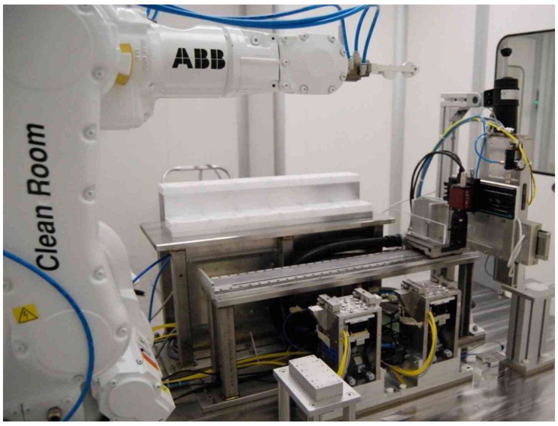

FIG. 3.5: The CUORE gluing (left) and assembly (right) workstations. Figure from Ref. [136].

that at low temperatures they firmly hold the crystals and compensate for the differential thermal contraction of copper and TeO_2. A NTD thermistor and a silicon heater are glued on each crystal. These sensors are directly bonded on pads at the end of one of the cables that bring the electrical signals from the bolometers to the top of the tower. The other end of each cable plugs into a connector that reads out the detector tower to the room temperature front-end electronics.

The CUORE-0 electronics provides a low-noise system for the read out of the signals and for the monitoring and optimization of the detector performance. The bolometer signals are passed through a several amplification and an anti-aliasing filtering. These are thus digitized by the data acquisition system and stored the data on disk for off-line analysis. In particular, the bolometer waveforms are sampled continuously and the complete stream are transferred to the computer for processing and storage. The data are stored in two forms, a continuous waveform format that stored 100% of the data, and a triggered format which selected a subset of the waveforms for further analysis [147].

3.3.1 Operation and performance

CUORE-0 collected data from March 2013 until March 2015 (Fig. 3.7). The first data-taking campaign lasted until September 2013, corresponding to a 2.0 kg yr exposure of ^{130}Te [153]. The detector operations resumed in November 2013, after performing some maintenance work on the cryostat. This resulted in a reduced microphonic noise and in an improved duty cycle. The final exposure of ^{130}Te was 9.8 kg yr.

The CUORE-0 data collection was organized in runs, each one lasting approximately one day. Once every other day, the data taking was paused to allow the refill of the cryostat LHe bath. Each refill introduced a down-time of $(2-3)$ hours. Runs were grouped into datasets, each containing about three weeks of $0\nu\beta\beta$ physics data. Both during calibration

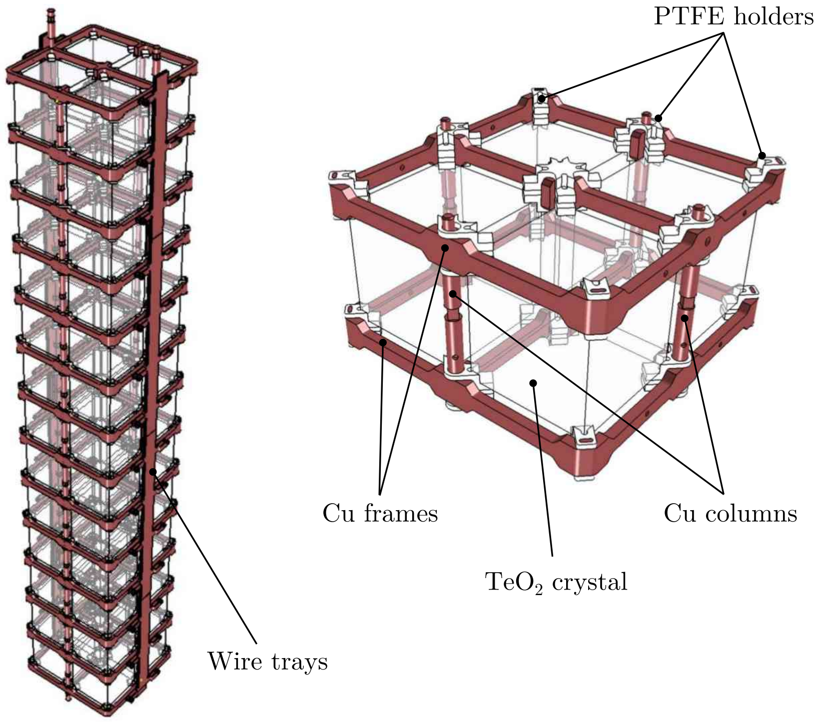

FIG. 3.6: Rendering of the CUORE-0 tower with a detail of a single floor. Figure from Ref. [136].

and physics data runs, pulser events were fired every 300 s on the bolometers. These pulses were used for the off-line correction of the detector gain instabilities induced by temperature drifts of the cryogenic system. In physics runs the signal trigger rate per bolometer was around 1 mHz, and it was around 60 mHz in calibration runs.

In the end, the duty cycle of the CUORE-0 detector was close to 80%, of which about two thirds of physics data used for the $0\nu\beta\beta$ analysis [136].

Bolometric performance

The CUORE-0 data allowed to directly verify the improvements in the bolometric performance achieved with the new CTAL, gluing and bonding procedures.

In order to better understand the degree of uniformity of the detector response, the distribution of the CUORE-0 base temperatures measured by the individual thermistors was analyzed. Before applying the bias current, all of the bolometers should be at the same temperature. Therefore, a narrow distribution of the measured temperatures is expected from a reproducible uniform assembly. A non-uniformity in the distribution reflects a non-uniformity in the coupling between the sensors (both thermistors and heaters) and the absorber, which is in fact critical for the optimization of the bolometric behavior.

The temperature T of the thermistor can be derived by inverting Eq. (2.6), once the parameters ρ_*, T_* and γ are known (see Sec. 2.4) and ρ is measured immediately after the detector cool down. The result is shown in Fig. 3.8. The ratio $T/T_{\rm avg}$, where $T_{\rm avg}$ is the average value over all the bolometers, is plotted both for CUORE-0 and Cuoricino (identical measurements were performed at the time). The Root Mean Square (RMS) of

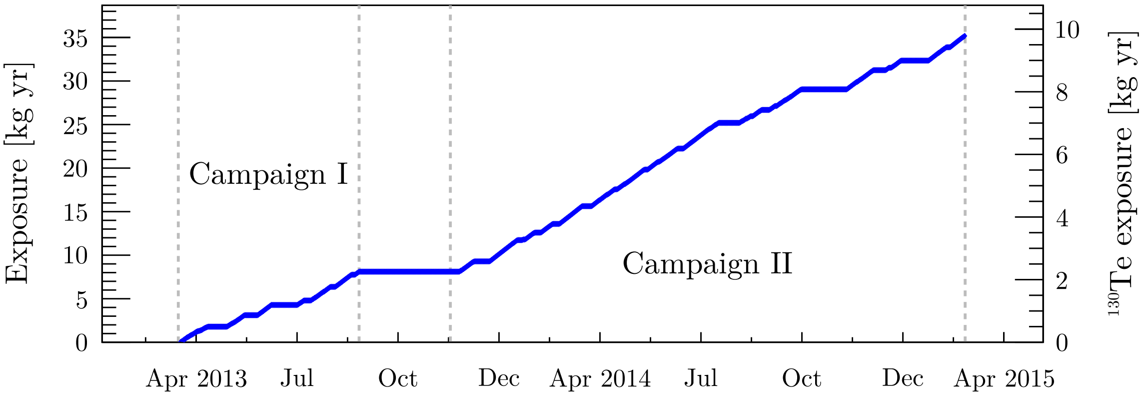

FIG. 3.7: Plot of the statistics accumulated by CUORE-0 over time. The vertical axis refer to the total TeO_2 (left) and to the ^{130}Te (right) exposures. Figure from Ref. [136].

the distribution decreases from 9% to 2% passing from the old to the new detector. The narrower distribution obtained with CUORE-0 is a clear demonstration of the improvement achieved with the new protocol adopted for CUORE.

From this analysis, the average working temperature for the two detectors could also be derived. The values of 10.05 mK and 8.02 mK were found for CUORE-0 and Cuoricino, respectively.

To monitor the performance of the bolometers, specific measurements were periodically carried out during the data-taking campaigns. The technical runs covered $\sim 2\%$ of the total CUORE-0 live time. They included the searches for the optimal working point (i. e. the bias current that maximizes the signal-to-noise ratio) and the daily working point measurements and scans with the pulser at low energy.

The identification of the working point proceeded through the evaluation of the bolometer voltage and of the baseline RMS amplitude of a fixed-energy reference pulse for each value of the bias current for every individual crystal. Referring to Sec. 2.4, the bolometer voltage V_{bol} was evaluated from two baseline noise measurements with the same bias current $I_B (= I_{\mathrm{bol}})$, but with opposite polarity. To eliminate possible voltage offsets at the input of the readout chain, V_{bol} was taken to be the difference of these two output baseline voltage values divided by the known gain of the readout chain. The baseline noise RMS was evaluated as the integral of the average noise power spectrum [147]. The amplitude of a reference pulse was obtained by averaging the waveforms of several pulser events.

In their working configuration, the resistances of the CUORE-0 bolometers had an average value of 26 MΩ, with an RMS of 8 MΩ. The values for I_B spanned over the range $(100 - 400)$ pA, with an average value of 250 pA and an RMS of 50 pA. The average CUORE-0 bolometer signal amplitude was defined as the ratio between the pre-gain pulse amplitude and the corresponding energy of the pulse. Its value was 75.6 $\mu\mathrm{V\,MeV^{-1}}$, with an RMS of 32.3 $\mu\mathrm{V\,MeV^{-1}}$ among the 51 active channels [136].

Regarding the daily technical measurements, a first type consisted in a scan with pulser events in the low energy range that was performed in each dataset to measure the trigger thresholds of the bolometers. The pulser events were increasing from 0 to 200 keV. After

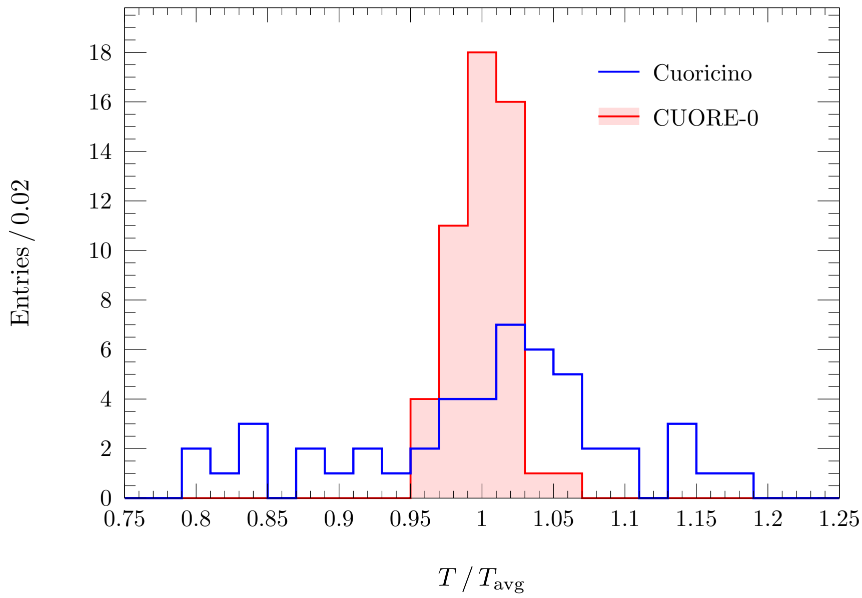

FIG. 3.8: Base temperatures of the individual bolometers normalized to their average temperature for Cuoricino and CUORE-0. The RMS of the distribution decreases from 9% to 2% passing from Cuoricino to CUORE-0. Figure from Ref. [136].

collecting about 50 pulses for each energy, it was possible to estimate the threshold. This was defined as the energy at which 90% of the pulses were detected by the standard signal trigger algorithm. The obtained values were ranging from 30 keV to 120 keV, with an average threshold of $\sim$ 70 keV.

A second measurement, performed daily, was the one of the detector resistances $R_{\mathrm{bol}} = V_{\mathrm{bol}}/I_B$, carried out performed in order to track the detector stability over time. The resistances of the CUORE-0 bolometers were found to be within a factor of 3 from each other, and they remained stable to within $\sim$ 3% over a dataset.

See Ref. [136] for more details on the described measurements.

Energy resolution

The CUORE-0 energy resolution was evaluated using the data collected during the calibration runs. The source consisted in two separate thoriated tungsten wires that were inserted between the OVC of the cryostat and the external lead shield (on opposite sides of the cryostat). The γ lines of the ^{232}Th decay chain were taken as a reference. In particular, the ^{208}Tl line (2615 keV) was used to estimate the single crystal and overall energy resolution in the ROI, thanks to the high statistics and the proximity to the $Q_{\beta\beta}$ of ^{130}Te ((2527.515 ± 0.013) keV, [154–156]).

Fig. 3.9 shows the distributions of the FWHM energy resolutions for both Cuoricino and CUORE-0, for each bolometer in each dataset. The effective mean (weighted harmonic mean) of the values are 5.8 keV (with an RMS of 2.1 keV) and 4.9 keV (with an RMS of 2.9 keV) for Cuoricino and CUORE-0, respectively (see Ref. [147] for more details on this

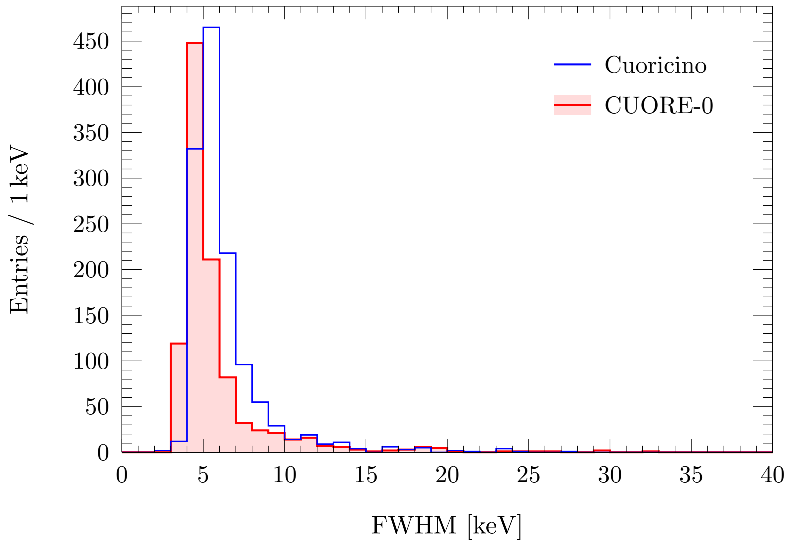

FIG. 3.9: Distribution of the FWHM energy resolution at the ^{208}Tl line (2615 keV) for each Cuoricino and CUORE-0 dataset measured during the detector calibrations. The effective mean is 4.9 keV in CUORE-0, while it was 5.8 keV in Cuoricino. Figure from Ref. [147].

analysis).

The CUORE goal of 5 keV FWHM in the ROI has been achieved in CUORE-0.

Background rate

Fig. 3.10 shows the final spectra of Cuoricino and CUORE-0 in the $(0-7.5)$ MeV region. The reduction of the background rate in CUORE-0 is clearly visible, although less up to 2.6 MeV, since the source of this background was mostly located in the outer shields of the cryostat, which was the same for both detectors.

In the energy region $(2.7-3.9)$ MeV, the background is dominated by degraded αs, with an almost flat behavior. The only important exception is the ^{190}Pt peak (Q_α = 3249 keV), which is a bulk contamination of the TeO_2 (coming from the platinum crucible for the crystal growth), but it does not affect the $0\nu\beta\beta$ background. In CUORE-0, a rate of (0.016 ± 0.001) counts keV^{-1} kg^{-1} yr^{-1} was measured for this flat background [78], a value about a factor 7 smaller than the one obtained with Cuoricino, which was of (0.110 ± 0.001) counts keV^{-1} kg^{-1} yr^{-1} in the same region [146].

In the ROI, the background rate measured by CUORE-0 was $(0.058 \pm 0.004\,(\text{stat.}) \pm 0.002\,(\text{syst.}))$ counts keV^{-1} kg^{-1} yr^{-1} [78]. This value corresponds to an improvement of a factor 3 with respect to that Cuoricino, which was (0.169 ± 0.006) counts keV^{-1} kg^{-1} yr^{-1} [146]. The α continuum, that was the major contribution to the Cuoricino background in the ROI, now constituted a minor component of the ROI background in CUORE-0. A severe improvement in this region is instead expected for CUORE, thanks to the better material selection for its custom-made cryostat (see Chap. 4) and to the scaling effects.

By using the measured α background index in CUORE-0 as an input to the Monte Carlo simulations of CUORE, it is possible to conclude that the background goal of

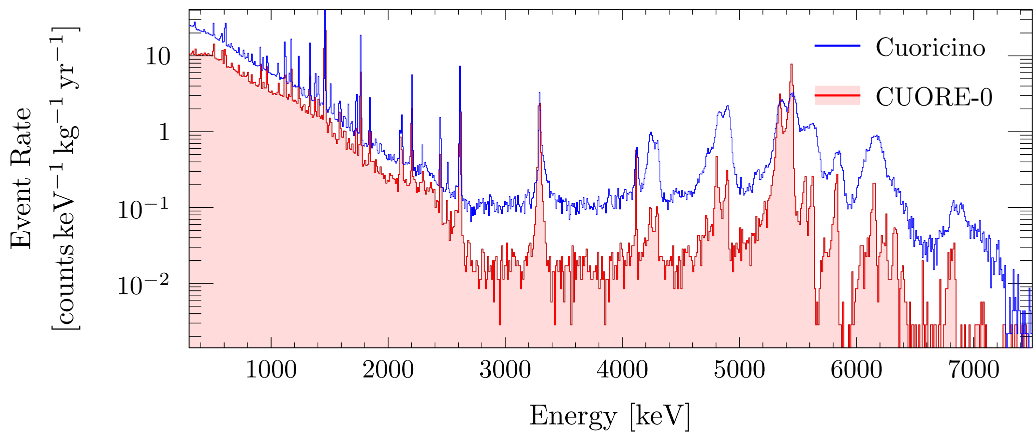

FIG. 3.10: Final spectra of Cuoricino and CUORE-0 in the $(0-7.5)$ MeV region. The reduced background rate in CUORE-0 is clearly visible, especially in the α region, where it is about a factor 7 smaller than in Cuoricino. Figure from Ref. [136].

0.01 counts keV^{-1} kg^{-1} yr^{-1} is within reach [157].

3.3.2 Results from the $0\nu\beta\beta$ search

The analysis for the $0\nu\beta\beta$ search interested the data collected during the physics runs, which covered $\sim 64\%$ of the total live time of CUORE-0. Details of the analysis can be found in Refs. [78, 147].

The $0\nu\beta\beta$ candidate events passed a series of selections aimed at discarding the low-quality data (e. g. periods with problems related to cryogenics) and at rejecting pile-up and noisy pulses. Furthermore, to reduce the background from decays depositing energy in multiple crystals (e. g. αs at crystal surfaces), an event was rejected if another occurred in the tower within a few ms. In the end, the total selection efficiency was $(81.6 \pm 0.6)\%$.

The high-statistics 2615 keV ^{208}Tl line in the calibration data was used to establish the detector response to a monoenergetic deposit near the ROI. The line shape was parametrized for each bolometer and dataset, the parameters being estimated with a simultaneous, Unbinned Extended Maximum Likelihood (UEML) fit. This line shape fit was repeated on a sequence of peaks of known energy between 511 keV and 2615 keV in the physics data in order to get a series of global scaling parameters. These were in turn used to treat the energy dependence of the resolution or possible differences in resolution between calibration and physics data. The (linear) fit of the resolution-scaling parameters allowed to estimate the FWHM at $Q_{\beta\beta}$.

To avoid the introduction of a bias in the analysis results, the physics data in the ROI underwent a "blinding" procedure that created an artificial peak at $Q_{\beta\beta}$ [153]. Thus, after unblinding the ROI by removing the artificial peak, it was possible to determine the yield of $0\nu\beta\beta$ events from a UEML fit in the energy window $(2470-2570)$ keV. The ROI contained 233 candidates in the total exposure of 9.8 kg yr of ^{130}Te. The fit result is shown in Fig. 3.11. The components are a signal peak posed at $Q_{\beta\beta}$, a peak at ~ 2507 keV from the ^{60}Co double-γs and a continuum background attributed to multi-scatter Compton

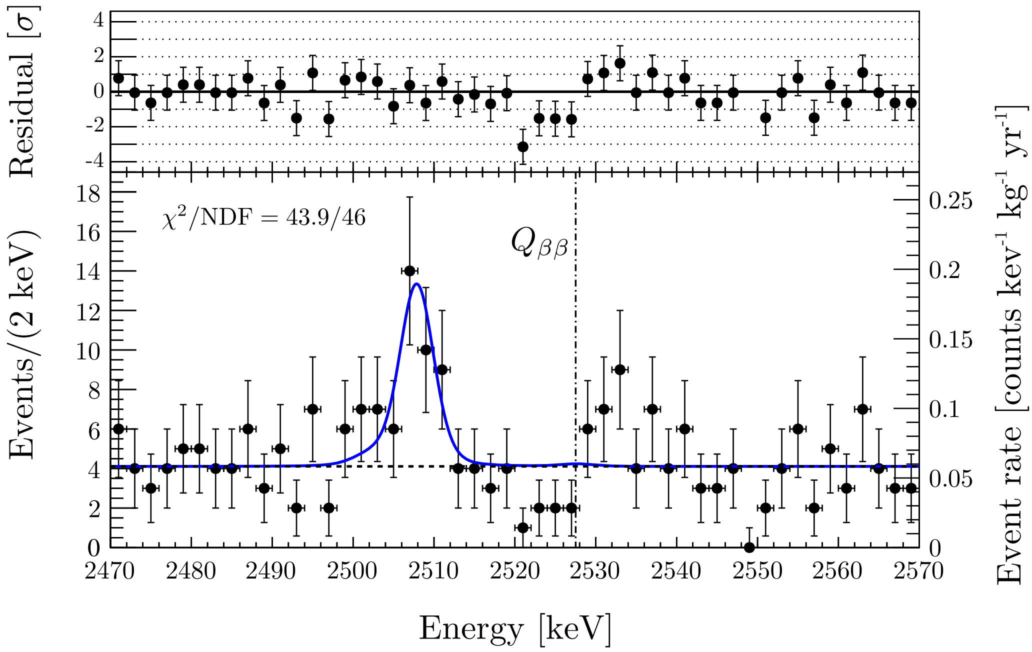

FIG. 3.11: (Bottom) Best-fit model from the UEML fit in the ROI overlaid on the data points. The data are shown with Gaussian error bars. The peak at $\sim 2507\,\text{keV}$ is attributed to ^{60}Co. The dashed line shows the continuum background component of the model. The vertical dot-dashed line indicates the position of the $Q_{\beta\beta}$ of ^{130}Te. (Top) Normalized residuals of the best-fit model and the binned data. Figure from Ref. [78].

events from ^{208}Tl and surface decays.

No evidence for the $0\nu\beta\beta$ was found and the 90% C. L. Bayesian upper limit for the decay amplitude was set

$$\Gamma^{0\nu} < 0.25 \cdot 10^{-24}\,\text{yr}^{-1} \tag{3.1}$$

or, in terms of half-life

$$S^{0\nu} > 2.7 \cdot 10^{24}\,\text{yr}. \tag{3.2}$$

By combining the CUORE-0 data with those from Cuoricino, the combined limit becomes

$$S^{0\nu} > 4.0 \cdot 10^{24}\,\text{yr}. \tag{3.3}$$

This is the most stringent limit on the $0\nu\beta\beta$ of ^{130}Te to date. The corresponding limit in terms of $m_{\beta\beta}$ can be obtained according to the procedure described in Sec. 1.6.

Measurement the $2\nu\beta\beta$ half-life

Another very important study that could be performed with CUORE-0 was the measurement of the $2\nu\beta\beta$ of ^{130}Te.

A Monte Carlo simulation allowed a detailed reconstruction of the sources responsible for the CUORE-0 counting rate [158]. The reconstruction of the detector background was able to identify the contribution coming from the $2\nu\beta\beta$ of ^{130}Te and to study impact of this source for the $0\nu\beta\beta$ search. This was estimated into $\sim 10\%$ of the events in the region

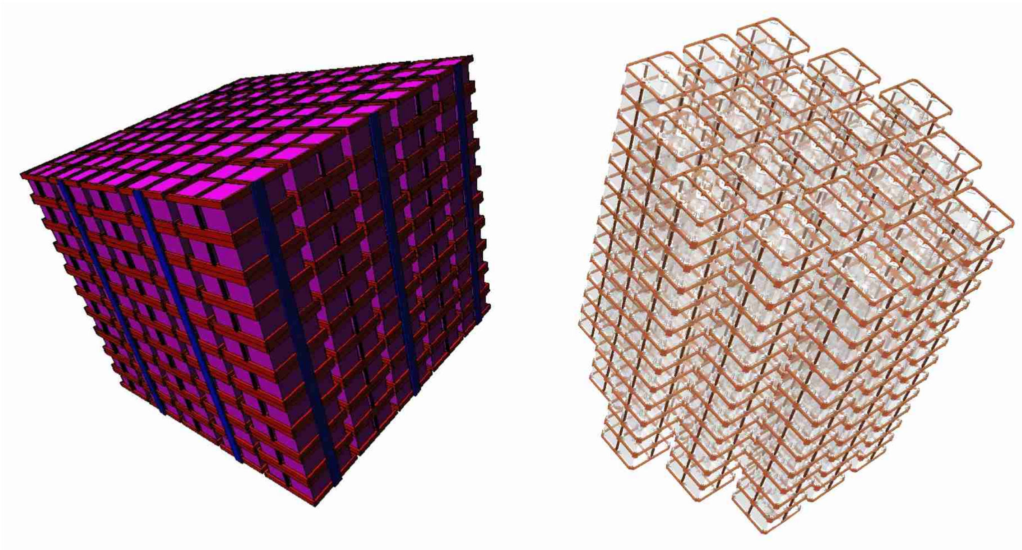

FIG. 3.12: Rendering of the CUORE detector. (Left) The original version proposed in Ref. [144]: an array of 1000 disposed into 25 10-floor towers. Each floor of a tower constitutes a single Cuoricino-like detector module. (Right) The final version: an array of 19 13-floor towers. Each tower constitutes a single CUORE-0-like module.

$(120 - 2600)$ keV.

With an exposure of 33.4 kg yr, this analysis also allowed to determine the half-life of the $2\nu\beta\beta$ of ^{130}Te:

$$t^{1/2}_{2\nu} = (8.2 \pm 0.2\,(\text{stat.}) \pm 0.6\,(\text{syst.})) \cdot 10^{20}\,\text{yr}. \tag{3.4}$$

This is the most accurate measurement to date.

3.4 CUORE

In the long way between the original proposal [144] and the actual detector construction, the design of CUORE has constantly evolved and improved thanks to the numerous studies and tests performed. In the final version, the detector consists of 19 towers, for a total of 988 TeO_2 crystals and more than 740 kg of weight,[10] $\sim$ 206 kg of ^{130}Te. CUORE will the largest detector operated as a bolometer by far. A comparison between the two versions in shown in Fig. 3.12

The full detector assembly took almost two years, from September 2012 to July 2014. The successful completion of the task definitively proved the effectiveness of the CTAL, gluing and bonding protocol. Before being installed inside the CUORE cryostat (see Chap. 4), the towers had to wait the end of the commissioning of the cryogenic system (see Chap. 5). Therefore, for other two years, these were stored inside the CUORE clean room into sealed containers constantly flushed with clean N_2 gas to prevent any contamination from Rn. The tower installation was performed in summer 2016. The extremely delicate operation was performed in a controlled clean room environment with Rn-free filtered air by a specif-

[10] A more precise value for the total mass of the crystals is 741.6 kg.

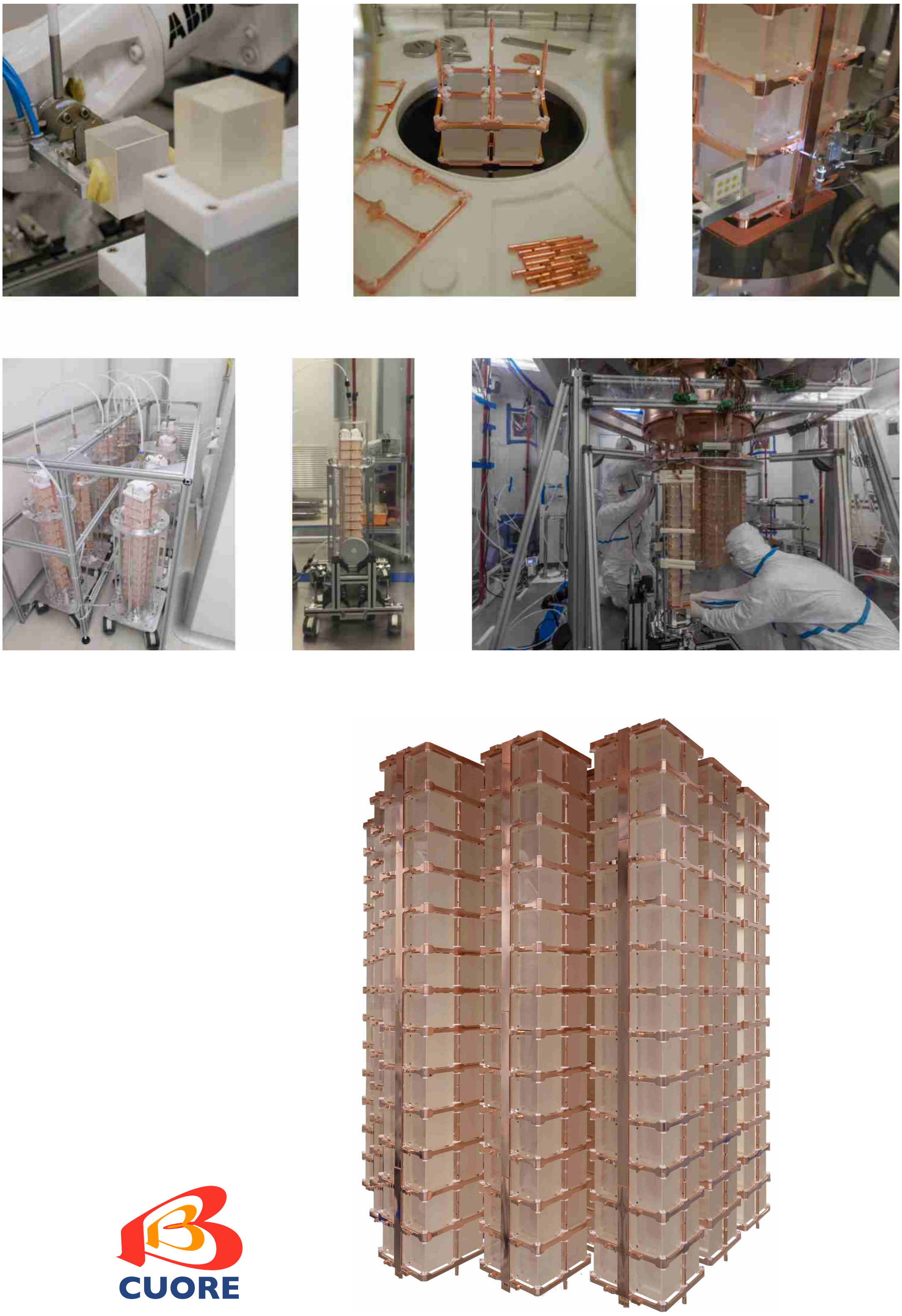

FIG. 3.13: The CUORE detector. (Top) Various phases of the detector construction (from left to right, from top to bottom): sensor gluing, tower mechanical assembly, sensor bonding, storing of the towers under N_2, tower preparation for the installation, tower installation. (Bottom) The complete 19-tower detector and the CUORE logo.

ically trained team. The detector commissioning is starting while writing (January 2017). A series of pictures taken during the various phases of the CUORE detector are shown in Fig. 3.13.

CUORE is expected to take data for a total 5 yr of live time. A large amount of data will be collected, which will allow several studies ranging over a broad variety of topics, from Dark Matter searches to studies of the bolometer thermal behavior. The main purpose will remain of course the search for the $0\nu\beta\beta$ of ^{130}Te.

CUORE-0 has already shown that, despite the considerable ambition, the expected performance of 5 keV FWHM energy resolution at $Q_{\beta\beta}$ and 0.01 counts $\mathrm{keV}^{-1}\,\mathrm{kg}^{-1}\,\mathrm{yr}^{-1}$in the ROI are within reach. If these requirements are satisfied, the projected 90% C. L. sensitivity after a total exposure of about 3700 kg yr ($\sim$ 1000 kg yr exposure of ^{130}Te, see Table 3.4) is [148]:

$$S^{0\nu} > 9.5 \cdot 10^{25}\,\mathrm{yr} \tag{3.5}$$

with a 5σ discovery potential of $3.0 \cdot 10^{25}$ yr.

This value is close to the current most stringent limit on the $0\nu\beta\beta$ process half-life (see Sec. 1.6). Despite the time to reach its final sensitivity is not irrelevant, it can be seen from Table 1.16 that CUORE will play an important role in the search for $0\nu\beta\beta$ even if compared with further future experiments.

Although external to this work topic, it is worth to mention that the future of the $0\nu\beta\beta$ search with thermal detectors will not be concluded with CUORE. In fact, a large number of R&D programs is already taking place, and more will start in the near future, with the goal of improving the CUORE performance [159].

The CUPID (*CUORE Upgrade with Particle IDentification*) project [160, 161] is a proposed future tonne-scale bolometric experiment that will use the experience, the expertise and the lessons learned in CUORE (as well as the infrastructure as much as possible) in order to achieve an enhanced sensitivity. CUPID aims to increase the source mass and dramatically reduce the backgrounds in the region of interest by means of isotopic enrichment, upgraded purification and crystallization procedures, new detector technologies, a stricter material selection, and possibly new shielding concepts. The ambition is to a reach sensitivities of the order of $(10^{27} - 10^{28})$ yr for the $0\nu\beta\beta$ half-life of the employed isotope.

Chapter 4

The CUORE cryostat

The CUORE cryogenic system has to guarantee the optimal operation of the detector for a live-time of years. Therefore, it has been designed to satisfy a set of stringent experimental requirements. The entire experimental volume must be kept at a stable base temperature of about 10 mK and the level of detector noise has to be minimized. The system must be instrumented with over 2500 wires for the detector readout. In addition, tight limits are imposed on the radioactive background coming from the cryogenic apparatus.

To comply all these requirements, a large custom cryogen-free cryostat cooled by PT refrigerators and by a high-power Dilution Unit (DU) for the circulation of the ^{3}He/^{4}He mixture has been designed (Fig. 4.1). To avoid radioactive background, only a few construction materials were acceptable and ~ 7 tonnes of shielding lead were integrated in the structure.

4.1 Cryostat design

Given its scale and complexity, the CUORE cryostat represented a completely new challenge in the field of the cooling technology. The design had to satisfy a set of very stringent experimental requirements:

- the experimental volume had to be sufficiently spacious to host the detector and part of the shielding, i. e. $\sim 1\,\mathrm{m}^3$ large;
- the detector base temperature had to allow the operation of the NTDs in optimal conditions. From the past experience, a suitable value was expected to be $\sim 10\,\mathrm{mK}$ (see Sec. 3.3.1);
- the radioactive background coming from the cryogenic apparatus had to be compatible with the CUORE sensitivity goal, which demands a total background rate of $\lesssim 0.01\,\mathrm{counts\,keV^{-1}\,kg^{-1}\,yr^{-1}}$in the $Q_{\beta\beta}$ energy region;
- the system reliability had to guarantee years of operation;

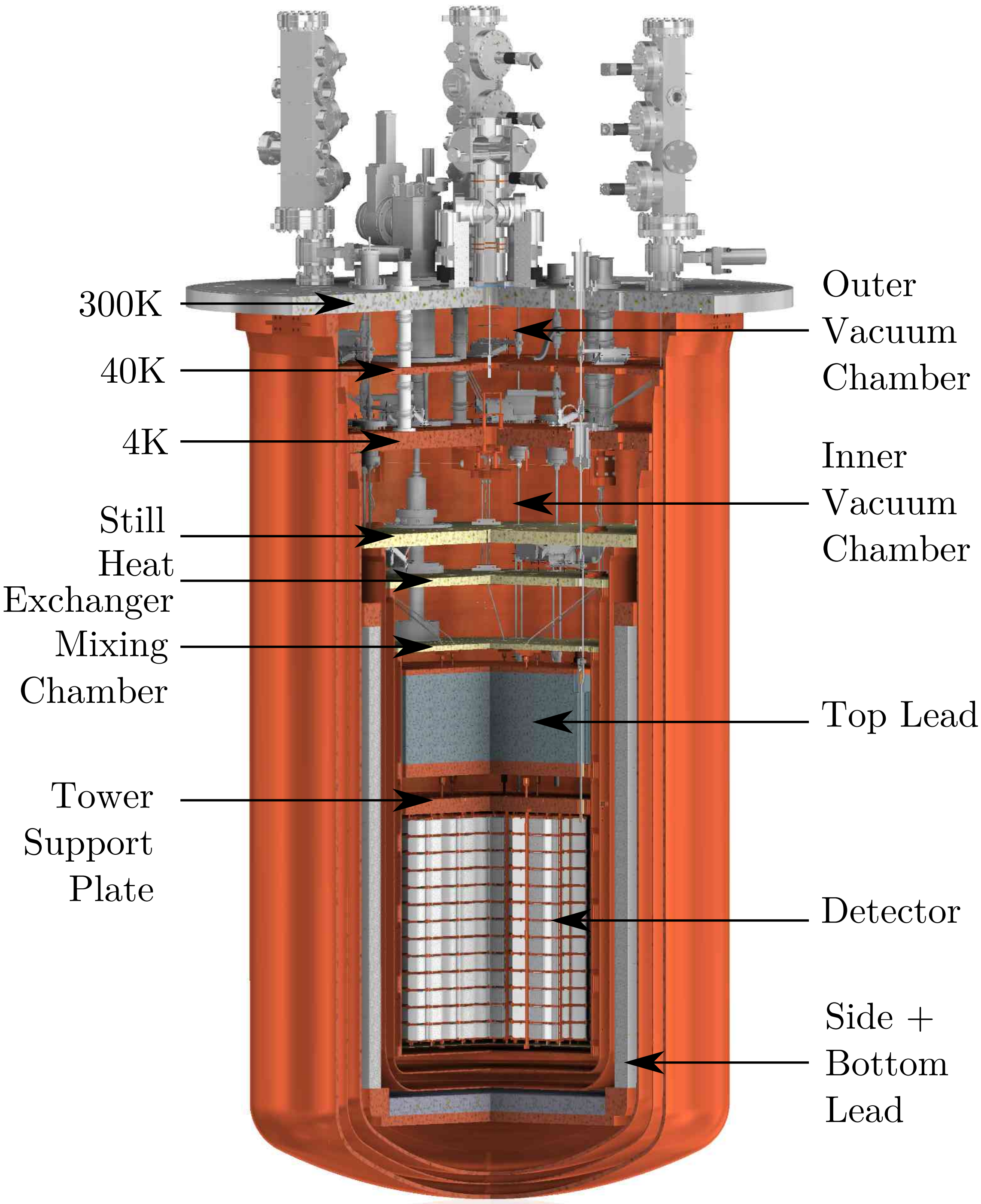

FIG. 4.1: Rendering of the the CUORE cryostat. The plates corresponding to the different thermal stages, the shielding lead the vacuum chambers.

- since LNGS are located in a seismic sensitive area, the design had to take into account the response of the system to seismic events.

In order to meet all the demands in the best possible way, the design of the cryostat proceeded in a recursive way. Starting from the "market availability" in terms of cooling technology, materials, production techniques, etc. it was possible to draft realistic, but conservative, thermal budgets. In turn, these could be used to perform a series of selections on the same cooling units, materials, etc. and improve the design accordingly.

The major outcomes of this process were the choices of relying on cryocoolers (PTs), instead of having a LHe bath, and on a single custom powerful DR unit, rather than on multiple commercial units. From the mechanical point of view, it was decided to adopt a "minimal" design, i. e. as plain as possible.

4.1.1 Mechanical requirements

The CUORE cryostat has to be a suitable low-noise environment to run a bolometric detector. Therefore, the issue of the noise abatement had to be considered since the early design phase. The first step in this direction was to cope with vibrations.

Mechanical vibrations generate power by means of micro-frictions. When this power is dissipated on the coldest stages, it can prevent the reach of a stable base temperature (see Sec. 5.7.1). On the detector, the impact is even more severe. The crystals are less coupled to the cooling unit and thus more sensitive to temperature changes. Furthermore, even if the effect is not relevant for the temperature, vibrational noise contributes to the overall noise, thus spoiling the energy resolution [162].

A series of devices had been conceived in order to mitigate the problem, protecting the detector against any external vibration source. The entire support structure was intended for decoupling the cryostat from the world. Insulating devices were placed at its basement and the cryostat was suspended to a platform positioned on top of the structure (Sec. 4.2). Since also PTs are a large source of vibrations, flexible connections between these and the cryostat were installed at the various thermal stages (Sec. 4.5.2). Finally, it was decided to further mechanically decouple the detector from the rest of cryostat, by suspending it to an external structure provided with a vibration damping stage (Sec. 4.2.3).

All the adopted solutions had to be then subjected to a compliance verification with the requests from the seismic analysis [163]. As a consequence, the internal cryostat structure had to be made able to respond to the accelerations induced by seismic events without suffering structural damages. For this purpose, articulated joints and gimbals that allow the relative movements of the individual vessels were introduced.

4.1.2 Materials

The cryostat design was targeted for rare event detection. Therefore, tight requirements were also imposed to the radioactivity content of the various components, paying particular attention to the Th and U bulk contaminations. To fulfill these additional constraints, a strict selection of both materials and the production techniques had to be performed [164].

As a first outcome, the use of copper instead of other materials, such as stainless steel, appeared as a mandatory choice for the largest masses, i. e. for plates and vessels. More generally, an extensive campaign of radioactivity measurements interested all the cryostat materials, thus allowing for an efficient selection. The obtained limits and results contributed to detailed Monte Carlo study performed in order to evaluate the expected background of CUORE [157].

All the vessels and plates are made of selected high purity copper produced by Aurubis. In particular, the chosen grade for the 40 K, the 4 K, the Still and the HEX vessels is the Oxygen-Free Electrolytic (OFE) copper. OFE copper (OFHC compound C10100) is the highest purity grade of copper at 99.99%. Assays of Cu OFE samples set only an upper limit of $6.5 \cdot 10^{-5}$Bq kg^{-1} and $5.4 \cdot 10^{-5}$Bq kg^{-1} for ^{232}Th and ^{238}U content, respectively.[1]

The 300 K vessel is also made of Cu OFE, except for the upper flange, which is of austenitic stainless steel, as well as the plate. The use of stainless steel for these parts guarantees a better mechanical stability and vacuum tightness. The same choice was not possible for the 4 K vessel due to the poor thermal conductivity of the steel at low temperatures [165].

The 40 K and the 4 K vessels and the corresponding plates are externally covered with 30 and 10 layers of superinsulation (RUAG COOLCAT 2 NW), each one consisting of a double high reflectivity aluminized mylar + low thermal conductivity polyester layers. The type and amount of employed material is the result of a compromise between the thermal load that can be borne by the 40 K and the 4 K stages due to radiation and the additional background introduced by the same superinsulation.

All the IVC internal plates have been gilded to guarantee better and durable thermal links between the same plates and all the components, e. g. temperature sensors and wire thermalizations.

The MC flange and plate, as well as the Tower Support Plate (TSP) and the detector frames, are made of ETP1 copper alloy (Electronic Tough Pitch, also called Cu NOSV by Aurubis). The Cu NOSV has been selected for its high conductivity at low temperatures ($RRR \geqslant 400$) and for the low hydrogen content, since hydrogen in copper releases heat due to the ortho-para conversion at low temperatures [166, 167].[2] The limits on the Cu NOSV bulk radioactivity are even more stringent than those on Cu OFE.

Finally, regarding the detectors shields, radio-pure lead of archaeological origin (see Sec. 6.2) was employed for the Internal Lateral and bottom Shield (ILS, see Sec. 6.3), while commercial lead was used for the Top Lead,[3] In both cases, the shield support plates

[1] In Ref. [164] a detailed description of the vessel production and machining can be found (special attention is paid to the description of the welding techniques employed to minimize radioactive contaminations).

[2] This phenomenon becomes relevant at the coldest stage due to the lower cooling power (see Sec. 5.2). The heat dissipation by the hydrogen ortho-para conversion in Cu OFHC can be of the order of a few pW g^{-1} after cooling at the Kelvin temperature.

[3] The Top Lead consists of 5 6 cm piled and sandwiched between two copper plates. In this case, the choice of the lead is less critical since between the this shield and the detector there are more than 9 cm of

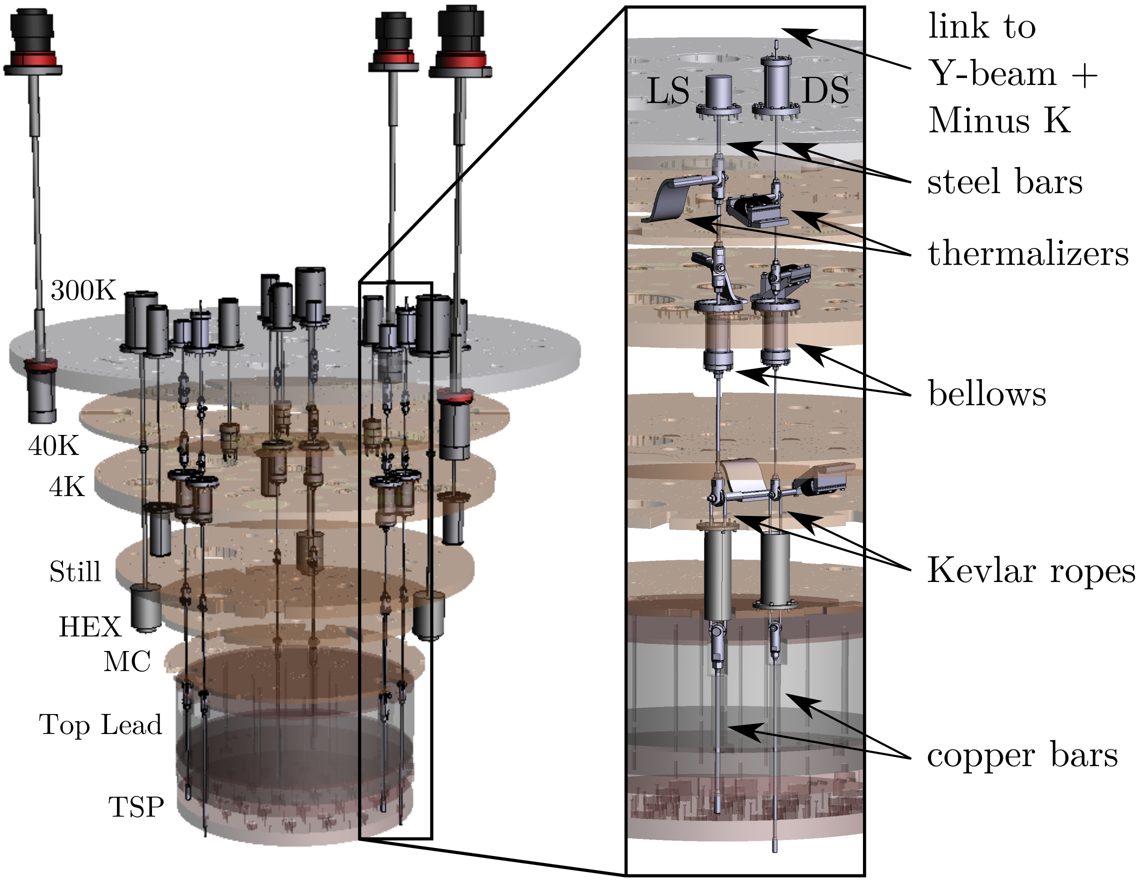

FIG. 4.2: Rendering of open cryostat with detailed view of the supporting elements. The zoom shows the details of the DS and LS components.

(and ring for the ILS, Fig. 6.5) are made of copper.

4.1.3 Final configuration

A schematic of the CUORE cryostat in its final configuration is shown in Fig. 4.1. The CUORE cryostat consists of six nested vessels, the innermost of which encloses an experimental volume of about 0.65 m^3. The different stages thermalize at about 300 K, 40 K, 4 K, 800 mK (Still), 60 mK (HEX) and 10 mK (MC).[4] In particular, the 300 K and the 4 K vessels are vacuum-tight: they enclose the Outer Vacuum Chamber (OVC) and the Inner Vacuum Chamber (IVC), respectively. The IVC contains the ILS and the Top Lead.

All the cryostat components are directly or indirectly held by the 300 K plate through a cascade system of bars for cryogenics application, 3 per plate to ensure a precise vertical alignment (Fig. 4.2). Each plate holds the corresponding vessel. The details of the load structure elements are reported in Tables. 4.3 and 4.4.

copper (Top Lead bottom plate + TSP).

[4]The values for the reference temperatures can actually be different (see Chap. 5). Anyway these ones are used, together with DU elements in the brackets, to indicate the corresponding thermal stages.

TABLE 4.3: (Left) Details of the cryostat support structure. (Right) Schematic of the plate support bars. The bar thermalizers (at the 40 K stage) are also shown.

Plate	Distance[a]	Support			
	[mm]	Bars	Material	Diam. [mm]	Link[b]
300 K	200/750[c]	ropes	steel	22	MSP – 300 K
40 K	195	B	SS316LN	8	300 K – 40 K
4 K	198	A	SS316LN	7.5	300 K – 4 K
Still	287	SS	SS316LN	18	300 K – Still
HEX	112	HS	Ti6Al4V	6	Still – HEX
MC	202	MCS	Ti6Al4V	4	HEX – MC
ILS	187[d]	rods	steel	20	Still – ILS
Top Lead	60	LS	SS316LN	8.7	300 K – Still[e]
			Kevlar K49	8×2	Still – MC
			Cu NOSV	12.2	MC – Top Lead
TSP	76.8	DS	SS316LN	12	Y-beam – 300 K
			SS316LN	6	300 K – Still[e]
			Kevlar K49	6×2	Still – MC
			Cu NOSV	9.3	MC – detector

[a]from the above plate
[b]the bars are thermalized at each thermal stage they pass
[c]from the bottom of the MSP/from the protruded shelves
[d]from the Still plate
[e]segmented: 300 K – 40 K / 40 K – 4 K / 4 K – 4 K / 4 K – Still

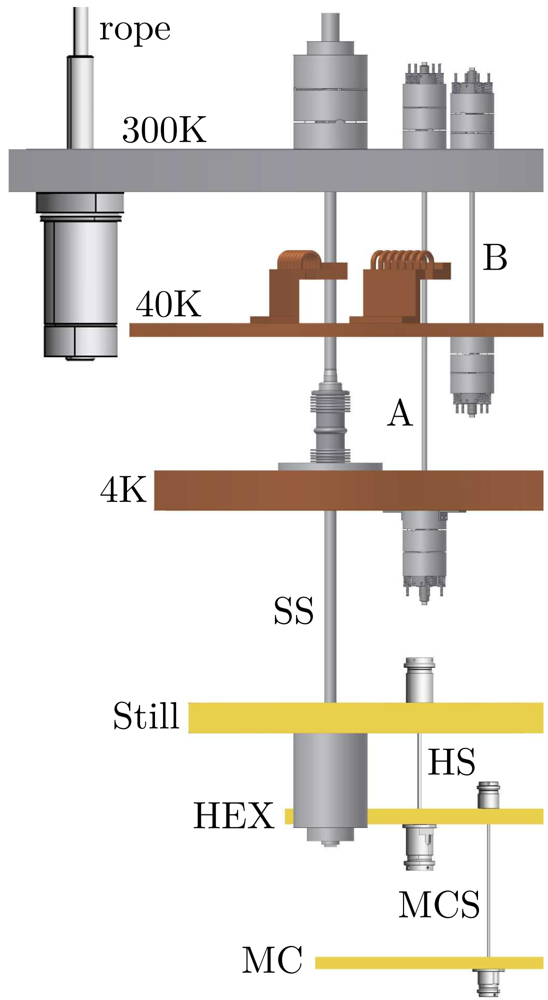

TABLE 4.4: CUORE cryostat dimension and mass inventory.

Part	(Inner) Diameter [mm]	Height [mm]	Thickness [mm]	Material	Mass [kg]	Total mass [kg]
Vessels						
300 K plate	2060	-	62	SS304L	1524	
300 K vessel	1603	3030	12	Cu OFE + SS304L	1960	3484
40 K plate	1573	-	20	Cu OFE	301	
40 K vessel	1503	2765	5	Cu OFE	682	984
4 K plate	1473	-	59	Cu OFE	838	
4 K vessel	1363	2471	10	Cu OFE	1169	2006
Still plate	1333	-	43	Cu OFE	504	
Still vessel	1110	1850	5	Cu OFE	328	832
HEX plate	1070	-	28	Cu OFE	205	
HEX vessel	1020	1650	5	Cu OFE	282	487
MC plate	980	-	18	Cu NOSV	111	
MC vessel	940	1365	5	Cu NOSV	330	442
Lead shields						
ILS (side)	1080	1568	60	Pb (Roman)	3900	
ILS (bottom)	1080		60	Pb (Roman)	623	
Rings (t/b)	1157/1080	80/95	88/98.5	Cu OFE	640	
Base plate	1150	-	35	Cu OFE	325	5488
Top Lead	900	-	300	Pb	2745	
Plates (t/b)	900	-	18/45	Cu NOSV	570	3316
Detector						
TSP	900	-	48	Cu NOSV	285	
Frames	-	-	-	Cu NOSV	71	
Crystals	-	-	-	TeO_2	742	1098

The 300 K plate is connected to the cryostat support structure via steel ropes. The 40 K, 4 K and Still plates are directly held by the 300 K plate via steel bars closed by CuBe gimbals.[5] The HEX plate is held by the Still plate and holds, in turn, the MC plate. The support bars of the HEX and MC plates are made of a Ti alloy (with low thermal conductivity) and closed by steel joints.

The ILS is positioned below the Still plate. It is mechanically attached to the Still plate but thermalized to the 4 K stage (Sec. 6.3). The Top Lead is held by the 300 K plate through the Lead Suspension (LS) bars (zoom in Fig. 4.2, see also Sec. 4.2.3). This shield positioned below the MC plate, but thermalized to the HEX plate.

Finally, the Detector Suspension (DS) bars hold the TSP, which is placed right below the Top Lead. The detector is not attached to the cryostat. It is held by an external structure, called Y-beam. The Y-beam is positioned upon the cryostat support structure and anchored to 3 mechanical insulators by Minus K™ Technology (see Sec. 4.2.3).

4.2 Cryostat support structure

The cryostat support structure has the double function of pure mechanical support of all the cryostat parts and of isolating the cryostat from the rest of the hut and any possible source of interference for the measurement. Its design underwent of a deep seismic analysis in order to study the structural response of the system to seismic events (see Ref. [163] for details). In Fig. 4.5, a schematic of the cryostat support structure is shown.

The basement consists of two $\sim (4.5 \times 4.5)\,\mathrm{m}^2, 600\,\mathrm{mm}$ reinforced concrete walls. The walls are connected by beams, also in reinforced concrete, located in between 3 of the 4 vertex pairs and a steel reinforcement brace is installed between the 2 parallel beams. The connection with the foundation takes place by means of four seismic insulators, consisting of supporting high damping rubber bearing devices, which allow for an effective decoupling of the seismic structure from the ground.

On top of the walls, four tubular 4.25 m tall sand-filled steel columns are installed around the perimeter. On the upper flanges of the columns, the so called Main Support Plate (MSP) is placed. This is constituted by a $(4.7 \times 4.1)\,\mathrm{m}^2$ grid of steel beams and holds, in turn, the detector supporting structure.

The 300 K plate, and the all cryostat masses in cascade, are held by 3 ropes attacked by shelves protruded from the beams. Instead, the detector is mechanically decoupled from the rest of the cryostat and connected to the Y-beam above the same cryostat directly anchored to the MSP passing through a Minus K™ insulation system.

Finally, the electronics is placed on another Y-beam shelf (anchored to the MSP) positioned right above the detector suspension Y-beam.

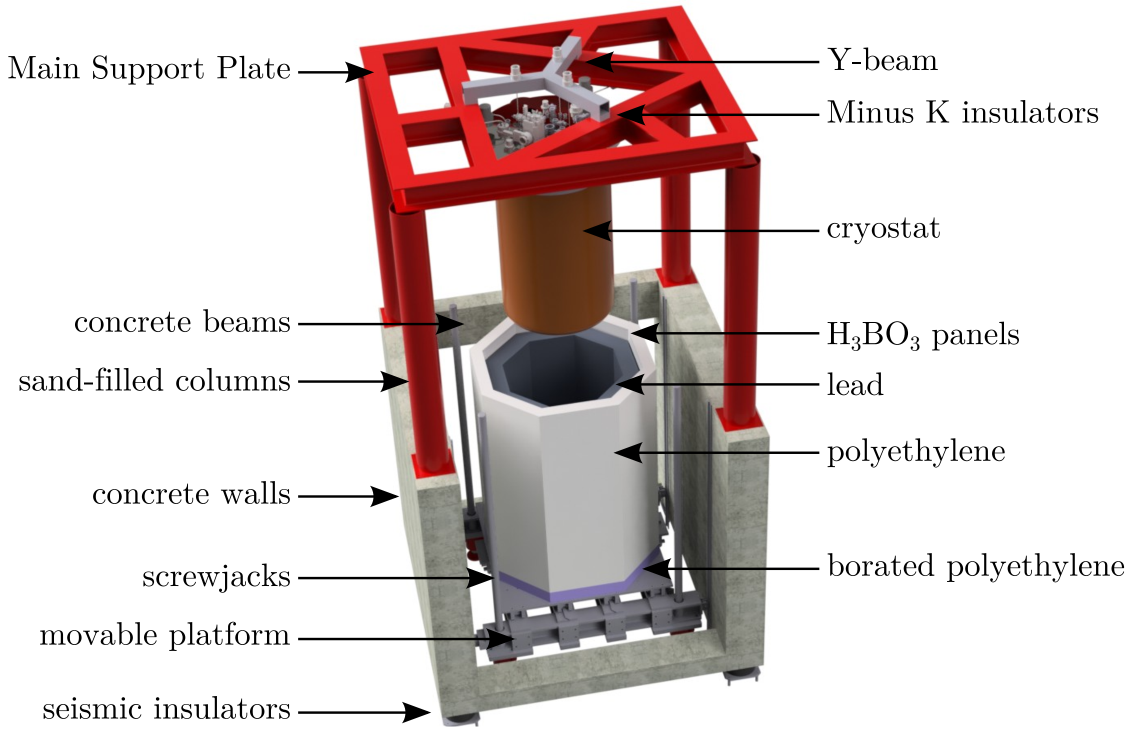

FIG. 4.5: Rendering of the cryostat support structure. The external shield sits on a movable platform that can be lifted to surround the cryostat during the detector operation. The shields are contained in a framed octagonal case not shown in the picture. The electronics Y-beam is also not shown.

4.2.1 Hut

The entire CUORE setup is installed inside a building in the Hall A of LNGS (Fig. 3.1), which contains all the experiment parts, including the cryostat and the cryogenic set up. A schematic of the hut is shown in Fig. 4.6.

The ground floor hosts the base of the cryostat support structure and the external shielding that will surround the 300 K vessel (Sec. 4.2). On the same level, the DU control panel and gas handling system, there are the PT compressors and the flexline sandbox and the compressor for circulation of the He during the cool down (Fast Cooling System, FCS, see Sec. 4.5.1).

The first floor hosts all the clean rooms, including the one with the cryostat. The 300 K plate lies at level of the ceiling. Its top side thus faces the upper floor.

The second floor hosts the Faraday cage with the front-end electronics and the CUORE control room. The Faraday cage also contains the pumping lines and the pumps for the IVC and the OVC volumes, the final portion of the PT flexlines and of the DU gas pipes and the motors of the hoist system for the vessel lifting. The environment is large enough to host the FCS cryostat during the cool down. Outside, all the racks are placed: 4 for the Data AcQuisition (DAQ), 2 for the Bessel filters, 1 for the cryostat monitoring and 1 for

[5]The CuBe gimbals below the Still bars have eventually been replaced with brass cylinders during the commissioning phase in order to make the cryostat structure more rigid (see Sec. 4.3).

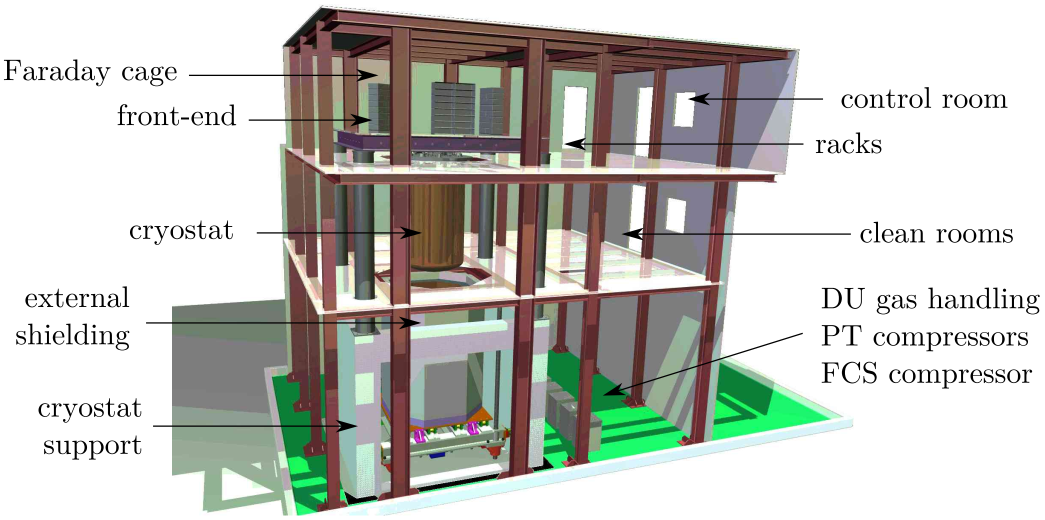

FIG. 4.6: Rendering of the CUORE hut in the Hall A of LNGS.

the DCS control.

Finally, on an external terrace, we find the compressors of the FCS cryostat and the system for the Rn-filtering of the cryostat clean room air (used during the detector installation). On the top of the hut, all the clean room filters and control panels are located.

4.2.2 External shielding

Once the CUORE detector will be operational, the whole cryostat will be protected from the external radioactivity by the External Lateral and bottom Shield (ELS).

The ELS consists of an octagonal shape structure internally covered with multiple shielding layers. Laterally, a 18 cm thick polyethylene layer contains 2 cm thick H_3BO_3 filled panels and a 25 cm thick lead layer. On the bottom, a 25 cm thick lead layer is placed over a 20 cm thick one of borated polyethylene (Fig. 4.5). The total mass is $\sim$ 70 tonnes of lead and $\sim$ 6 tonnes of polyethylene.

The ELS sits on a movable platform placed right below the cryostat. This can horizontally slide on rails to allow the movements of parts inside the cryostat clean room. When the cryostat is open, the vessels lay on the top of the ELS and are raised and lowered by the hoist system.

A lifting system composed of 4 screwjacks (500 kN each) allows the platform to be raised to the upper floor, with the ELS thus reaching the top of the cryostat. The ELS will then be anchored to the cryostat support structure in order to improve the system rigidity. It will also be constantly flushed with N_2 gas to prevent the accumulation of Rn.

4.2.3 Detector suspension system

The CUORE detector is not anchored to the cryostat, but it hangs from the Y-beam. The Y-beam is positioned upon the MSP, on top of 3 Minus K mechanical insulators. The Minus K insulators consists of a particular arrangement of springs that acts like a soft spring when subjected to small displacements, despite the heavy loads they can bear (the total mass of detector + TSP is $\sim$ 1 tonne). This behavior allows for very low natural frequencies for the spring-mass system, resulting in an effective cut-off of the transferred vibration spectrum close to 0.5 Hz (low-pass filter).

From the Y-beam, 3 stainless steel bars constitute the first stage of the DS bars.[6] The steel part is composed of 5 segments, thermalized at the 40 K, 4 K and Still stages. Between the latter thermal contact and the detector, a double Kevlar rope is used to minimize the heat inlet.[7] Finally, the last segment of the DS bars is made of high purity copper rod, chosen for the low radioactivity content. A schematic of the complete DS bars is shown in Fig. 4.2.

4.3 New implementations after the commissioning

As it was shown, the final design of the CUORE cryostat is the result of a series of choices (and compromises) aimed at satisfying several demanding requests. The outcome is a cryogenic infrastructure unique in its kind. The CUORE cryostat is, in this sense, a "prototype".

From a practical point of view, this means that it was not always possible to accurately foresee the implications or the consequences of part of the decisions taken during the design phase. To this extent, the commissioning phase proved to be fundamental in order to become familiar with cryogenic system. As it will be shown in Chap. 5, the acquired experience allowed to actually improve the cryostat configuration, sometimes reconsidering the initial choices.

The major change with respect to the original design interested the joints of the various support bars. The presence of the PTs, even if not firmly anchored to the plates, combined with the "flexible" structure optimized to provide the best response to a seismic events, proved to be incompatible with the operation of a detector inside the cryostat. In fact, during the first test runs, the entire structure was behaving like an articulated pendulum and the relative plate movements were generating micro-frictions that were in turn inducing a too high vibrational noise, or even preventing to reach a stable base temperature.

Among the adopted countermeasures, it was decided (see Sec. 5.10.3 for details):

- to block the relative movements of the plates by fixing part of the joints;
- to rigidly anchor (horizontally) the 300 K plate to the MSP.

These decisions aimed at making the cryostat internal structure more rigid. In this way, it was possible to discharge part of vibrations from the PTs towards the outside. The

[6] Below the 300 K plate, the structure of the DS and LS bars is the same, apart from the dimensioning (see Table 4.3).

[7] Poly-paraphenylene terephthalamide, branded Kevlar, is an aramid fiber with very good mechanical and thermal properties. In particular, Kevlar K49 is used in cable and rope products also used in cryogenic applications. The high tensile strength ($\gtrsim 3.5$ MPa) guarantees the capability of holding heavy loads with small cross section, while the extremely low thermal conductivity ($\sim 4 \cdot 10^{-3}\,\mathrm{W\,m^{-1}K^{-1}}$) makes it a good insulating material.

TABLE 4.7: Maximum design differential pressures for the OVC and IVC vessels that can be stood by the volumes during the different phases of operations.

Vessel	V [m^3]	ΔP_{max} [bar]	
		$\Delta P_{\text{in-out}}$	$\Delta P_{\text{out-in}}$
OVC	5.86	0.1	1.01
IVC	3.44	1.5	1.1

drawback was the partial compromise of the seismic safety of the cryostat.[8] Anyway, this choice appeared as mandatory in order to be able to operate a detector, as it was successfully demonstrated (see Chap. 7).

Since the seismic insulators at the base of the cryostat support structure natural oscillation frequencies for the structure of the order of $(1-3)$ Hz that contribute to the detector noise, a blocking system will be installed. This consists in a series thin metal plates transversally inserted between the structure basement and the foundation that will prevent any oscillation. The steel plates act as "mechanical fuses" and will break in case structure undergoes a strong acceleration (such as during a seismic event), thus not compromising the seismic safety of the support structure.

4.4 Pressure and vacuum

The 300 K and the 4 K vessels must be able to keep the vacuum of the order of 10^{-4} mbar at room temperature (see also App. A.1). At the same time, these two vessels must be able to stand both internal and external overpressure without worsening of the vacuum specifications and avoiding plastic deformations.

In operating conditions, the OVC is subjected to an external overpressure equal to the environmental pressure. Instead, the IVC is essentially in pressure equilibrium between the outside and the inside during normal operation, while it has to stand ~ 1.3 bar of internal overpressure due to the FCS He during the initial phase of the cool down (see Sec. 4.5.1). In addition, leak checks may require for both the volumes to stand either an external or an internal overpressure.

The wall thicknesses were calculated according to the ASME code [168] and a linear buckling analysis was performed with ANSYS in order to satisfy the operating pressure requirements. These are reported in Table 4.7. The limiting differential pressure were calculated to be 2.0 bar and 2.3 bar for the OVC and IVC vessel respectively.

The pumping system is constituted by a scroll pump (Scrollvac SC 30D by Leybold with 26 $m^3\,h^{-1}$ pumping speed) backing two turbomolecular pumps, one for each volume (ATH 300 by Adixen for the OVC and HiPace™ 300 by Pfeiffer for the IVC). In particular,

[8] The cryostat seismic safety regards the detector and the same cryostat. It is not related to the safety of the working people. This is guaranteed by the cryostat support structure, designed to resist to seismic events (Sec. 4.2).

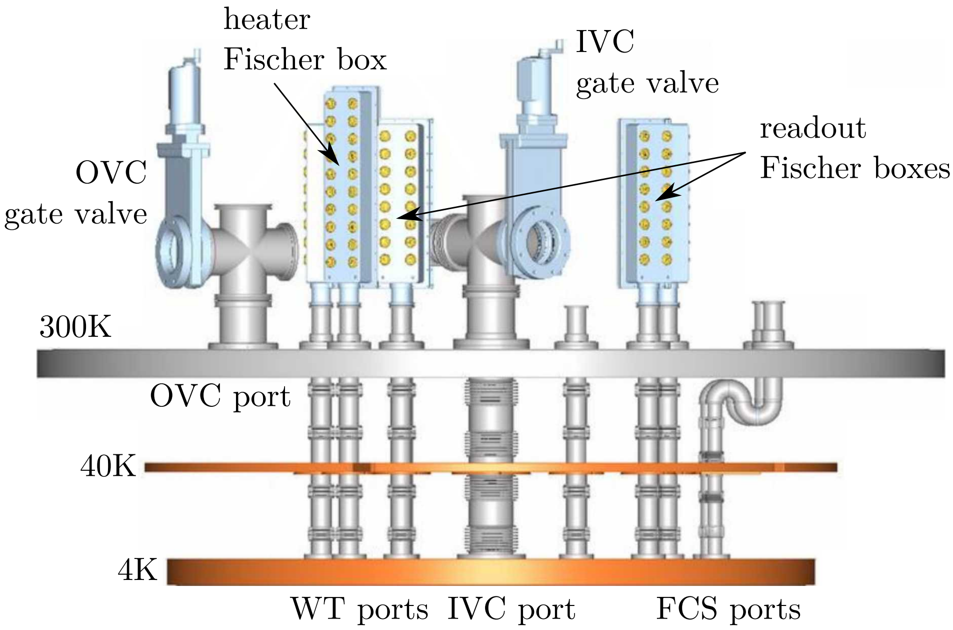

FIG. 4.8: Schematic of the the OVC and IVC ports. The wiring ports for the readout of the OVC and IVC diagnostic sensors are not shown in the picture.

the IVC turbomolecular pump is characterized by an elevated compression factor for He ($\gtrsim 10^8$), fundamental to avoid the presence of any gas residual during the cool down.

A charcoal getter with integrated heater and thermometer is placed below the 4 K plate. This is activated in order to absorb the residual He after the FCS has been switched off.[9]

The vacuum tightness of the cryostat is guaranteed by a series of gaskets positioned between the different volume interfaces. In particular, an elastomer ring at the 300 K plate-vessel interface seals the OVC from the external ambient. Instead, for the IVC, a tubular metallic seal (Helicoflex™ model HNV 200 by Technetics) is mounted inside a centering ring on the flange of the 4 K vessel.[10]

The OVC has 2 access ports (Fig. 4.8): 1 DN100 pumping port and 1 DN40 wiring port for the readout of the diagnostic sensors (thermometers and pressure gauges). The IVC has several access ports: 1 DN100 pumping port, 7 DN40 Wire Tray (WT) ports for the detector readout (5), the heater control (1) and the readout of the diagnostic sensors (1) and 2 DN40 ports for the inlet/outlet of the FCS He (Sec. 4.5.1). Furthermore, there are 4 DN50 ports for the sliding of the source wires of the Detector Calibration System (DCS, see Sec. 4.6) and 3 DN16 ports for the readout of the DU sensors embedded in the DU system.

Elastomer o-rings are used to seal the various OVC and IVC ports at the level of the 300 K plate, while indium gaskets are used for the IVC ports at the level of the 4 K plate.

Radiation baffles are present inside the pumping and FCS ports. The IVC port baffles consist a series of 4 D-shaped steel foils fixed to a bar anchored to the port at the level

[9]The charcoal getter, also referred as carbon pump, has been inserted at the end of the cryostat commissioning since this element makes it difficult to perform the leak checks.

[10]Elastomer o-rings cannot be used at cryogenic temperatures since they would freeze, while the use of both indium and Kapton sealings would be unpractical given the dimension of the flange.

of the 300 plate. The different orientation of the D-shaped foils interrupts any straight line of sight between the 300 K and the 4 K plates and, at the same time, leaves sufficient throughput for the pumping. On the 4 K side, a copper box fixed to the plate (part of the DCS, see Ref. [169] for details) prevents the port to directly face the Still plate. The FCS port baffles consist in a series of 6 D-shaped steel foils sandwiched between Kapton layer (high absorptivity, looking down) and an aluminized mylar one (high reflectivity, looking up). They baffles were fixed to a bar anchored to the 4 K plate. In this case, the bar could not be a unique element, since linked to the coldest stage. PTFE insulators were thus inserted along the bar (one close to each baffle) to reduce the overall conduction.

Inside the WT ports, instead, the baffle function is performed by the PTFE spirals that guide the wires (the path is not straight to allow for their thermalization, see Sec. 5.8.1).

4.5 Cool down

The cool down of the CUORE cryostat employs different systems (Fig. 4.9). These are thus (at least partially) integrated in the cryostat. The first phase of the cool down, to $\sim 50\,\mathrm{K}$ at all thermal stages, is driven by the FCS. In fact, the effort would be too large for the lone PTs (see App. A.3).

The PTs are turned on a few days later and, when the FCS is no more effective, this is definitely switched off. The PTs brings the 40 K and 4 K stages to their base temperatures (PT first and second stages, respectively) and the inner stages to a temperature close to that of the 4 K stage.

The final IVC temperatures are reached after the DU is turned on. The DU completes the cool down and guarantees the coldest stage temperatures, maintaining the detector at $\sim 10\,\mathrm{mK}$.

4.5.1 FCS

The FCS is the custom designed apparatus that pre-cools the whole cryostat mass inside the IVC (included the detector) down to $\sim 50\,\mathrm{K}$, initially alone and then supported by the PTs. The FCS injects cold He gas inside the IVC and forces its circulation in a dedicated cooling circuit. The gas temperature at the IVC entrance is initially $\sim 200\,\mathrm{K}$ and decreases to $\sim 50\,\mathrm{K}$ with the proceeding of the cryostat cool down. This He is cooled inside an external cryostat powered by 3 Gifford-McMahon (GM) coolers (AL600 by Cryomech) and circulated by a compressor (Busch Mink MM 1322 AP). The AL600 cooling power is much higher than that of a PT415, being 1800 W at 300 K and 350 W at 50 K.[11] A schematic of the FCS gas circuit is shown in the left panel of Fig. 4.10. In the right panel, a rendering of the FCS external cryostat is shown.

After entering the CUORE cryostat, the gas passes through a S-tube (a siphon that hinders the radiation path) and reaches the IVC (Fig. 4.9). From the 4 K plate, a splitted

[11] GM coolers could not be installed on the cryostat since the cooling is obtained by moving pistons. The generated vibrations would not allow to run any a bolometric experiment.

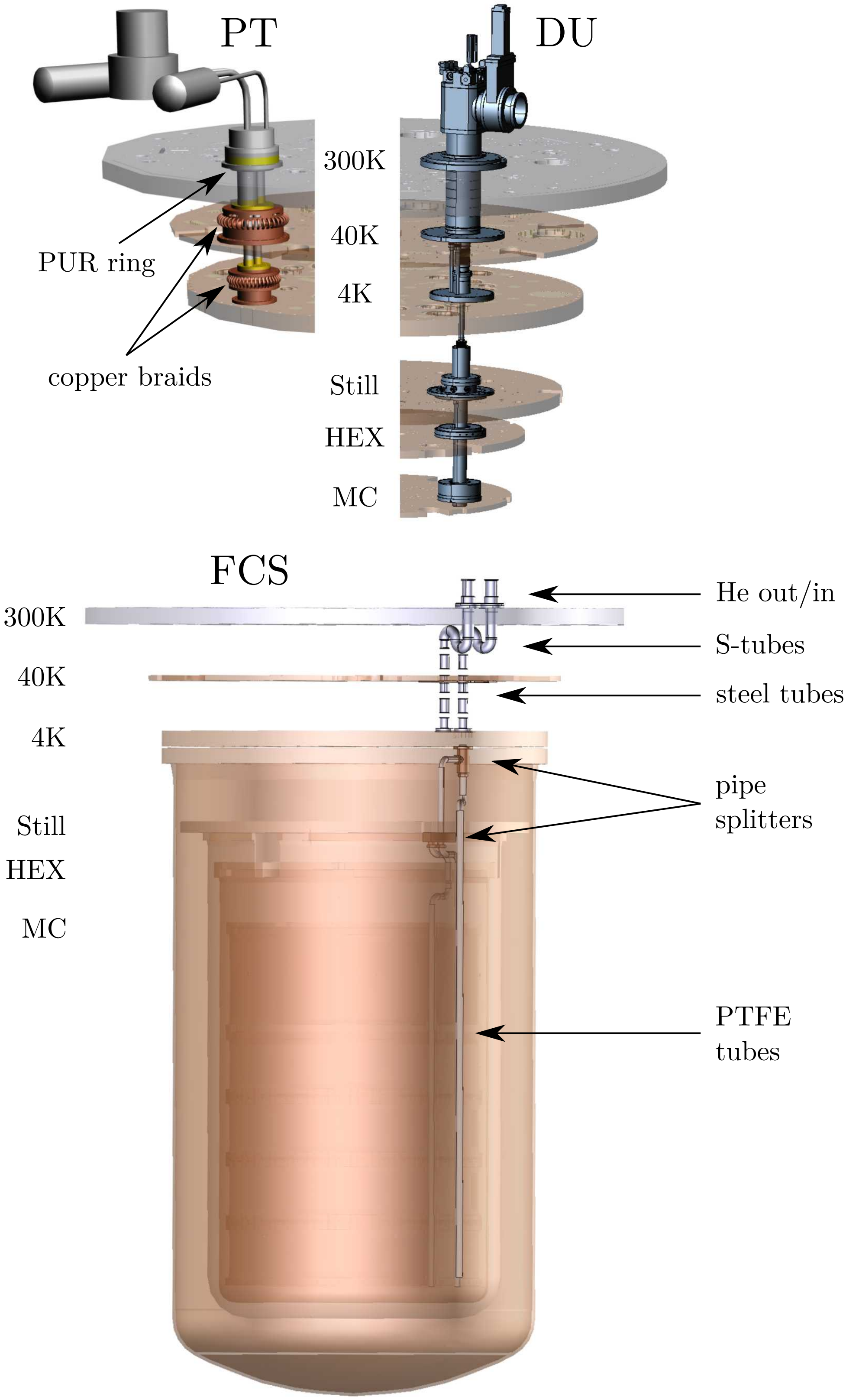

FIG. 4.9: Renderings of the CUORE cryostat with zooms on the single cool down subsystems. (Top, Left) One of the five PTs (the thermalizations are actually gilded to guarantee better and durable thermal contacts). (Top, Right) DU. (Bottom) FCS. The interruptions along the steel tubes correspond to the bellows, not inserted in the picture.

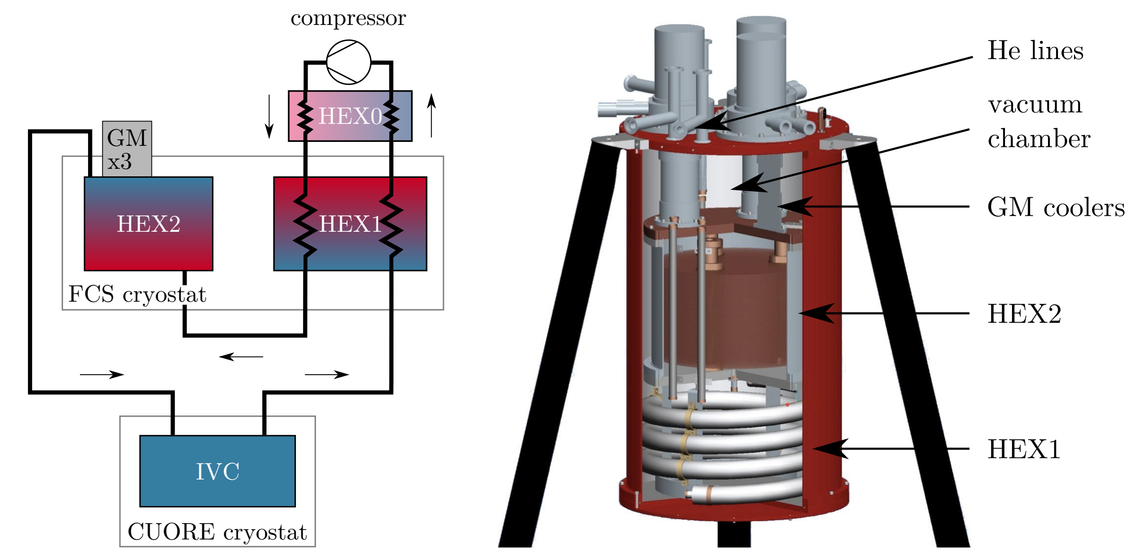

FIG. 4.10: The CUORE FCS. (Left) Schematic of the gas circuit. The arrows indicated the direction of the He flow. (Right) Rendering of the external cryostat for the He cooling.

path guides the He towards the bottom of the ILS and of HEX and MC vessels through PTFE tubes (chosen for the low thermal conductivity and high radiopurity). A second port on the IVC plate allows the exit of the gas, that can thus restart to follow the circuit.

The FCS is able to keep the cool down time within ∼ 20 days (see Secs. 5.9 and 5.10). In principle, the system could provide better performance, but some important requirements must be fulfilled in order to guarantee a safe operation, both for the CUORE cryostat and for detector:

- the IVC pressure must never exceed 1.3 bar, to avoid any risk of damaging the cryostat sealings;
- the circuit pressure must never be lower than the environmental pressure, to prevent any air return inside the line;
- the temperature inside the FCS cryostat must always be lower than 202 K (Rn melting point) while circulating, creating a cryo-pump for the Rn and thus preventing its injection inside the CUORE cryostat;
- excessive temperature gradients must be avoided on the most sensitive parts, i. e. on the detector, due to its intrinsic fragility and on the IVC vessel, since it is vacuum tight.

These conditions translate into constraints on the He circulation flow. In particular, the motor speed is always much lower than the nominal value of 50 Hz, which guarantees a pumping speed of 280 $m^3\,h^{-1}$. It ranges from ∼ 20 Hz during the initial phase of the cool down, to a few Hz in the final one (see Sec. 5.10.1). The minimum frequency is limited by the parasitic power dissipations along the circuit, especially at the level of the He inlet

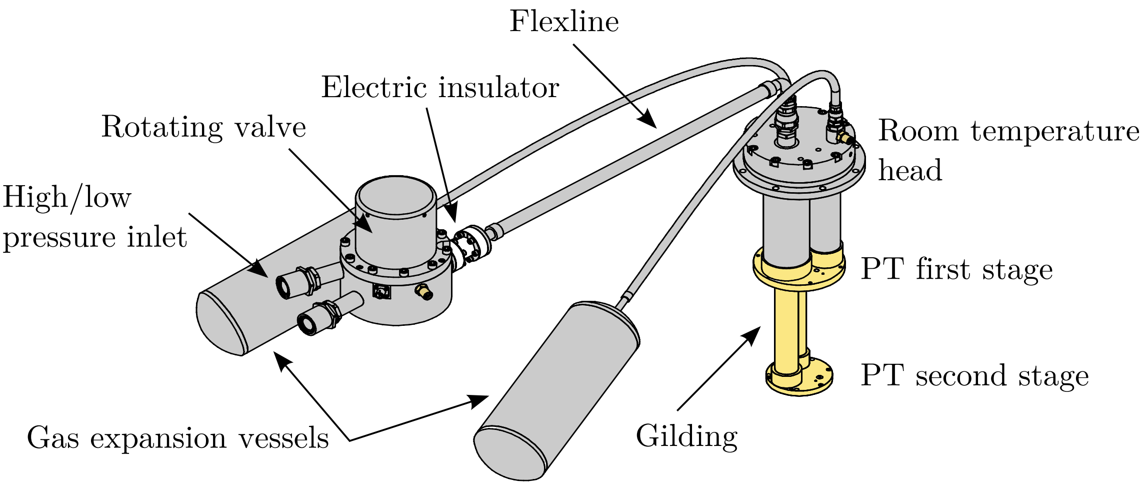

FIG. 4.11: Rendering of a CUORE PT.

and outlet in the CUORE cryostat, that warm up the circulating gas (see the lower plot in Fig. 5.17). With a too low flow, the gas would enter the CUORE cryostat with a temperature actually higher than that of the inner cryostat stages.

The PTs are turned on a few days after FCS, typically when the IVC temperatures are close to 200 K. At this point their contribution to the total cooling power is $\sim 1/3$ (see the upper plot in Fig. 5.16). When they begin to drive the cool down (at ~ 50 K), the FCS compressor is turned off and the He extracted from the IVC.[12] PTs can then reach base temperature in a few days.

4.5.2 PTs

PTs are cryocoolers with no moving parts at low temperatures. Their use increase the total duty cycle of the experiment with respect to a LHe bath cryostat, due to the absence of cryogens to refill.

A PT consists of a compressor with rotating valve used to generate an oscillating pressure, a regenerator and one or more thin-walled tubes with heat exchangers at both ends (Fig. 4.11). These latter units are the actual pulse tubes, after which the cryocooler is named. The basic cooling effect relies on a periodic pressure variation and a displacement of the working gas (He) in the pulse tubes.[13]

The absence of moving parts at low temperatures diminishes the magnetic interferences and guarantees a higher reliability with respect to others cryocoolers, such as GM coolers. Moreover, this strongly reduces the amount of vibrational noise generated during its operation.

The compressor and the rotating valve still remain significant sources of mechanical

[12] The removal of the cold He must be performed very slowly, a few liters per minute. In fact, the amount of gas inside the IVC is large, being roughly equivalent to 6 bar at ambient temperature in a volume of $\sim 3.5\,\mathrm{m}^3$ and thus a considerable flow would freeze the several o-rings of the IVC port and damage the pumps.

[13] See e. g. Refs. [93, 111] for a detailed (and quantitative) description of the operation of a PT.

vibrations, but the largest contribution comes from the pressure waves generated by the compressed He that powers the PTs. The latter cause the periodic deformation of all the flexlines, both those connecting the compressor to the rotating valve and those connecting the rotating valve to the room temperature head. Furthermore, the pressure waves induce the cyclical expansion of the actual pulse tube, both along and perpendicularly to the PT axis. Therefore, the PT vibrational noise would be too high to allow the functioning of the detector without an appropriate series of countermeasures.

In CUORE, a remote motor option has been chosen for the PTs, i. e. the rotating valves are separated from the PT heads. Apart from reducing the amount of vibrations, this also allows to separate the valve grounding from the main one, and thus to electrically decouple the PT (and the cryostat) from the external world.[14]

Inside the cryostat, flexible thermalizations consisting in copper braids link the cold heads of each PT to the cryostat flanges at the 40 K and 4 K stages, thus making a softer connection between the PTs and the cryostat plates. At the level of the 300 K plate, a PolyURethane (PUR) ring is placed around the PT flange to reduce the amount of transmitted vibrations (Fig. 4.9).

The rotating valves, the gas inlet lines and the expansion vessels are suspended to the ceiling of the Faraday cage by means of elastic bands to further absorb the vibrations. Any contact between these elements and the MSP (and all the cryostat support structure) has been avoided. Electrical insulators have been inserted on all the flexlines from and to the PT compressors, before the entrance in the Faraday cage in order to guarantee the electrical decoupling from the PT compressors. Finally, close to the compressors, the flexlines enter a sandbox to reduce the vibration transmission.

The residual amount of vibrations can be minimized by acting on the frequency of the rotating valves. These devices are designed to alternatively connect the pulse tube to the high- and low-pressure side of the compressor with a frequency close to 0.7 revolutions per second (1.4 Hz for the complete cycle). The combined operation of multiple PTs thus generate an "interference pattern" for the vibrations induced by the He pressure waves. The real situation is actually complicated, given the asymmetry of the system (PT location of inside the cryostat, slight differences among the PTs (see App. A.2), cryostat geometry). However, the use of a micro stepping controller to drive the motor heads allows to stabilize the system. Therefore, by identifying the configuration characterized by the the lowest level of vibrations, it is possible to perform an active noise cancellation.

The 5 CUORE PTs are PT415-RM by Cryomech with remote motor option (2 ft $\simeq$ 61 cm flexline). The nominal cooling power is 1.2 W at 4.2 K and 32 W at 45 K while the lowest temperature achievable is close to 3 K in case of no thermal load. These values actually show a worsening in performance with respect to a PT415. This performance loss is induced by the remote motor, and it is estimated in $\sim 10\%$ of the cooling power per feet of the flexline.

[14] A not efficient grounding of the various cryostat components represents a noise source for the detector (see Sec. 5.10.3).

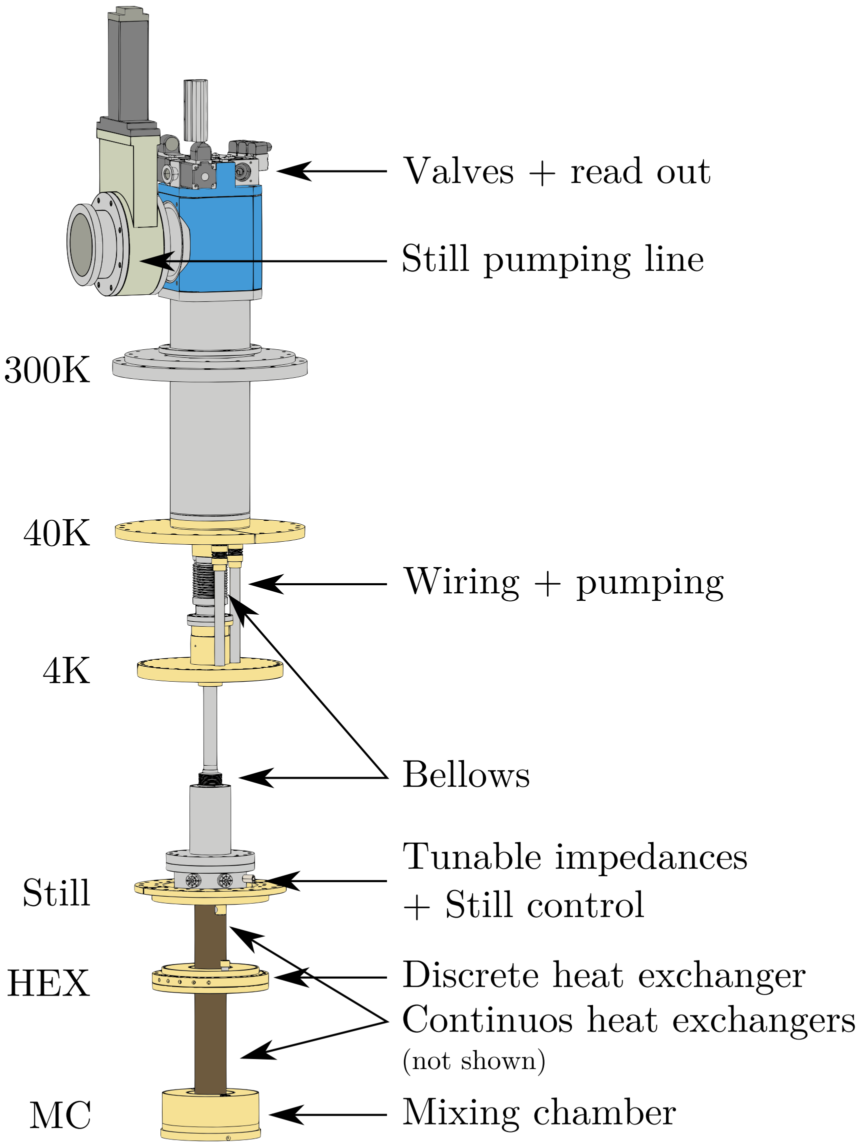

FIG. 4.12: Rendering of the CUORE DU.

The cooling power of 3 PTs would be enough to guarantee the outer stage base temperatures. However, in a conservative approach, it was decided to keep a spare PT in case one would fail. Actually, since an inactive PT constitutes a relevant thermal load for the system, the request for a spare PT implies the need for 2 extra PTs (see App. A.2.1).

4.5.3 DU

In order to operate the NTDs in the CUORE cryostat, a base temperature of $\sim 10\,\mathrm{mK}$ has to be reached and maintained in a stable way. In a conservative approach, the target for the base temperature was set to 8 mK. This value represented a challenge for the CUORE DU, given the presence of the detector, the large masses at the various thermal stages and the presence of 2600 readout wires.

The requirements on the cooling power at the various stages and on the achievable base temperature could be made only for the "bare" DU. The corresponding values after the integration inside the CUORE cryostat had to be extrapolated from simulations. In particular, it was estimated that, by moving the DU from the test cryostat to the CUORE cryostat, the additional thermal loads would have increased the minimum base temperature of $\sim 2\,\mathrm{mK}$. Therefore, the requests were made for a DU base temperature of $6\,\mathrm{mK}$.

The CUORE DU is a high-power Joule-Thomson custom designed DU by Leiden Cryogenics (Fig. 4.12, see also Sec. 5.2 for details on the DU characterization).

The DU is provided with 2 lines for the incoming mixture. This configuration allows to continue the run in case one of the lines becomes unusable. The lines enter the DU at the level of the 300 K plate. Below the 40 K plate, they exit the DU and split into two. The 2 halves of the same original line are thermalized between the two cold thermal stages of a PT.[15] Each line then passes through a thermalizer anchored to the 4 K plate (App. A.4). The thermalizers have been added to prevent that the combination of an unusable line with the failure of the PT with the other line would interrupt the run.

Since the DU is mounted in a cryogen-free cryostat, there is no 1 K pot. Therefore, the incoming mixture thermalizes inside the Still. During the cool down, the mixture is cooled to $< 1\,\mathrm{K}$ thanks to the Joule-Thomson expansion. The condensing stage is equipped with a tunable impedance (valve inside the Still) that allows to regulate the mixture flow before the closure of the cryostat (see App. A.6).

Apart from guarantying a spare line for the mixture circulation, the presence of two independent condensing lines also allows to work in higher cooling power mode during the cool down by circulating with both lines, reaching flows of $\sim 8\,\mathrm{mmol\,s^{-1}}$.

To reach and maintain the MC base temperature, the flow has to be reduced. On the one side, at high flows the incoming mixture contributes in a dominant way to the total heat load on the MC stage.[16] On the other, the dilution process, and thus the cooling power, is proportional to the flow. The optimum value is found around $\sim 1\,\mathrm{mmol\,s^{-1}}$ (see Sec. 5.2.1). The flow can then be tuned by injecting power (a few mW) on the Still with a heater inside the same Still.

4.6 DCS

A system of external sources could not work for the calibration of CUORE, due to the self-shielding action of the detector. A homogeneous illumination of the crystals would require sources with different intensities to be deployed in successive phases. The source activities should also be large enough to guarantee a sufficient survival rate after penetrating the vessels and the ILS. Therefore, the DCS has been integrated in the cryostat.

The function of the CUORE DCS is to deploy the calibration sources into the cryostat,

[15] 3 of the 5 PTs are provided with a condensing line welded all around the part between the first and the second thermal stage, i. e. the colder pulse tube.

[16] In fact, the lowest temperature in a DR is reached during the "single shot", i. e. when the mixture recirculation is interrupted not returning the pumped ^{3}He.

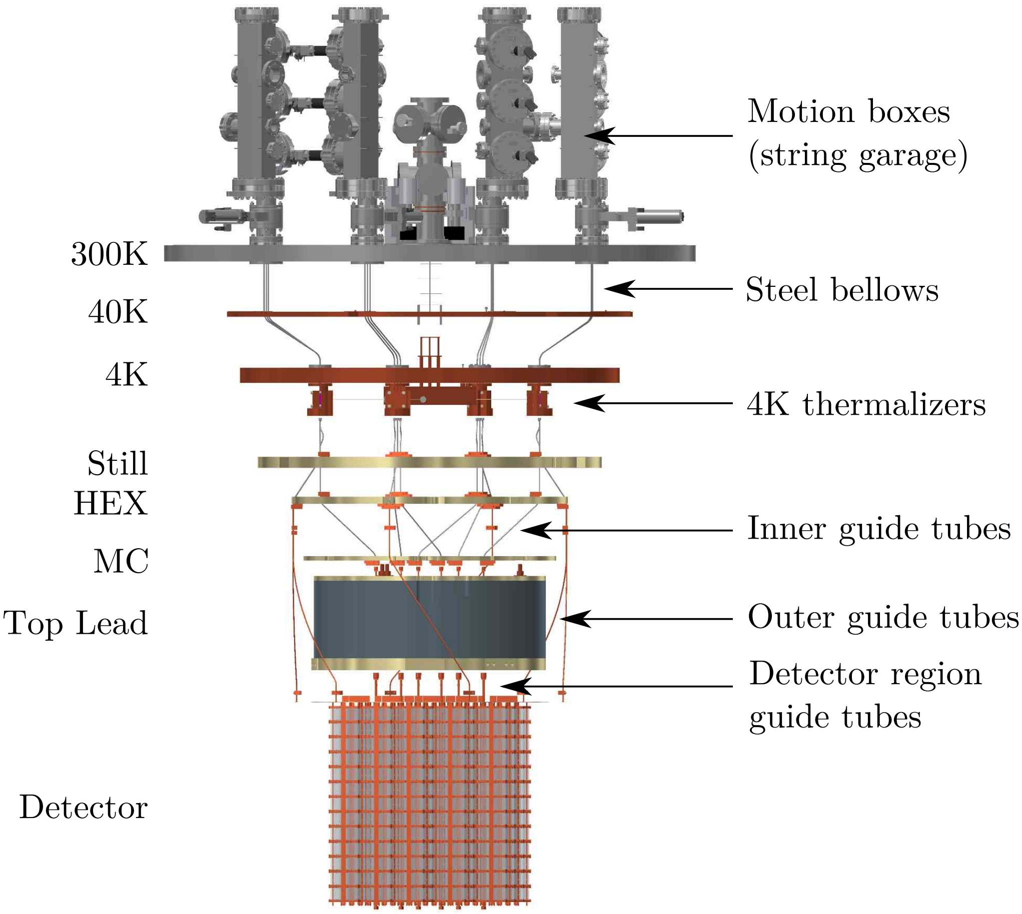

FIG. 4.13: Rendering of the cryostat with detailed view of the DCS components. Figure from Ref. [169].

thermalizing them at the various stages, without affecting the operating temperature of the detectors. The design and construction of the system has been largely driven not only by the thermal requirements of cryogenics, but also from the strict radiopurity request of the experiment.

A schematic of the DCS is shown in Fig. 4.13, while a detailed description can be found in Ref. [169]. The DCS is based upon 12 radioactive source strings that are able to move, under their own weight, through a set of guide tubes that route them from outside the cryostat to their locations around and between the towers. During physics data taking, these source strings are wound on spools in dedicated motion boxes installed on the 300 K plate to protect the detector from the same sources. The boxes are connected to the IVC through gate valves.

The source material is commercially available thoriated tungsten with measured activity [170]. Small portions of wire are cut and fit into capsules. Depending on the capsule required activity (in turn depending on the final capsule position relative to the detector), the wire is cut at different lengths. For CUORE, ^{232}Th sources are a natural choice due to the numerous lines from the decay chain, especially the strong 2615 keV line of ^{208}Tl, which allows for precise energy calibration close to $Q_{\beta\beta}$. Anyway, the system is flexible enough to permit the substitution of the calibrating sources. [17]

4.7 Cryostat monitoring system

A series of parameters is monitored during the various phases of the run, from the cool down to the working regime. These span over a very broad range of categories and involve many subsystem:

- cryostat (general): IVC and OVC pressure, temperature of different components, power injected on the various heaters, turbomolecular pump speed;
- DU: pressures along the circuit, temperatures inside the cryostat, mixture flow, Still mixture level and injected power, valve/pump configuration, compressor pressure and cooling water temperature;
- PTs: temperatures of the 2 cold stages, motor rotation phase, compressor high and low He pressures, current and He gas, oil and cooling water temperatures;
- FCS: pressures and temperatures along the gas circuit (including CUORE and external cryostat), He flow, Busch compressor frequency, GM compressor high and low He pressures, current and He gas, oil and cooling water temperatures;
- DCS: temperatures along the guide tubes, motion box pressure, string position;
- leak rate (for residual gas measurements in the various volumes).

Apart from collecting important data from the various subsystems, the correlation of different information allows for a deeper and more complete understanding of what is actually happening to the cryogenic apparatus. Therefore, a very large amount of data has been acquired during the cryostat commissioning (see Chap. 5). Their analysis is fundamental for the understanding of the cryostat behavior, whether everything is properly functioning or a problem has occurred.

4.7.1 Thermometry

The CUORE cryostat is provided with ~ 50 thermometers with diagnostic purposes. This number was actually higher during the commissioning runs. The temperature range to be monitored spans over a very broad interval of values. It goes from the environmental temperature ($\sim 295\,$K), before the staring of the cool down, to the detector base temperature ($< 10\,$mK). An adequate set of different thermal sensors is thus fundamental.

Temperatures from hundreds down to a few K are measured via commercial silicon diodes resistance thermometers (DT-470 and DT-670 Series by LakeShore). For temperatures $< 1\,$K down to some tens of mK, Ruthenium oxide (RuO_2) resistors are used, both commercial (Lake Shore, RX-102A Series) and custom made.

[17] Dedicated measurements with both ^{60}Co and ^{56}Co are planned in order to study some unclear effects (shifting) observed in sum and escape peaks [147].

On the MC, a MFFT-1 Noise Thermometer (NT) by Magnicon and a Cerium Magnesium Nitrate (CMN) thermometer allow to monitor the temperature down to a few mK. The two sensors are calibrated by referring to a superconductive Fixed Point Device (FPD). Both the CMN and the FPD are by milli-Kelvin Technologies (see App. A.5 for details on these device performance).

Finally, regarding the TSP, the innermost part of the cryostat close to the detector, the device bulk radioactivity adds another stringent constraint on the sensors. Therefore, below the Top Lead, only custom made "bare chip" diodes thermometers can be used to monitor the cool down due to the radioactivity constraints, while NTDs are used for the temperature monitoring and for the stabilization system.

Chapter 5

Cryostat commissioning

The CUORE cryostat is a very complex and, despite the large masses involved, a very delicate machine. Design and construction basically from scratch were required for most of its components and numerous tests had to be performed to verify the correct functioning of the various parts. At the same time, attention had to be paid to ensure that any addition or modification to the apparatus did not compromise the overall performance.

A long period (~ 4 years) proved to be necessary in order to reach the final and complete cryostat configuration, before the installation of the CUORE detector. Nonetheless, this commissioning resulted in an environment which is stable from the cryogenic point of view, shielded from external radioactivity and suitable to run a bolometric array.

5.1 Brief history

The construction of the 4 K outer cryostat and of the DU proceeded roughly in parallel between 2009 and 2012 and preliminary validation tests at the construction sites were performed with dedicated setups on both the subsystems to check the compliance with the design specifications.[1]

After the arrival at LNGS and the installation inside the clean room (summer 2012), the outer cryostat was equipped with the PTs and the cool down to 4 K was tested during Run 0.1 and Run 0.2 (Table 5.1). The DU was also delivered to LNGS (April 2012) and further tests were performed inside an independent cryostat.

Then, the DU was installed inside the CUORE cryostat, together with the inner vessels and plates (December 2013 - January 2014) and the first cool down to 10 mK with the "complete" setup was performed during Run 1.1. Actually, two more runs, Run 1.2 and Run 1.3, proved to be necessary in order to reach and maintain a stable base temperature at each stage, due to some problems of power dissipation.

The next step consisted in the installation of the CUORE detector readout wiring (October 2014), 2600 wires with the related boxes for the connection to the towers on one

[1]The details on the construction of the 4 K outer cryostat are reported in Ref. [164].

TABLE 5.1: Summary of the CUORE cryostat commissioning at LNGS. For each test run, goals and schedule are reported.

Run	Duration	Cold test		Milestones
	Oct 2012 - Jan 2014	Oct 2012 - Aug 2013	(many)	DU standalone tests
0	Jul 2012 - Aug 2013	Mar 2013 - Apr 2013 Jul 2013 - Aug 2013	(0.1) (0.2)	4 K outer cryostat: achieving and maintaining base T
1	Sep 2013 - Oct 2014	Mar 2014 - Apr 2014 May 2014 - Jun 2014 Aug 2014 - Oct 2014	(1.1) (1.2) (1.3)	merging 4 K cryostat and DU installation of inner plates and vessels achieving and maintaining base T
2	Oct 2014 - Jan 2015	Nov 2014 - Jan 2015		detector wiring installation
3	Jan 2015 - Sep 2015	Jul 2015 - Sep 2015		Top Lead installation TSP installation cool down with FCS
4	Jul 2015 - Mar 2016	Nov 2015 - Mar 2016		ILS installation Mini-Tower performance optimization

side and to the electronics on the other. This paved the way to the possibility of operating a bolometric detector inside the CUORE cryostat. A small array, the Mini-Tower (see Chap. 7), was thus assembled (May 2014) and positioned under the MC plate (October 2014) as a test detector and the first attempt of data acquisition were performed during Run 2.

After its assembly, the Top Lead was integrated in the cryostat (May 2015). The installation of the TSP (June 2015) allowed to move the Mini-Tower to the position of a CUORE tower. The addition of the Top Lead to the system required the use of the FCS, previously assembled and tested on its own (March - July 2015), to help the cool down. The FCS will always be used from Run 3 on.

In the meanwhile, the ILS was being produced (July - October 2015, see Chap. 6). Its installation (October 2015) allowed to perform a last, long-term test run with the "fully loaded" cryostat, apart from the detector. During Run 4, many studies and tests were performed on the Mini-Tower in order to optimize the detector performance in view the forthcoming CUORE.

With the successful run of a bolometric detector inside the cryostat, the commissioning phase of the CUORE cryogenic system could be considered finally concluded. After Run 4, it was thus possible to start all the operations in view of the CUORE detector installation.

Table 5.1 summarizes the schedule and goals of the cryostat commissioning, while in Table 5.2 an inventory of the cryostat components during the various runs is reported.

TABLE 5.2: CUORE cryostat part installation during the commissioning runs. The symbols ✓ (×) indicate installation (absence) of the considered element. See the text for more details.

Part	Run 0	Run 1	Run 2	Run 3	Run 4
Load structure					
Outer vessels [a]	✓	✓	✓	✓	✓
Inner vessels [b]	×	✓	✓	✓	✓
DS/LS (300 K to 4 K)	×	✓	✓ [c]	✓	✓
DS/LS (4 K to Still)	×	✓/× [d]	×	✓	✓
TSP	×	×	×	✓	✓
Lead shields					
Top Lead	×	×	×	✓	✓
ILS	×	×	×	×	✓
Vacuum					
OVC port	✓	✓	✓	✓	✓
IVC port	✓	✓	✓	✓	✓
Cool down					
DU	×	✓	✓	✓	✓
mixture thermalizers	×	×	×	✓	✓
PTs	3	4	4	5	5
FCS (OVC parts)	×	✓	✓	✓	✓
FCS (IVC parts)	×	×	×	✓	✓
Read out					
WT ports	✓ [e]	✓	✓	✓	✓
detector wiring	×	×	✓	✓	✓
Mini-Tower	×	×	✓	✓	✓
DCS					
motion boxes	×	1	1	4	4
OVC tubes	×	✓	✓	✓	✓
4 K thermalizer	×	×	× [f]	✓	✓
IVC tubes	×	×	× [f]	✓	✓

[a] 300 K, 40 K, 4 K plates + shields
[b] Still, HEX, MC plates + shields
[c] Loads attached at the end of the bars
[d] Removed in Run 1.3
[e] 1 port missing
[f] 1 part over 4 installed

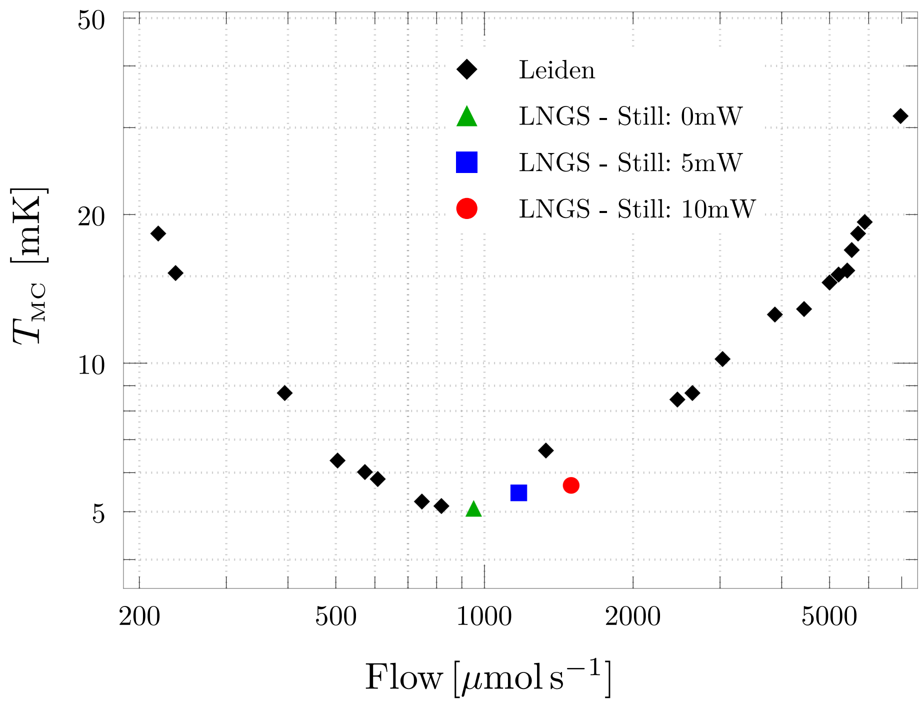

FIG. 5.3: Dependence of the MC temperature on the mixture flow. The black markers refer to the test performed at Leiden (August 2011), while the colored ones to the test at LNGS inside a test cryostat (April 2013).

5.2 DU characterization

The CUORE DU has to guarantee the achievement and maintain of cryostat inner stage temperatures, thus allowing detector operation at 8 mK (see the discussion in Sec. 4.5.3). The value of 6 mK in the DU design specifications was considered an adequate target for the base temperature, considering the different arrangements inside the test cryostat and inside the complete CUORE cryostat.

Given the CUORE cryostat configuration in terms of thermal loads at the various stages, the required cooling power for the DU were 3 mW at the Still stage, 125 μW at the HEX stage and 4 μW at the MC stage (at 10 mK).

Several tests were performed at the construction site (Leiden, The Netherlands) in order to characterize the DU in terms of cooling power and mixture flow. The characterization was then repeated after the arrival of the DU at LNGS. The DU test cryostat was installed at the ground floor of the CUORE hut, provided with 2 of the CUORE PTs and connected to the gas handling system.

5.2.1 Optimal flow

In a DR, the mixture flow depends on three factors:

- the pumping throughput on the Still;
- power dissipated at the Still stage (either by parasitic heat loads or by injection

through a heater);

- the surface of the Still.

Since the first two factors are fixed once the DR is assembled (the second being determined by the gas handling system), the study of the flow was done by injecting different powers on the Still and monitoring the MC temperature. The result is shown in Fig. 5.3 (black markers). The optimal value was found to be $\sim (800 - 1000)\,\mu\mathrm{mol\,s^{-1}}$.

It has to be noted that the plot refers to the "bare" DU. Once this will be inserted in the CUORE cryostat, due to the much larger complexity, the presence of additional dissipated powers will require higher flows for compensation (see Sec. 5.10.2).

5.2.2 Cooling power

The cooling power at a certain temperature coincides with the power that has to be dissipated on the MC stage in order to stabilize it at that temperature. After setting a reasonable value for the circulation flow, it is thus possible to verify the effective cooling power of the DU by directly injecting power on the MC plate through a heater. The result of the characterization at Leiden is shown in the upper panel of Fig. 5.4. The obtained values were 2 mW at 100 mK (3 mW at 123 mK) and 4 µW at 10 mK, larger than the requested ones.

At LNGS, more series were recorded for different mixture flows close to the optimal range already identified. In the lower panel of Fig. 5.4, a zoomed view of the $\dot{Q}$ *vs.* T_{MC} plot with the new points is presented. The new performance of the DU was compatible with the previous one when no power was injected on the Still, while it improved to $\sim 6\,\mu\mathrm{W}$ at 10 mK with a mixture flow of $1500\,\mu\mathrm{mol\,s^{-1}}$.

It can be seen that adding power on the Still, on the one side, raises the minimum achievable temperature. On the other, the circulation at higher flows is associated to a higher cooling power. The values for no power injected on the MC are also added in the plot of Fig. 5.3, showing compatibility with the measurement at Leiden.

5.3 Run 0.1

The commissioning of the CUORE cryostat at LNGS began with the assembly of the 4 K outer cryostat. The goal of this first phase was to verify the apparatus performance both in terms of vacuum and achievable temperature. First, the 300 K, 40 K and 4 K plates were installed. An extensive leak check campaign was needed in order to test all the vacuum seals of the several feedthroughs at the level of OVC (o-rings) and IVC (indium sealings). Then, the corresponding vessels were also installed. The success of the subsequent vacuum tightness tests allowed to proceed with a first cool down to 4 K with the "not loaded" cryostat.

The progress of the Run 0.1 cool down is shown in the upper plot of Fig. 5.5, where the plate temperatures are taken as a reference (a similar behavior can be identified for all

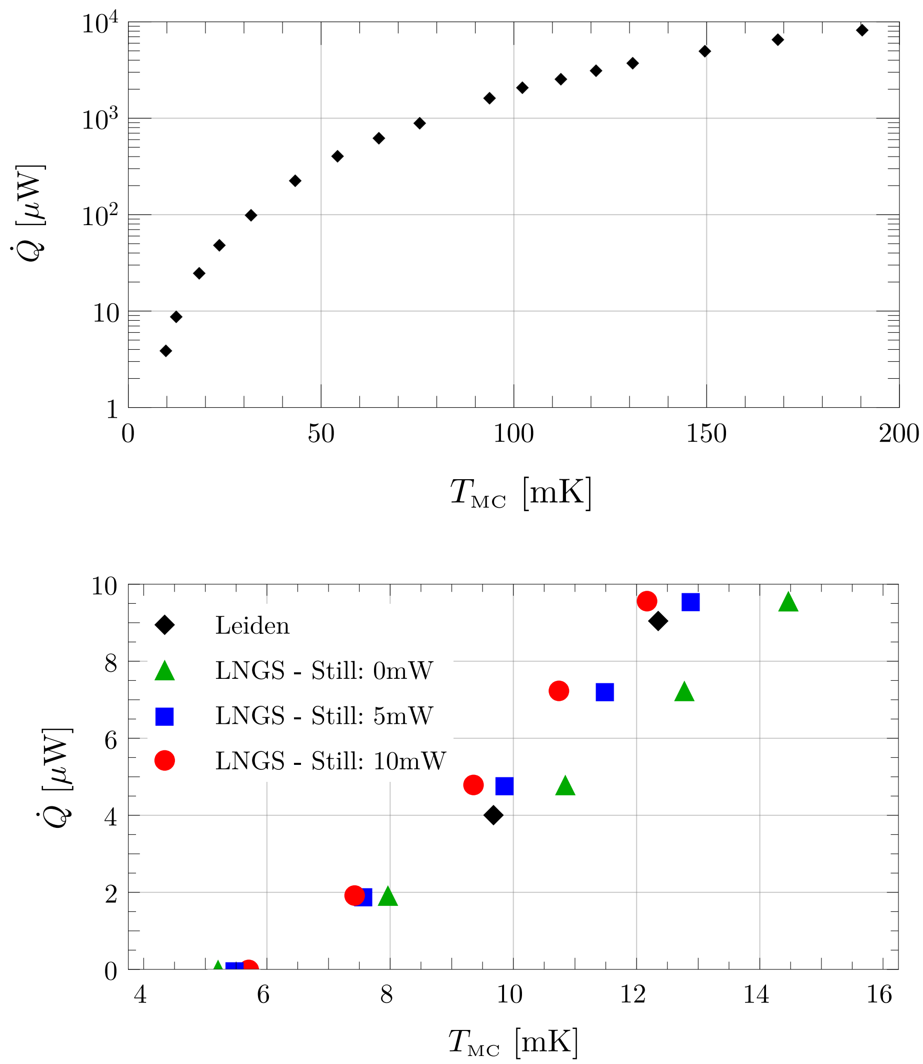

FIG. 5.4: DU cooling power as a function of the MC temperature. (Top) Test performed at Leiden. (Bottom) Zoom of the lowest temperature region with the inclusion of LNGS test results. It can be seen the latter results show a better performance of the DU for increased values of the flow.

the elements thermalizing at the same temperatures). As it can be seen from the figure, the initial temperature drop is much steeper for the 40 K plate. This is due to the smaller mass at the 40 K stage and to the higher cooling power of the PT first stage with respect to the second. Then, the slope flattens some tens of Kelvin below $\sim$ 100 K. Instead, 4 K stage cooling proceeds more slowly and "recovers" in the final part, after matching the 40 K stage temperature.

The cryostat was initially provided with 3 PTs, but only 2 were operational, due to problems on the third compressor. Therefore, the cool down was proceeding slowly and, after about 13 days since its start, the system was stabilizing at the temperatures of $\sim$ 55 K and 7 K for the 40 K and 4 K stages, respectively.[2] The situation improved by refilling the

[2]At the end of a cool down, each temperature can be assumed to be homogeneous over the whole plate + vessel system, with the maximum gradient expected to be $\lesssim 0.2$ K. During the cool down, instead,

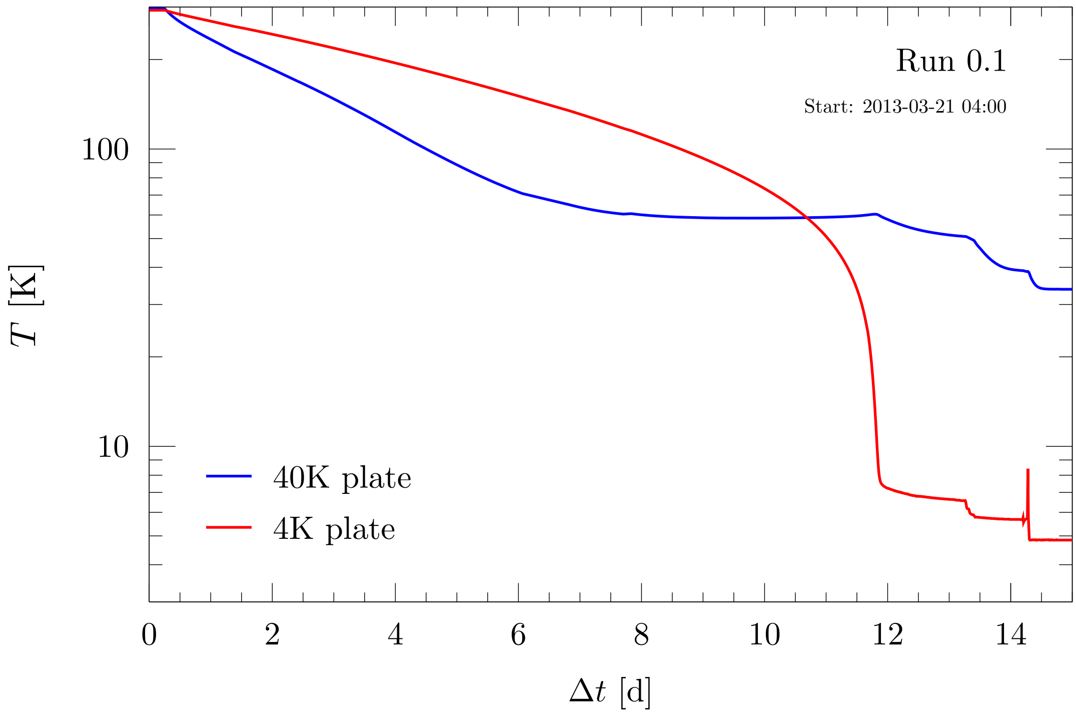

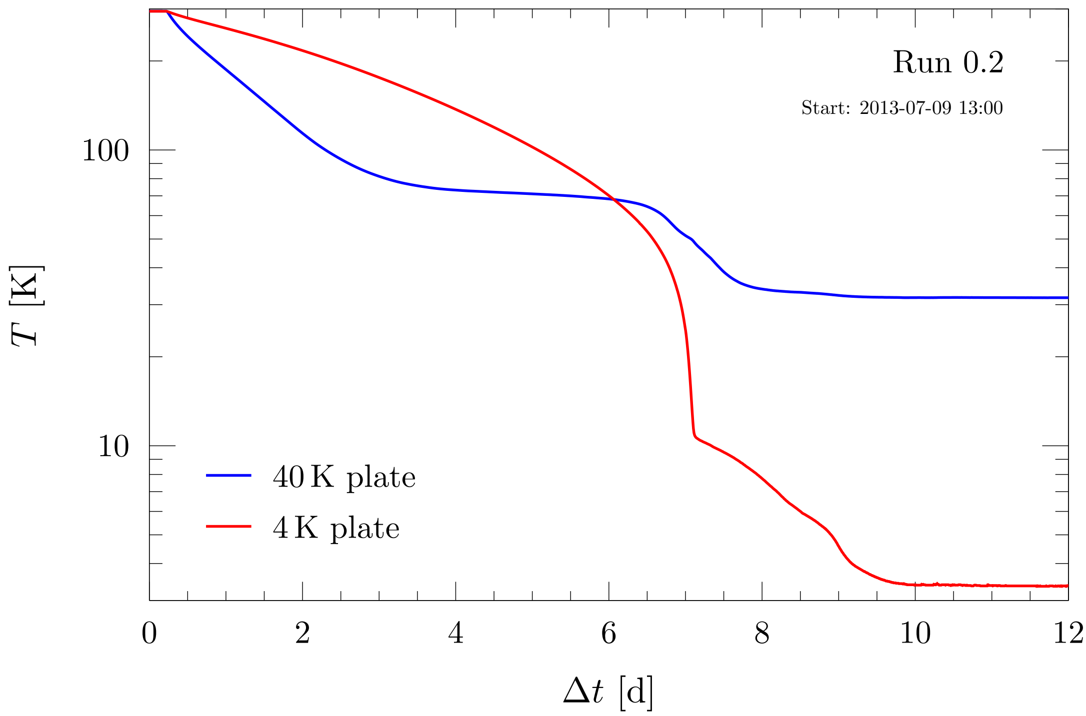

FIG. 5.5: Temperatures of the 40 K and 4 K stages during the cool down of the 4 K outer cryostat. (Top) Run 0.1: in about 14 days the final values of 33.5 K and 5 K are reached at the 40 K and 4 K stages, respectively. The bump on day 13 is due to the He refill of the 2 PTs, while the spike on day 14 to the turning on of the third PT. (Bottom) Run 0.2: in 12 days the final temperatures of 32 K and 3.4 K are reached at the 40 K and 4 K stages, respectively. Below $\sim$ 10 K (after day 7), the cool down is driven by the stainless steel mass, due to the much higher heat capacity with respect to copper.

PTs to the optimal pressure (see App. A.2), but still the foreseen final temperatures were too high ($\sim$ 38 K and 5.7 K) due to the presence of an inactive PT. In fact, by turning also the third PT on (after the compressor repair) the situation improved. The effect is clearly visible in the plot (it corresponds to the spike on day 14). In about 14 days the final temperatures of 33.5 K and 4.8 K were reached at the 40 K and 4 K stages, respectively.

The achieved temperatures were actually higher than what expected from simulations. This could either mean the presence of incorrect assumptions in the modeling or the presence of an unexpected large power dissipation. The finding, during the cryostat opening, of 2 WT port baffles fallen on the 4 K plate suggested that the latter hypothesis could indeed be correct.[3]

5.4 Run 0.2

The preparation for a second cool down began immediately after the conclusion of Run 0.1. The baffles were repaired and new monitoring thermometers were added to the system. In the meanwhile, a "dummy" load constituted by $\sim$ 100 kg of stainless steel was installed below the 4 K plate in order to perform some load tests on the DCS.

The progress of the Run 0.2 cool down (still with 3 PTs) is shown in the lower plot of Fig. 5.5. From a comparison with the previous run, it can be seen that almost half of the time is needed for the system to reach $\sim$ 70 K, where the temperature is the same for both the stages. Instead, the final part of the 4 K stage cool down (below $\sim$ 10 K) is driven by the stainless steel mass, due to the much higher heat capacity with respect to copper. In 12 days since the start of the cool down, the final temperatures of 32 K and 3.4 K are reached at the 40 K and 4 K stages, respectively. These values are compatible with what expected.

The recorded temperature were compliant with the requirements and the cool down could be considered a successful test of the 4 K outer cryostat performance. It was thus decided to proceed with the installation of the inner plates and vessels.

5.5 Run 1.1

Some major intervention, i. e. the removal of the 40 K plate, that needed to undergo a new cleaning cycle, the insertion of the last WT tube and the addition of the FCS steel tubes (refer to Fig. 4.9), required the disassembly and reassembly of the of outer cryostat. Anyway, with the successful installation of the Still, 50 mK and MC plates and vessels and the insertion of the DU, it was possible to prepare the first cold run with the "complete"

the temperatures on the single stages can significantly vary. Gradients up to almost 40 K were measured between the bottom of the 40 K vessel and the corresponding plate.

[3]Since the Fischer box and all the detector wiring were not present, temporary baffles had been inserted in the WT tubes. These consisted in series of 6 thin aluminum disks slightly smaller than tube section hanging from above by means 3 wires anchored to the tube blind flanges (at the level of the 300 K plate).

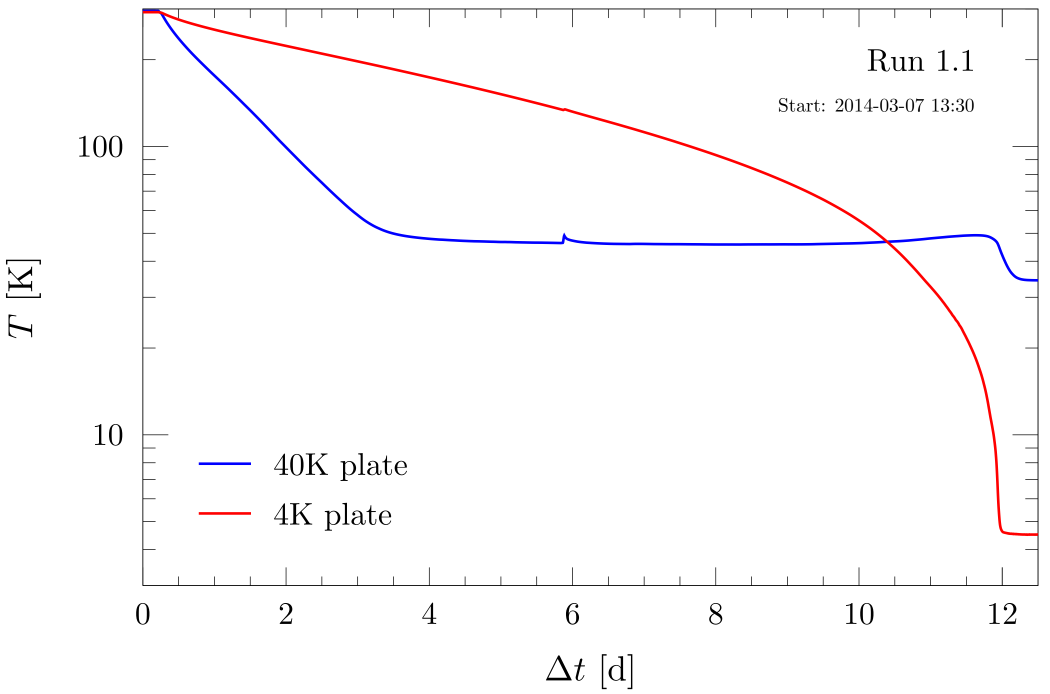

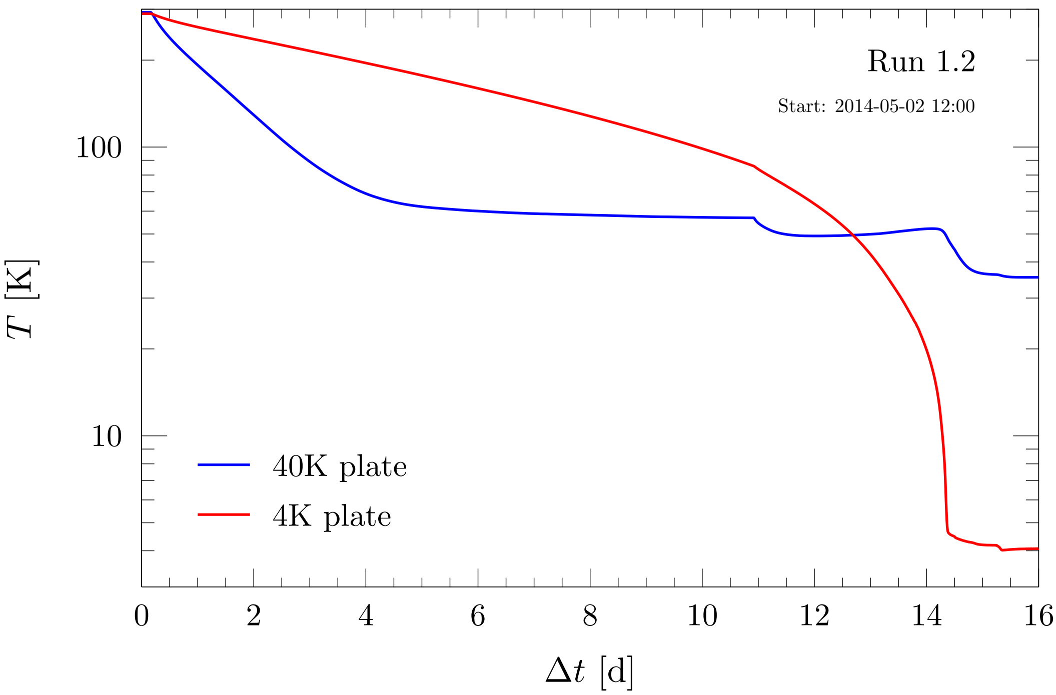

FIG. 5.6: Temperatures of the 40 K and 4 K stages during the first two cool down with the complete cryostat. (Top) Run 1.1: in about 12 days the final values of 35 K and 4.5 K are reached at the 40 K and 4 K stages, respectively. The bump on day 6 is due to the introduction of additional exchange gas in the IVC. (Bottom) Run 1.2: in about 16 days the temperatures of 35.5 K and 4.1 K are reached at the 40 K and 4 K stages, respectively. Actually, after a few more days of system optimization, the stable temperatures of 34.5 K and 3.9 K are reached. The bump on day 11 is due to the He refill of the PTs.

cryostat. The cryostat was provided with 4 of the 5 PTs, since the fifth one was sent back to the Cryomech for repair after experiencing some problems while testing it.

The progress of the cool down of Run 1.1 is shown in the upper plot of Fig. 5.6. The 40 K and 4 K stages thermalized at the temperatures of 35 K and 4.5 K after about 12 days since PTs were turned on. Unexpected behaviors and evidences of power dissipation by parasitic sources at the different thermal stages were emerging from the temperature data analysis.

A first series of attempts was performed in order to try to solve the radiation problems but, unfortunately, without success. Anyway, the estimated injected power was low enough to allow the circulation of the mixture. The DU was turned on about one week after the reach of the PT base temperature. The initial temperature of the inner stages were therefore 14.5 K at the Still stage, 9 K at the HEX stage and 6.5 K at the MC stage. The DU performed very well and, after one day of circulation (first ^{4}He and then ^{3}He), the temperatures inside the IVC had already stabilized. However, the flow rate was very high (of the order of 3000 μmol s^{-1}) and thus the final values were 1.05 K at the Still stage, 93 mK at the HEX stage and 14 mK at the MC stage. Therefore, the following days were again devoted to the solving of the power dissipation problems, but no relevant change in the base temperature could be observed. Only with the single shot during the mixture recovery, the MC temperature could reach $\sim$ 10.2 mK (the Still being at 800 mK).

5.5.1 Power dissipation problems

Already during the cool down, a first problem was identified in a bad thermalization of the SS bars at the level of the 40 K stage (refer to the figure in Table 4.3). As it is shown in the upper plot of Fig. 5.7, a temperature compatible with that of the 40 K plate was reached only by the SS 1 bar, while SS 2 and SS 3 stabilized at the much higher temperatures of 84 and 48 K, respectively. In particular, in the case of the SS 2 bar, the bump on the temperature plot was clearly identifiable with the detachment of the bar thermalizer.

Furthermore, a sudden rise in temperature was observed at all the inner stages once the exchange gas was pumped from the IVC (lower plot in Fig. 5.7). Instead, the same was not observed on the 4 K plate, whose temperature remained stably at $\sim$ 4.5 K since the end of the cool down. Initially, this was thought to be due to a not complete thermalization of the CuBe gimbals holding the Still plate. However, the exact same behavior was observed also after new exchange gas was injected in the IVC and pumped, indicating that the power leak was not due to some heat load from a not well thermalized part, but rather to a stable power injection from the outer stages. In fact, if the former hypothesis was correct, no temperature rise should have reappeared. Or, at least, a much smoother one, which should have anyway saturated and begun to cool down again. Therefore, this behavior was a clear indication of the presence of radiation and of unaccounted conductances between the Still and the higher temperature stages. An estimate of the power dissipation gave values as high as $\sim$ 100 mW (see App. A.7.1).

The possible sources of radiation were identified in the IVC, FCS and WT ports, all

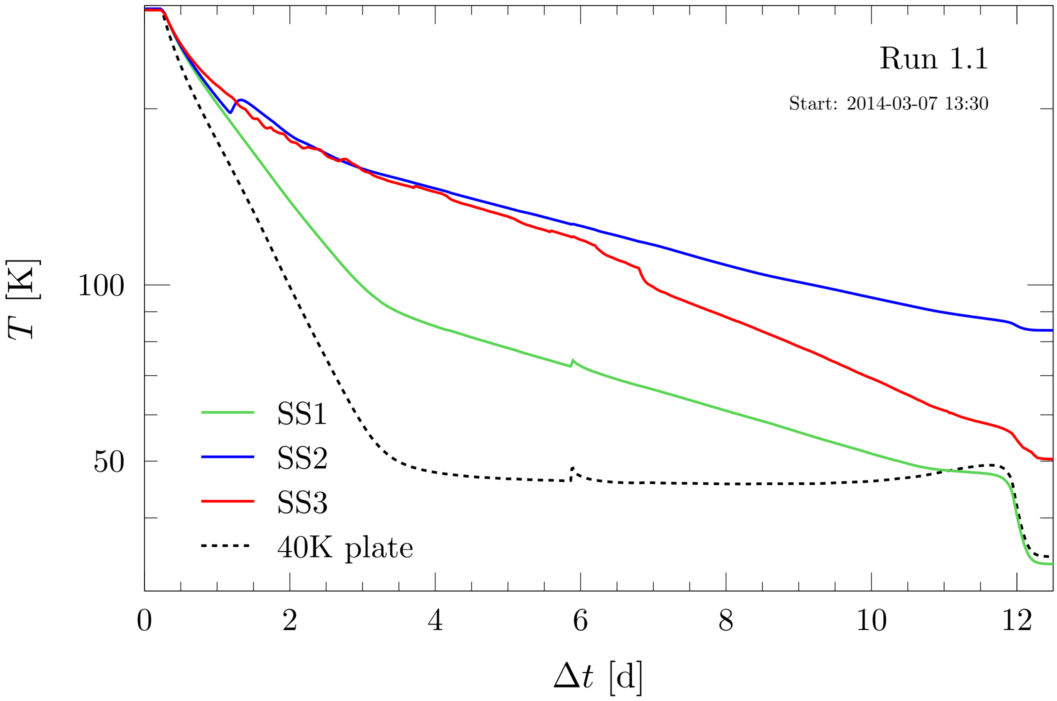

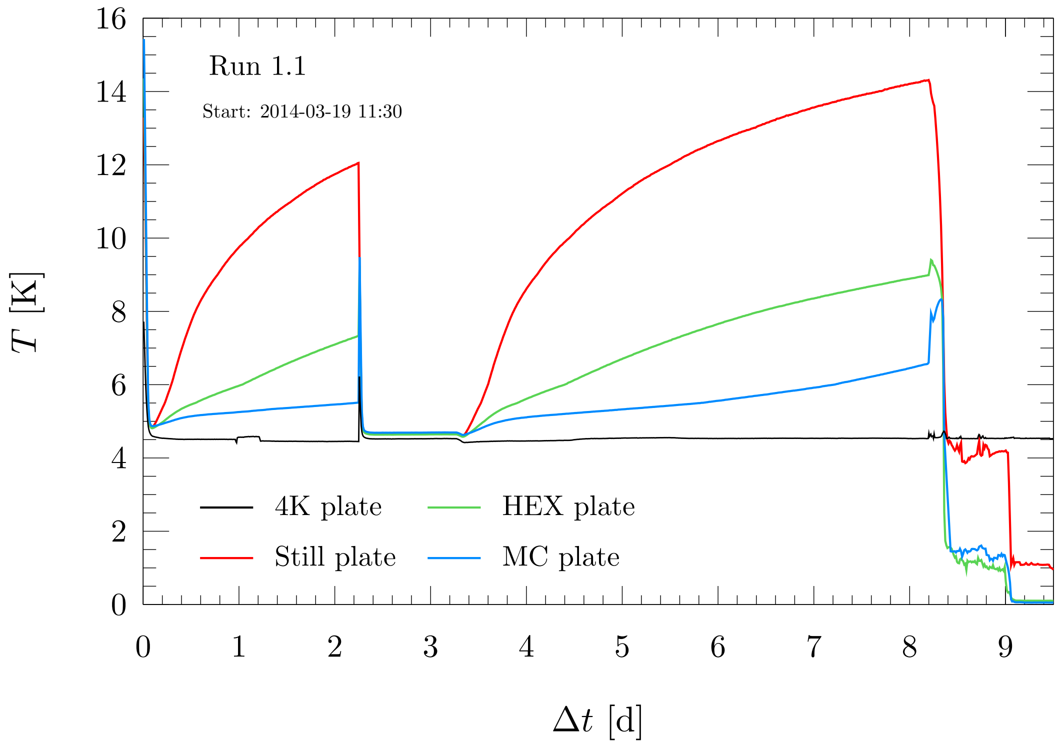

FIG. 5.7: Problems encountered during Run 1.1. (Top) Bad thermalization of the SS bars at the level of the 40 K stage. The bump on the SS 2 temperature plot is due to a partial detachment of the bar thermalizer. (Bottom) IVC stage temperatures in the final part of the cool down. The temperature rise is caused by power dissipation. The drop between the two bumps is due to the introduction of exchange gas (~ 1 mbar at T_{amb}) in the IVC. The one after the second bump is due to the start of the mixture circulation.

elements that could be creating a line of sight between the 300 K and the Still plate (refer to Fig.4.8).[4] Another risk was that the LS and DS bars, at the time unloaded and arriving at the level of the Still plate (refer to Fig. 4.2) were not properly thermalizing at the various stages, since the thermalizers were designed to work with the bars in traction.

As an attempt of solution that could be performed without completely warming up the cryostat, temporary baffles were inserted inside the FCS tubes. These consisted into wires with ~ 15 foosball balls strung together (he balls had previously been chamfered to fit the tubes and coated with reflective paint). The cryostat temperature was brought to about $(35-45)$ K by turning off the PTs and the IVC was put in overpressure in He (with respect to ambient pressure) to prevent any air return. Unfortunately, no change in the inner stage temperatures was observed, thus indicating that either the FCS was not a major source of power dissipation or the baffles were not effectively working.

5.6 Run 1.2

Since nothing else could be done with the closed cryostat, it was decided to warm up and check all the thermalizations in the outer stages (outside the IVC). As expected, some problems were found with the SS bar thermalizers at the 40 K stage. All the soldering of the A and SS bar thermalizations (between the bars and the thermalizers) were remade both at the 40 K and the 4 K stages.[5]

The cool down of Run1.2 began immediately after the completion of the various operations. Its progress is shown in the lower plot of Fig. 5.6. In about 16 days, the temperatures of 35.5 K and 4.1 K were reached at the 40 K and 4 K stages, respectively. A few days of optimization of the cryogenics system allowed to further decrease the temperatures down to stable 34.5 K and 3.9 K, respectively. These values proved the effectiveness of the performed actions. However, they also indicated part of the problems still needed to be addressed.

In fact, after the removal of the exchange gas, the temperature rise at the Still level was observed again, reaching 15 K in two weeks. This confirmed that the best candidate to explain the injected power were indeed conductances and thermal radiation.

During the preparation of the cool down, a diode was installed on one of the DS bars just outside the IVC. Its temperature was thus expected to be close to that of the 4 K plate. Instead, it stabilized at ~ 12.5 K at the end of the cool down. By assuming a similar behavior for all the DS and LS bars, all the suspensions together could thus represent a significant source of power dissipation, with the bellows radiating on the Still stage.[6]

To test the hypothesis that the IVC port could represent a source of radiation (it might constitute a line of sight between the 300 K and the Still plates), the IVC port was gently cooled with liquid nitrogen at the level of the 300 K plate. A temperature close to

[4] The effectiveness of the WT tube baffles was not sure and while no radiation baffles were present inside the tubes.

[5] Given the complex cryostat configuration, in the case of the SS bar thermalizers at the 4 K stage, indium was used instead of solder.

[6] This hypothesis will be later more deeply investigated (see Sec. 5.8).

-13° C was reached at the entrance of the IVC port, while the cryostat was still at the PT base temperature. Since the radiant emittance is proportional to the fourth power of the temperature, a the effect of the cooling was expected to be visible in case the hypothesis was correct. However, no significant change in temperature was observed either at the 4 K or at the Still stages.

In the end, seen the analogy with Run 1.1, it was decided not to start the cool down with the DU.

5.7 Run 1.3

After the second failed attempt to solve the power dissipation problem, but with more information acquired, it was decided to address the issue of thermal radiation in a more drastic way. A series of measures was thus adopted in order to deal with all the possible sources, namely

- permanent baffles were installed inside the FCS steel tubes (see Sec. 4.4) while the design of the baffles inside the WT ports was improved;[7]
- the design of the DCS parts inside and below the IVC port was changed, helping in blocking the radiation transmission;
- every through-hole on the inner plates was covered with copper tape;
- the last steel segments of each LS and DS bar was removed (refer to Fig. 4.2) and the extremities of the bellows were connected to the 4 K plate with copper wires, thus creating conductive links.

Furthermore, the number of thermometers was increased at all the stages to allow for a more complete diagnostic and a deeper understanding of the cryostat behavior and two radiation sensors were installed under the 4 K and Still plates.[8]

The cool down of Run 1.3 could start also in this case once all the operations were concluded. Its progress is shown in the upper plot of Fig. 5.8. To simulate the effect of the FCS, 650 mbar of He at 185 K ($\sim$ 1020 mbar at T_{amb}) were introduced inside the IVC as exchange gas and a refill to 630 mbar at 95 K ($\sim$ 1920 mbar at T_{amb}) was later performed (the effects are clearly visible in the figure). The IVC-to-OVC leak rate, constantly monitored, reached the highest value of $\sim 10^{-3}\,\mathrm{mbar\,l\,s^{-1}}$ at the moment of the refill. This indicated the presence of a leak between the two vacuum chambers. [9] Anyway, the cool

[7] The new design of the WT tube baffles was similar to that of the FCS tube ones. In this case, the original aluminum disks were covered with Kapton (looking down) and aluminized mylar (looking up) and the bars were anchored to the blind flanges on the 300 K plate.

[8] Each radiation sensor consists of a "bare" RuO_2 thermometer glued on a copper foil ($\sim 10\,\mathrm{cm^2}$) which is weakly linked to a surface. In presence of power dissipation, radiation becomes the dominant thermalization channel. A heater is also glued on the foil to allow a quantitative estimate of the dissipated power.

[9] A leak between IVC and OVC had already observed during the previous runs. Such a leak can be a problem during the cool down phase since it directly links the IVC the external world, thus dissipating a lot of power. However, once the cryostat is cold (if the cool down can anyway proceed), the effect of the leak is practically irrelevant because now there is no more gas He circulating.

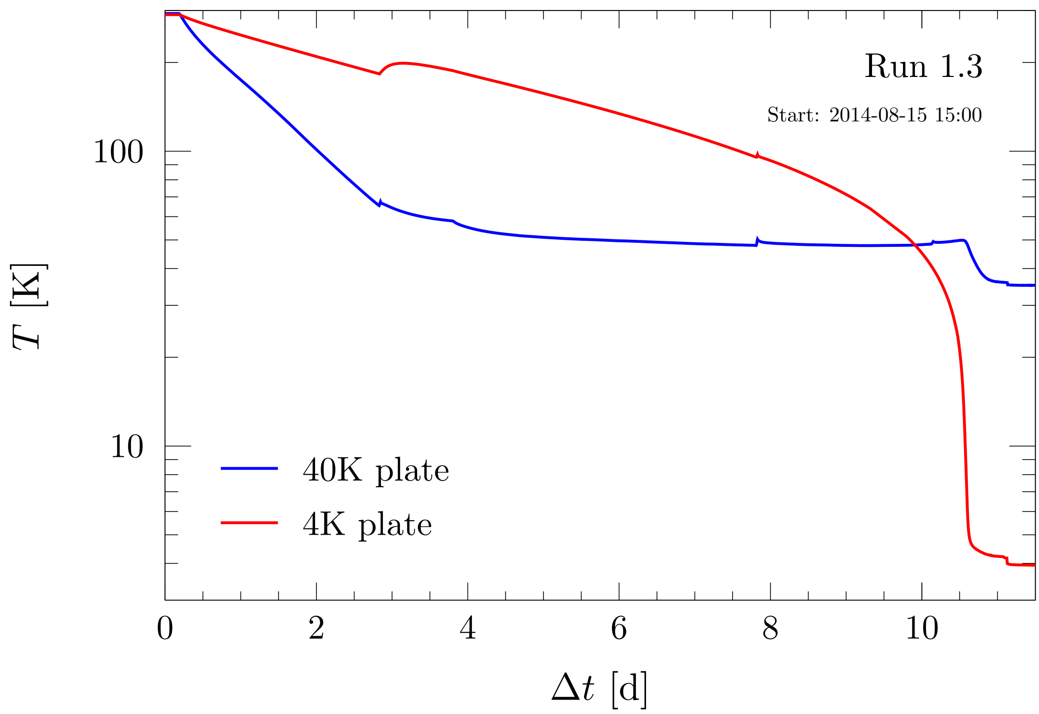

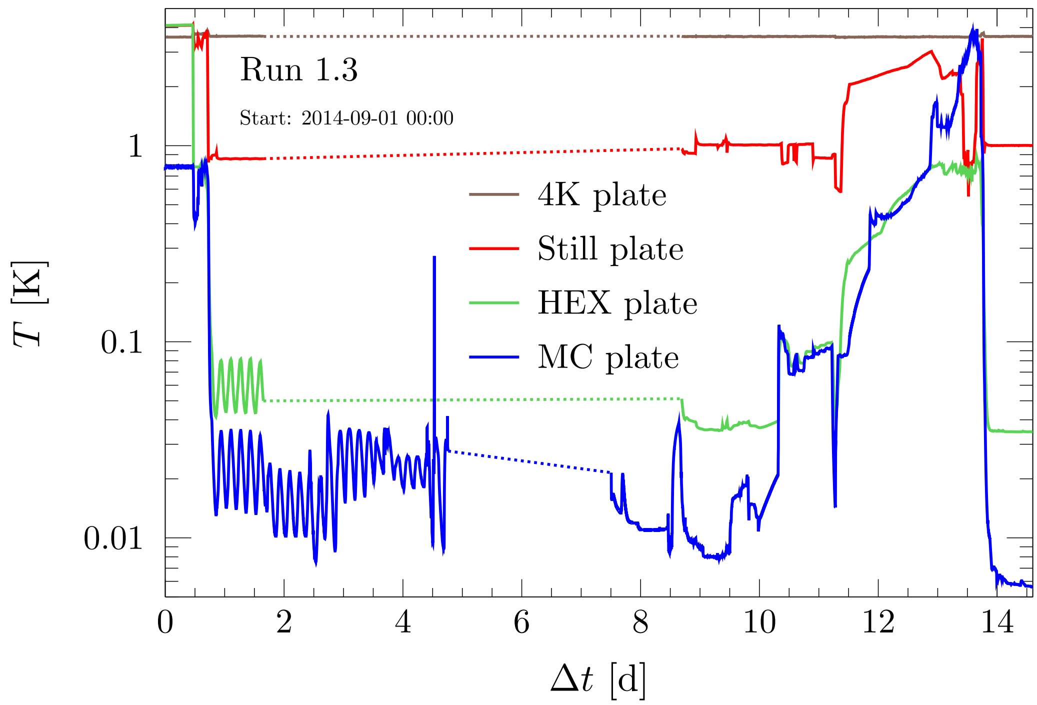

FIG. 5.8: Cool down of Run 1.3. (Top) Temperatures of the 40 K and 4 K stages: the final values of 35.3 K and 4.0 K are reached in $\sim$ 11 days since the PTs were turned on. After a few more days of system optimization, the final stable temperatures are 34.9 K and 3.8 K. The bump on day 3 is due to the introduction of $\sim$ 650 mbar of exchange gas inside the IVC to simulate the effect of the FCS. The effect of a gas refill on day 8 is also visible. (Bottom) IVC stage temperatures during the circulation with the DU. Initial noise problems related to mechanical vibrations prevent to cool down to base temperature (see the discussion in the text). The final temperatures of 1 K, 35 mK and 6 mK are reached after one day since the beginning of a second circulation. The dotted lines cover the period of unplugged sensors.

down proceeded regularly, showing that such a leak did not constitute an issue. After ~ 11 days since the PTs were turned on, the 40 K and 4 K stages reached 35 K and 4.1 K, respectively. In a few more days of optimization of the cryogenics system, these values were further decreased down to stable 34.5 K and 3.9 K.

These stable temperatures were very encouraging. In particular, the values for the radiation sensors were perfectly compatible with those of the corresponding plates. More important, no significant warm up of the inner stages was observed after the removal of the IVC exchange gas, showing that the problem of power dissipation had been mostly cured. In fact, the total dissipated power was estimated to be a fraction of mW (see App. A.7.1). Therefore, it could be possible to proceed with the circulation with the DU. As it can be seen from the lower plot in the figure, the temperature drop is sudden and very steep and temperatures closed to the expected ones were indeed reached in less than one day. However, the same plot also shows a new encountered problem: the temperatures inside the IVC begin to oscillate once the system approaches base temperature. To understand the causes of such a behavior in order to adopt appropriate countermeasures took a while (see Sec. 5.7.1). Anyway, in about two weeks it was possible to start to circulate again (the mixture was collected to facilitate part of the operations). This time the cool down proceeded as expected. The mixture flow was slightly high, 1550 μmol s^{-1}, but the stable values of 1 K, 35 mK and 6 mK were obtained in about one day for the Still, HEX and MC stages, respectively. A check of the base temperature stability could thus be performed (see Sec. 5.7.2).

5.7.1 Temperature oscillations

By lowering the minimum temperature, the system became sensitive to much smaller power dissipations. This allowed a new problem to show up, i. e. the lowest temperatures exhibited an oscillatory behaviour at the HEX, MC and, to a lesser extent, at the Still level.[10] The temperature variations were due to mechanical vibrations inducing power dissipations at the various cold stages through micro-frictions.

Therefore, a campaign of vibration measurements with dedicated diagnostic sensors was performed. In particular, a set of 3 (movable) accelerometers was placed on the 300 K plate and one of 3 geophones had been previously installed on the 4 K plate, thus allowing a complete study along the radial, tangential and transverse directions.[11] The measurements were carried out in different cryostat configurations, namely with the 300 K free or anchored to the MSP and with all, part or none of the PTs switched on.[12]

The main conclusion was that the PTs are the cause of the temperature oscillations, the physical sources of vibrations generated by the He pressure waves, the compressors

[10] Later, a re-analysis of the previous runs allowed to identify the same problem also in those cases, even if in a less significant way.

[11] Actually, one of the geophones (that along the radial direction) broke during the measurements.

[12] Some of the results is reported in Ref. [171]. However, part of the conclusion, i. e. that the situation in terms of vibrations improves with the free cryostat, is incorrect since the role of the flexlines in transmitting the vibrations was not considered.

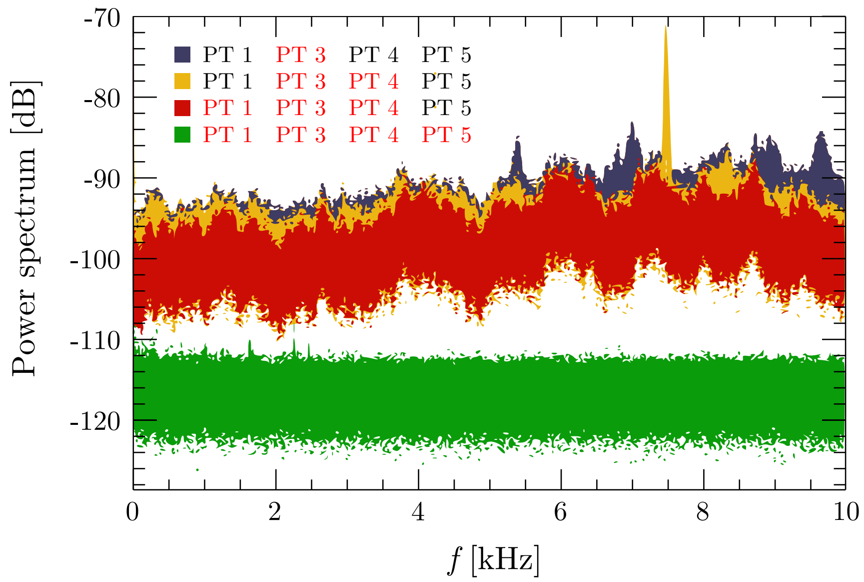

FIG. 5.9: Noise power spectra of the transverse oscillations acquired with the accelerometer installed on the 300 K plate in different PT configurations. The black (red) color refers to the switched on (off) PTs.

and the rotating valves (see the discussion in Sec. 4.5.2). In Fig. 5.9, the study of the transverse oscillations is shown. In particular, the noise power spectra acquired with the corresponding accelerometer on the 300 K plate are plotted. As it can be seen, the ratio between the spectra in case of switched on and switched off PTs is about 10. Moreover, it was also observed that, as it happens for the cooling power (see App. A.2), the single PT contributions to the total noise is not equivalent, despite all the PTs are the same model.

The cryostat support structure is designed to ideally decouple the cryostat from the rest of the world, so that this is protected from any external noise source that could interfere with the running measurements. However, the same choice is not effective if the noise is directly generated on or inside the cryostat. On the contrary, in this case, to reduce the amount of vibrations one has to make the cryostat structure as rigid as possible and to re-couple it with the external world in order to damp the movements.

This idea proved to work. As a matter of fact, by completely blocking the 300 K plate, the temperature oscillations very dramatically suppressed, as it can be seen from the lower plot of Fig. 5.8 (the operation was done between days 6 and 7). This allowed to reach stable value for the base temperatures.

5.7.2 Base temperature stability

The minimum temperature registered during the DU construction and test phases was already lower the accepted value of 6 mK (see Fig. 5.4). However, the compliance to the base temperature requirement had to be subsequently tested again in the CUORE cryostat.

The monitoring of the MC temperature at a few mK was performed through the CMN thermometer (see App. A.5.1). A period of no intervention on the cryostat allowed the

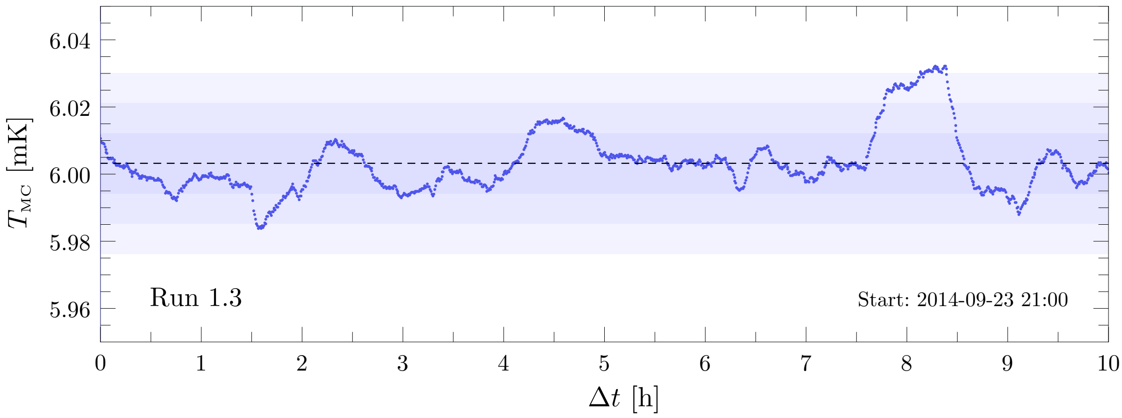

FIG. 5.10: Base temperature temporal evolution over a 10 hour period with "undisturbed" cryostat during Run 1.3. The MC temperature is (6.003 ± 0.009) mK. The dashed line indicates the average value, while the shaded regions correspond to 1σ, 2σ and 3σ intervals.

system to reach its most stable configuration. The MC temperature temporal evolution for a 10 hour interval was studied as a reference for the long time stability. The obtained plot is shown in Fig. 5.10. The average value in this interval is (6.003 ± 0.009) mK, with almost no deviation greater than 3σ. This result is compliant with the DU design specification. It also allowed to consider Run 1.3 (and thus the first phase of the cryostat commissioning) successfully completed.

5.8 Run 2

With the successful conclusion of Run 1.3, it was possible to proceed with the next step of the cryostat commissioning, namely the installation of the detector wiring.

The wiring structure and a proper thermalization system had already been identified and designed during precedent studies (see Sec. 5.8.1). Therefore, the installation operations and the related checks were successfully completed in a short time.

However, before starting with the new cool down, other upgrades of the cryogenic system were implemented. In particular, a major renewal interested the thermometry for the cryostat diagnostic, since during Run 1.3 a significant fraction of the channel had been either lost during the cool down or presented a noisy readout due to loose connections. All the sensors were removed and individually checked and the PT-100 thermometers were substituted with the more reliable silicon diodes. Moreover, new thermalizers consisting in threaded copper columns with embedded pins for the connection of the thermometer with the readout wiring were installed on the plates. These allowed for an easier plug/unplug of the sensors, thus reducing the possibility of damaging both the same sensors and the wires.

Another change in the design interested the mixture condensing circuit. In the test cryostat configuration, after exiting the DU below the 40 K plate, one half of each original line was thermalizing on 2 different PTs (see Sec. 4.5.3). Within the idea of keeping 2 interchangeable lines (one spare of the other), the system was reconfigured so that now

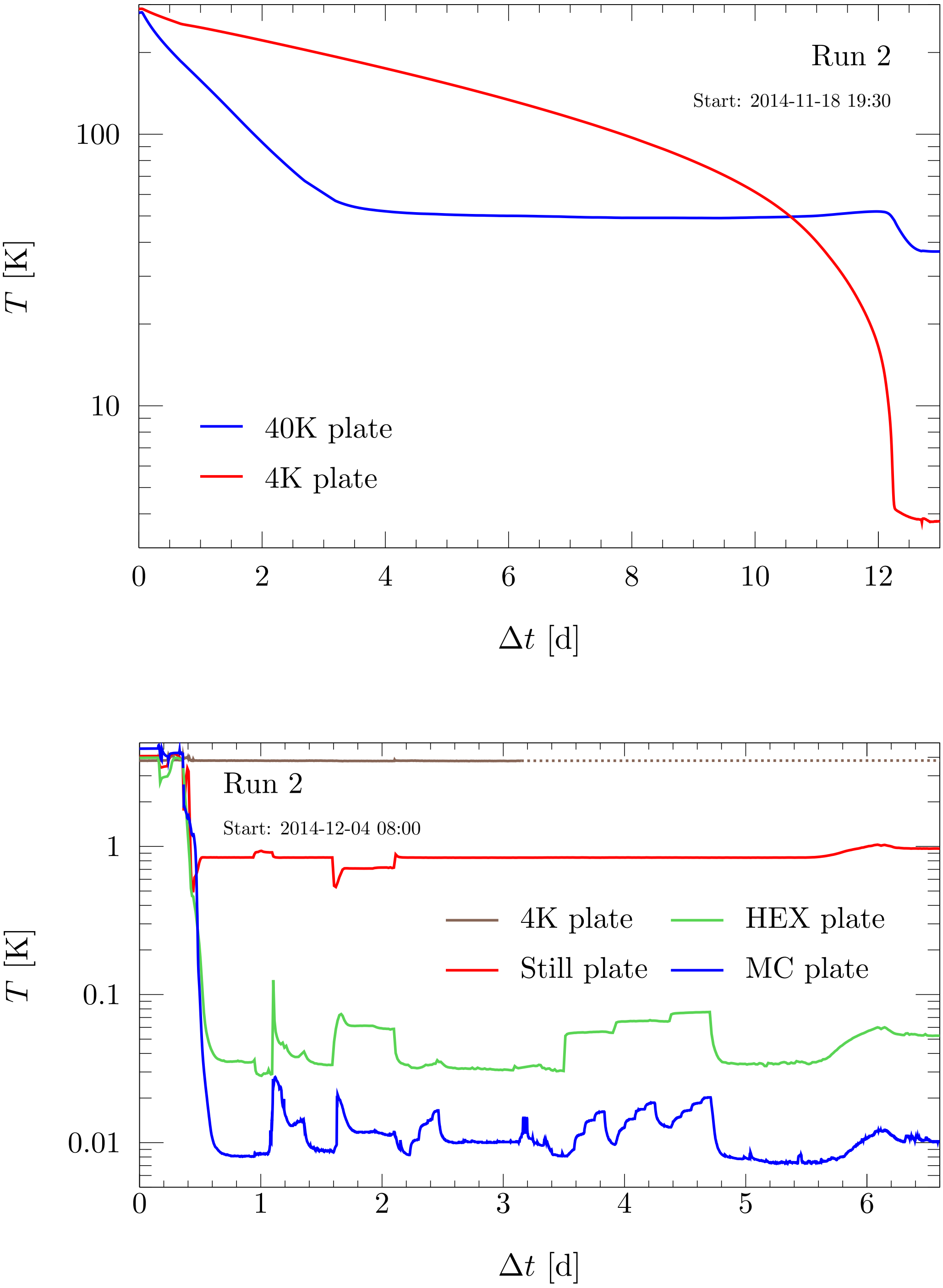

FIG. 5.11: Cool down of Run 2. (Top) Temperatures of the 40 K and 4 K stages: the final values of 36.5 K and 3.8 K are reached in about 12 days since the PTs were turned on. (Bottom) Inner stage temperatures during the circulation with the DU. In less than one day, the temperatures of 0.84 K, 35 mK and 8.1 mK are reached at the Still, HEX and MC stages, respectively. The regular structure observables since day 1 are due to DU characterization tests. The lowest base temperature of 7.3 mK is achieved on day 5. The bump at the Still and, consequently, at the HEX and MC stages around day 6 is an effect of the superleak (the He film reaches the Still plate). The dotted line covers the period of unplugged sensor.

the two halves of the original line thermalized on the same PT. In this way, the failure of one of the two PT would not imply the impossibility of running the DU, and therefore the need to stop the measurement.

To study the issue of power dissipation inside the IVC, it was was decided to investigate the LS and DS bars as power sources. As already mentioned, there was the possibility that the thermalizer at the 4 K and 40 K stages were not working effectively (see Sec. 5.5.1). Therefore it was decided to attach different masses (copper disks) to the end of the LS bellows and to compare the effect of the bar traction on the temperatures.

Finally, with the installation of the wiring, and thus with the possibility of operating a bolometric detector inside the CUORE cryostat, the Mini-Tower test detector was positioned under the MC plate. The expectations of observing signals by physical event were low, since the MC plate is coupled to the cryostat structure and thus very noisy in terms of vibrations. However, this test could give a first series of hints about the behavior and performance of the NTD sensors.

The cool down of Run 2 proceeded smoothly and it took $\sim$ 13 days to reach the stable temperatures of 36.5 K and 3.8 K for the 40 K and the 4 K stages, respectively. Its progress is shown in the upper plot of Fig. 5.11. After a few days it was possible to start the circulation. In less than one day, stable temperatures were reached at all the inner stages. The final values of 0.84 K and 35 mK for the Still and the HEX, respectively, while a base temperature of 7.3 mK was maintained for $\sim$ 12 hours with a mixture flow of $\sim 1260\,\mu\mathrm{mol\,s^{-1}}$.

The impossibility of going further down in temperature, even with the high flow, was an indication of power dissipation at the MC stage. However, soon the effects of a superleak inside the DU had clearly become visible (see Sec. 5.8.2). If, on the one side, this represented the emergence of a new problem, on the other it also meant that the same leak could likely be the cause for the high base temperature. Indeed, this was later confirmed to be the case and, during Run 4, DU performance still compliant with the original requirements were achieved (see Sec. 5.10.2).

Regarding the cryostat diagnostic, precious information were obtained from the studies of power dissipation. By placing two thermometers on one of the FCS S-tube (refer to Fig. 4.9), it was discovered that the temperatures at the end of the cool down are very high. In particular, the values of 285 K and 282 K were obtained for the first (bottom) and second (top) bend, respectively. This showed that the contribution to the total power dissipation inside the IVC coming from the two steel tubes was relevant, before the insertion of appropriate baffles. Furthermore, the monitoring of the LS and DS temperatures at the various stages confirmed that, without the masses they were suppose to hold, also these elements were contributing to the total dissipated power, although not in a predominant way (see App. A.7.2).

Despite the issue of the superleak, Run 2 could be considered successful, demonstrating that the addition of the wiring did not worse significantly the cryogenic performance (see Sec. 5.8.1).

5.8.1 Wiring effect on temperatures

To bring the signal from the MC to the outside of the cryostat, a system of woven ribbon cables with 13 twisted pairs of NbTi wires (100 µm diameter) with a CuNi coating (5 µm thickness) and a NOMEX™ texture was adopted [172, 173]. These high impedance links, for a total amount of 2600, are ideal for low temperature detectors where the front-end electronics is at room temperature. In fact, NbTi becomes superconductive at 9.2 K and it is a poor thermal conducting metal above this temperature, featuring a small heat transport in both conditions.

By design, the wiring thermalization down to 4 K occurs via radiation transmission. Radiation is not enough sufficient below this temperature (the emittance is proportional to the fourth power of the temperature) and a conductive link is the only possible way of thermalization. In particular, some important factors had to taken into account:

- the residual length at the various thermal stages: for the thermistor and heater wires, the total ribbon length is of 2.4 m and 3.0 m, respectively. Of these, $\sim$ 1.2 m are needed to thermalize to 4 K, $\sim$ 0.4 m to reach the Still stage. Furthermore, the maximum wire length must be left below the HEX stage, to minimize the heat conduction to the MC and to favor the plugging into the junction boxes;
- the absence of the 1 K pot thermal stage;
- the difficulty of thermalizing the cables due to the intrinsic fragility (an excessive pressure could break the insulating coating of the wires).

These considerations guided the choices for the design of the thermalizer, the positioning of the same thermalizers on the plates and the positioning of the wire thermalizations along the ribbons.

The thermalization system had already been tested both in its "radiative" [174] and "conductive" [175] parts. Anyway, after its installation inside the CUORE cryostat, it was fundamental to verify the actual impact on the cryogenic performance. This was done by monitoring the plate and wire temperatures at the various stages, especially the MC temperature.

In particular, a summary of the results concerning the wire temperatures is reported in Table 5.12, together with those obtained in the test of Ref. [175]. It can be seen that, with the exception of those related to the higher temperatures, the values are compatibles.[13] Regarding the plate temperatures, the final values are reported in Sec. 5.8. Also in this case, the values are still compliant with the original requests, taking into account the presence of the superleak for the higher MC temperature.

[13] The higher temperature registered below the 4 K stage are due to the erroneous choice of the thermometers. The use of silicon diodes instead of RuO_2 thermometers distorted the read out due to the power dissipated by the same sensors at those temperatures with the weak thermal link of the wires. As a matter of fact, the temperatures registered just after powering the LakeShore monitors were lower than $\sim$ 5.5 K and then saturated to the values reported in the table.

TABLE 5.12: Wire temperatures at the inner stages. In the test run, two thermometers are placed between each pair of plates, very close to the thermalizers. During Run 2, one thermometer is placed half-way within two plates.

	$T_{4\,\mathrm{K-Still}}$ [K]	$T_{\mathrm{Still-HEX}}$ [mK]	$T_{\mathrm{HEX-MC}}$ [mK]
Test run, [175]	3.55 – 1.32	870 – 315	78
Run 2 (WT 2)	8.65	475	93
Run 2 (WT 4)	7.25	460	75

5.8.2 Superleak

After about 6 days since the start of the circulation, a sudden increase in the mixture flow and in the condensing circuit pressures was observed. This was a clear signal of a considerable heat load on the Still. In particular, the flow value passed from 1280 μmol s^{-1} to more than 3 mmol s^{-1} in $\sim$ 15 hours. As an immediate consequence, all the IVC stage temperatures increased as well (bottom panel of Fig. 5.11).

The IVC volume was pumped and, by connecting the leak detector to the back of the turbomolecular pump, a signal of more than 10^{-3} mbar l s^{-1} was detected (in the ^{4}He mode). The leak rate stabilized at a value close to 10^{-4} mbar l s^{-1} and did not further decrease even after some days of pumping. This was not completely excluding the possibility of residual exchange gas trapped in "dead volumes" (e. g. the wiring Fischer boxes) to be the source of the signal. However, the amount of He was quite large and the most plausible hypothesis was thus the presence of a leak in the DU circuit.

As a definitive confirmation, it was decided to recirculate the mixture, monitoring the leak rate together with the other parameters. In case of a leak, the same effects observed after the previous circulation were expected to reappear within a similar amount of time. In fact, the moment for the leak rate signal to show up depends only on the geometry of the system (cryostat masses and volumes and position of the leak). More specifically, it requires that the superfluid-He reaches a stages with high enough temperature ($\Rightarrow$ high enough vapor pressure), leading to an enhanced evaporation. Considered the DU structure and time elapsed, the most probable location for the leak was one of the soft weldings of the lower heat exchanger, between the HEX and the MC plates. This hypothesis subsequently proved to be right.

The evolution of both the leak rate and the mixture flow during the test is reported in Fig. 5.13. The leak rate drops from the initial value of $\sim 10^{-5}$ mbar l s^{-1} to $5{\cdot}10^{-9}$ mbar l s^{-1} following the temperature drop caused by the circulation, due to the cryopumping effect of the cold surfaces. The He start immediately to come out from the leak and spread around from there, accumulating inside the IVC. Since the liquid is in the superfluid phase, it also climbs the vertical surfaces.

The leak rate is stable until the film is covering only the coldest surfaces. When the film reaches a sufficiently warm stage, the He begins to extensively evaporate. The signal

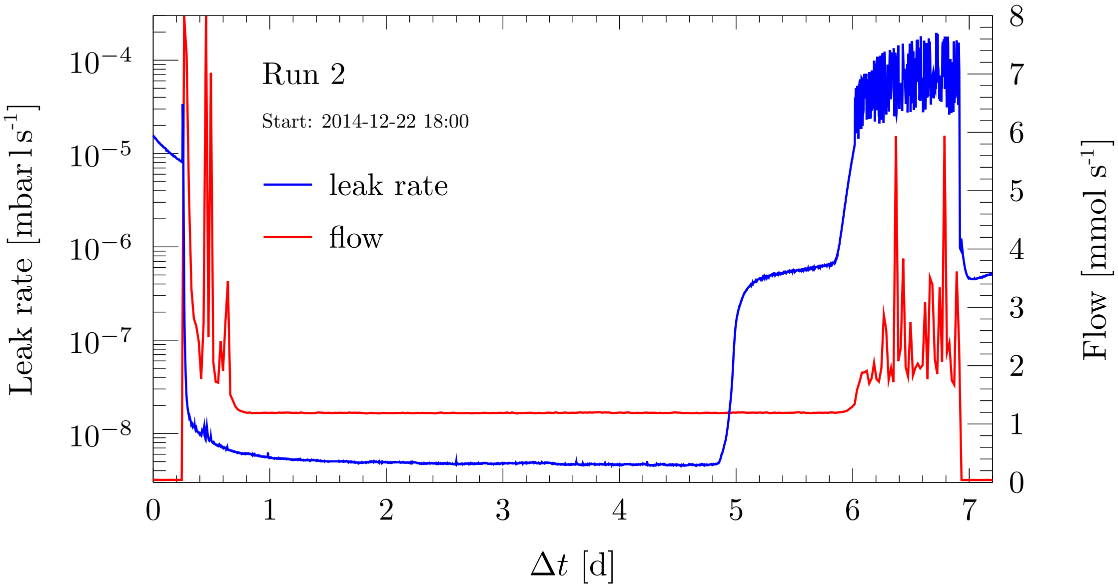

FIG. 5.13: Evolution of the leak rate signal in presence of the superleak. The IVC stages are initially at the PT temperature. With the start of the circulation, the leak rate drops following the temperature drop, thanks to the cryopumping effect of the cold surfaces. For about 5 days the He accumulates and spread around, also climbing the vertical surfaces since it is in the superfluid phase. When it reaches a stage sufficiently warm, it begins to extensively evaporate. The leak rate increase is sudden and steep: about 2 order of magnitudes in ~ 5 hours. The "step" on day 5 is maybe due to the reach of the bottom of the Still plate. On day 6, the He film is on Still plate and the gas exchanges heat with the 4 K stage. The heat load is very large, thus the mixture flow jumps from 1200 μmol s^{-1} to initially 2 and then up to 6 mmol s^{-1}. With the mixture collection (day 7), the leak rate drops due to the cool down caused by the single shot.

immediately rears up, increasing of about 2 order of magnitudes in ~ 5 hours.

To obtain leak rate values of the order of 10^{-4} mbar l s^{-1} took one day more.[14] After 6 days since the start of the circulation, the He film was on the Still plate, and the gas was exchanging heat with the 4 K stage. The heat load, too large for the Still, caused a jump in the mixture flow from 1200 μmol s^{-1} to initially 2 and then up to 6 mmol s^{-1}. This timing was perfectly coinciding with what observed the first time, thus confirming the hypothesis of the leak.

By switching the detection mode of the leak detector, it was possible to monitor the ^{3}He signal. This was $\sim (2-3)\cdot 10^{-11}$ mbar l s^{-1}, close to the instrument sensitivity. Even by assuming a non optimal instrument calibration, this value was anyway not compatible with that obtained with the ^{4}He detection mode, since the ^{3}He concentration in the mixture is never lower than $\sim 1\%$ (see Fig. 2.6). It was therefore a superleak, fully permeable by ^{4}He thanks to its superfluidity, but only partially or in no way permeable by ^{3}He (see Ref. [111] for details).

The investigation of the superleak required the transfer of the DU back in the test

[14] For almost one day the signal flattened when a new "unstable equilibrium" was reached. A possible scenario (even if only hypothetical) is that the superfluid film has reached to bottom of the Still plate having already completely covered the inner vessel. In fact, the timing seems (roughly) compatible with the assumptions of a $\sim 50\,\mathrm{m}^2$ area for the vessels and plates and a film thickness of a few nm [111].

cryostat. In fact, the cool down and warm up periods in the CUORE cryostat would have made impossible to perform multiple tests. Moreover, with the smaller surfaces, the leak effects would have become visible well before than 5 days due to the much reduced surfaces.

The leak check campaign was actually short because the movement of the DU further open the leak, so that it became visible already at room temperature. It was found on the soft welding on the top of the lower heat exchanger, as expected. To be sure, it was decided not only to repair the leak, but to reinforce all the soft weldings. The superleak had been fixed.

During the checks, a new cold leak (open only at cryogenics temperatures) was found on one on the DU In joints. This was also immediately repaired by remaking all the sealings.

Since the DU was in the test cryostat, it was decided to perform some flow measurement at room and cold temperatures (the full cool down time in the test cryostat is of ~ 3 days) regulating the Still impedances in order to find an optimal configuration. The fragility of the original system led to the decision of choosing a more stable configuration, even if renouncing to the possibility of tuning the valves without breaking the In sealing (see App. A.6 for details).

5.9 Run 3

Once the final leak check campaign was concluded without any more signs of leak, the DU was reinserted into the main cryostat. The next steps consisted in the installation of the TSP and of the Top Lead, the latter being previously assembled in an external facility (CR environment). The Mini-Tower was thus moved from below the MC plate to below the TSP.

The last PT (PT 2) was finally shipped to LNGS. This was thus tested and installed in the CUORE cryostat. All the 5 PTs were now present and operational. In the meanwhile, custom designed and fabricated thermalizers for the 2 condensing lines were installed on the 4 K plate (App. A.4) in order make the mixture circulation with the DU independent from the thermalization of the lines on the PTs (see the discussion in Sec. 4.5.3).

During the cool down of Run 3, the FCS was employed for the first time (see Sec. 4.5.1). This required the installation outside the MC, HEX and Still shields of PTFE tubes to carry the cold He inside the IVC and the connection of the FCS circuit to the cryostat (Fig. 4.10). The DCS guide tubes outside the HEX vessel were also installed. With the Top Lead in position, the pipe configurations was now completed down to the TSP (only the tubes to be inserted among the towers were missing).

The normal procedures for the cool down were also modified. Together with the pumping of the OVC, the IVC was now over-pressurized with He (1.1 bar). The cool down was started by turning on the Busch compressor, while the PTs were turned on after about one week. During the cool down, the FCS gas circuit needed to be periodically refilled

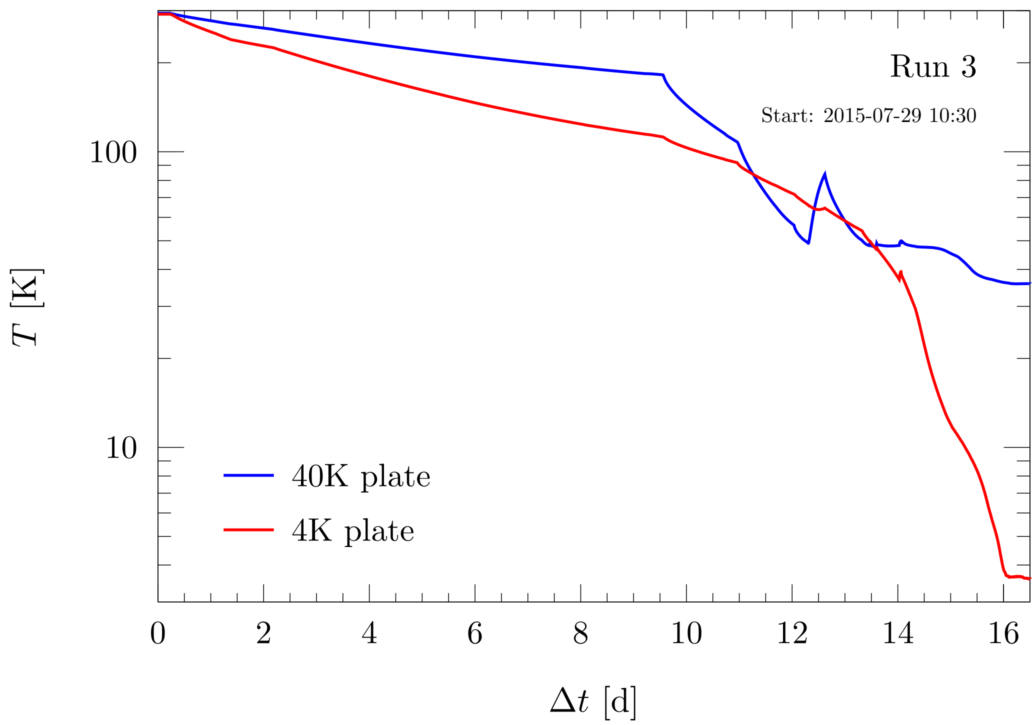

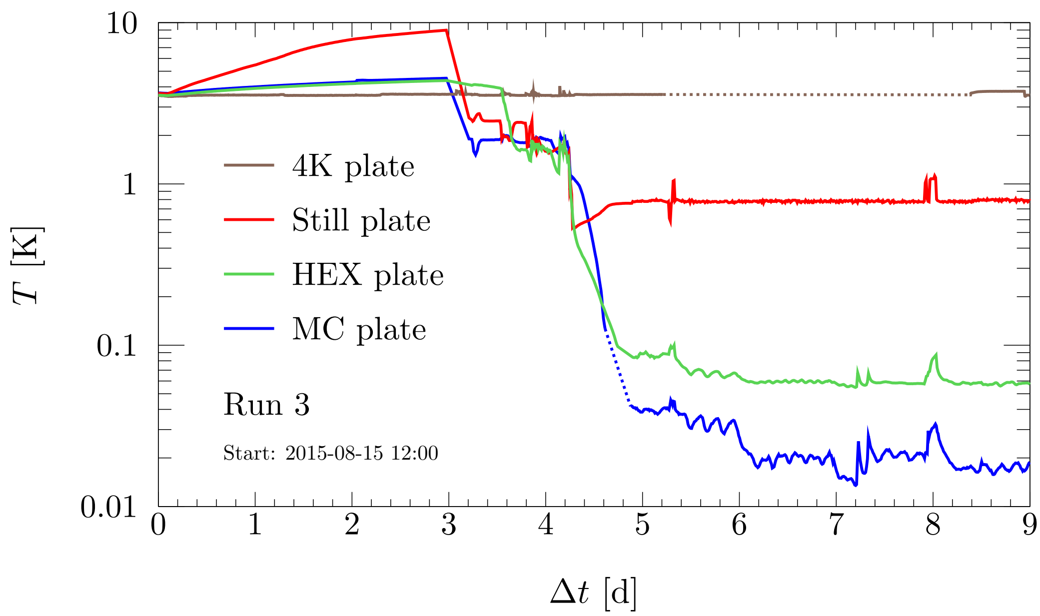

FIG. 5.14: Cool down of Run 3. (Top) Temperatures of the 40 K and 4 K stages: the final values of 35.8 K and 3.6 K are reached in about 16 days since the FCS was turned on. The bumps on days 10, 11 and 12 correspond to the turning on of PT 2 and PT 4, PT 1 and PT 3 and PT 5, respectively. The steep temperatures rise on day 12 is due to a power outage of the FCS compressor. The cool down restart with the restarting of the compressor, which is anyway turned off the day after. (Bottom) Inner stage temperatures after the removal of the IVC exchange gas. The initial rise is due to power dissipation caused by a DCS Fischer cable (immediately unplugged). The decrease down to ~ 2 K is obtained by circulating a small amount of gas in the DU. The dilution begins on day 4. The temperature of 0.78 K is reached at the Still stage, while only oscillating values are obtained for the HEX and MC stages. In particular, $(58-60)$ mK and $(18-22)$ mK are reached at the former and the latter, respectively. The dotted lines cover the period of unplugged sensors.

with He in order to maintain the same pressures and gradients,[15] while the compressor frequency had to be tuned according to the cryostat temperatures in order to optimize the heat exchange.

The progress of the cool down is shown in the upper plot of Fig. 5.14. The 40 K and 4 K stage base temperatures were reached in about 16 days. The final values were 35.8 K and 3.6 K, respectively. After the removal of the IVC exchange gas, a rise in temperature similar to those encountered during Runs 1.1 and 1.2 (see Sec. 5.5.1) was observed. The source of the power dissipation was identified with an electric issue related to a DCS component. In fact, once the corresponding cable was unplugged, the temperatures began to recover immediately. Anyway, in order to exclude the presence of a leak, the DU was started with circulating only a small amount of gas. This brought all the inner stages to a temperature close to ~ 2 K. No sign of leak was observed. In the end (the circulation proceeded then in the standard way), 0.78 K were reached at the Still stage, while the oscillating values of $(58 - 60)$ mK and $(18 - 22)$ mK were obtained for the HEX and MC stages, respectively.

The analysis of the temperature oscillations performed during Run 1.3 (Sec. 5.7.1) already allowed to identify the largest source of the problem with the mechanical vibrations induced (either directly or indirectly) by the PTs. Anyway, a new series of measurements was carried out during Run 3. Apart from confirming the previous conclusions, these deepened studies gave precious information on how to proceed in order to significantly reduce the amount of vibrations.

One of the attempt consisted in the use of a micro-stepping controller for the PT motor heads. Unfortunately, making the connection for the linear motor required the switching off of the PT. While this was done for one of the PT thermalizing the condensing line, the following warm up might have been the cause of choke in the condensing line, with some impurities (frozen at lower temperature) that could have made their way to the thin capillaries when they were warm. The flow on the other condensing line was too small to restart the circulation, therefore it was decided to stop the run.

Despite the recurrence of the oscillation problem, Run 3 was a successful test of the TSP and Top Lead integration in the cryostat. Their installation did not spoil the system performance and the monitoring of the temperatures showed an efficient thermalization to the corresponding thermal stages all over the cool down, with final values perfectly compatible with those of the corresponding stages. The case of the Top Lead is plotted in Fig. 5.15, together with the temperature of the HEX plate.

5.10 Run 4

The preparation for Run 4 started in parallel with the cool down of Run 3, with the production of the ILS (Sec. 6.5.2). At the conclusion of the Run 3 cold test, it was thus possible to proceed with the installation of the shield (Sec. 6.6).

The set up of a dedicated environment was required for the installation of the shield,

[15] The refill of the gas circuit was done with clean He directly evaporated from a dewar.

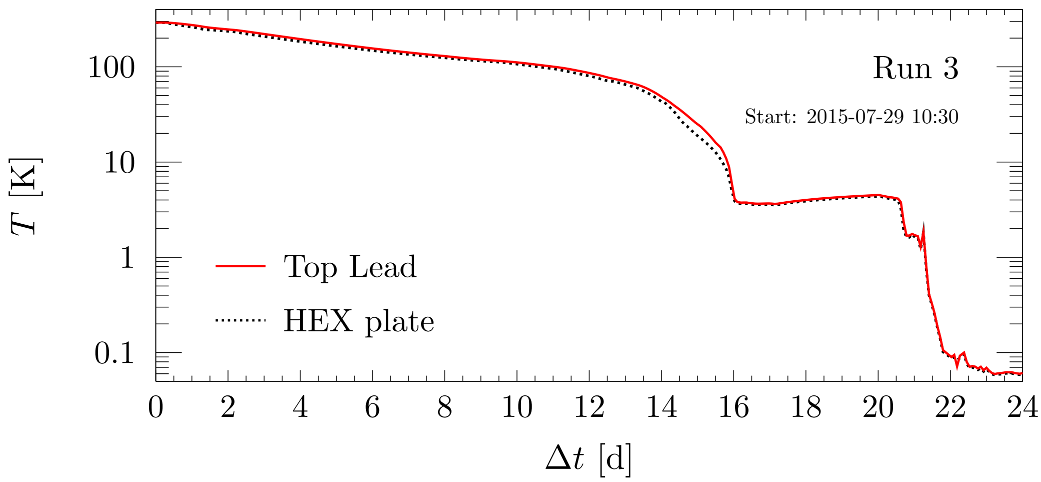

FIG. 5.15: Temperature of the Top Lead during the cool down of Run 3. The HEX plate temperature is shown as a reference. The effect of turning off the FCS on day 14 is clearly visible as a slightly worsening of the lead thermalization process. This anyway immediately recovers once the lead becomes superconductive ($T_c\,(\mathrm{Pb}) = 7.2\,\mathrm{K}$).

which could thus be assembled under the cryostat and from there directly lifted to its position (outside the Still vessel). With its integration, the cryostat finally reached its final configuration.

On the cryostat, the mixture flow of the line that did not allow to circulate during Run 3 was increased by reducing the corresponding impedance at the Still level.

A series of operations were performed in order to suppress the temperature oscillations. These aimed both at directly improving the PT configuration and at reducing the vibration transmission from the 300 K plate to the lower temperature stages (see Sec. 5.7.1).

Three of the five flexlines going from the PT rotating valves to the room temperature heads were substituted with longer ones to reduce the amount of vibrations. In order to make the cryostat structure more rigid, bars were inserted inside the SS bar gimbals, while PTFE holders were added on the HEX and MC plates in order to block the extremities of the HS and MCS bars (refer to the figure in Table 4.3). Moreover, during the cold test, steel clamps were installed on the MSP to horizontally anchor the 300 K plate (and the cryostat) to the support structure.

Run 4, in all its phases, represented the definitive test before proceeding with the installation of the CUORE detector. We had to demonstrate:

- the effectiveness of the FCS in keeping the cool down time within ∼ 20 days in presence of the full cryostat mass (apart from the detector);
- the ability of the DU of reaching and maintaining a stable base temperature for a long period (months);
- the suitability of the cryogenic environment, in terms of low noise, for the run of the Mini-Tower test detector;

- the effectiveness of the shield system (external + internal) for protection against radioactivity.

These points will be deeply investigated in Secs. 5.10.1, 5.10.2 and 5.10.3 and in Chap. 7. All the results were successfully achieved. With the end of Run 4, the CUORE Collaboration declared concluded the cryogenic system commissioning phase.

5.10.1 Cool down

The cool down of Run 4 represented a fundamental step for the whole cryostat commissioning and a major test for the FCS. The goal was to keep the time to reach the PT base temperature within 20 days, in presence of the full IVC mass (~ 13 tonnes).

The cool down proceeded smoothly, as it can be seen from the upper plot of Fig. 5.16. The PTs were switched on 3 days after the starting of the FCS, which was turned off after 11 days, when the IVC reached a temperature of ~ 50 K. It took ~ 17 days to reach 35.4 K and 3.8 K at the 40 K and 4 K stages. Due to some problems related to the compressor cooling water, it actually took a few more days to reach stable PT base temperatures. The final values were 34.5 K and 3.4 K.

Fig. 5.17 allows a more detailed view of the first part of the cool down, with the use of the FCS. In the upper plot, the dependence of the cool down speed on the Busch compressor frequency is shown taking the 4 K stage as a reference. At the beginning, higher frequency values guarantee a more effective cool down, allowing for a larger gas flow. Later, when more and more enthalpy has to be extracted from the He, the frequency has to be constantly reduced. The improvement with the tuning are visible on days 1, 7, 8 and 9. The switching on of the PTs (on day 3) translates into a dramatic improvement in the cool down speed and, after one day, the PT contribution to the total cooling power is already $\sim 1/3$.[16]

After about 9 days since the start of the cool down, the FCS becomes ineffective for the 4 K. In fact, the cool down speed worsens when restarting the system after a forced interruption of the gas circulation. This is more visible from the lower plot in the figure, where the different temperatures along the FCS circuit are shown (refer to Figs. 4.9 and 4.10). On day 9, the temperature of the He entering the cryostat is actually higher than that of the 4 K stage. For the next 2 days, the FCS remains anyway useful for the cool down of the inner stages and, in particular, of the Top Lead.

The DU was turned on immediately after PT base temperature was reached (lower plot in Fig. 5.16). A chock in the used condensing line required to switch to the other one, the same that did not allow to circulate the mixture during Run 3. The cool down cool proceed, thus showing that the intervention on the line impedance was successful. The MC base temperature was reached in only 3 days. The final temperature were 0.76 K, 65 mK and 6.3 mK at the Still, HEX and MC stages, respectively.

The cool down could be considered successful.

[16] Imagine to continue the red curve keeping the trend it had on day 2

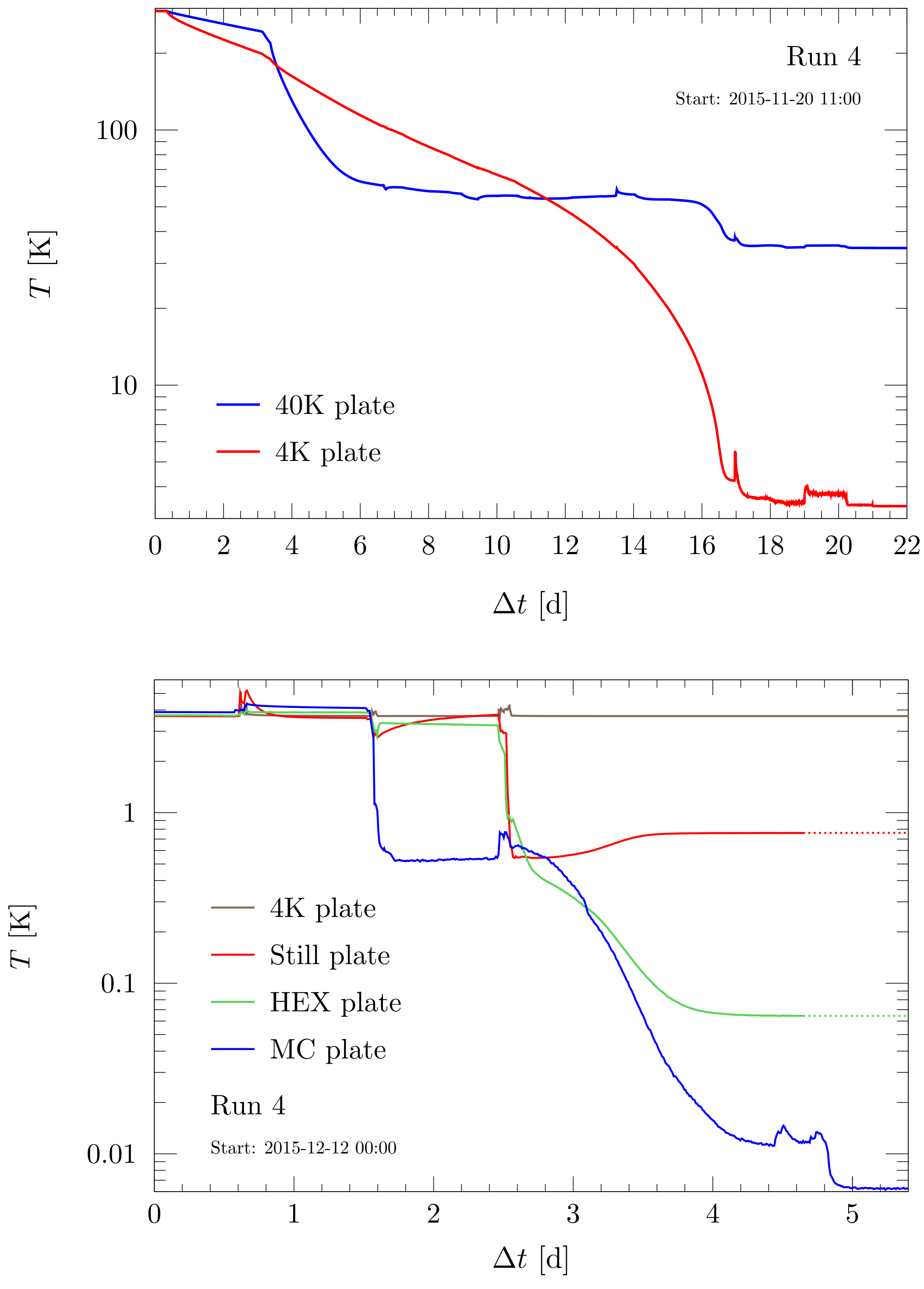

FIG. 5.16: Cool down of Run 4. (Top) Temperatures of the 40 K and 4 K stages: the final values of 34.5 K and 3.4 K are reached in about 22 days since the FCS was turned on. The double slope change on day 3 is due to the turning on of PT 1 and PT 3 and PT 2, PT 4 and PT 5, respectively. The FCS is turned off on day 11. The irregular behavior on days 6, 9 and 14 is due to problems with the cooling water of the compressors. The spike on day 17 is due to an accidental venting of the IVC. (Bottom) IVC stage temperatures during the circulation with the DU. The condensation of ^{3}He begins on day 1, while the dilution on day 2. The structure in the MC temperature on day 4 is due to the formation of a chock in the mixture condensing line. The cool down resumes by switching to the other line. The dotted lines cover the period of unplugged sensors. The reached base temperatures are 0.76 K, 65 mK and 6.3 mK for the Still, HEX and MC stages, respectively.

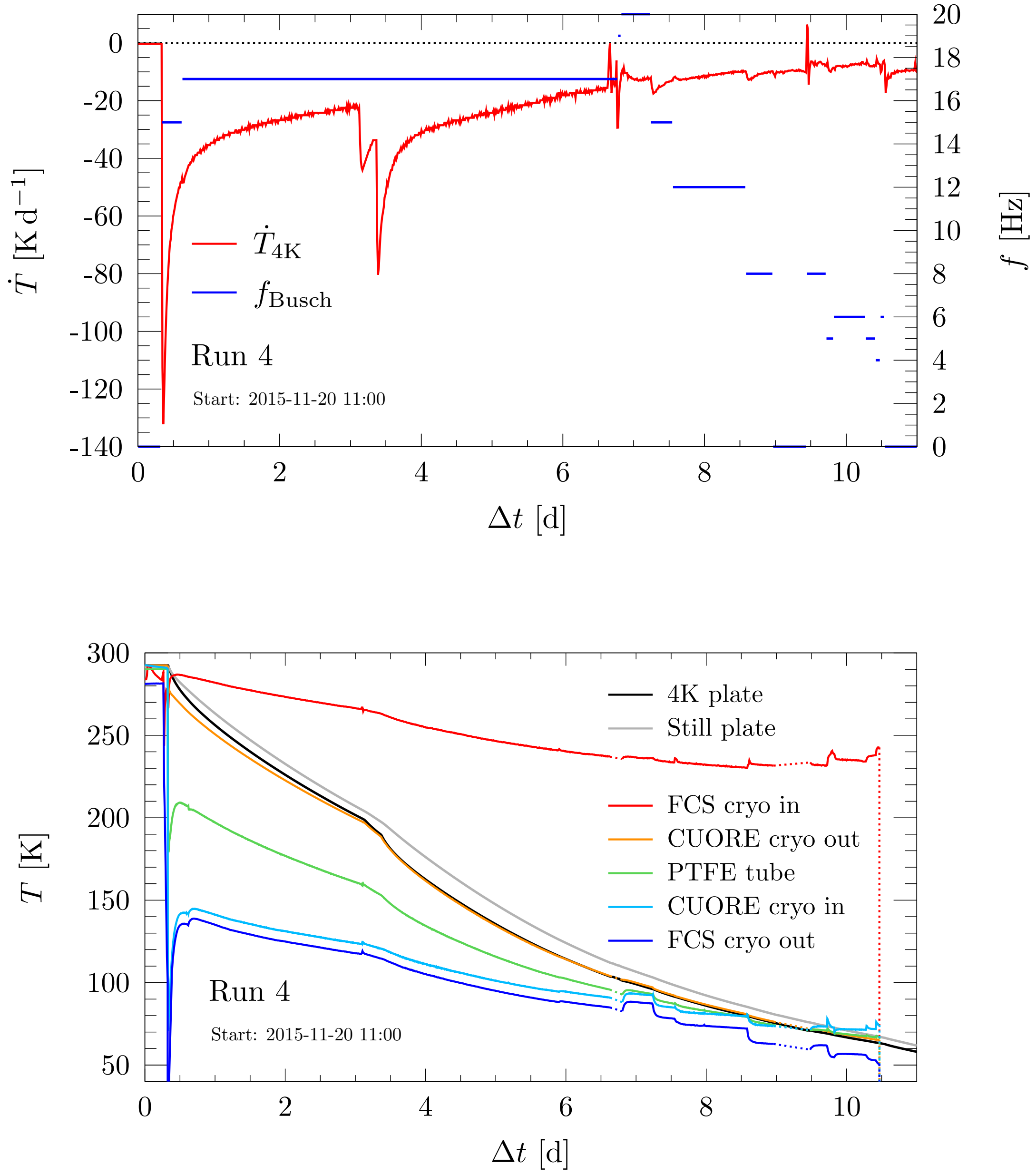

FIG. 5.17: Detail of the cool down with the FCS. (Top) Cool down speed of the 4 K stage. A higher frequency for the Busch compressor is effective in the first part of the cool down, while it has to be constantly reduced during the last days of operation of the FCS. The improvement with the tuning are visible on days 1, 7, 8 and 9. The spikes on day 3 are due to the switching on of the PTs. The irregular behavior on days 6 and 9 is due to problems with the cooling water of the compressors. The dotted line at 0 separated the cool down from the warm up. (Bottom) Temperature in different positions along the FCS circuit, from the exit to the return into the FCS cryostat. The 4 K and Still stage temperatures are also plotted. All the temperatures are constantly reducing with the proceeding of the cool down. The FCS becomes ineffective around day 9 (the 4 K stage temperature is lower than that of the incoming gas). The tuning of the compressor frequency from day 7 is clearly visible. The dotted lines cover the period of problem with cryogenic system.

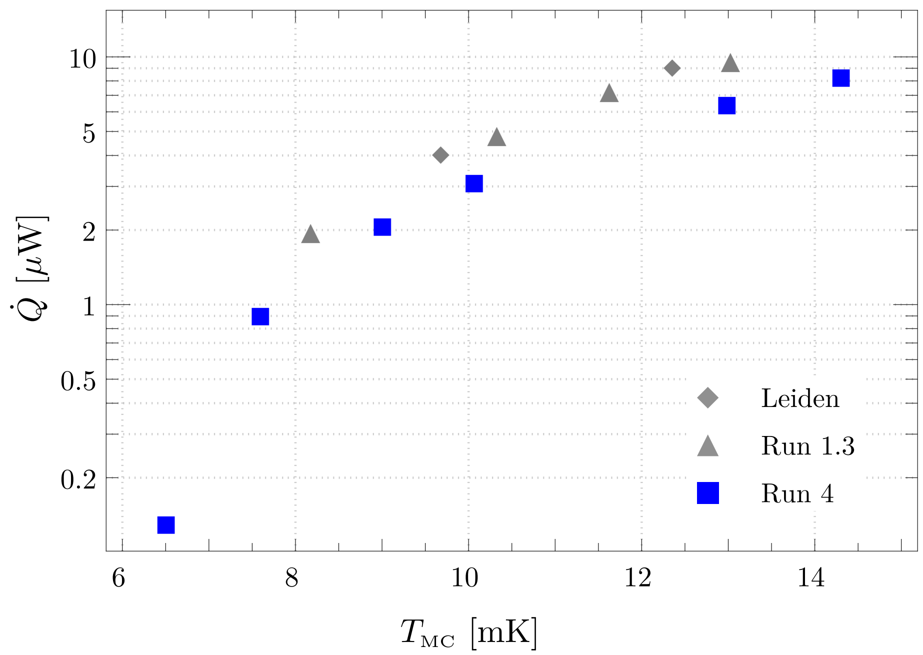

FIG. 5.18: DU cooling power as a function of the MC temperature during Run 4. The values obtained during the characterizations at Leiden (plots in Fig. 5.4) and at LNGS during Run 1.3 are also reported.

5.10.2 DU performance

After the initial tests (see Sec. 5.2), studies of the DU cryogenic performance were repeated during the various commissioning runs. Also part of the Run 4 cold test was devoted to a new DU characterization, both in terms of cooling power and base temperature, with the "fully loaded" cryostat.

The effective cooling power was measured by directly injecting power on the MC plate through a heater. The result is shown in Fig. 5.18. The mixture flow during the characterizations is within the range $(1010 - 1020)\,\mu\mathrm{mol\,s^{-1}}$. As it can be seen, despite the much larger cryostat mass in the final configuration, the new values are very close to the initial ones and $3\,\mu$W at $10\,$mK ($5\,\mu$W at $12\,$mK) are perfectly compatibles with the original requests.

Regarding the MC base temperature, it should be sufficient to notice that of the almost 4 months of duration of the cold test, more than 1 month of operation was actually performed at MC base temperature.[17] To allow a quantitative estimate of the base temperature stability, a period of 2 days with no intervention on the cryostat could be taken as a reference. The MC temperature temporal evolution during this interval is shown in Fig. 5.19. The average value is $(6.32 \pm 0.04)\,$mK, with a few deviations greater than 2σ recorded. Despite the much more complex system, this value is still compliant with the design specification of the "bare" DU.

During the final run, a MC temperature of $6.25\,$mK was reached with a PT off (PT 3).[18]

[17]For the remaining time, the higher temperature is due to the interventions performed on the cryostat.
[18]The lower temperature value shows that the previous circulation flow was not optimized.

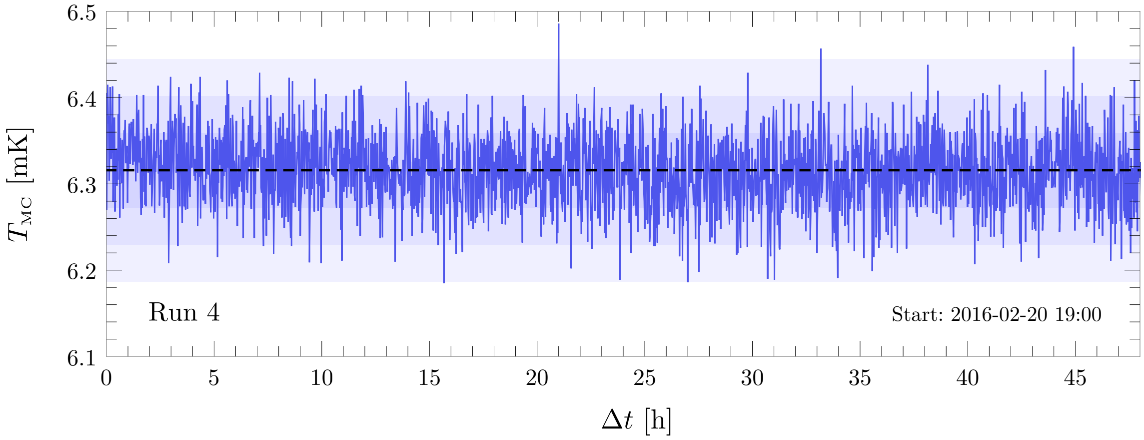

FIG. 5.19: Base temperature temporal evolution over a two days period with "undisturbed" cryostat during Run 4. The MC temperature is (6.32 ± 0.04) mK. The dashed line indicates the average value, while the shaded regions correspond to 1σ, 2σ and 3σ intervals.

The larger flow of 1180 µmol s^{-1} was induced by the loss of cooling power at the 4 K stage, that caused a larger heat load at the Still level. The new configuration was maintained for $\sim$ 2 days (Fig. 5.20). The stability of the working conditions demonstrated the feasibility of running with only 4 operational PTs.

5.10.3 Noise abatement

The solutions already adopted in order to reduce the amount of vibrations were surely effective, allowing to reach stable temperatures at each stage. However, a lot of work still needed to be done in order to be able to run a bolometric detector. In retrospection, the analysis of the final Mini-Tower data (see Sec. 7.4), allowed to estimate the initial RMS resolution. This was found to be as high as tens of MeV.

The Mini-Tower made it possible to directly monitor the response of the system to any operation performed, and so to observe potential improvements or worsening of the situation, by studying the acquired noise Power Spectral Density (PSD). Large part of Run 4 was thus devoted to the understanding of the noise generation and propagation system and to the (almost on-line) analysis of the spectra.

The bolometric signal is affected by the detector temperature. Therefore, the largest noise source was identified with mechanical vibrations, which were in turn producing temperature variations. In particular, the PT compressors, were introducing a peak at $\sim$ 140 Hz (plus the related harmonics), while the motor heads one at their rotation frequency, i. e. $\sim$ 1.4 Hz (plus the related harmonics). Moreover, each movement on the MSP was also inducing vibrations at the level of the detector, by the transmission either through the cryostat structure (support bars down to the MC plate + TSP thermalizers) or through the DS system (passing via the Y-beam).

The series of obtained progresses indicated that the most effective solutions were those going in the direction of making the cryostat structure more rigid and of further reducing the vibration transmission.

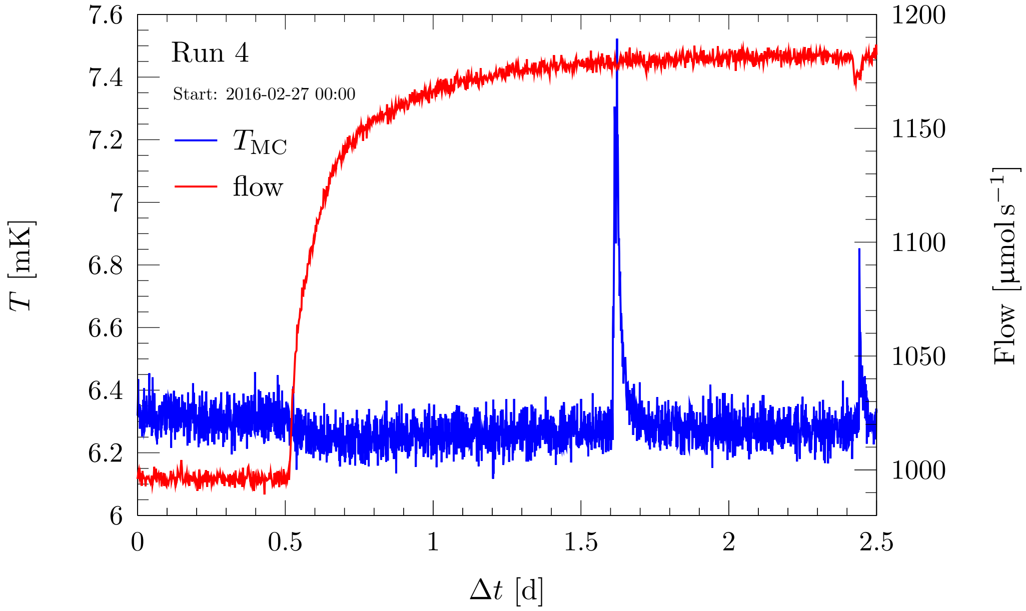

FIG. 5.20: Base temperature and mixture flow while running with only 4 operational PTs. The rise in the flow is due to the switching off of PT 3, while the effect of the LN_2 trap refill is visible midway through day 2. The two spikes in the MC temperature are due to the insertion and to the removal of the calibration source for the Mini-Tower detector, respectively.

Regarding the cryostat support structure (see Sec. 4.2), wood wedges were inserted at its base in order to hold it fast to the ground. At the second floor, small portions of the grid around the steel columns were cut to prevent any contact between these and the hut. The external staircase was also detached from the same hut. Finally, steel clamps were installed under the MSP to firmly anchor it to the 300 K plate.

After the raising, the whole mass of the ELS ($\sim$ 80 tonnes) is supported by the 4 screwjacks (see Sec. 4.2.2). Despite being safe from the mechanical and seismic point of view, the system pressing against the walls actually makes the whole cryostat support structure to oscillate. In fact, the stiffness of the base insulators is of $\sim 4\,\mathrm{kN\,mm^{-1}}$ [163]. Therefore, it was decided to detach the lead shield from the walls by removing the rail wheels guiding the raising and lowering movements.[19]

Regarding the flexlines from the compressor to the PTs, these were hanged with ropes under the second floor ceiling, carefully avoiding any touch with the MSP. The same was done with the rotating heads and the He reservoirs, previously placed on the MSP.

Furthermore, it was noticed that the same electronics cables were transmitting vibrations to the detector. These had to be hanged as well. Indeed, a puzzling result was being obtained. The situation looked better with the blocked Minus K system rather than when this was active. Eventually, we figured out that a couple of electronics cable were passing over the Y-beam. When these were removed from the Y-beam, the vibration isolation system performed as expected.

[19] Of course, these were reinserted at the conclusion of the run.

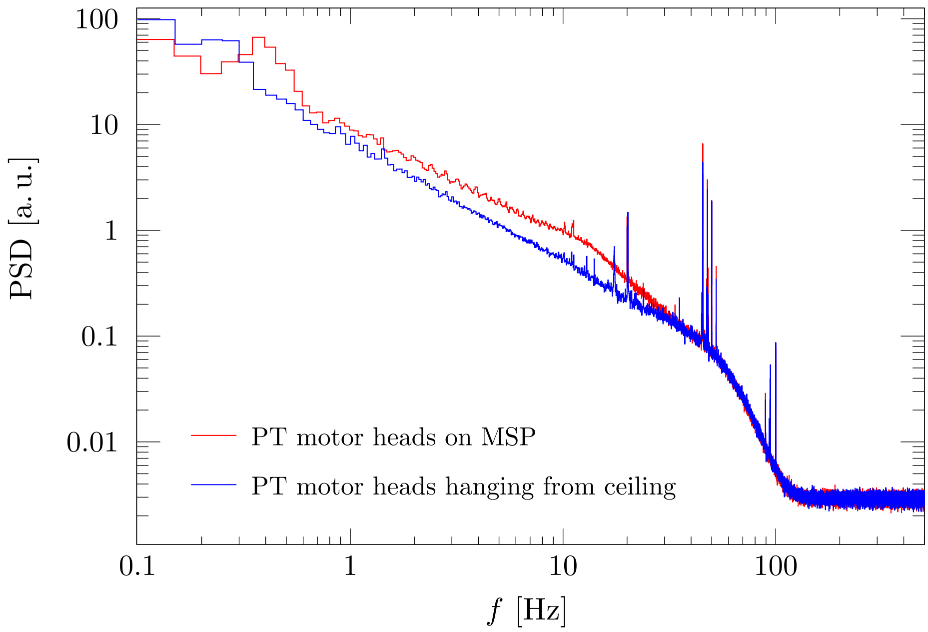

FIG. 5.21: Comparison between noise PSD in the range $(0.1 - 500)$ Hz acquired with the Mini-Tower detector (Channel 1) in the two configurations of PT motor heads placed on the MSP (read line) and hangings from the hut ceiling (blue curve). The noise suppression over a wide frequency range is clearly visible in the latter case.

Once the issue with the temperature vibrations had been solved, other contributions to the noise were emerging. Another noise source could be identified with a not efficient grounding of the various electronics, DAQ , but also cryostat components. The adopted solution, actually working, consisted in a unified grounding configuration.[20]

Finally, minor contributions from acoustic noise and microphonism were also observed. Despite these were not compromising the Mini-Tower performance, they will be specifically addressed during the CUORE detector commissioning. Regarding the former, it is likely that acoustic insulators will be installed inside the Faraday cage. Regarding the latter, specific test runs will be performed in order to optimize the electronics.

In Fig. 5.21, an example of comparison between noise PSD corresponding to different system configuration is shown. In particular, the 2 spectra were acquired when the PT motor heads were placed on the MSP and hangings from the hut ceiling, respectively. In this case, the noise suppression over a wide frequency range is clearly visible in the latter configuration.

Eventually, the Mini-Tower performance will prove the success obtained in creating a suitable cryogenic environment for the run of a bolometric detector.

[20]Although working, this ad-hoc configuration will be completely modified in CUORE. In fact, with the complete installation of all the electronics and DAQ components, a much more efficient grounding system was designed.

Chapter 6

Excursus: the production of the CUORE Roman lead shield

The CUORE detector is completely surrounded both laterally below and above by lead shields. In particular, the ILS is made of ancient Roman lead. This is characterized by an extremely low radioactivity and it is practically depleted of ^{210}Pb.

The uniqueness of this material makes it ideal for the experiment. However, handling and manufacturing objects that are to all effects archaeological artifacts, i. e. the Roman lead ingots, required additional care during every single operation and working phase of the ILS production.

6.1 The ingots

The lead ingots used for the CUORE ILS come from the shipwreck "Mal di Ventre A" (MVA). From the shipwreck, 983 stamped lead ingots were recovered during three campaigns between 1989 and 1991 (the last being funded by INFN and specifically supported by Fiorini). The majority of the ingots is stored at the National Archaeological Museum of Cagliari, where some samples are also exposed. Part of the ingots ($\sim$ 50 lead pigs) is exposed at the Cabras Civic Museum while another fraction ($\sim$ 40 lead pigs) is stored/exposed at LNGS. By a common agreement between the Archaeological Superintendence of Cagliari and Oristano and the INFN, a fraction of the total was destined to be used in low background physics experiments at LNGS. This consisted in $\sim$ 270 lead pigs among those with the minor archaeological interest and the less preserved.

The MVA shipwreck was found at a depth of about 30 m in the sea loch between Mal di Ventre Island and Sardinia. The site location is shown in Fig. 6.1. The low depth, if on the one hand considerably facilitated the recovery operations, on the other favored illegal looting and did not prevent the sea waves from dispersing the materials of the wreck [176]. Mal di Ventre Island is constantly subjected to Mistral winds and its coasts present abundance of reefs very dangerous for navigation. But, in ancient times, this site

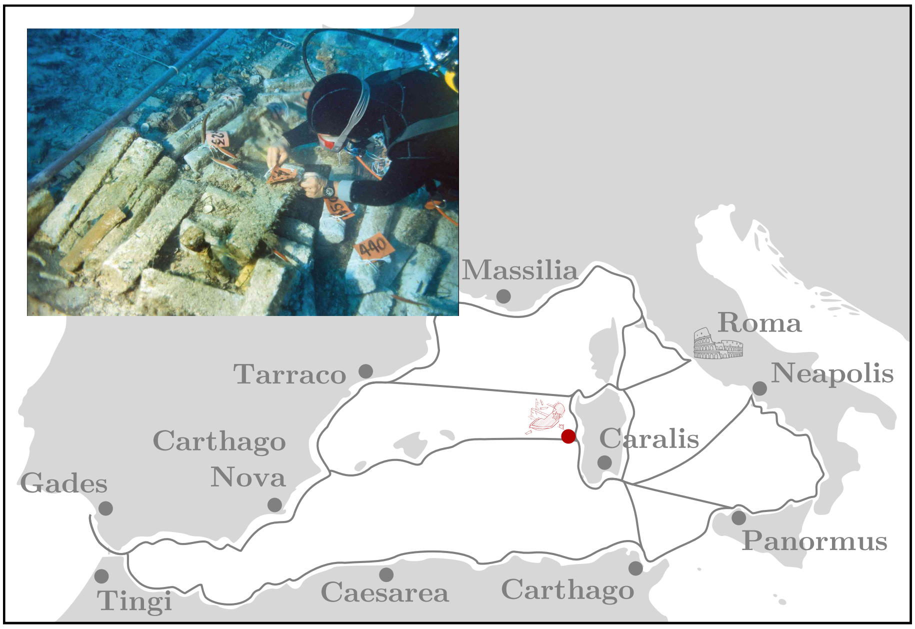

FIG. 6.1: Ancient sea routes for the trade of the Hispanic lead. The red dot indicates the position of the MVA shipwreck [176]. (Corner) Picture taken during the lead ingot recovery.

represented an obliged way for many trade routs from Spain passing through Sardinia towards Sicily, South Italy and North Africa (Fig. 6.1), and thus it became scene of many shipwrecks. Among these, the MVA shipwreck. In particular, in this case one can imagine that the ship, a *navis oneraria* 36 m long and 12 m wide coming from Spain, tried to receive protection from the strong winds by approaching the coasts and, doing so, it may have hit against the reefs and, dragged by the Mistral, it placidly sank about a mile from the island.

All the ingots from MVA have dorsal cartouches with name of their manufacturer. The most common stamp, identified on about 80% of the ingots, belongs to the company of *Caius et Marcus Pontilieni*, (SOC·MC·PONTILIENORVM·M·F = *Soc(ietas) M(arci et) C(ai) Pontilienorum M(arci) F(iliorum)*) (Fig. 6.2). The fact that a ingot of the same family was found in Cartagena, supports the hypothesis that their origin must be placed in the mining districts dislocated near this city. Indeed, *Carthago Nova* in the late II - I century b. C. represented the most important mining area in the western Mediterranean, whose products were exported on a massive scale. Anyway, the isotopic composition analysis performed on the MVA and on a large number of other Roman ingot samples, definitively proves that the formers belong to the Cartagena ore district [177, 178].

The shape of the lead pigs (flat and rectangular basis and parabolic transverse profile), the weight (~ 33 kg on average) and the almost constant size (basis: $46-47$ cm, back: $42-44$ cm, height: ~ 9 cm) trace back to the Spanish production of the late Republican Age, i. e. around half of the I century b. C.. An almost contemporary dating was also estimated for the rest of ingots, mainly thanks to the comparisons with similar artifacts recovered in this area of the Mediterranean basin. See Ref. [176] for further details on the

FIG. 6.2: Pictures of two ingots from the MVA shipwreck. (Top) A very well preserved lead pig exposed at the Cabras Civic Museum. The cartouche SOC·MC·PONTILIENORVM·M·F is clearly readable. (Bottom) One of the typical lead pigs used for the production of the CUORE shield.

historical context of the origin of the ingots.

6.2 Roman lead radioactive contamination

Due to its high Z, reasonable cost, mechanical properties and low activation cross section for environmental neutrons, lead is an excellent shielding material. The contamination from the ^{232}Th, ^{235}U and ^{238}U chains is very low in most of the commercial samples. However the secular equilibrium is broken by ^{210}Pb. This isotope, whose β decay has a half-life of 22.3 yr and a 63.5 keV transition energy, represents an important component of environmental radioactivity [180]. The decay of ^{210}Pb is in fact followed by the β decay of ^{210}Bi to ^{210}Po ($t^{1/2} = 5.013\,\mathrm{d}$, $Q_\beta = 1162.7\,\mathrm{keV}$) and by the α-decay of ^{210}Po to ^{206}Pb ($t^{1/2} = 138.376\,\mathrm{d}$, $Q_\alpha = 5407.46\,\mathrm{keV}$). The presence of ^{210}Pb can therefore affect the background rate (and thus the sensitivity) of low background experiments, such as the Dark Matter and $0\nu\beta\beta$ searches.

The ^{210}Pb contamination in modern lead can be very high, of the order of $\mathrm{kBq\,kg^{-1}}$ for common lead, but its content can be drastically reduced (the lower the content, the higher the price) down to a fraction of $\mathrm{Bq\,kg^{-1}}$ [179]. In the ancient lead, ^{210}Pb is expected to be totally absent. Moreover, even if it is a minor effect, in this case the overburden of water has prevented the chemical contaminations of the lead to be activated by cosmic ray neutrons.

A series of measurements were carried out on ingot samples from the MVA shipwreck, more specifically from an ingot of the Pontilieni company, in order to actually characterize the radioactive contamination of the lead. The different techniques used included neutron activation analysis (NAA) to ascertain the chemical impurities, γ-ray spectroscopy to determine the U and Th chain and the ^{40}K contamination (in secular equilibrium) and bolometric measurements to evaluate the contamination of ^{210}Pb [179, 181, 182].

TABLE 6.3: Impurity concentrations in samples of Roman lead. Column 2 & 3: measurement on a single ingot (Pontilieni company) performed with NAA analysis (results as reported in Ref. [179]). Column 4 & 5: measurement on the lead after melting (more producers) performed with spark mass spectroscopy.

Element	Concentration [ppm]			
	Pontilieni I	Pontilieni II	Mixed I	Mixed II
Ag	45 ± 2.5	58 ± 5	88 ± 11	70 ± 4.7
As	0.5 ± 0.2	0.012 ± 0.004	7.4 ± 0.8	3.1 ± 1.1
Bi			41 ± 2.1	34 ± 1.6
Cd			0.4 ± 0.1	0.3 ± 0.1
Cu		1270 ± 100	1260 ± 170	1140 ± 450
Fe			3.8 ± 0.5	4.6 ± 2.3
Mn				
Ni	4.5 ± 0.5	3.0 ± 0.2	6.8 ± 0.5	10 ± 0.8
S				
Sb	0.09 ± 0.01	0.1 ± 0.01	170 ± 7	47 ± 3
Se	0.98 ± 0.1	1.4 ± 0.2		
Sn			3.8 ± 4.9	< 1
Te			1.3 ± 0.2	0.9 ± 0.1
W	< 0.02			
Zn	0.5 ± 0.1	< 20	0.7 ± 0.1	0.6 ± 0.2
Pb			$(99.84 \pm 0.07)\%$	$(99.87 \pm 0.04)\%$

More recently, analysis with spark mass spectroscopy were performed during the shield casting operations (see Sec. 6.5.2). In this case, the impurity concentrations reflect the effective composition of the CUORE ILS, since the contributions from the ingots coming from different producers are included. The results are shown in Table 6.3, together with those from Ref. [179] on Pontilieni lead samples for comparison. It can be seen that the concentrations for part of the elements are quite similar in both the measurement campaigns, while for others the variation varies by orders of magnitude (e. g. for As and Sb). This denote the use of different processes in the purification of the molten material or the use of different metals by the various producers [183]. Anyway, it is remarkable that the purity of this two thousands years old lead is close to 99.9%, a value compatible with that of lead from modern production. In fact, judging from the low concentration of silver (< 100 ppm) in the MVA ingots, it is very likely that the lead has been de-silvered.[1]

The measurements of γ-spectroscopy were performed at LNGS with a extremely low radioactivity HPGe detector [179]. The spectra in the low energy region are reported in Fig. 6.4 for the Roman lead samples and for samples from modern lead (both commercial and low radioactivity) for comparison. The effect of the bremsstrahlung and the presence

[1]The Roman society needed large quantities of both lead and silver and the production of the latter was often a byproduct of production of the former. In particular, it seems that to recover silver from lead was economically convenient when the Ag concentration exceeded about 100 ppm [184].

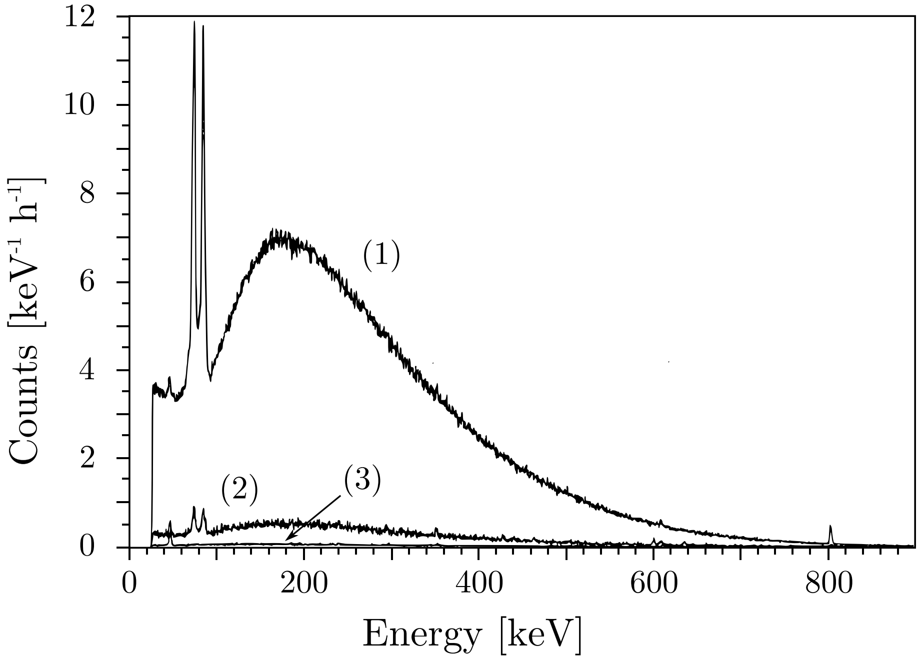

FIG. 6.4: Spectra in the region to 900 keV recorded with shields made with various types of lead: (1) common modern lead; (2) modern lead with a certifed content of less than 20 Bq kg^{-1}of ^{210}Pb; (3) Roman lead from the MVA shipwreck. Figure from Ref. [179].

of the X-ray peaks generated by ^{210}Pb is clearly visible in the samples of modern lead and completely absent in those of ancient lead.[2]

Regarding the content of ^{210}Pb, the upper limit for the activity of this isotope of about 4 mBq kg^{-1}was set by the bolometric analysis, the most sensitive in this case. This value is five orders of magnitude lower than that in common modern lead, but also two orders of magnitude lower than that for the specially prepared low radioactivity lead.

6.3 Shield overview

A rendering of the CUORE ILS is shown in Fig. 6.5. The ILS is positioned inside the IVC between the 4 K and the Still vessels (Fig. 4.1). The shield is held by the Still plate through 3 stainless steel threaded rods that cross the ILS throughout its length. Due to the very large mass and dimensions (Table 4.4), it would have been impossible to rely on the DU cooling power for the ILS thermalization. Therefore this is thermalized to the 4 K stage.

The lead is enclosed between a copper support plate at the bottom and a copper ring on the top. The side of the ILS is constituted by 26 lead rings, each one composed by 6 sectors, 3 with a central hole for the support rods and 3 with a lateral recess for the thermalization bars. The bottom of the ILS, instead, is a compact disk made of 18 lead

[2] It has to be reported that the continuum counting rates for the blank are above those for the Roman lead samples, as a consequence of the less effective shielding. Furthermore, the γ-peak at 46.5 keV is also due to the blank.

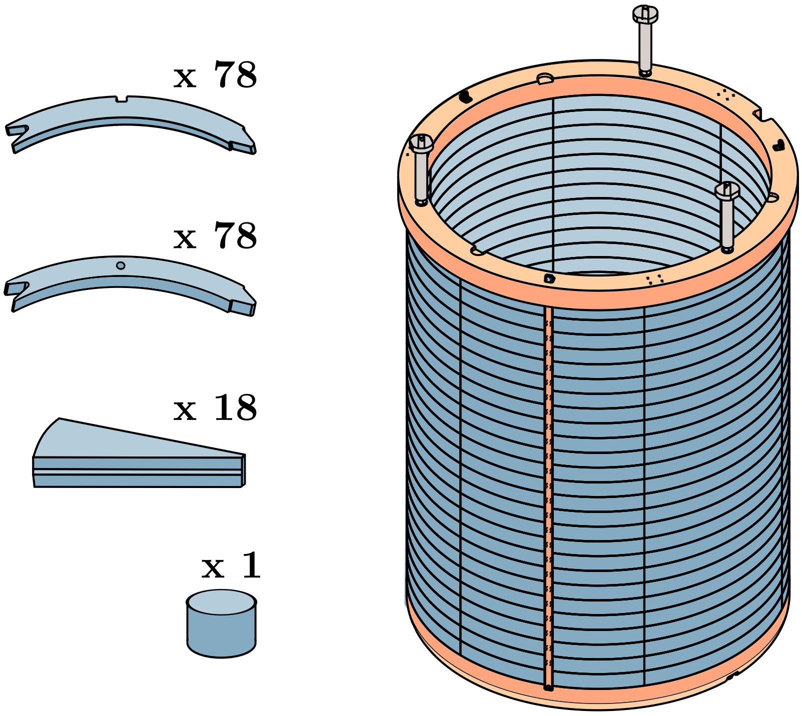

FIG. 6.5: Rendering of the CUORE ILS and of the single components made of ancient Roman lead. The numbers indicate the how many of each part are present in the shield.

slices plus a central plug. Together, side and bottom almost completely close any line of sight with a 6 cm thick lead layer.

The thermal link to the 4 K stage consists in copper braids connecting the 4 K plate to the ILS top ring. The full thermalization of the shield is guaranteed by thin sector-shaped copper foils placed between each pair of rings. These are in turn connected to 3 copper bars running across the ILS side. The bars thermally link the top ring to the support plate, thus allowing for thermalization of the latter and of the bottom lead.

The link to the Still plate is not a problem since the steel thermal conductivity is poor at low temperatures. Together, the heat conduction of the support structure and the radiative heat transfer from the ILS, dissipate $\sim 240\,\mu$W[3] and $\sim 110\,\mu$W, respectively, on the Still stage. Given that the cooling power at this stage is ~ 3 mW (sec. 5.2), a power dissipation of $\lesssim 350\,\mu$W is therefore tolerable.

6.4 Preliminary operations on the ingots

After lying for two thousands years on the sea floor, the ingots were covered by residues of seaweeds and shells and by a thick layer of limestone. Moreover the surfaces were mostly corroded. Before proceeding with the casting, the removal of the outermost layer appeared therefore as a necessary step to prevent the excessive formation of dross and slag during the lead melting. The waste could in fact enter the mold along with the molten lead, with

[3]See Ref. [165] for the of conductivity of SS 316LN at low temperatures.

FIG. 6.6: (Left) Cut of the ingot producer cartouche. (Right) Ingot after the cut.

the risk of introducing additional contamination in the final pieces.

However, the first operation to be performed on the ingots consisted in the cutting of the top parts, those containing the cartouches and thus those with the most significant archaeological value. The cutting operation was designed together with the Archaeological Superintendence of Cagliari and Oristano in order to be as less invasive as possible and to minimize the risk of damaging the cartouches.[4] It was thus decided to proceed with a horizontal cutting, to be performed by a power hacksaw. A jet of coolant/lubricant was constantly supplied to the saw blade since the surface to cut was quite large ($\sim$ 150 cm^2) and the operating time was of several hours per day (about one hour per ingot for $\sim$ 8 ingots per day). Due to preciousness of the material, the lead chips ($\sim$ 100 kg in the end) were all collected, although not used for the CUORE shield, since they should have been washed from the lubricant before the casting.

The whole operation was documented and pictures before, during and after the cut were taken for each ingot (Fig. 6.6). The cut cartouches have been stored, waiting either for the shipment back to the National Archaeological Museum of Cagliari or for the installation of a permanent exposition at LNGS.

The "cleaning" of the lead pigs was carried out with the dry-ice blasting technique.[5] Due to the high toxicity of the lead powder, the whole operation had to be performed in a dedicated environment (sealed and isolated from the external world) by specialized workers (provided with all the personal protective equipment). To guarantee a better result, still minimizing the amount or removed material, each ingot underwent two cleaning cycles. The final appearance after this operation is shown in Fig. 6.7.

These operations interested 233 ingots, corresponding to about 6.5 tonnes of material. Considering the amount of lead required for the CUORE shield, for a safe number of spare parts and for an equivalent volume of the kettle (see Sec. 6.5.2), this value was exceeding the needs of about 1.3 tonnes. Although this may seem to leave a too large margin (i. e. more ingots than actually needed were used), it has to be noticed that performing a successive

[4]In fact, the damaged cartouches that have been damaged was in total of about 5 over 270.

[5]During dry-ice blasting, dry ice, i. e. the solid form of CO_2, is accelerated in a pressurized air stream and directed toward a surface in order to clean it.

FIG. 6.7: Lead pigs after dry-ice blasting.

reduced cycle of cutting and cleaning operations on a small number of ingots (to be used in other occasions in the future) would have implied an increased cost and a more severe risk of damaging the cartouches than doing the same operations during this large-scale cycle. Also, an uncertainty that had to be considered consisted in the content of soil, small rocks and mineral remains inside the lead pigs that could reduce the effective amount of lead.

6.5 Casting of the Roman lead

The casting proved to be the most delicate operation involving the ingots. The major risk to be averted consisted in a possible contamination of the material and especially a contamination from Rn when the lead was in the molten phase.[6] A dedicated procedure was therefore established, and checks and tests took place all over the initial part of the casting period. This "debugging" turned out to be considerably long, but it allowed to reach and maintain high cleanliness standards and to actually minimize the risks for the lead.

6.5.1 Working environment

The casting was performed at the MTH Metalltechnik Halsbrücke GmbH & Co. KG foundry in Halsbrücke (Germany). MTH is specialized in manufacturing lead parts for the use in radio-protection and had already experienced the collaboration with physics projects (e. g. with the OPERA experiment [185]).

However, due to the peculiarity of our requirements, we imposed a much more stringent series of constraints. Therefore, a dedicated room was set up for the Roman lead casting and provided with all the equipment needed for the various operations:

- **electric furnace** with aspiration pump for the lead. Both the kettle ($45\times45\times35\,\mathrm{cm}^3$) and the pump (custom made centrifugal pump) were new and made of stainless steel.

[6] Actually, also contamination from modern lead could represent a concrete risk, since the casting was performed in a lead foundry.

FIG. 6.8: Pictures of the furnace. (Left) Overview of the furnace with the kettle, the closing structure and the ventilation system. On the back, the temperature control panel is also visible. (Center, top) The covered kettle: the entering pipes are the N_2 line, the pump lines and the temperature probe, respectively. (Center, bottom) Morning cold kettle refill. (Right, top) Kettle open for slug removal. (Right, bottom) Pre-heating of the parts to facilitate the kettle hot refill.

FIG. 6.9: Pictures of the mold. (Left) Closed mold. (Center, top) Open mold - shield side part configuration. (Center, bottom) Open mold - shield bottom part configuration. (Right, top) Pump pipe heating. (Right, center) Mold mouth flushed with N_2 while pouring the lead. (Right, bottom) New casted sector as appeared at the mold opening.

FIG. 6.10: Cut of the Roman lead. (Left) Ingot cutting before refill. (Center) Detail of a cut ingot section with the presence of a cavity with cotunnite crystals. (Right) Removal of the casting riser.

A closed structure connected to the ventilation system topped the kettle, which was anyway completely covered (Fig. 6.8);

- **hydraulic mold**. All the parts were custom designed and made of aluminum or stainless steel (Fig. 6.9);
- **nitrogen gas** (4.8 grade N_2 from Praxair) with the related lines for the constant flushing of the molten lead;
- **band saw** (Metallkraft VMBS 2012 HE) with high-speed steel blade (HSS, M42, $4,030 \times 20 \times 0.9\,\mathrm{mm}^3$ by Lenox). The table was covered with a stainless steel plate and custom blocks (also in stainless steel) were welded to it in order to fit the casted sector shape. No lubricant was ever used during the cutting operations;
- **table** able to carry more than $\sim 200\,\mathrm{kg}$ of weight. The table was covered with a stainless steel plate with the shield ring pattern engraved on the surface;
- **utensils** and **consumables**. All the tools coming to direct contact with the casted parts were made of stainless steel or aluminum bronze.

6.5.2 Process

The full cycle of activities covered about the whole day. The first operation (in the early morning) was the kettle refill with the ingots (Fig. 6.8). In order to maximize the amount of lead that could be inserted, it was decided to cut the lead pigs in two halves (Fig. 6.10).[7] In particular, it has to be noticed that, since the pump required the presence of at least $\sim 200\,\mathrm{kg}$ for the optimal functioning, the kettle could never remain completely empty.

The furnace could then be turned on and both its and the kettle temperatures were set to about $500\,^\circ\mathrm{C}$ ($T_{\mathrm{melt}} = 327.46\,^\circ\mathrm{C}$ for lead). In the meanwhile, it was possible to proceed with the cut of the casting raisers of the parts produced during the previous day. This and, in general, all the operations implicating the handling of the casted parts were always

[7] This allowed to find numerous cavities inside the ingots with the presence of minerals as the product of corrosion of the lead in the sea water, namely cotunnite ($PbCl_2$, Fig. 6.10) [181].

FIG. 6.11: New casted sectors. The casting raisers are still attached to the pieces.

performed wearing powder-free gloves (Fig. 6.10) and the involved surfaces and tools were cleaned as frequently as possible with isopropyl solution.

When the furnace temperature reached $(250-300)\,^{\circ}\mathrm{C}$, we flushed N_2 gas on the lead ($25\,\ell\ \mathrm{min}^{-1}$). The flow was never interrupted until advanced cool down at the end of the working day. This allowed to keep the O_2 level in the kettle $\lesssim 2\%$ when the lead was in the molten phase and thus to prevent a contamination from Rn. The mold heaters were also turned on and set to $(210-250)\,^{\circ}\mathrm{C}$. Once all the temperatures reached the established values, it was possible to begin with the casting.

The casting operation sequence (Fig. 6.9) required about half an hour for each new part. It started with the heating (with an acetylene flame) of the pump pipe connecting the kettle to the mold. In the meanwhile, N_2 ($15\,\ell\ \mathrm{min}^{-1}$) was flushed in mold for about two minutes. Then, the N_2 was rapidly brought at the level of the mold mouth and the molted lead was poured inside the mold.[8] After waiting for $(5-10)$ min, the mold was opened. The new sector or slice (attached either to the fixed or to the movable side of the mold) was hooked up with a wise and moved to the table (Fig. 6.11) and an identification number was engraved on the casting raiser.

The absence of a release agent in the mold caused a sudden solidification of the lead, thus resulting in a lower quality of the surfaces (less smooth), especially those far from the casting raiser. Apart from the aesthetic issue, this implied the need for more attention in handling the parts due to the greater ease in dirtying the surfaces. However, the risk of introducing any contamination from an external agent was in this way completely avoided.

The morning refill of the kettle could allow the casting of at most 8 sectors. After these, the remaining lead level was ~ 15 cm. Then, it was necessary to perform another refill but, in this case, with the molten lead inside the kettle. This "hot refill" was mainly done with the casting raisers. Indeed their masses, being of $(5-7)$ kg *vs.* ~ 25 kg of the final part, constituted a good material reservoir. Instead, only a minimum amount of half-ingots was used during this operation since the presence of cavities inside the ingots could case molten lead splashes, thus with a non negligible risk of injuries. To facilitate the melting of the

[8] The first ~ 20 kg of molten lead were actually not used since they collected possible contamination from the (new) pump pipe.

FIG. 6.12: Compliance test of a new ring (Left) and of the bottom disk (Right).

FIG. 6.13: (Left) Each casted part is wrapped in a vacuum sealed plastic bag. (Right) Box ready for shipment to LNGS.

new inserted parts, these were actually placed on the edge of the furnace few hours before the refill in order to pre-heat up to $(70-80)\,°\mathrm{C}$ (Fig. 6.8).

Periodically, a few times along the whole production, the removal of the slag on the lead surface proved to be necessary (Fig. 6.8). The collection of the material was performed with a kitchen skimmer. During both the slag removals and the hot refills, the kettle was actually open to air for less than two minutes. If this interval was not enough, the time to restore the nitrogen atmosphere was anyway given to the system before resuming the operation.

Every evening, after the casting, if the number of sectors was enough (each day only one type of sector was casted), it was possible to proceed with the compliance test of new rings. These were assembled by following the pattern engraved on the table surface and a jig was used to check the correct hole positions (Fig. 6.12). If the test was successful, a new identification code (ring letter A to Z followed by the a sequence number) was engraved on each sector. In the end, a similar check was performed also for the bottom disk.

The last operations on the new casted parts consisted in the sealing in plastic bag and

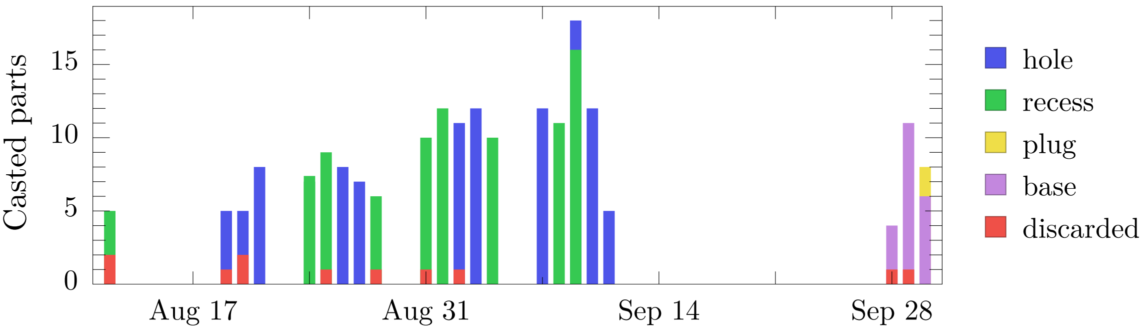

FIG. 6.14: Statistics of the ILS casted parts. The different colors refer to the various typology of sectors (see Sec. 6.3). The activity interruption after the first day was due to problems with some parts of the mold (then substituted), while the one in the central part of September was due to the modification of the mold to allow the casting of the base sectors.

in the assembly of the box for the shipment (Fig. 6.13). Despite the easiness in principle, in practice it was very hard to handle the sectors due to the large mass and to the fragility of the bags. Protective plastic sheets had to be wrapped around the most sharp parts (extremities and central parts for the sectors with the recess) before proceeding with the sealing and more than one bag could be used if the vacuum was broken the first time. This actually happened numerous times, especially during the positioning in the boxes, where even the smallest adjustments required the lifting of the sectors. But in the end, we were able to prevent the exposure of all the parts to dust, air and moisture during the storage period at MTH and the shipment to LNGS.

The casting of the Roman lead at MTH took place between August and September 2015. Preliminary meetings between the INFN and the MTH personnel and inspections at the foundry allowed to define a general protocol for the casting process but the final version here summarized could be established only after the first days of working activity. The whole casting was continuously monitored and assisted by at least one scientific supervisor.

A summary of the casting statistics is shown in Fig. 6.14. It can be seen a constant increase of the weekly production and, conversely, a reduction of the discarded parts.

In the end, 194 parts were casted (including spare and discarded parts).[9] The realization of the CUORE ILS has been the largest scale melting ancient lead by far.

6.6 Shield assembly

After the lead arrival at LNGS, it was possible to begin with the assembly of the ILS. Since it was not feasible to work directly inside the cryostat clean room, a dedicated environment had to be prepared in the CUORE hut in order to guarantee adequate cleanliness standards (Fig. 6.15).

First, the disk and the base ring were assembled. Then, the thermalization bars and the threaded rods were installed. The construction proceeded from bottom to top by

[9] Additional lead pigs were casted to recover all the lead present in the mold at the end of the CUORE ILS part production.

alternating rings and copper foils The central plug and part of the sector with the hole needed to be machined before their insertion. The whole set of operations took few days in the second half of October 2015.

Once the assembly was completed, the shield was lifted, attached to the cryostat and equipped with thermometers. It was then possible to start Run 4.

FIG. 6.15: (Left) Pictures taken during the shield assembly. (Right) The ILS attached to the CUORE cryostat.

Chapter 7

Results from the Mini-Tower

The final goal of the cryogenic system commissioning was to show that the CUORE cryostat constitutes a suitable environment to run a bolometric array. In order to prove it, a test detector, the Mini-Tower, was operated inside the cryostat.

A campaign of acquisition and analysis of the Mini-Tower data interested a large part of Run 4. The study of the collected information allowed to figure out how to optimize the cryogenic performance, especially the energy resolution.

7.1 The Mini-Tower detector

In the identification of a proper bolometric setup to be operated as a test detector for CUORE inside the cryostat, a series of requirements needed to be satisfied:

- the structure had to be sufficiently close to that of CUORE. The detector had to be a valid representative of possible future issues for CUORE itself in order to indicate possible solutions;
- the number of bolometers had to allow the collection of a good statistics in a short time to avoid delays of the commissioning;
- the setup had to be easy to handle and "flexible" (e. g. in terms of positioning, cable path, ...) according to the variable demands by the cryostat (in evolution during the commissioning phase).

Given the previous considerations, the adopted design consisted in a smaller version of a CUORE tower. A structure made of 2 floors, was therefore assembled starting from salvaged parts from the detector assembly: the TeO_2 crystals, for a total amount of 8, the copper frames and columns, the PTFE holders, the wire trays and covers of the CUORE detector (left panel of Fig. 7.1).In particular, the 4 crystals composing the top floor were those tested during the CCVR 10 [131].[1] Instead, the 4 composing the bottom floor were

[1]The CUORE Crystal Validation Runs (CCVRs) were cryogenic measurements designed to test the TeO_2 crystals upon their arrival at LNGS. In each CCVR, 4 crystals randomly chosen from a batch were

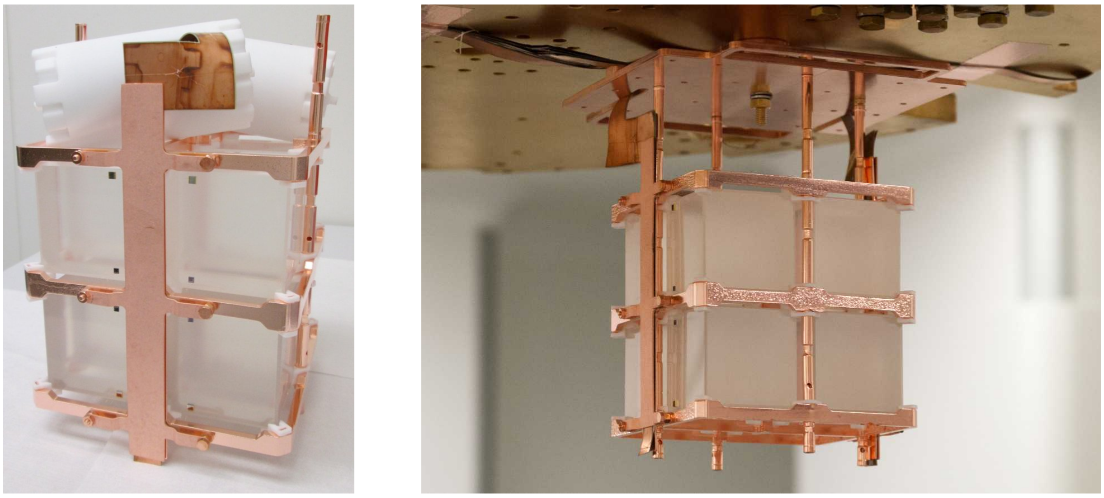

FIG. 7.1: The Mini-Tower bolometric array. (Left) The detector after the assembly. (Right) Mini-Tower attached to the MC plate before the cool down of Run 2.

crystals rejected for the CUORE assembly due to an accidental exposure to Araldite vapors occurred during the sensor gluing phase. The crystal gluing, the tower mechanical assembly and the wire bonding procedures followed the new CUORE protocol defined for the construction of the CUORE detector (see Sec. 3.2.3).

Furthermore, the use of the CUORE electronics and the DAQ allowed to test and debug CUORE tools not only for the setting adjustments and the parameter monitoring, but also for the data analysis.

7.2 Operating conditions

The Mini-Tower was first installed inside the CUORE cryostat during Run 2 (see Sec. 5.8). Since the TSP was not present at the time, a temporary support was prepared to allow the detector installation just below the MC plate. However, the MC plate is coupled to the cryostat structure and no vibration damping system was inserted between this and the detector. The expectations of observing a signal were low due to the too high noise level. In fact, this did not allow to reach a sufficient sensitivity to identify the pulses. Moreover, the effects of the leak became visible on the detector already ~ 1 day after the circulation, soon before the increase of the leak rate signal (see Sec. 5.8.2).

By moving the Mini-Tower anchoring from below the MC plate to the TSP after its installation in the next run (Run 3) surely improved the situation. Unfortunately, this time it was the premature interruption of the cold test to prevent the study of the detector response.

It was only during Run 4 that an extensive campaign of data acquisition could be performed. First, the analysis of the noise power spectra acquired with the Mini-Tower made

mounted in a setup similar to that of a CUORE tower and operated as bolometers in order to test the performance and the compliance to the strict radiopurity requests.

TABLE 7.2: Bolometer characteristics at the selected working point (stars in Fig. 7.3).

Channel	V_{bias} [V]	V_{bol} [mV]	I_{bol} [mA]	R_{bol} [MΩ]
1	3.03	17.7	301.1	58.8
2	5.01	13.2	499.7	26.4
3	3.53	18.1	351.4	51.4
4	3.53	13.7	351.3	39.0
5	2.01	16.9	199.7	84.7
6	2.01	16.2	199.8	81.0
7	3.53	17.5	351.5	49.7
8	3.22	15.8	320.5	49.2

it possible to study the response of the system to the various applied solution for the noise abatement (see Sec. 5.10.3).

The final working configuration was obtained by rigidly coupling the cryostat to the MSP, by blocking the support structure to the basement and by suspending all the external cables and the cryostat connection lines to the ceiling. The ELS was raised and thus surrounding the cryostat and the Minus K™ isolation system was activated.[2] The situation could be further improved by switching off the ventilation and the Rn abatement system inside the cryostat clean room.

It was then possible to proceed with the detector setup. As described in Sec. 2.4, in order to obtain the readout voltage signal, a steady bias voltage has to be applied to the NTDs. The choice for a proper value for this bias voltage is made by constructing a set of load curves at different temperatures. The result is shown in Fig. 7.3. Each plot refers to a Mini-Tower bolometer. The stars indicate the working points, situated just before the inversion point in order to maximize the signal amplitude and the signal-to-noise ratio.[3]

The identification of the working point on the curve allows to reconstruct the corresponding values of V_{bol}, I_{bol} and R_{bol}. These values are reported in Table 7.2. It can be seen that the spread among the channels is quite large for each of the parameters. In particular, the various I_{bol} (except for channel 2) are the range of CUORE-0 [136]. The same happens for R_{bol}, although T is lower in this case ($\sim 6.3\,\mathrm{mK}$ *vs.* $10.05\,\mathrm{mK}$ of CUORE-0).

7.3 Data analysis

The final data taking with the Mini-Tower consisted in a 4-run dataset (DS3013 from runs R300555, R300557, R300560 and R300562) covering almost 60 hours. Of these, about 18 hours saw the presence of an external calibration source (^{232}Th from a thoriated tungsten electrode). In Fig. 7.4, a scatter plot with the event distribution as a function of the time

[2] A dummy load of $\sim 800\,\mathrm{kg}$ of lead bricks was temporary placed on the Y-beam to simulate the effect of the detector.

[3] Actually, some of the V_{bias} had to be changed due to some problems related to the electronics.

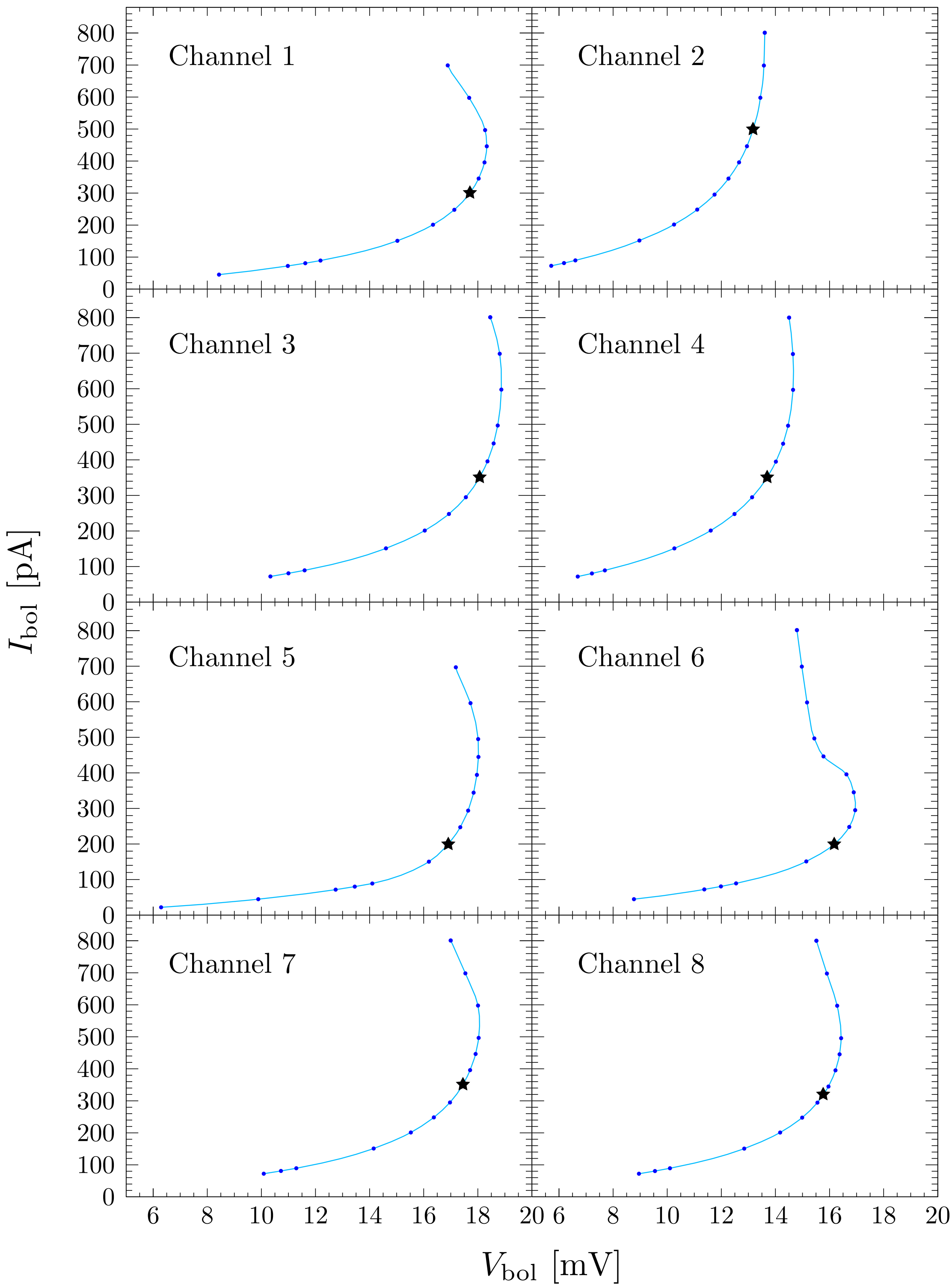

FIG. 7.3: $V-I$ load curves for the characterization of the Mini-Tower detector. The stars indicate the chosen working point.

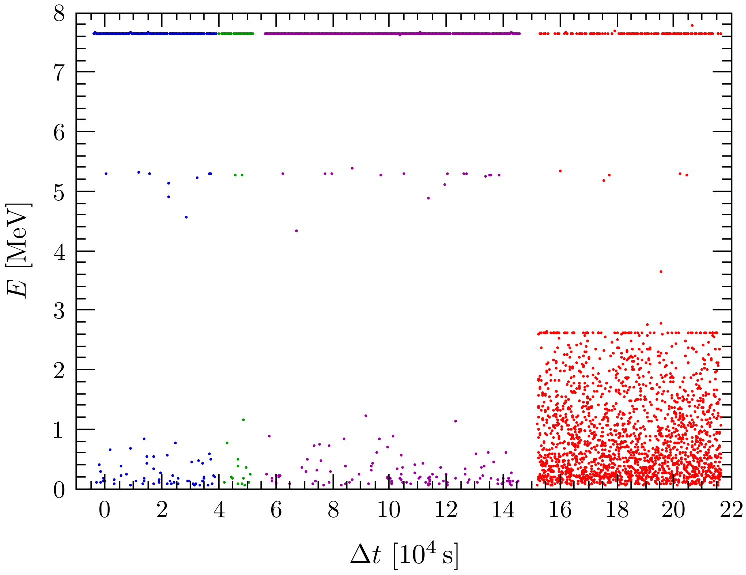

FIG. 7.4: Event distribution in time of Channel 1. The different colors refer to the different runs of dataset DS3013: R300555 (blue), R300557 (green), R300560 (purple), R300562 (red). The presence of the calibration source during run R300562 translates in a much larger event rate. In particular, the 2615 keV ^{208}Tl is clearly visible. The line at $\sim$ 7650 keV is generated by the pulser heater events.

is shown.

The data were collected using a custom designed DAQ software package, called Apollo, which had already been used in CUORE-0 and will be used in CUORE. The software reads the continuous data stream from the digitizing boards and writes a corresponding continuous data file that stores all waveform data information.

At the same time, Apollo triggers on the waveforms when the signal derivative passes a set threshold and separately writes the triggered events. Each event consists in a portion of continuous waveform (collected at 125 Hz) spanning from 1 s before to 4 s after the trigger. A typical pulse is shown in the left panel of Fig. 7.5. The event waveform is stored in the triggered data file with other event information, e. g. the channel, the trigger time, the event number, . . .

The data processing was performed with another software customarily designed for CUORE, called Diana. Diana is a modular software. It loops through all the triggered wave forms and processes each of them in a series of production steps. At the end of this operation, the data format will pass from triggered files to Root NTuples ready for the physics analysis.

The data processing consisted in the following steps:

- preprocessing;
- amplitude evaluation;
- gain stabilization;
- energy calibration;

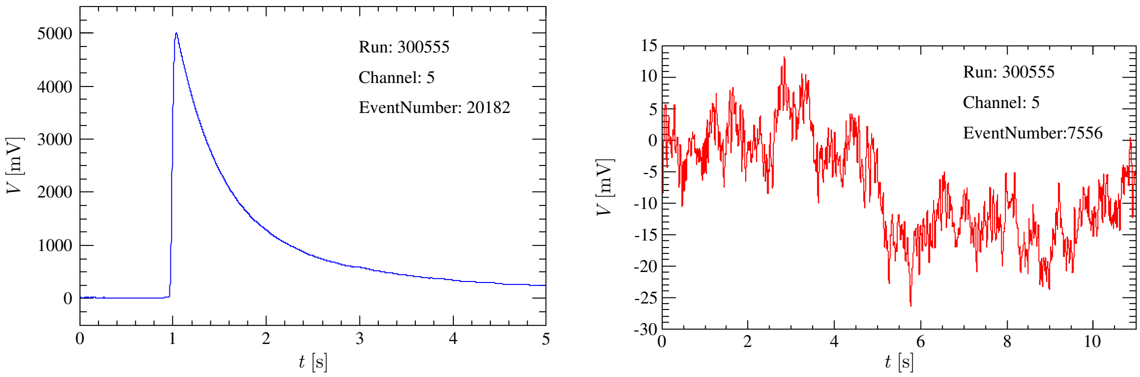

FIG. 7.5: Example of Mini-Tower events. (Left) Signal pulse from the 2615 keV ^{208}Tl line. (Right) Typical noise event.

- (coincidence rejection).

This action list mostly coincides with that for the CUORE-0 and CUORE data analysis. However, the used modules have been specifically edited (and simplified) for the Mini-Tower. Furthermore, the data blinding for the $0\nu\beta\beta$ analysis (see Sec. 3.3.2) did not interest the Mini-Tower data.

7.3.1 Preprocessing

During the preprocess, Diana first measures the pretrigger, i. e. the 1 s region before the trigger. In particular, the software evaluates the slope and the RMS of the pretrigger data to determine the detector behavior before the event occurs.

Then, it counts the number of pulses in the event. After differentiating the pulse and determining the RMS of the derivative, each peak in the differentiated waveform (local maximum) is counted as a pulse if the value exceeds 5 times the RMS.

7.3.2 Amplitude evaluation

Since thermal pulses are superimposed to stochastic noise, a simple " maximum - minimum" algorithm would not provide an optimal estimate of the pulse amplitude. In turn, this would not give the best achievable energy resolution. Therefore, the Optimum Filter (OF) technique [186] is used for the analysis of CUORE (and predecessors) data, including those from the Mini-Tower.[4]

The underlying idea of the OF is to build a filter that, when applied to the raw-pulse, produces a pulse with the maximized signal to noise ratio. The filtered pulse is then used to evaluate the signal amplitude. In the frequency domain, the OF transfer function $H(\omega)$ is given by

$$H(\omega) = K\,\frac{S^*(\omega)}{N(\omega)}\,\mathrm{e}^{-\mathrm{j}\,\omega\,t_{\max}} \tag{7.1}$$

[4]For CUORE-0 and CUORE, a generalized decorrelating OF has also been implemented in Diana, which accounts for correlations amongst the channels [147, 187].

where $S(\omega)$ is the Fourier transform of the ideal acquired signal, i.e. a reference pulse which represents the response of the system to an energy deposition, $N(\omega)$ is the noise power spectrum, while t_{max} is the delay of a given pulse with respect to the reference one. An appropriate normalization factor K is needed to obtain the correct event energy.

The role of the OF is to weight the frequency components of the signal in order to suppress those frequencies that are more affected by the noise. As it can be seen from Eq. (7.1), the waveform filtering requires the knowledge of both the reference pulse and the noise PSD $N(\omega)$.

For each detector, the average pulses were built by using the 2615 keV ^{208}Tl events in the calibration run.[5] The averaging process consists of two steps: the alignment of the pulses and the actual averaging. Diana measures the peak position (in time) of each pulse. This is determined by differentiating the pulse and interpolating where the derivative crosses from positive to negative. Then, all the pulses are aligned so that the maxima occur at the same time. After the alignment, the pulses are linearly averaged together.

The noise PSD is obtained by acquiring many detector baselines in the absence of thermal pulses and averaging the corresponding square modulus of the Fourier transform (Wiener–Khinchin theorem). In fact, apart from triggered events, Apollo also collects random triggers intended to be stochastic noise samples. In the right panel of Fig. 7.5, a typical noise event is shown. These triggers are fired at evenly spaced intervals of 200 s.

In Fig. 7.6, an example of average pulse (top panel) and noise PSD (bottom panel) before and after the filtering process are shown.

From the filtered waveforms, Diana evaluates the pulse amplitude by locating and interpolating the pulse peak. In particular, the peak identification algorithm searches for the first maximum after the trigger. In order to reduce rounding errors, this, together with the immediate neighboring samples, are interpolated with a parabolic function. The amplitude is defined as the global maximum of the parabola, and the time of the peak position as the time of this maximum.

7.3.3 Gain stabilization

As described in Sec. 2.5, a fundamental issue when operating a bolometer is to maintain a constant detector response, since the gain depends on the working temperature.

The gain correction, or “stabilization”, against the temperature variations usually uses the constant energy heater pulses as a tracer of the gain instabilities. The heaters are pulsed every 300 s with a voltage pulse of 100 µs duration. The Joule heating in the chip in turn heats the crystal, simulating a particle event. The voltage is set so that the heater pulse reconstructed energy is of the order of $(7-8)$ MeV, well above the natural radioactivity region. Apollo automatically triggers on heater pulses and the corresponding events are

[5] More in general, for the CUORE analysis, the average pulse is measured for each channel in each dataset. The data production process is repeated twice. The first time using the pulser heater events as substitutes for those from the 2615 keV ^{208}Tl line since the energy is still unknown. Instead, the second time with the actual physics events.

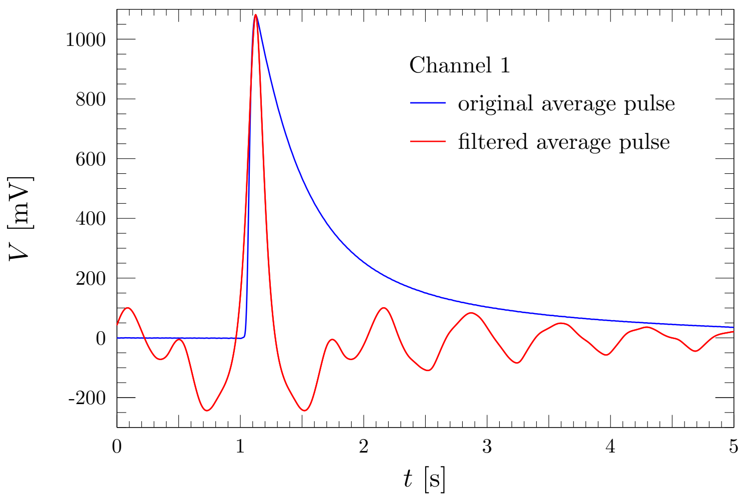

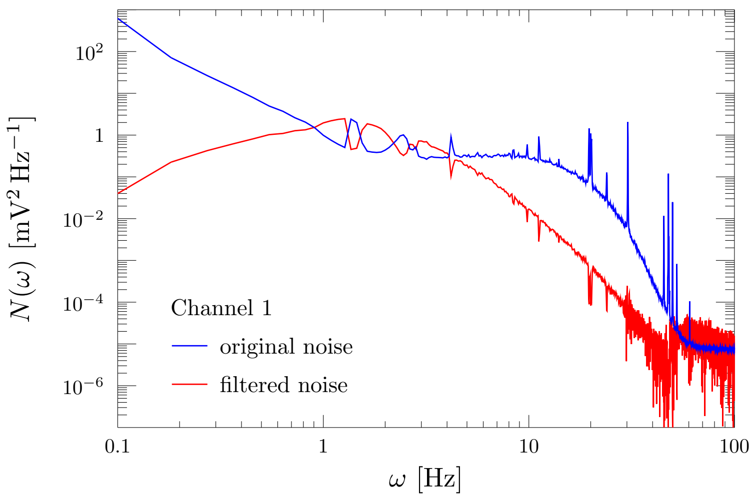

FIG. 7.6: Example of average pulse (top) and noise PSD (bottom) before and after the filtering with the OF.

flagged.

Diana measures the gain dependence on temperature by a linear fit of the stabilization pulse amplitude *vs.* the value of the baseline just before the pulse. In fact, this is an indicator of the temperature. Once this relationship is known for each channel, the amplitude of all the pulses is corrected accordingly, namely a linear scaling is assumed and the amplitude is divided by the amplitude of heater pulse with the same baseline value.

Temperature stabilization

It is worth to notice that the above mentioned gain stabilization works for temperature variations of the order of a few percent. More generally, if the intrinsic instabilities in the cryogenic system cause larger temperature fluctuations in the detector, these will spoil the energy resolution.

To compensate for these instabilities, a Proportional-Integral-Derivative (PID) controller had already been implemented in Cuoricino [188] and CUORE-0 [136] and an im-

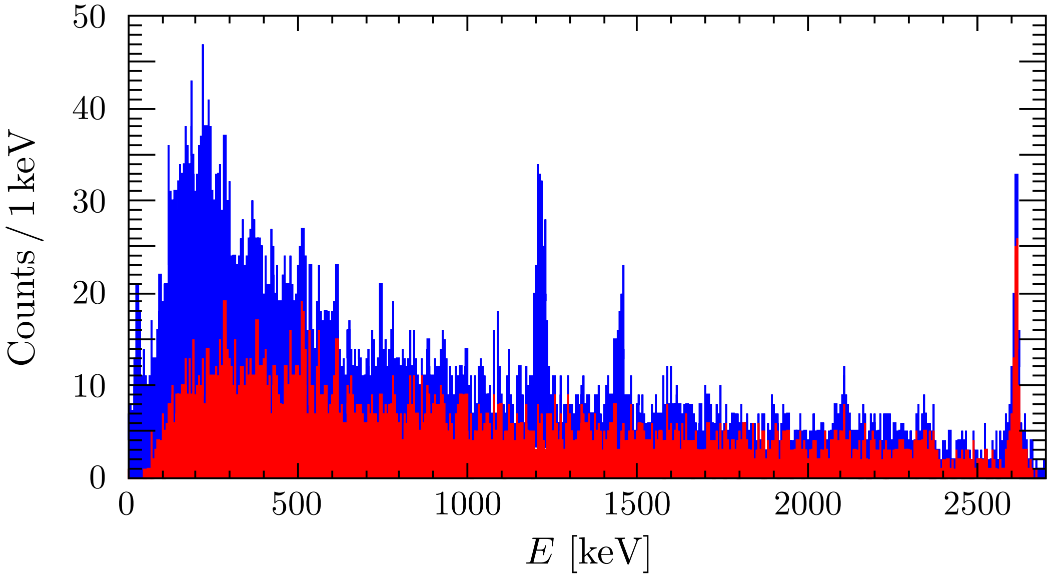

FIG. 7.7: Combined spectra in the region (0 − 2700) keV before (blue) and after (red) the application of the cuts on the pulse shape. The peak at ∼ 1200 keV is due to the heater pulser events on Channel 7, while the one at ∼ 1400 keV is due to a mis-calibration problem on Channel 8 during one of the runs.

proved version will be implemented in CUORE. The PID controller is a control loop feedback mechanism that continuously calculates the difference between the desired working temperature and the measured one and applies a correction accordingly. The temperature acquired by NTDs placed on the TSP (see sec. 4.7.1) is taken a reference. The chosen value is a few mK above base temperature. In this way, compensations are possible both in raising and decreasing its value. The temperature is stabilized by an offset-correcting circuit in the front-end channel, which generates the reference operating point for the feedback loop. A variable power is injected on the TSP via a heater accordingly. With this configuration, it was actually possible to minimize the effects of the cryogenic apparatus instabilities on the detectors.

Unfortunately, along with the tests of the Mini-Tower detector, the CUORE PID controller was also being tested and it was thus not operational during the data taking. In fact, this was done at the MC temperature (∼ 6.3 mK). On the other hand, this also makes it realistic to expect improvements in the future CUORE performance.

7.3.4 Pulse shape analysis

The CUORE detectors do not allow to perform any particle identification. Therefore, it is not possible to reject the contribution to the background rate by knowing either the different kind of radiation (α *vs.* β/γ) or the event topology (surface events). However, "bad" events like noise spikes, pile-up or events with a non properly measured energy can be recognized by means of proper shape factors which isolate the classes of pulses corresponding to single particle interactions. In particular, the following pulse shape properties are considered:

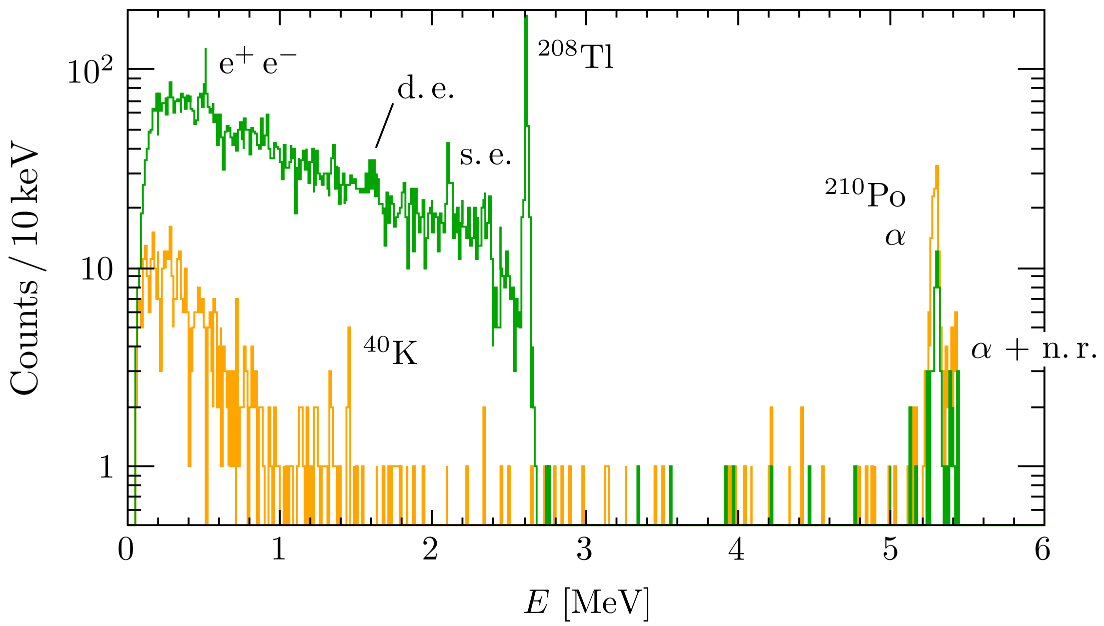

FIG. 7.8: Calibration (green) and background (orange) spectra obtained with the Mini-Tower. It is possible to identify some peaks due to the presence of the calibration source: electron-positron annihilation ($e^+ e^-$), ^{208}Tl with single and double escapes. The ^{40}K and ^{210}Po (α and α + nuclear recoil) peaks due to the known radioactive background are also visible.

- rise time, defined as the amount of time needed for the pulse to rise from 10% to 90% of its total heigh. It is usually of the order of a few tens of ms;
- decay time, defined as the amount of time needed for the pulse to decrease from 90% to 30% of its total heigh. It is usually of the order of a few hundreds of ms;
- TVL (Test Variable Left) and TVR (Test Variable Right), indicators (χ^2 statistics) of how much the filtered pulse differs from the filtered reference pulse on the left and right side with respect to the maximum, respectively;
- baseline slope, defined as the best fit slope of the first part of the pretrigger.

The distributions of these variables vary from channel to channel and are dependent on the energy. Consequently, the applied cuts had to be specifically tuned for each channel. The results are shown in Fig. 7.7, where the combined spectrum is shown before and after the application of the cuts on the pulse shape.[6] The cut efficiency, estimated as the fraction of events in the 2615 keV line that survives pulse-shape cuts, is of about 78%.

7.3.5 Energy calibration

After the amplitudes had been corrected for gain, it was possible to calibrate the pulse amplitudes with respect to known energies thanks to the energy scale provided by the external source inserted during the calibration run.

[6]A channel to channel (and dataset to dataset) tuning of the cuts was not feasible for CUORE-0 and it will not surely be possible for CUORE. In these cases, all the variables of interest are normalized in order to create a set of new equivalent variables with distributions independent channel, dataset and energy [147].

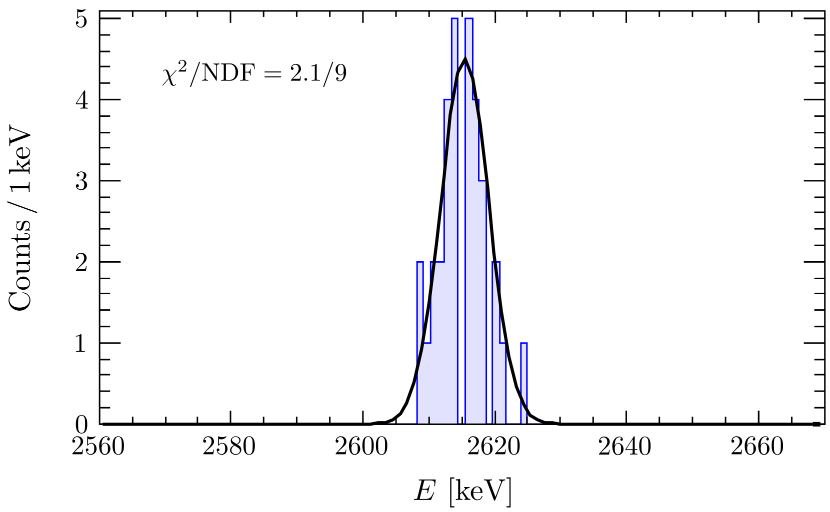

FIG. 7.9: Zoom on the 2615 keV ^{208}Tl peak region with Channel 2. The peak is fitted with a pure Gaussian function with mean (2615 ± 0.7) keV and FWHM (8.6 ± 2.2) keV.

Diana usually looks for 7 peaks from the ^{232}Th spectrum. Once enough calibration peaks are located, they are fit with a single Gaussian plus a linear background.[7] A second degree polynomial with forced passage through the origin is thus used as regression function from stabilized amplitude to peak energy for the means of the Gaussians.

The calibration algorithm used for the Mini-Tower is a (simplified) version of the one of CUORE-0 and CUORE. In fact, in this case most of the peaks were not identifiable and the software needed to be guided in the positioning of at least a few peaks. As a regression function, a linear polynomial was used. The calibration spectrum is shown in Fig. 7.8.

7.4 Mini-Tower performance

After the application of the cuts on the pulse shape, it was possible to study the final performance obtained with the Mini-Tower detector.

First, by looking at the 2615 keV ^{208}Tl line and considering the single bolometer gain, the signal amplitude was found to be on average $(60 - 75)\,\mu\mathrm{V\,MeV^{-1}}$, depending on the crystal. Although the range is quite large, this result can be compatible with the one obtained with CUORE-0 (see Sec. 3.3.1).

Then, the energy resolution could be measured. The baseline (0 keV), ^{208}Tl line (2615 keV) and pulser ($E_\mathrm{p} \simeq (7-8)$ MeV) energies were considered as references. The peak were fitted with a pure Gaussian. An example is shown in Fig. 7.9, while the full results are shown in Table 7.10.[8]

Values close to 10 keV FWHM energy resolution were very promising considering that further improvements and optimizations could still be performed, both on the system and

[7] Two of the peaks are actually fitted with two Gaussians (same width and fixed distance in between) since they are double peaks.

[8] Similar values (actually better on some channels) were also obtained by analyzing a former dataset (DS3008).

TABLE 7.10: Final FWHM energy resolution obtained with the Mini-Tower detectors at different energies. The case "@ 0 keV" refers to the baseline resolution.

Channel	FWHM [keV]			
	@ 0 keV	@ 2615 keV	@ pulser	(E_p [keV])
1	7.2	8.9	7.8	(7647)
2	8.1	8.6	8.6	(8075)
3	26.1	28.8	26.0	(8019)
4	10.2	12.6	10.9	(7623)
5	12.1	27.1	13.1	(8159)
6	15.3	11.5	16.9	(8325)
7	26.6	30.3	31.4	(1213)
8	31.0	31.8	25.7	(7535)

on the working conditions. More in general, the obtained results were satisfactory to consider Run 4 positively concluded. The success of the run led in turn to the conclusion of the CUORE cryostat commissioning.

7.5 Considerations on the background

As already mentioned in final part of Sec. 3.3.1, the almost flat background of CUORE-0 in the energy region $(2.7-3.9)$ MeV is dominated by degraded αs.

By looking at the Mini-Tower data in the same energy range and by excluding the $(3.1-3.4)$ MeV region due to the presence of the ^{190}Pt peak, a total of 8 counts survived the cuts (see the background spectrum in Fig. 7.8). Since the total exposure during the background runs is 0.028 kg yr, it is possible to estimate an "α-index" of (0.32 ± 0.12) counts keV^{-1} kg^{-1} yr^{-1}.

The fact that we get a value almost 20 times larger than CUORE-0 is not worrisome. In fact, it has to be considered that the Mini-Tower has been exposed to air (and thus to Rn) and directly manipulated by operators (and thus exposed to ^{40}K) for long periods between the runs. It is likely to assume the high rate to be caused by contamination successive to the assembly. A similar situation was not faced by the CUORE towers (see Sec. 3.4).

The observation of the counts around the ^{210}Po peak allows for an interesting (although qualitative) consideration. ^{210}Po α-decays with a 99.99% probability. The decay half-life is ~ 138 d, the reaction Q-value is 5407 keV and the α energy 5304 keV.

As it can be seen from Fig. 7.8, the Mini-Tower resolution allows to distinguish 2 peaks, which are due to either the absorption of the lone α particle and to the absorption of α particle + nuclear recoil, respectively. The former situation occurs if the decay takes place on the crystal surface or if the emitted α comes from an external source (e. g. copper frames, PTFE holders, . . .). Therefore, the contributions to the peak are expected to be equal from all the crystals, as actually observed, since the decaying ^{210}Po is a product of the Rn chain.

The latter situation occurs if the decay takes place inside the crystal, due to its intrinsic bulk contamination. The single contributions to the peak thus depend on the radiopurity of the raw material and on the crystal age. Te and Po are chemically affine, and so some Po impurities can be expected, but the amount can be assumed to be the similar for all the CUORE crystals. In this case, the amount of events from ^{210}Po will decrease according to the decay half-life time. The fact that we observed a much larger counting when comparing the newer crystals (those from the CCVR) with the older ones is compatible with the different production times.

Appendix A

Cryogenics: calculations and data analysis

A.1 Vacuum considerations

Due to the FCS, we can assume to have pure He as residual gas inside the IVC after pumping. This represents the worst scenario since ^{4}He is the only gas with a relevant vapor pressure at cryogenic temperatures (still $\sim 800\,\mathrm{mbar}$ at $4\,\mathrm{K}$ [111]).[1]

At low pressure and temperature, the "heat leak", i. e. the heat transfer by this residual gas, can be approximated by [189]:[2]

$$\dot{Q}\ \left[\mathrm{W\,m^{-2}}\right] = \frac{1}{100}\ C\ a\ P\,[\mathrm{mbar}]\ \Delta T\,[\mathrm{K}] \tag{A.1}$$

where P is the volume pressure, C is a constant of the gas and a is the gas accommodation coefficient. The values $C \simeq 2.1$ and $a = 0.5$ can be taken for He at a few K. By expecting each vessel to constitute a sealed ambient, the temperature difference ΔT is that between two next stages.

The limit on the pressure tolerated by the system can be obtained by inverting Eq. (A.1). Therefore, its value depends on the considered thermal stages. Let us assume that the maximum heat transfer corresponds to 1/3 of the inner stage cooling power. The result is shown in upper part of Table A.1. The most stringent requirement on the vacuum inside the IVC is $\sim 10^{-8}\,\mathrm{mbar}$.

The IVC turbomolecular pump speed is $\sim 255\,\mathrm{l\,s^{-1}}$ (Sec. 4.4). The leak rate corresponding to the maximum P would thus be $\sim 5\cdot 10^{-6}\,\mathrm{mbar\,l\,s^{-1}}$. However, it has to be considered that the complex structure of the IVC volume increases the pumping impedance, and so the actual pumping speed is much lower. As a consequence, the maximum tolerated leak rate is also lower.

During Run 2 (Sec. 5.8.2), it was observed that a leak of the order of $10^{-4}\,\mathrm{mbar\,l\,s^{-1}}$ affected the detector behavior in ~ 1 day. After this period, it became impossible to

[1] Actually the vapor pressure of ^{3}He is higher, but its natural abundance is $1.37\cdot 10^{-6}$. Instead N_2 constitutes $\sim 78.1\%$ of air, but its vapor pressure is already $10^{-11}\,\mathrm{mbar}$ at $20\,\mathrm{K}$.

[2] This formula actually applies down to $4\,\mathrm{K}$. We are assuming its validity also for lower temperatures.

TABLE A.1: Maximum pressure tolerated by the various thermal stages due to the residual gas heat leak. The values are computed by inverting Eq. (A.1). The surface are taken from Table 4.4 (including the lone vessels). The cooling powers come from Secs. 5.2 (HEX and Still) and 5.10.2 (MC) and from App. A.2 (4 K and 40 K).

Stage	T [K]	A [m^2]	$\dot{Q}_{\text{power}}$ [W]	$P_{\max}$ [mbar]
MC	0.01	9.45	$3.0 \cdot 10^{-6}$	$2.1 \cdot 10^{-8}$
HEX	0.06	12.21	$5.0 \cdot 10^{-4}$	$1.8 \cdot 10^{-7}$
Still	0.8	14.84	$3.0 \cdot 10^{-3}$	$2.5 \cdot 10^{-7}$
4 K	3.5	24.08	2.5	$1.1 \cdot 10^{-5}$
40 K	35	29.66	$1.0 \cdot 10^{2}$	$4.3 \cdot 10^{-5}$

operate the Mini-Tower. If we assume that a similar behavior scales with the size of the leak, in order to run CUORE without getting disturbed for some years, a period ~ 1000 times longer, we should require a limit on the leak rate ~ 1000 tighter. Therefore, this should not exceed 10^{-7} mbar l s^{-1}.

Similar considerations on the vacuum requirements can be applied to the OVC. The main different in this case,especially for the 40 K stage, is that other gases contribute to the total pressure. Anyway, the hypothesis of pure He as residual gas still gives a fair approximation. The result is shown in the lower part of Table A.1. The most stringent vacuum requirement for the OVC is that from the 4 K stage, $\sim 10^{-5}$ mbar. The OVC turbomolecular has a lower speed than the IVC one, and the leak rate corresponding to the maximum P is now $\sim 10^{-3}$ mbar l s^{-1}. As discussed in Sec. 5.7, a similar value for the leak rate was reached during Run 1.3 after refilling the IVC with He (630 mbar at ~ 100 K) due to the IVC-to-OVC leak. Although the effect was clearly visible on the temperatures, this did not prevent the continuation of the cool down.

A.2 PT characterization

As already mentioned in Sec. 4.5.2, the 5 CUORE PTs are all PT415-RM by Cryomech. The behavior and the cooling power at the different temperatures are thus expected to be very similar. Anyway, before the installation in the CUORE cryostat, a more complete characterization in a test cryostat interested the PTs. Here, we report the results for the studies of PT 3 and PT 5.

Since the cooling power depends on the compressor pressure, a preliminary pressure scan needed to be performed in order to find the optimal range. In principle, working at higher pressures (although considering the finite dimension of the PT) guarantees better results, but this cannot be the only criterion for the choice in the case of CUORE.

PTs are designed to run for long periods at base temperature, while the cool down time is usually short, of the order of a few hours. In our case, instead, the cool downs last for

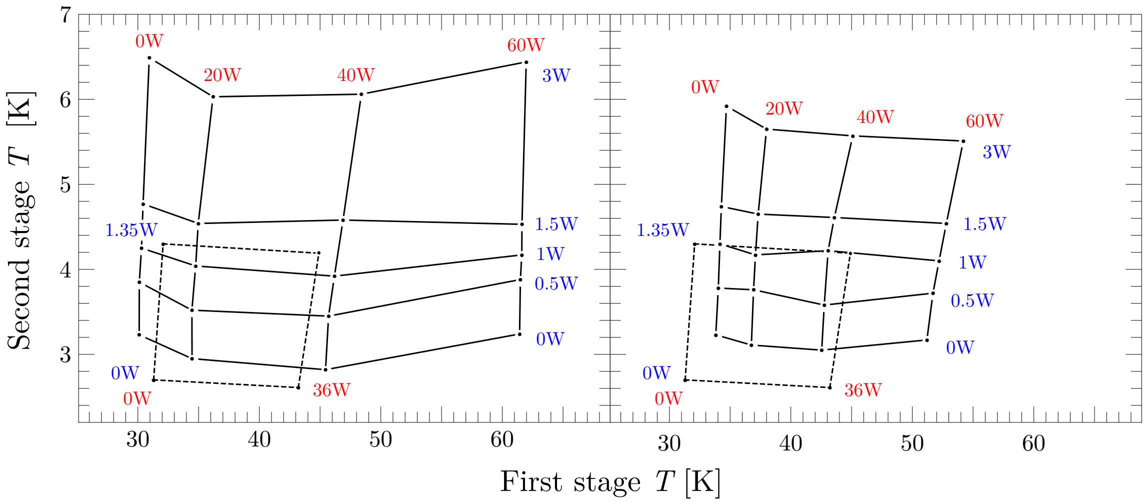

FIG. A.2: Thermal characterization of PT 3 (left) and PT 5 (right). The red (blue) values are the dissipated powers injected on the first (second) stage of the PT and are associated to the vertical (horizontal) lines. The dashed lines refer to the nominal values for a PT415-RM with 1 ft flexline.

several days. Since working with high pressure at high temperatures implies a larger effort for the compressors, we must reduce the pressure, at least in the initial phase of each cool down. Once the temperatures are low enough, it is possible to refill the compressors with additional gas, thus improving the cool down performance.

In the end, the He pressure spans over the broad range $(250-310)$ psi ($\simeq (17-21)$ bar), the specific working point actually depending on the run phase.[3]

The thermal characterization is performed by injecting power on the two thermal stages and recording the corresponding base temperatures [190]. The results is shown in the left and right panels of Fig. A.2 for PT 3 and PT 5, respectively. The nominal characterization (PT415-RM, 1 ft flexline) is superimposed as a reference. It can be seen that the 2 PTs, and more in general all the PTs, have slightly different behaviors. In particular, PT 5 shows better performance at higher dissipated power, thus in a situation closer to the real one when operated in the CUORE cryostat.

A.2.1 Power dissipation by inactive PT

The presence of an inactive PT constitutes a very large heat load for the cryostat, since it creates a direct solid link between the cold stages the external environment. The evaluation by Cryomech of the power dissipation from one inactive PT415 is in fact 8.6 W at the first stage (between 300 K and 35 K). Since the relevant quantity for the calculation is the temperature difference between the two thermal stages, it is then possible to roughly estimate the power loss between two generic temperatures at the first stage $T_{\rm high}$ and $T_{\rm low}$

[3]Actually, the working pressure depends also on the compressor type (the CUORE PTs are powered by CP1010 (4) and CP1110 (1) compressors by Cryomech).

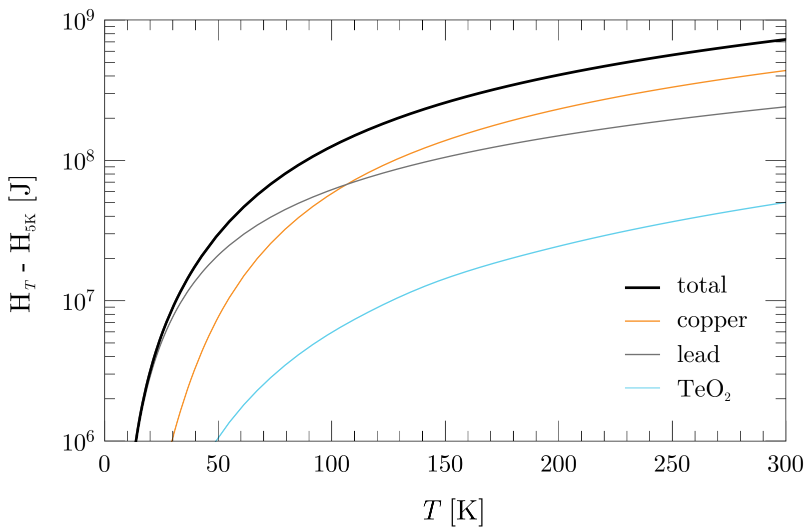

FIG. A.3: IVC enthalpy as a function of the temperature. The contributions from the different materials are derived from the specific heat at different temperatures of copper [191], lead [192] and TeO_2 [124] and from the masses of the single components (Table 4.4).

with a simple proportion:

$$P_{\text{loss}}[\text{W}] = \frac{(T_{\text{high}} - T_{\text{low}})\ [\text{K}]}{265} \cdot 8.6\,. \tag{A.2}$$

Instead, the power dissipation at the second stage, between 35 K and 4 K, is estimated by Cryomech to be ~ 0.4 W.

The fraction of heat conduction due to the convection of the gas inside the PT is $\lesssim 20\%$. Therefore, by emptying an inactive PT from the He, an improvement of the situation is expected at the first stage. On the contrary, a worsening is expected at the second stage since now the lowest temperature is facing a higher temperature, as actually observed during a dedicated test.

A.3 Cool down to 50 K

The total mass of the IVC components, between copper, lead and TeO_2, is ~ 13.5 tonnes. The heat content of the system to be extracted during the cool down is therefore very large. Quantitatively, the enthalpy difference between the room (295 K) and the PT first stage (40 K) temperatures is

$$\Delta H = \int_{40\,\text{K}}^{295\,\text{K}} C_{\text{IVC}}(T)\,\text{d}T = 6.9 \cdot 10^8\,\text{J}. \tag{A.3}$$

As it can be seen from Fig. A.3, this fraction corresponds to more than 95 % of total enthalpy of the system.

PTs alone would take too much time to reach base temperature. In fact, the cooling power at the second stage of a PT415-RM is at most $\gtrsim 100$ W close to 300 K. It quickly

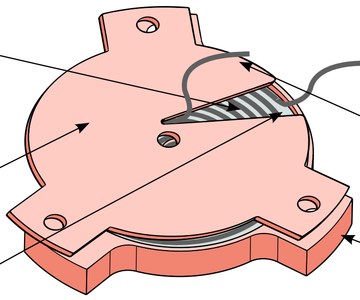

FIG. A.4: Rendering of the thermalizer of the mixture at 4 K installed during Run 3. The condensing line is In-soldered inside a copper frame installed on the 4, K plate.

decreases at lower temperatures, down to less than 50 W already at 100 K.[4] Moreover, PTs are designed to work at high temperatures only for short periods.

Imagining to cool the IVC mass down to 77 K using the enthalpy of LN_2 would not be feasible. The amount of nitrogen to handle would be very large, about 2000 ℓ even if able to exploit the whole enthalpy (up to the liquid-gas phase transition), but realistically closer to double this value (considering only the cold gas). But, most important, little control could be exercised on the cool down conditions, with a concrete risk of causing thermal shocks for the detector.

Therefore, a dedicated apparatus has been designed for the CUORE cryostat in order to cool the whole IVC (and detector) mass down to $\sim$ 50 K: the Fast Cooling System.

A.4 Mixture thermalization at 4 K

The thermalization of the mixture is one of the most critical among the technological aspects in a cryogen-free DR, since it involves a large power dissipation.

In the CUORE cryostat, the PTs are used to thermalize the mixture to $\sim$ 4 K during the circulation by forcing its passage in a circuit welded around the same PTs, between the two thermal stages (see Sec. 4.5.3). This choice is very convenient since it uses part of the PT cooling power that would remain otherwise unused. However, it also implies that the operation of the DU relies upon the correct functioning of a sub-set of the PTs.

In the idea of having two interchangeable condensing lines, a first change in the original DU configuration (passing from the test cryostat to the CUORE cryostat), was implemented during Run 2. This allowed to reduce the dependence on the PTs of the circulation (see Sec. 5.8).

During Run 3, two thermalizers for the mixture, one for each condensing line, were installed on the 4 K plate (Sec. 5.9) between the circuit on the PTs and the reinsertion of the condensing lines into the DU. The thermalizers compensate for possible performance worsening up to the loss of one of the PT thermalizing the mixture and guarantee a better stability of the inlet mixture temperature.[5]

[4] The full characterization of the PT up to environmental temperature is provided by Cryomech.

[5] As already mentioned, this solution allows for the continuation of the run in the unfortunate situation

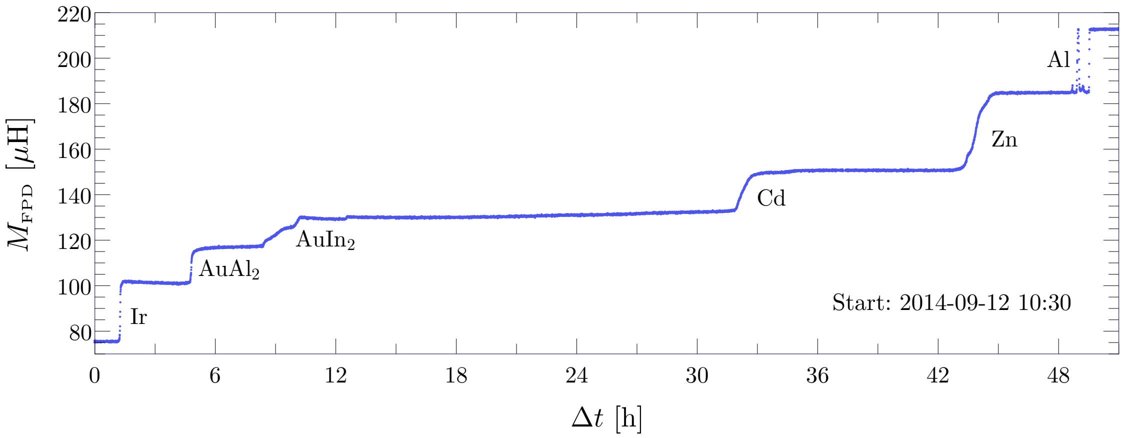

FIG. A.5: FPD inductance variation during part of the warm up in Run 1.3 dedicated to the calibration of the CMN thermometer. The superconductive transitions are clearly visible.

A rendering of the thermalizer is shown in Fig. A.4. The condensing line is In-soldered inside a copper frame which is in turn screwed on the 4 K plate. In order to guarantee the effectiveness of the solution, it was necessary to make sure that the time needed for the mixture to pass through the thermalizer (t_{CL}) is long enough to allow for the thermalization (t_{therm}). The most critical moment coincides with the initial phase of the circulation, when the mixture flow gets close to 10 mmol s^{-1} and the compressor pressure is about 2.5 bar.[6] t_{therm} can be derived starting from the He gas conductivity.

A rough estimate, obtained by assuming fixed values for the quantities involved in the calculations, gives $\sim$ 30 ms. Even if the He gas conductivity and heat capacity at a few K depend on the temperature [193], this result can be considered sufficiently conservative. t_{CL} is simply the ratio between the product of the gas molar density times the line volume and the flow.

By using a capillary of 0.8 mm in diameter, a spiral of $\sim$ 1 m is sufficiently long to give a value for $t_{\mathrm{CL}} \simeq t_{\mathrm{therm}}$ even for high mixture flows. Indeed, the time to pass through the thermalizer further increases to some hundreds of ms during the standard circulation at $\lesssim$ 1 mmol s^{-1}.

A.5 MC stage temperature monitoring

The readout of the temperatures in the range from some tens down to a few mK requires particular attention. Commercial RuO_2 resistors (and even most of the custom ones) cannot be employed below $\sim$ 50 mK [111] and the use of specific (and delicate) devices is thus needed.

The CUORE cryostat is provided with a CMN thermometer (see Sec. 4.7.1), positioned on the MC plate. This sensor was initially the only one sensitive at the lowest temperatures.

in which one of the lines is unusable and the PT thermalizing the other line has failed.

[6] Actually, the dependence of the DU functioning on a PT in this (transitory) phase is not an issue, since we are interested in the long term regime of the circulation. Anyway, this consideration allows for more conservative calculations.

During the commissioning, a NT was added (the CMN is still kept for redundancy). For both the CMN and the NT, reference temperature values are taken with respect to the set of superconductive transitions of a FPD, also placed on the MC plate. These transitions are very narrow and highly reproducible and span over a very broad range of temperatures thanks to the presence of both alloys and single crystal samples (table in Fig. A.6), allowing for a precise calibration of the sensors.

Thanks to these devices, it is possible to constantly monitor the MC behavior, perform characterizations of the DU and check the base temperature stability. They also provide a reference value for the detector temperature.

A.5.1 CMN + FPD sensors

The small mutual inductor of the FPD is used as a four-wire sensor, connected to the bridge electronics. The electronics provides a high stability DC output signal proportional to the mutual inductance signal. Most of the transitions are always clearly visible, but a smooth temperature variation is required to distinguish those occurring at the lowest temperatures. In addition, it also allows to more accurately identify the transition middle point, which corresponds to the reference temperature. Indeed, a good precision is needed to fully exploit the high resolution of the CMN, which is of the order of 5 μK at 10 mK. Fig. A.5 shows the FPD inductance variation during a controlled and very slow warm up performed during Run 1.3.

The paramagnetic salt of the CMN follows the Curie's law, hence the inductance M is inversely proportional to the temperature T:

$$\frac{1}{T\ [\mathrm{mK}]} = \frac{1}{C_1} M\ [\mu\mathrm{H}] - \frac{C_2}{C_1} \quad \Rightarrow \quad T\ [\mathrm{mK}] = \frac{C_1}{M\ [\mu\mathrm{H}] - C_2} \tag{A.4}$$

where C_1 and C_2 are two constants (this choice for the parametrization is made according to the CMN manual). By calibrating the CMN, it is thus possible to convert its inductance into a value for the MC temperature. It has to be noted that the values of C_1 and C_2 depend not only on the electronics input parameters, but also on the FPD and CMN configuration in the experimental setup. Therefore, a precise temperature readout requires new calibration for every cold run. In the plot of Fig. A.6, the (T^{-1} *vs.* M) linear fit obtained during the CMN calibration in Run 1.3 is shown as an example.

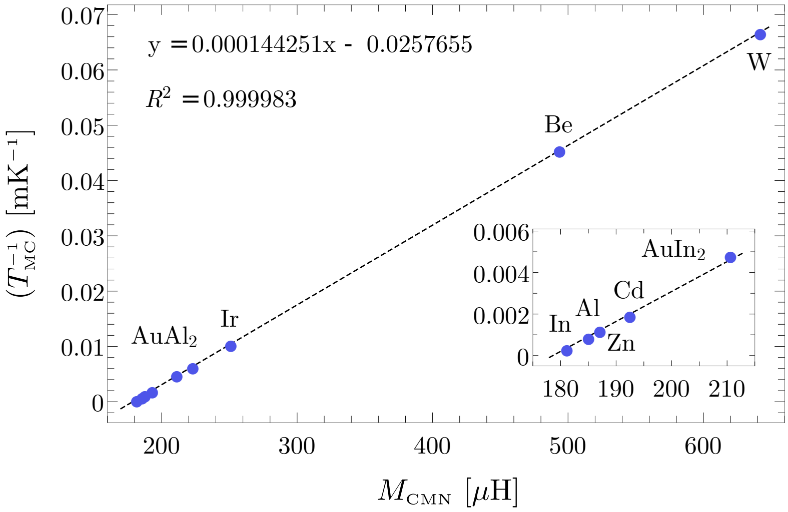

Compound	T_c [mK]
In	3300
Al	1175
Zn	840
Cd	520
$AuIn_2$	208
$AuAl_2$	161
Ir	97
Be	22
W	15

FIG. A.6: (Left) Calibration of the CMN thermometer during Run 1.3. The dependence of the temperature as a function of the device inductance is described by Eq. (A.4). The calibration points correspond to the superconductive transitions of the FPD. In the sub-plot, the lower temperature region is zoomed in. (Right) FPD reference transition temperatures used for the CMN calibration.

A.5.2 NT

The diagram of a Magnetic Field Fluctuations Thermometer or, simply NT, is the following [194]:

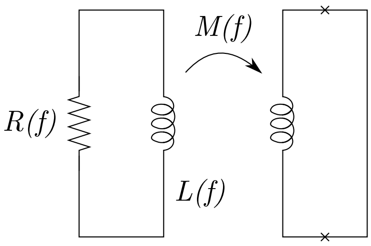

$R(f)$ and $L(f)$ denote the frequency dependent resistance and inductance of the noise resistor, which consists in an high purity copper based sensor. The thermal noise currents inside the copper body cause magnetic-field fluctuations across its surface. These are inductively detected by a SQUID gradiometer ($M(f)$ is the mutual inductance) as Thermal Magnetic Flux Noise (TMFN).

The PSD of the noise is proportional to the thermodynamic temperature according to Niquist's theorem, while that of the TMFN can be described by the following empirical relation [195]:

$$S_\Phi(f,T) = \frac{S_0(T)}{\left(1+(f/f_c)^{2a}\right)^b}. \tag{A.5}$$

Here, $S_0(T)$ is the zero-frequency value of $S_\Phi(f,T)$ and it is proportional to the temperature for a fixed configuration of the SQUID gradiometer + temperature sensor. f_c is the characteristic fall-off frequency of the TMFN. It is determined by the geometry of the metallic temperature sensor and by its distance to the gradiometer and electrical conductivity. Its

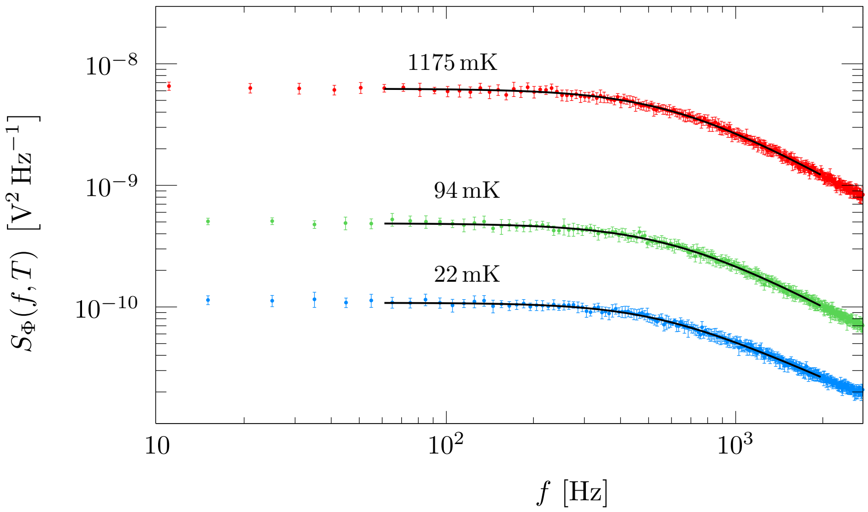

FIG. A.7: PSD of TMFN recorded with the NT during Run 1.3 and related fit with the function of Eq. (A.5) in the frequency range $(60 - 2000)$ Hz. The temperature values come from the read out of the CMN thermometer. Adapted from Ref. [171].

value, together with those of a and b, can be assumed to be constant.[7] In this case, S_Φ shows a "low-pass-like" frequency dependence which is independent of temperature.

Since the shape of the PSD of the TMFN is independent of temperature, all the device characteristic parameters can be obtained by fitting $S_\Phi(f,T)$ with Eq. (A.5) at a known $T_{\rm ref}$. It has to be noted that the calibration of the NT requires only one calibration point. The temperature can be calculated as following:

$$T = T_{\rm ref}\,\frac{S_0(T)}{S_0(T_{\rm ref})} \tag{A.6}$$

where $S_0(T)$ is obtained from a fit of the corresponding TMFN spectrum measured at T.

The MFFT-1 software already returns a temperature value as output with a relative error of less than 1% at a few mK. Therefore, the NT readout it's immediate once both the SQUID working point and the calibration point have been set.

During Run 1.3, a prototype NT was installed on the MC plate in order to test its performance. In this case, the temperature value had to be derived starting from the PSD of the TMFN according to the procedure described above. In Fig. A.7, the PSD acquired at 3 different MC temperatures are shown (some electronic noise components, e. g. 50 Hz and its harmonics, are already filtered out). The fits are performed with the function of Eq. (A.5) in the frequency range $(60 - 2000)$ Hz.

The obtained values of S_0 are plotted *vs.* temperature in Fig. A.8. It can be seen that the best fit value for the intercept is different from zero, which translates into a fixed off-set for the temperature value. This is due to the introduction of additional noise by the custom data acquisition system, not optimized for the NT read out. The problem

[7]The sensor body is made of copper (without magnetic impurities) and thus its electrical conductivity is roughly constant in the mK - few K temperature range.

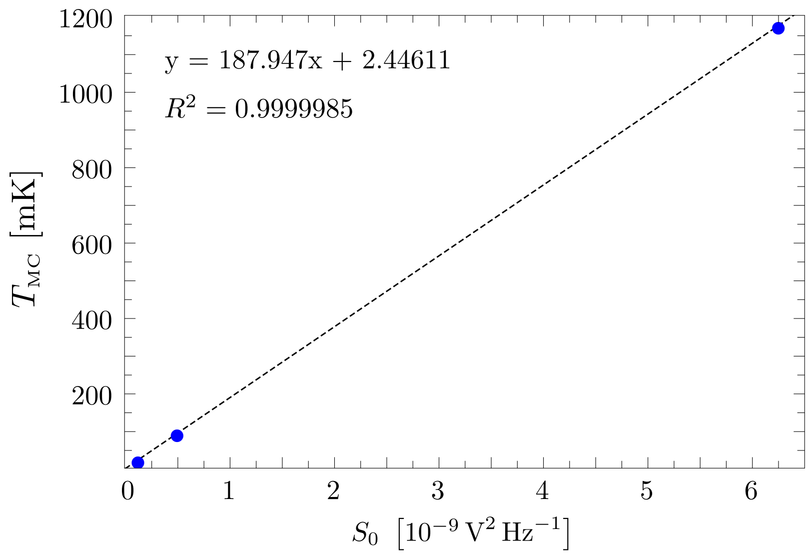

FIG. A.8: Calibration of the NT during Run 1.3. The dependence of the temperature as a function of the zero-frequency value is described by Eq. (A.6). The calibration points correspond to the fit of Fig. A.7. The non-zero value for the intercept is due to the introduction of additional noise by the custom data acquisition system.

will in fact disappear with the use of the specific MFFT-1 electronics and software (the temperature values coincide with the reference FPD transitions). Anyway, it can be also be seen from the plot that linearity is maintained over more than 3 decades of temperature.

A.6 Still impedance characterization

The CUORE DU is provided with 2 condensing lines for the mixture circulation (see Sec. 4.5.3). These are called 6 and 7 from the numbering of the corresponding valves at the entrance of the DU. Each line has an impedance at the Still level (Fig. A.9, see also Fig. 4.5.3), which is tunable when the cryostat is open and sets the mixture flow during the normal operation.

The adjustment of the impedances was initially performed during the DU tests and then repeated at the end of Run 1.3. An accurate characterization of the impedances was carried out during Run 2.

We used the leak detector to get an indication of the flow. A small amount of He ($\sim$ 45 mbar) was put at the level of the valves entering the DU and the readout was performed at the end of the Still pumping line after opening either valve 6 or 7. The measurement was repeated multiple times with both the lines during the cool down and warm up. The results is shown in Fig. A.10. A factor ~ 10 between the flows was observed. This implied that the two lines were not equivalent, making it impossible for one to be the spare of the other. In the case of line 6, the unexpected different behavior during the cool down and the warm up was found to be due to the squirming of the bellow containing the spring (later repaired).

Once the DU was moved to the test cryostat, it was decided to reproduce the characteri-

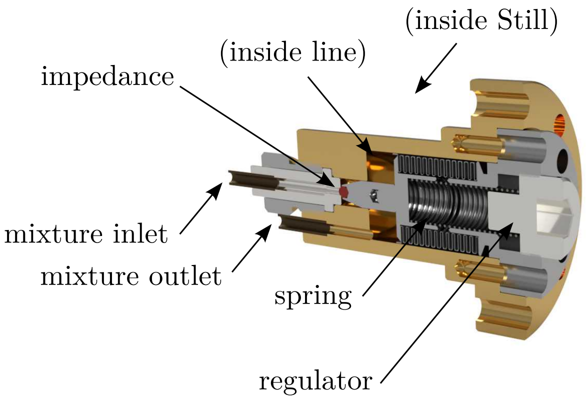

FIG. A.9: Rendering of the Still tunable impedance. The configuration of the regulation system was actually changed during the commissioning (see the text for details).

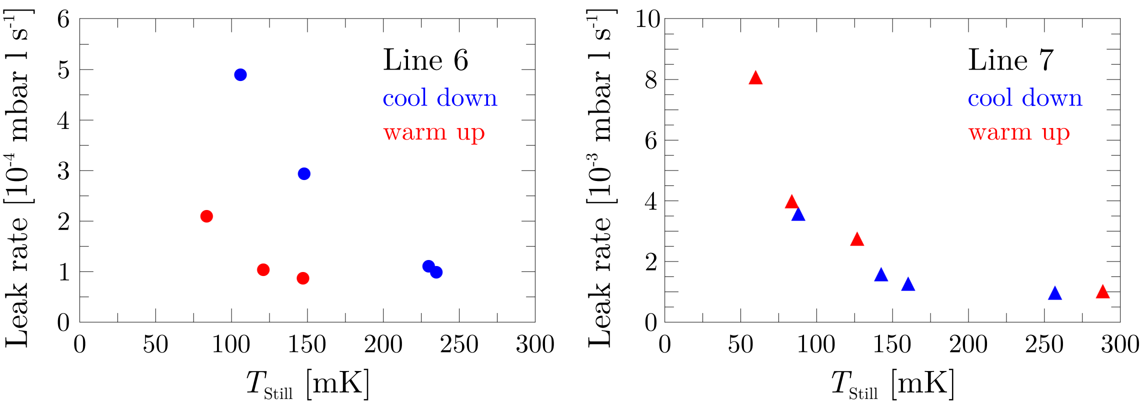

FIG. A.10: Characterization of the tunable impedances in terms of gas flow performed during Run 2. The different behavior during cool down and warm up of the impedance of line 6 is due to impedance squirmed bellow.

zation and to tune the impedances in order to get similar flows in the 2 lines. Unfortunately, it was noted that, despite closed values could be obtained at room temperature, the result at lower temperature were different and not fully reproducible. It was thus decided to switch to a less flexible, but more reliable, regulation system.

In the original configuration, the tuning was set by tightening a screw that was pressing against a spring inside a sealed bellow, which in turn was pressing against the actual impedance (Fig. A.9). The bellow guaranteed the separation between the mixture ambient and the external world. In the new configuration, the screw and the bellows have been removed and the tuning of the impedance is made by using spacers of different thickness that press against the spring. The removal of the bellow requires that now an indium seal (that isolate the mixture ambient) must be broken and remade each time the impedance is tuned. Although less comfortable, this configuration decreases the risks for the circulation, more easily avoiding problems like an excessively low flow at cryogenic temperature.

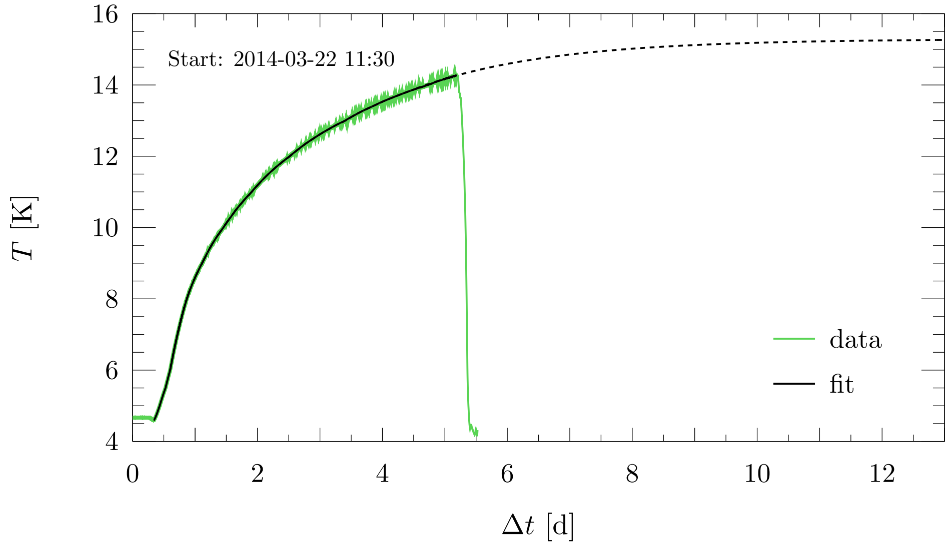

FIG. A.11: Still stage temperature rise during the cool down of Run 1.1 (zoom of the corresponding plot in Fig. 5.7). The fit curve is obtained by superposing multiple fits performed along temporal sub-intervals (see the discussion in the text). The dashed part is the continuation of the last fit function.

A.7 Problem investigation

Custom analysis, even if based on simple tools, are needed in order to cope with any situation in which an anomalous behavior from the cryostat is observed. Depending on the specific, the results can consist either in rough estimates or in more precise evaluations. Anyway, they have to indicate the direction to follow (or to exclude) in search of the solution of the occurred problem.

A.7.1 IVC temperature rise after exchange gas removal

The heat flow resulting from a temperature gradient in a material is given by

$$\dot{Q} = \int_{T_1}^{T_2} G(T)\,\mathrm{d}T \tag{A.7}$$

where the thermal conductivity $G(T)$ as a function of the temperature can be extrapolated from the (T *vs.* t) plot describing the temporal evolution of the system temperature.

Starting from Eq. (A.7), the following procedure was used to estimate the amount of dissipated power by parasitic sources on the inner cryostat stages after the removal of the exchange gas inside the IVC.

Referring to the case of Run 1.1 as an example (lower plot of Fig. 5.7) and in particular to the Still stage, the data series, plotted alone in Fig. A.11, was fitted with an exponential function, namely

$$T = T_0 - A \cdot \exp\left(-\frac{t - t_0}{\tau(T)}\right) \quad \text{with} \quad \tau(T) \equiv \frac{C(T)}{G(T)}. \tag{A.8}$$

TABLE A.12: Estimate of the dissipated power in the IVC during Run 1.1. The different temperatures describe: the initial situation of the system after the removal of the exchange gas (T_{in}), the system at the start of the mixture circulation (T_{circ}) and the system at the (ideal) thermal equilibrium (T_{eq}).

Stage	T_{in} [K]	T_{circ} [K]	T_{eq} [K]	$\dot{Q}$ [mW]		
				$(T_{\text{in}} - T_{\text{circ}})$	$(T_{\text{circ}} - T_{\text{eq}})$	$(T_{\text{in}} - T_{\text{eq}})$
Still	4.6	14.3	15.4	80	12	92
HEX	4.6	9.0	9.5	7	1.5	8.5
MC	4.6	6.5	7.8	3.5	1	4.5

The dependence of the specific heat $c(T)$ on T at low temperatures (in the range $(4.2 - 30)$ K) is known for copper [191]:

$$\begin{aligned} c(T)\ [J\,\text{mol}^{-1}\,\text{K}^{-1}] \;=\;& 6.94000 \cdot 10^{-4}\, T + 4.76249 \cdot 10^{-5}\, T^3 \\ & + 1.05866 \cdot 10^{-9}\, T^5 + 1.02870 \cdot 10^{-10}\, T^7 - 1.68191 \cdot 10^{-13}\, T^9 \\ & + 9.01270 \cdot 10^{-17}\, T^{11} - 1.13003 \cdot 10^{-20}\, T^{13}. \end{aligned} \tag{A.9}$$

Therefore, the heat capacity $C(T)$ could be simply obtained by dividing $c(T)$ by the Cu atomic mass and multiplying it by the Still mass (plate + vessel, see Table 4.4).

Multiple fits were performed for different fractions of the curve, each time extracting the parameter τ and calculating the corresponding $G(T)$. The integral of Eq. (A.7) was thus approximated to a discrete sum.

In the considered case, the system had not yet reached the equilibrium when the mixture circulation was started, thus producing the temperature drop. Therefore, the temperature rise had to be ideally continued not to neglect a fraction of the total power. This "missing" contribution could be estimated by using the parameters extracted from the final fit of the curve.

The same procedure was used to estimate the dissipated power on the other thermal stages (HEX and MC) by considering the corresponding curves in Fig. 5.7 and using the correct values for the masses in the calculation of the heat capacities.

The result is shown in Table A.12. The total amount of dissipated power inside the IVC during Run 1.1 was estimated to be about 100 mW.

A.7.2 Bad thermalization of LS and DS bars

As already mentioned in Sec. 5.5.1, the LS and DS thermalizers were designed to work with the bars in traction, with the risk of not being effective otherwise. Therefore, a power dissipation inside the IVC coming from the LS and DS bars could represent one of the possible sources of the problems encountered both in Run 1.1 and in Run 1.2.

During the preparation of Run 2, different masses (copper disks) were attached just

Position		T [K]			
		No load		12 kg	48 kg
40 K	top	72.7	-	69.9	68.8
	bottom	45.3	42.7	42.5	41.4
	Cu	37.4	-	37.6	37.7
	plate	37.4	-	37.1	-
4 K	top	17.8	-	15.2	16.9
	bottom	12.6	9.0	5.3	10.5
	Cu	3.7	-	3.7	3.7
	plate	3.7	-	3.8	3.8

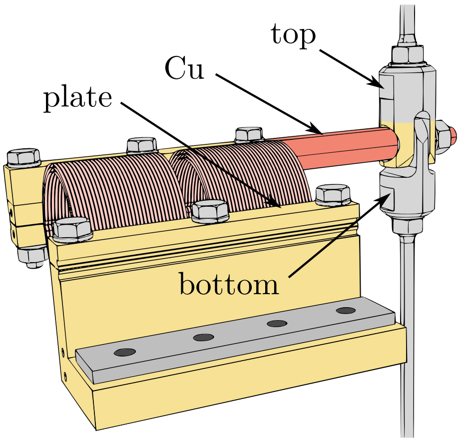

TABLE A.13: (Left) Temperatures along the LS and DS bars recorded during Run 2. Different loads are attached to the IVC bellows: no load (LS 3 and DS 1), 12 kg (LS 2) and 48 kg (LS 1). (Right) Rendering of a DS/LS bar thermalizer at the 4 K stage (see also Fig. 4.2). The arrows indicate the position of the diodes.

below the suspension bellows (refer to Fig. 4.2). In particular, LS 2 was loaded with a 12 kg mass, LS 1 with a 48 kg one. No loads were attached to LS 3 and to the DSs. By monitoring the temperature at different positions along the bars (picture in Table. A.13), it was possible to compare, at least qualitatively, the effect of the traction on the final temperatures.

The results is shown in the table of Fig. A.13. It can be seen that attaching the load to the LS bar actually improved the thermalization, when considering the case of 12 kg (refer to the "bottom" temperatures).[8] In the case of the 48 kg mass, a further improvement was present at the 40 K stage. Instead, at the 4 K stage, unexpected higher temperatures were observed. The value registered by the "top" diode could be due to an inefficient thermalization of the sensor, but that of the "bottom" diode remained unexplained.[9]

The power injected inside the IVC by the LS and DS bars during Run 1.1 and Run 1.2 could be easily calculated. The value of the stainless steel thermal conductance at low temperature is known [165], as well as the bar dimensions (Table 4.3). By taking the values of 12.5 K and 4 K as references for the 4 K and Still thermalizer temperatures, the result was $\sim$ 4 mW. Although constituting a small fraction of the total 100 mW of estimated dissipated power (App. A.7.1), this value represented a non negligible heat load for the Still stage.

Anyway, with the installation of the Top Lead and the TSP (see Sec. 5.9), the thermalizations behaved as expected. By considering a reference bar for the LSs and DSs, values close to $\sim$ 1.3 K and $\sim$ 1.6 K were registered at the level of the Still thermalizer both during Run 3 and Run 4.

[8]The value of 12.5 K had already been obtained with the unloaded DS 2 during Run 1.2 (see Sec. 5.6).
[9]Even if this would represent a stupid mistake, it is not possible to exclude an accidental switch of this thermometer with the corresponding one on LS 2, loaded with 12 kg.

List of Abbreviations

$0\nu\beta\beta$	Neutrinoless double beta decay
$2\nu\beta\beta$	Two-neutrino double beta decay
CCVR	CUORE Crystal Validation Run
CMB	Cosmic Microwave Background
CMN	Cerium Magnesium Nitrate (thermometer)
CTAL	CUORE Tower Assembly Line
CUORE	Cryogenic Underground Observatory for Rare Events
CUPID	CUORE Upgrade with Particle IDentification
DAQ	Data AcQuisition
DCS	Detector Calibration System
DR	Dilution Refrigerator
DS	Detector Suspension
DU	Dilution Unit
ELS	External Lateral Shield
FCS	Fast Cooling System
FWHM	Full Width Half Maximum (energy resolution)
FPD	Fixed Point Device
GM	Gifford McMahon (cooler)
HEX	Heat EXchanger
IBM	Interacting Boson Model
IH	Inverted Hierarchy
ILS	Internal Lateral Shield
INFN	Istituto Nazionale di Fisica Nucleare
ISM	Interacting Shell Model
IVC	Inner Vacuum Chamber
LNGS	Laboratori Nazionali del Gran Sasso
LS	(Top) Lead Suspension
MC	Mixing Chamber
MiDBD	Milan Double Beta Decay (experiment)
MIT	Metal-Insulator Transition
MSP	Main Support Plate
NH	Normal Hierarchy
NME	Nuclear Matrix Element
NT	Noise Thermometer
NTD	Neutron Transmutation Doping/ed (technique/sensor)
OF	Optimum Filter
OFE	Oxygen-Free Electrolytic (copper) (OFHC C10100)
OFHC	Oxygen-Free High thermal Conductivity (copper)
OVC	Outer Vacuum Chamber
PID	Proportional-Integral-Derivative (controller)
PSD	Power Spectral Density
PSF	Phase Space Factor
PT	Pulse Tube (refrigerator)
PTFE	PolyTetraFluoroEthene
PUR	PolyURethane
QRPA	Quasiparticle Random Phase Approximation

ROI	Region Of Interest
RMS	Root Mean Square
SM	Standard Model
TMFN	Thermal Magnetic Flux Noise
TSP	Tower Support Plate
TVL	Test Variable Left
TVR	Test Variable Right
UEML	Unbinned Extended Maximum Likelihood (fit)
WT	Wire Tray

Regarding the $0\nu\beta\beta$ experiments reported in Table 1.16, see the corresponding references.

List of Figures and Tables

Acknowledgements / Ringraziamenti

I want to thank O. Cremonesi, P. Gorla, C. Bucci and L. Canonica for patiently helping and supporting me during all the activities at the labs and for constantly supervising my work. I thank J. J. Gómez Cadenas, A. Nucciotti and B. Schwingenheuer for reading and reviewing this thesis. A special thanks goes to F. Vissani and S. Marcocci for working together during my first research activity. I really want to thank anyone I met and worked with during these years. This thesis is also the result of their contribution.

Al di là dei ringraziementi formali, penso sia giusto ringraziare i molti che, in modi diversi, hanno preso parte a questo lavoro. Perciò, davvero, grazie a tutti!

Alcune menzioni un po' più esplicite sono però doverose. Senza queste persone, non sarei mai potuto arrivare fin qui. Il primo ringraziamento va quindi a Paolo e a Carlo, non credo ci sia nemmeno bisogno di spiegare il perché.

Ringrazio poi Lucia, per tutto l'aiuto datomi durante questi anni e, purtroppo per lei, per avermi sopportato tutti i giorni in ufficio.

Ringrazio Oliviero e Chiara per i numerosi insegnamenti e consigli e per avermi fatto conoscere il mondo di CUORE.

Ringrazio tutti gli amici e colleghi degli uffici vicini, chi più chi meno di passaggio. Con loro ho potuto condividere il tempo trascorso qui, sia dentro che fuori la fisica. L'elenco è lunghissimo: Nello, Vivek (grazie per le innumerevoli ore passate al ping-pong!), Daria, Irene, Laura, Claudia, Nic, Alexey, Sachi, Giovanni, Andrea (grazie per tutto l'aiuto con Latex), Luigi, Salvatore, Marisa, . . . (scusate se non ho scritto tutti, ma per la lista completa rimando alle varie referenze nella tesi). E poi Lucio, Pierpaolo, Alessandro, Leo ($\times 2$), con cui ho potuto vivere la parte più hardware delle attività dei laboratori.

Ringrazio tutti gli amici e colleghi del GSSI, con i quali ho potuto studiare e lavorare, ma soprattutto vivere insieme i primi mesi dell nuova esperienza del dottorato. Ringrazio in particolare Simone, con cui ho condiviso i miei primi lavori "scientifici" (che, come mi ha fatto notare n volte Paolo, mi hanno portato ad avere un Marcocci index = 3).

In modo speciale ringrazio Francesco, da lungo tempo ormai più amico che professore.

In generale, voglio ringraziare i LNGS e il GSSI, per le numerose e preziose opportunità che mi hanno dato e per le esperienze che mi hanno consentito di fare. In particolare, per avermi spedito ad Hamamatsu e a Dresda.

Riguardo a Dresda, colgo l'occasione per ringraziare anche Caio e Marco Pontilieni – per inciso, non ho ancora capito se Caio sia figlio di Marco o entrambi siano figli di un altro Marco, ma non ho mai avuto occasione di chiedergielo – per la loro massiccia (6.5 t) donazione alla fisica del neutrino. Con questo gesto hanno mostrato di essere avanti di duemila anni rispetto ai loro tempi. Ma, soprattutto, li ringrazio, insieme al Prof. Fiorini, per avermi dato un'occasione in più di divertirmi con la ricerca.

Un ringraziamento particolare va al Prof. Damiani che, per primo, mi ha trasmesso la passione per la fisica. E a Mauro, che mi ricorda che la ricerca non si chiude con la fisica.

In maniera indiretta, molte altre persone mi hanno consentito di portare a termine questo percorso. Ringrazio perciò tutti gli amici di Lècco e dintorni, senza cui sarebbe stato impossibile non impazzire.

E per concludere, correndo il rischio di diventare patetico, il ringraziamento più grande non pu'o che andare alla mia famiglia. A mia madre, a mio padre e a mio fratello, ma anche agli innumerevoli parenti (un grazie speciale a Emma, Ilaria, Cecilia e Giorgia), senza i quali non sarei quello che sono.

Bibliography

[1] P. A. M. Dirac, *The Quantum theory of electron*, Proc. Roy. Soc. Lond. A **117**, 610 (1928).

[2] P. A. M. Dirac, *The Quantum theory of electron. Part II.*, Proc. Roy. Soc. Lond. A **118**, 351 (1928).

[3] E. Majorana, *Theory of the Symmetry of Electrons and Positrons (in Italian)*, Nuovo Cim. **14**, 171 (1937).

[4] G. Racah, *On the symmetry of particle and antiparticle (in Italian)*, Nuovo Cim. **14**, 322 (1937).

[5] W. H. Furry, *On transition probabilities in double beta-disintegration*, Phys. Rev. **56**, 1184 (1939).

[6] M. Goeppert-Mayer, *Double beta-disintegration*, Phys. Rev. **48**, 512 (1935).

[7] R. Saakyan, *Two-Neutrino Double-Beta Decay*, Ann. Rev. Nucl. Part. Sci. **63**, 503 (2013).

[8] M. A. Luty, *Baryogenesis via leptogenesis*, Phys. Rev. D **45**, 455 (1992).

[9] S. Dell'Oro, M. Marcocci, S.and Viel and F. Vissani, *Neutrinoless double beta decay: 2015 review*, Adv. High Energy Phys. **2016**, 2162659 (2016).

[10] G. Feinberg and M. Goldhaber, *Microscopic tests of symmetry principles*, Proc. Nat. Ac. Sci. **45**, 1301 (1959).

[11] B. Pontecorvo, *Superweak interactions and double beta decay*, Phys. Lett. B **26**, 630 (1968).

[12] M. Mitra, G. Senjanovic and F. Vissani, *Neutrinoless Double Beta Decay and Heavy Sterile Neutrinos*, Nucl. Phys. B **856**, 26 (2012).

[13] V. Tello, M. Nemevsek, F. Nesti, G. Senjanovic and F. Vissani, *Left-Right Symmetry: from LHC to Neutrinoless Double Beta Decay*, Phys. Rev. Lett. **106**, 151801 (2011).

[14] S. L. Glashow, *Partial Symmetries of Weak Interactions*, Nucl. Phys. **22**, 579 (1961).

[15] S. Weinberg, *A Model of Leptons*, Phys. Rev. Lett. **19**, 1264 (1967).

[16] A. Salam, *Weak and Electromagnetic Interactions*, 8th Nobel Symposium, Lerum, Sweden, May 1968 , 367 (1968).

[17] S. Weinberg, *Baryon and Lepton Nonconserving Processes*, Phys. Rev. Lett. **43**, 1566 (1979).

[18] P. Minkowski, *$\mu \to e\gamma$ at a Rate of One Out of 10^9 Muon Decays?*, Phys. Lett. B **67**, 421 (1977).

[19] T. Yanagida, *Horizontal symmetry and masses of neutrinos*, Proc. Workshop Baryon Number of the Universe and Unified Theories, Tsukuba, Japan, February 1979 , 95 (1979).

[20] M. Gell-Mann, P. Ramond and R. Slansky, *Complex Spinors and Unified Theories*, Proceedings of the Supergravity Workshop, Stony Brook, New York, USA, September 1979, 315 (1979).

[21] R. N. Mohapatra and G. Senjanovic, *Neutrino Mass and Spontaneous Parity Violation*, Phys. Rev. Lett. **44**, 912 (1980).

[22] B. Pontecorvo, *Mesonium and anti-mesonium*, Sov. Phys. JETP **6**, 429 (1957), [Zh. Eksp. Teor. Fiz. **33**, 549 (1957)].

[23] A. Strumia and F. Vissani, *Neutrino masses and mixings and ...*, (2006), arXiv:hep-ph/0606054 [hep-ph] .

[24] M. C. Gonzalez-Garcia and Y. Nir, *Neutrino masses and mixing: Evidence and implications*, Rev. Mod. Phys. **75**, 345 (2003).

[25] S. M. Bilenky, J. Hosek and S. T. Petcov, *On Oscillations of Neutrinos with Dirac and Majorana Masses*, Phys. Lett. B **94**, 495 (1980).

[26] E. Fermi, *Trends to a theory of β ray emission (in Italian)*, Ric. Sci. **4**, 491 (1933).

[27] H. Weyl, *Electron and Gravitation. 1. (in German)*, Z. Phys. **56**, 330 (1929).

[28] A. J. Long, C. Lunardini and E. Sabancilar, *Detecting non-relativistic cosmic neutrinos by capture on tritium: phenomenology and physics potential*, J. Cosm. Astropart. Phys. **1408**, 038 (2014).

[29] F. Wilczek and A. Zee, *Operator Analysis of Nucleon Decay*, Phys. Rev. Lett. **43**, 1571 (1979).

[30] K. Choi, K. Jeong and W. Song, *Operator analysis of neutrinoless double beta decay*, Phys. Rev. D **66**, 093007 (2002).

[31] F. Bonnet, M. Hirsch, T. Ota and W. Winter, *Systematic decomposition of the neutrinoless double beta decay operator*, J. High Energy Phys. **1303**, 055 (2013), [Erratum: J. High Energy Phys. **1404**, 090 (2014)].

[32] F. Capozzi, E. Lisi, A. Marrone, D. Montanino and A. Palazzo, *Neutrino masses and mixings: Status of known and unknown 3ν parameters*, Nucl. Phys. B **908**, 218 (2016).

[33] L. Wolfenstein, *Neutrino Oscillations in Matter*, Phys. Rev. D **17**, 2369 (1978).

[34] S. Mikheev and A. Y. Smirnov, *Resonance Amplification of Oscillations in Matter and Spectroscopy of Solar Neutrinos*, Sov. J. Nucl. Phys. **42**, 913 (1985).

[35] S. Abe *et al.* (KamLAND Collaboration), *Precision Measurement of Neutrino Oscillation Parameters with KamLAND*, Phys. Rev. Lett. **100**, 221803 (2008).

[36] F. Vissani, *Signal of neutrinoless double beta decay, neutrino spectrum and oscillation scenarios*, J. High Energy Phys. **9906**, 022 (1999).

[37] F. N. D. Kurie, J. R. Richardson and C. Paxton, *The Radiations Emitted from Artificially Produced Radioactive Substances. I. The Upper Limits and Shapes of the β-Ray Spectra from Several Elements*, Phys. Rev. **49**, 368 (1936).

[38] C. Kraus *et al.*, *Final results from phase II of the Mainz neutrino mass search in tritium beta decay*, Eur. Phys. J. C **40**, 447 (2005).

[39] V. N. Aseev *et al.*, *An upper limit on electron antineutrino mass from Troitsk experiment*, Phys. Rev. D **84**, 112003 (2011).

[40] J. Angrik *et al.* (KATRIN Collaboration), *KATRIN design report 2004* (2005).

[41] P. J. Doe *et al.* (Project 8 Collaboration), *Project 8: Determining neutrino mass from tritium beta decay using a frequency-based method*, (2013), arXiv:1309.7093 [nucl-ex] .

[42] L. Gastaldo *et al.*, *The Electron Capture ^{163}Ho Experiment ECHo: an overview*, J. Low Temp. Phys. **176**, 876 (2014).

[43] B. Alpert *et al.*, *HOLMES - The Electron Capture Decay of ^{163}Ho to Measure the Electron Neutrino Mass with sub-eV sensitivity*, Eur. Phys. J. C **75**, 112 (2015).

[44] M. P. Croce *et al.*, *Development of holmium-163 electron-capture spectroscopy with transition-edge sensors*, J. Low. Temp. Phys. **184**, 958 (2016).

[45] F. Capozzi, E. Di Valentino, E. Lisi, A. Marrone, A. Melchiorri and A. Palazzo, *Global constraints on absolute neutrino masses and their ordering*, (2017), arXiv:1703.04471 [hep-ph] .

[46] T. J. Loredo and D. Q. Lamb, *Bayesian analysis of neutrinos observed from supernova SN-1987A*, Phys. Rev. D **65**, 063002 (2002).

[47] G. Pagliaroli, F. Rossi-Torres and F. Vissani, *Neutrino mass bound in the standard scenario for supernova electronic antineutrino emission*, Astropart. Phys. **33**, 287 (2010).

[48] J. Ellis, H. T. Janka, N. E. Mavromatos, A. S. Sakharov and E. K. G. Sarkisyan, *Prospective Constraints on Neutrino Masses from a Core-Collapse Supernova*, Phys. Rev. D **85**, 105028 (2012).

[49] J. Lesgourgues, G. Mangano, G. Miele and S. Pastor, *Neutrino Cosmology* (Cambridge University Press, 2013).

[50] S. Dell'Oro, S. Marcocci, M. Viel and F. Vissani, *The contribution of light Majorana neutrinos to neutrinoless double beta decay and cosmology*, J. Cosm. Astropart. Phys. **1512**, 023 (2015).

[51] P. A. R. Ade *et al.* (Planck Collaboration), *Planck 2015 results. XIII. Cosmological parameters*, Astron. Astrophys. **594**, A13 (2016).

[52] N. Palanque-Delabrouille *et al.*, *Constraint on neutrino masses from SDSS-III/BOSS Lyα forest and other cosmological probes*, J. Cosm. Astropart. Phys. **1502**, 045 (2015).

[53] A. J. Cuesta, V. Niro and L. Verde, *Neutrino mass limits: robust information from the power spectrum of galaxy surveys*, Phys. Dark Univ. **13**, 77 (2016).

[54] E. Di Valentino, E. Giusarma, O. Mena, A. Melchiorri and J. Silk, *Cosmological limits on neutrino unknowns versus low redshift priors*, Phys. Rev. D **93**, 083527 (2016).

[55] E. Giusarma, M. Gerbino, O. Mena, S. Vagnozzi, S. Ho and K. Freese, *Improvement of cosmological neutrino mass bounds*, Phys. Rev. D **94**, 083522 (2016).

[56] N. Palanque-Delabrouille *et al.*, *Neutrino masses and cosmology with Lyman-alpha forest power spectrum*, J. Cosm. Astropart. Phys. **1511**, 011 (2015).

[57] X. Zhang, *Impacts of dark energy on weighing neutrinos after Planck 2015*, Phys. Rev. D **93**, 083011 (2016).

[58] L. Amendola *et al.* (Euclid Theory Working Group), *Cosmology and Fundamental Physics with the Euclid Satellite*, (2016), arXiv:1606.00180 [astro-ph.CO] .

[59] Y. B. Zel'dovich and M. Y. Khlopov, *The Neutrino Mass in Elementary Particle Physics and in Big Bang Cosmology*, Sov. Phys. Usp. **24**, 755 (1981).

[60] O. Cremonesi and M. Pavan, *Challenges in Double Beta Decay*, Adv. High Energy Phys. **2014**, 951432 (2013).

[61] S. R. Elliott and P. Vogel, *Double beta decay*, Ann. Rev. Nucl. Part. Sci. **52**, 115 (2002).

[62] J. J. Gómez-Cadenas and J. Martìn-Albo, *Phenomenology of neutrinoless double beta decay*, Proc. of Science **(GSSI14)**, 004 (2015).

[63] R. G. H. Robertson, *Empirical Survey of Neutrinoless Double Beta Decay Matrix Elements*, Mod. Phys. Lett. A **28**, 1350021 (2013).

[64] J. Kotila and F. Iachello, *Phase space factors for double-β decay*, Phys. Rev. C **85**, 034316 (2012).

[65] E. Caurier, G. Martinez-Pinedo, F. Nowacki, A. Poves and A. P. Zuker, *The Shell model as unified view of nuclear structure*, Rev. Mod. Phys. **77**, 427 (2005).

[66] J. Menéndez, A. Poves, E. Caurier and F. Nowacki, *Disassembling the Nuclear Matrix Elements of the Neutrinoless beta beta Decay*, Nucl. Phys. A **818**, 139 (2009).

[67] F. Šimkovic, V. Rodin, A. Faessler and P. Vogel, *$0\nu\beta\beta$ and $2\nu\beta\beta$ nuclear matrix elements, quasiparticle random-phase approximation, and isospin symmetry restoration*, Phys. Rev. C **87**, 045501 (2013).

[68] J. Hyvarinen and J. Suhonen, *Nuclear matrix elements for $0\nu\beta\beta$ decays with light or heavy Majorana-neutrino exchange*, Phys. Rev. C **91**, 024613 (2015).

[69] J. Barea, J. Kotila and F. Iachello, *$0\nu\beta\beta$ and $2\nu\beta\beta$ nuclear matrix elements in the interacting boson model with isospin restoration*, Phys. Rev. C **91**, 034304 (2015).

[70] F. Šimkovic, G. Pantis, J. D. Vergados and A. Faessler, *Additional nucleon current contributions to neutrinoless double beta decay*, Phys. Rev. C **60**, 055502 (1999).

[71] J. Barea, J. Kotila and F. Iachello, *Nuclear matrix elements for double-β decay*, Phys. Rev. C **87**, 014315 (2013).

[72] V. A. Rodin, A. Faessler, F. Šimkovic and P. Vogel, *On the uncertainty in the $0\nu\beta\beta$ decay nuclear matrix elements*, Phys. Rev. C **68**, 044302 (2003).

[73] V. A. Rodin, A. Faessler, F. Šimkovic and P. Vogel, *Assessment of uncertainties in QRPA $0\nu\beta\beta$ nuclear matrix elements*, Nucl. Phys. A **766**, 107 (2006).

[74] F. Šimkovic, S. M. Bilenky, A. Faessler and T. Gutsche, *Possibility of measuring the CP Majorana phases in $0\nu\beta\beta$ decay*, Phys. Rev. D **87**, 073002 (2013).

[75] A. Faessler, G. L. Fogli, E. Lisi, V. Rodin, A. M. Rotunno and F. Šimkovic, *Overconstrained estimates of neutrinoless double beta decay within the QRPA*, J. Phys. G **35**, 075104 (2008).

[76] J. Suhonen and O. Civitarese, *Probing the quenching of g_A by single and double beta decays*, Phys. Lett. B **725**, 153 (2013).

[77] J. Engel and J. Menéndez, *Status and future of nuclear matrix elements for neutrinoless double-beta decay: a review*, Rep. Prog. Phys. **80**, 046301 (2017).

[78] K. Alfonso *et al.* (CUORE Collaboration), *Search for Neutrinoless Double-Beta Decay of ^{130}Te with CUORE-0*, Phys. Rev. Lett. **115**, 102502 (2015).

[79] M. Agostini *et al.* (GERDA Collaboration), *Background free search for neutrinoless double-β decay of ^{76}Ge with GERDA*, Nature **544**, 5 (2017).

[80] A. Gando *et al.* (KamLAND-Zen Collaboration), *Search for Majorana Neutrinos near the Inverted Mass Hierarchy Region with KamLAND-Zen*, Phys. Rev. Lett. **117**, 082503 (2016).

[81] S. Dell'Oro, S. Marcocci and F. Vissani, *New expectations and uncertainties on neutrinoless double beta decay*, Phys. Rev. D **90**, 033005 (2014).

[82] R. Brugnera and A. Garfagnini, *Status of the GERDA Experiment at the Laboratori Nazionali del Gran Sasso*, Adv. High Energy Phys. **2013**, 506186 (2013).

[83] S. Elliott, *Initial Results from the MAJORANA DEMONSTRATOR*, (2016), [To appear on J. Phys. Conf. Ser.].

[84] L. Pattavina (LUCIFER Collaboration), *Scintillating bolometers for the LUCIFER project*, J. Phys. Conf. Ser. **718**, 062048 (2016).

[85] R. Arnold *et al.* (NEMO-3 Collaboration), *Result of the search for neutrinoless double-β decay in ^{100}Mo with the NEMO-3 experiment*, Phys. Rev. D **92**, 072011 (2015).

[86] V. Alenkov *et al.* (AMoRE Collaboration), *Technical Design Report for the AMoRE $0\nu\beta\beta$ Decay Search Experiment*, (2015), arXiv:1512.05957 [physics.ins-det] .

[87] D. R. Artusa *et al.* (CUORE Collaboration), *Searching for neutrinoless double-beta decay of ^{130}Te with CUORE*, Adv. High Energy Phys. **2015**, 879871 (2015).

[88] A. Wright, *Future neutrinoless double beta decay search experiments*, (2016), [To appear on J. Phys. Conf. Ser.].

[89] L. Yang, *Status and prospects for the EXO-200 and nEXO experiments*, (2016), [To appear on J. Phys. Conf. Ser.].

[90] K. Asakura *et al.* (KamLAND-Zen Collaboration), *Results from KamLAND-Zen*, AIP Conf. Proc. **1666**, 170003 (2015).

[91] C. Licciardi, *The sensitivity of the nEXO experiment to majorana neutrinos*, (2016), [To appear on J. Phys. Conf. Ser.].

[92] J. Martìn-Albo *et al.* (NEXT Collaboration), *Sensitivity of NEXT-100 to neutrinoless double beta decay*, J. High Energy Phys. **05**, 159 (2016).

[93] C. Enss and H. Siegfried, *Low-Temperature Physics* (Springer, 2005).

[94] M. Pedretti, *The single module for Cuoricino and CUORE detectors: tests, construction and modelling*, (2004), [Ph. D. thesis, University of Insubria].

[95] M. Vignati, *Model of the Response Function of CUORE Bolometers*, (2010), [Ph. D. thesis, University of Rome - La Sapienza].

[96] Y. B. Levinson, *Propagation of Nonequilibrium Phonons with Frequency Down-conversion (Anthracene)*, Mol. Cryst. Liq. Cryst. **57**, 23 (1980).

[97] A. Alessandrello *et al.*, *Preliminary results on the performance of a TeO_2 thermal detector in a search for direct interactions of WIMPs*, Phys. Lett. B **384**, 316 (1996).

[98] M. Barucci, C. Brofferio, A. Giuliani, E. Gottardi, I. Peroni and G. Ventura, *Measurement of Low Temperature Specific Heat of Crystalline TeO_2 for the Optimization of Bolometric Detectors*, J. Low Temp. Phys. **123**, 303 (2001).

[99] H. C. Stahl, *Cryogenic Particle Detection* (Springer, 2005).

[100] E. E. Haller, N. P. Palaio, M. Rodder, W. L. Hansen and E. Kreysa, *Ntd germanium: A novel material for low temperature bolometers*, in *Neutron Transmutation Doping of Semiconductor Materials*, edited by R. D. Larrabee (Springer US, 1984) pp. 21–36.

[101] C. Erginsoy, *On the Mechanism of Impurity Band Conduction in Semiconductors*, Phys. Rev. **80**, 1104 (1950).

[102] N. F. Mott, *Conduction in non-crystalline materials*, Philos. Mag. **19**, 835 (1969).

[103] B. I. Shklovskii and A. L. Efros, *Electronic Properties of Doped Semiconductors* (Springer, 1984).

[104] A. Alessandrello *et al.*, *Methods for response stabilization in bolometers for rare decays*, Nucl. Instrum. Meth. A **412**, 454 (1998).

[105] E. Andreotti, C. Brofferio, L. Foggetta, A. Giuliani, B. Margesin, C. Nones, M. Pedretti, C. Rusconi, C. Salvioni and M. Tenconi, *Production, characterization, and selection of the heating elements for the response stabilization of the CUORE bolometers*, Nucl. Instrum. Meth. A **664**, 161 (2012).

[106] H. London, Proc. 2nd Int. Conf. on Low Temp. Phys. , 157 (1951).

[107] H. London, G. R. Clarke and E. Mendoza, *Osmotic Pressure of He^3 in Liquid He^4, with Proposals for a Refrigerator to Work below 1° K*, Phys. Rev. **128**, 1992 (1962).

[108] P. Das, R. De Bruyn Ouboter and K. W. Taconis, Proc. 9th Int. Conf. Low Temp. Phys. , 1253 (1965).

[109] G. Frossati, *On the Mechanism of Impurity Band Conduction in Semiconductors*, J. Phys. Colloques **39**, C6–1578 (1978).

[110] D. J. Cousins, S. N. Fisher, A. M. Guénault, R. P. Haley, I. E. Miller, G. R. Pickett, G. N. Plenderleith, P. Skyba, P. Y. A. Thibault and M. G. Ward, *An Advanced Dilution Refrigerator Designed for the New Lancaster Microkelvin Facility*, J. Low Temp. Phys. **114**, 547 (1999).

[111] F. Pobell, *Matter and Methods at Low Temperatures* (Springer, 2007).

[112] A. Alessandrello, D. V. Camin, E. Fiorini, A. Giuliani and G. Pessina, *Thermal detection of particles using bolometric devices*, Nucl. Instrum. Meth. A **264**, 93 (1988).

[113] W. E. Gifford and R. C. Longsworth, *Pulse-Tube Refrigeration*, Trans. ASME J. Eng. Ind. **3**, 264 (1964).

[114] J. P. Joule and W. Thomson, *On the thermal effects experienced by air in rushing through small apertures*, Phil. Mag. **4**, 481 (1852).

[115] S. P. Langley, *The Bolometer and Radiant Energy*, Proc. Am. Acad. Arts Sci. XVI , 342 (1881).

[116] P. Curie and A. Laborde, *On the heat spontaneously released by the salts of radium (in French)*, C. R. Acad. Sci. **136**, 673 (1903).

[117] D. H. Andrews, R. D. Fowler and M. C. Williams, *The Effect of Alpha-particles on a Superconductor*, Phys. Rev. **76**, 154 (1949).

[118] F. Simon, *Application of Low Temperature Calorimetry to Radioactive Measurements*, Nature **135**, 763 (1935).

[119] E. Fiorini and T. O. Niinikoski, *Low Temperature Calorimetry for Rare Decays*, Nucl. Instrum. Meth. A **224**, 83 (1984).

[120] A. Drukier and L. Stodolsky, *Principles and applications of a neutral current detector for neutrino physics and astronomy*, Phys. Rev. D **30**, 2295 (1984).

[121] S. H. Moseley, J. C. Mather and D. McCammon, *Thermal detectors as x-ray spectrometers*, J. Appl. Phys. **56**, 1257 (1984).

[122] A. Alessandrello, C. Brofferio, D. Camin, O. Cremonesi, E. Fiorini, A. Giuliani and G. Pessina, *A Cryogenic tellurium detector for rare events and gamma-rays*, Phys. Lett. B **247**, 442 (1990).

[123] W. Dutton, W. A. Charles Cooper, *The Oxides and Oxyacids of Tellurium*, Chem. Rev. **66**, 657 (1966).

[124] G. K. White, S. Collocott and J. G. Collins, *Thermal properties of paratellurite (TeO_2) at low temperatures*, J. Phys. Condensed Matter **2**, 7715 (1990).

[125] F. R. Kroeger and C. A. Swenson, *Absolute linear thermal-expansion measurements on copper and aluminum from 5 to 320 K*, J. Appl. Phys. **48**, 853 (1977).

[126] R. A. H. El-Mallawany, *Tellurite Glasses Handbook: Physical Properties and Data* (CRC Press, 2002).

[127] Y. Chu, Y. Li, Z. Ge, G. Wu and H. Wang, *Growth of the high quality and large size paratellurite single crystals*, J. Cryst. Growth **295**, 158 (2006).

[128] C. Arnaboldi *et al.*, *Production of high purity TeO_2 single crystals for the study of neutrinoless double beta decay*, J. Cryst. Growth **312**, 2999 (2010).

[129] C. Arnaboldi, C. Brofferio, C. Bucci, P. Gorla, G. Pessina and S. Pirro, *1.3 kg bolometers to search for rare events*, Nucl. Instrum. Meth. A **554**, 300 (2005).

[130] L. Cardani, L. Gironi, J. W. Beeman, I. Dafinei, Z. Ge, G. Pessina, S. Pirro and Y. Zhu, *Performance of a large TeO_2 crystal as a cryogenic bolometer in searching for neutrinoless double beta decay*, J. Instrum. **7**, P01020 (2012).

[131] F. Alessandria *et al.*, *CUORE crystal validation runs: results on radioactive contamination and extrapolation to CUORE background*, Astropart. Phys. **35**, 839 (2012).

[132] A. Alessandrello, C. Brofferio, D. V. Camin, O. Cremonesi, E. Fiorini, A. Giuliani, G. Pessina and E. Previtali, *The first underground low radioactivity bolometric system*, Proc. 3rd Int. Workshop on Low Temp. Det. for Neutrinos and Dark Matter , 253 (1989).

[133] P. G. Catalano, G. Cavinato, F. Salvini and M. Tozzi, *Structural analysis of the Gran Sasso Laboratories of INFN (in Italian)*, Mem. Soc. Geol. It. **35**, 647 (1986).

[134] M. Ambrosio *et al.* (MACRO Collaboration), *Vertical muon intensity measured with MACRO at the Gran Sasso Laboratory*, Phys. Rev. D **52**, 3793 (1995).

[135] H. Wulandari, J. Jochum, W. Rau and F. von Feilitzsch, *Neutron flux at the Gran Sasso underground laboratory revisited*, Astropart. Phys. **22**, 313 (2004).

[136] C. Alduino *et al.* (CUORE Collaboration), *CUORE-0 detector: design, construction and operation*, J. Instrum. **11**, P07009 (2016).

[137] A. Giuliani *et al.*, *A low temperature TeO_2 detector to search for double beta decay of ^{130}Te*, Proc. Joint Int. Lepton Photon Symposium at High Energies (15th) and European Phys. Soc. Conf. on High-energy Phys. , 670 (1991).

[138] A. Alessandrello *et al.*, *A search for neutrinoless double beta decay of ^{130}Te with a bolometric detector*, Nucl. Phys. B (Proc. Suppl.) **28 A**, 229 (1992).

[139] A. Alessandrello *et al.*, *Milano experiment on $0-\nu\ \beta\beta$ decay of ^{130}Te with a thermal detector*, Nucl. Phys. B (Proc. Suppl.) **31**, 83 (1993).

[140] A. Alessandrello *et al.*, *A New search for neutrinoless beta beta decay with a thermal detector*, Phys. Lett. B **335**, 519 (1994).

[141] A. Giuliani *et al.*, *The Milano-Gran Sasso experiment on double beta decay using thermal dettectors*, Proc. 27th Int. Conf. on High-energy Phys. , 943 (1994).

[142] C. Brofferio *et al.*, *Improvements in Te-130 double beta decay search with cryogenic TeO-2 array detectors*, Nucl. Phys. B (Proc. Suppl.) **48**, 238 (1996).

[143] C. Arnaboldi *et al.*, *A Calorimetric search on double beta decay of ^{130}Te*, Phys. Lett. B **557**, 167 (2003).

[144] E. Fiorini, *CUORE: A cryogenic underground observatory for rare events*, Phys. Rep. **307**, 309 (1998).

[145] A. Alessandrello *et al.*, *Large mass, low temperature, low background detectors*, Nucl. Instrum. Meth. A **315**, 263 (1992).

[146] E. Andreotti *et al.*, *^{130}Te Neutrinoless Double-Beta Decay with CUORICINO*, Astropart. Phys. **34**, 822 (2011).

[147] C. Alduino *et al.* (CUORE Collaboration), *Analysis techniques for the evaluation of the neutrinoless double-β decay lifetime in ^{130}Te with the CUORE-0 detector*, Phys. Rev. C **93**, 045503 (2016).

[148] F. Alessandria *et al.* (CUORE Collaboration), *Sensitivity of CUORE to Neutrinoless Double-Beta Decay*, (2011), arXiv:1109.0494 [nucl-ex] .

[149] C. Bucci *et al.*, *Background study and Monte Carlo simulations for large-mass bolometers*, Eur. Phys. J. A **41**, 155 (2009).

[150] A. Giachero, *Characterization of cryogenic bolometers and data acquisition system for the CUORE experiment*, (2008), [Ph. D. thesis, University of Genoa].

[151] F. Alessandria *et al.*, *Validation of techniques to mitigate copper surface contamination in CUORE*, Astropart. Phys. **45**, 13 (2013).

[152] E. Buccheri, M. Capodiferro, S. Morganti, F. Orio, A. Pelosi and V. Pettinacci, *An assembly line for the construction of ultra-radio-pure detectors*, Nucl. Instrum. Meth. A **768**, 130 (2014).

[153] D. R. Artusa *et al.* (CUORE Collaboration), *Initial performance of the CUORE-0 experiment*, Eur. Phys. J. C **74**, 2956 (2014).

[154] S. Rahaman, V. V. Elomaa, T. Eronen, J. Hakala, A. Jokinen, A. Kankainen, J. Rissanen, J. Suhonen, C. Weber and J. Äystö, *Double-beta decay Q values of ^{116}Cd and ^{130}Te*, Phys. Lett. B **703**, 412 (2011).

[155] M. Redshaw, B. J. Mount, E. Myers and F. T. Avignone, *Masses of Te-130 and Xe-130 and Double-beta-Decay Q Value of Te-130*, Phys. Rev. Lett. **102**, 212502 (2009).

[156] N. D. Scielzo *et al.*, *Double-beta decay Q values of Te-13-, Te-128, and Te-120*, Phys. Rev. C **80**, 025501 (2009).

[157] C. Alduino *et al.* (CUORE Collaboration), *The projected background for the CUORE experiment* (2016), internal note (unpublished).

[158] C. Alduino *et al.* (CUORE Collaboration), *Measurement of the Two-Neutrino Double Beta Decay Half-life of ^{130}Te with the CUORE-0 Experiment*, Eur. Phys. J. C **77**, 13 (2017).

[159] G. Wang *et al.* (CUPID Collaboration), *R&D towards CUPID (CUORE Upgrade with Particle IDentification)*, (2015), arXiv:1504.03612 [physics.ins-det] .

[160] G. Wang *et al.* (CUPID Collaboration), *CUPID: CUORE (Cryogenic Underground Observatory for Rare Events) Upgrade with Particle IDentification*, (2015), arXiv:1504.03599 [physics.ins-det] .

[161] D. R. Artusa *et al.* (CUORE Collaboration), *Exploring the Neutrinoless Double Beta Decay in the Inverted Neutrino Hierarchy with Bolometric Detectors*, Eur. Phys. J. C **74**, 3096 (2014).

[162] M. Vanzini *et al.*, *High-resolution bolometers for rare events detection*, Nucl. Instrum. Meth. A **461**, 293 (2001).

[163] R. Ardito and F. Perotti, *Seismic analysis of support structure for the CUORE experiment cryostat (in Italian)* (2011), INFN report (unpublished) [updated in 2016].

[164] F. Alessandria *et al.*, *The 4K outer cryostat for the CUORE experiment: Construction and quality control*, Nucl. Instrum. Meth. A **727**, 65 (2013).

[165] M. Barucci, L. Lolli, L. Risegari and G. Ventura, *Measurement of thermal conductivity of the supports of CUORE cryostat*, Cryogenics **48**, 166 (2008).

[166] M. Schwark, F. Pobell, W. P. Halperin, C. Buchal, J. Hanssen, M. Kubota and R. M. Mueller, *Ortho-para conversion of hydrogen in copper as origin of time-dependent heat leaks*, J. Low Temp. Phys. **53**, 685 (1983).

[167] M. Koláč, B. S. Neganov and S. Sahling, *Low Temperature Heat Release from Copper: Ortho-Para Conversion of Hydrogen*, J. Low Temp. Phys. **59**, 547 (1985).

[168] American Society of Mechanical Engineers (ASME), *Boiler & Pressure Vessel Code* (2010), Sec. VIII, Div. 1.

[169] J. S. Cushman *et al.*, *The detector calibration system for the CUORE cryogenic bolometer array*, Nucl. Instrum. Meth. A **844**, 32 (2017).

[170] K. J. Thomas, A. R. Smith, Y. D. Chan, E. B. Norman, B. S. Wang and D. L. Hurley, *Low background counting at the LBNL low background facility*, AIP Conf. Proc. **1549**, 20 (2013).

[171] S. Marcocci, F. Piastra and P. Gorla, *Hands on CUORE: investigation on the vibrations and temperature control of the cryostat*, Proc. of Science **(GSSI14)**, 023 (2015).

[172] E. Andreotti *et al.*, *The low radioactivity link of the CUORE experiment*, J. Instrum. **4**, P09003 (2009).

[173] A. Giachero, C. Gotti, M. Maino and G. Pessina, *Characterization of high impedance connecting links for Bolometric detectors*, Nucl. Instrum. Meth. A **718**, 229 (2013).

[174] V. Datskov, *CUORE wiring port heat load tests* (2011), internal report (unpublished).

[175] C. Ligi and M. Iannarelli, *CUORE wiring test at $T < 4\,K$* (2014), internal report (unpublished).

[176] C. Bigagli, *The Hispanic lead trade along the attested routes in the western Mediterranean basin (in Italian)*, Empúries **53**, 155 (2002).

[177] L. Pinarelli, D. Salvi and G. Ferrara, *The source of ancient Roman lead, as deduced from lead isotopes: the ingots from the Mal di Ventre wreck (western Sardinia, Italy)*, Sci. Technol. Cultural Heritage **4**, 79 (1995).

[178] P. R. Trincherini, C. Domergue, I. Manteca, A. Nesta and P. Quarati, *The identification of lead ingots from the Roman mines of Cartagena (Murcia, Spain): the role of lead isotope analysis*, J. Roman Archaeology **22**, 123 (2009).

[179] A. Alessandrello *et al.*, *Measurements of internal radioactive contamination in samples of Roman lead to be used in experiments on rare events*, Nucl. Instrum. Meth. B **142**, 163 (1998).

[180] G. Heusser, *Low-radioactivity background techniques*, Ann. Rev. Nucl. Part. Sci. **45**, 543 (1995).

[181] A. Alessandrello *et al.*, *Measurements on radioactivity of ancient roman lead to be used as shield in searches for rare events*, Nucl. Instrum. Meth. B **61**, 106 (1991).

[182] A. Alessandrello *et al.*, *Measurements of low radioactive contaminations using bolometric detectors*, Nucl. Instrum. Meth. B **83**, 539 (1991).

[183] M. Clemenza *et al.*, *Development of a multi-analytical approach for the characterization of ancient Roman lead ingots*, J. Radioanal. Nucl. Chem. **311**, 1495 (2017).

[184] R. F. Tylecote, *A History of Metallurgy* (Maney Publishing for the Institute of Materials, 1992) [2nd edition].

[185] R. Acquafredda *et al.*, *The OPERA experiment in the CERN to Gran Sasso neutrino beam*, J. Instrum. **4**, P04018 (2009).

[186] E. Gatti and P. F. Manfredi, *Processing the Signals From Solid State Detectors in Elementary Particle Physics*, Riv. Nuovo Cim. **9**, 1 (1986).

[187] J. L. Ouellet, *The Search for $0\nu\beta\beta$ Decay in ^{130}Te with CUORE-0*, (2015), [Ph. D. thesis, University of California - Berkeley].

[188] C. Arnaboldi, C. Bucci, S. Capelli, P. Gorla, E. Guardincerri, A. Nucciotti, G. Pessina, S. Pirro and M. Sisti, *The temperature stabilization system of CUORICINO: An array of macro bolometers*, IEEE Trans. Nucl. Sci. **52**, 1630 (2005).

[189] R. J. Corruccini, *Gaseous heat conduction at low pressures and temperatures*, Vacuum **7-8**, 19 (1959).

[190] E. Ferri, *Pulse Tubes characterization* (2013), Internal report (unpublished).

[191] J. W. Arblaster, *Thermodynamic Properties of Copper*, J. Phase Equil. Diff. **36**, 422 (2015).

[192] J. W. Arblaster, *Thermodynamic properties of lead*, Comput. Coupling Phase Diagrams Thermochem. **39**, 47 (2012).

[193] R. D. Mc Carty, *Thermodynamic Properties of Helium 4 from 2 to 1500 K at Pressures to 10^8 Pa*, J. Phys. Chem. Ref. Data **2**, 139 (2009).

[194] J. Engert, D. Heyer, J. Beyer and H. J. Barthelmess, *Noise thermometry at low temperatures: MFFT measurements between 1.6 K and 1 mK*, J. Phys. Conf. Ser. **400**, 05203 (2012).

[195] J. Beyer, D. Drung and A. Kirste, *A Magnetic-Field-Fluctuation Thermometer for the mK Range Based on SQUID-Magnetometry*, IEEE Trans. Appl. Supercond. **17**, 760 (2007).